

University of St Andrews



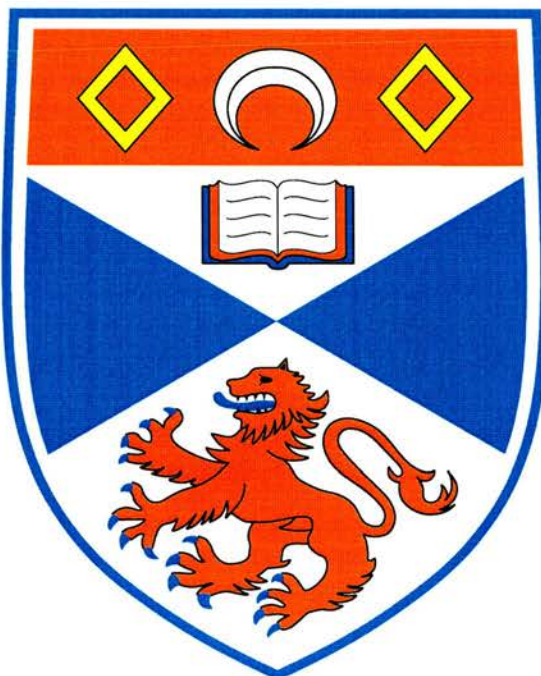
Full metadata for this thesis is available in
St Andrews Research Repository
at:

<http://research-repository.st-andrews.ac.uk/>

This thesis is protected by original copyright

Nature of 3D Magnetic Reconnection

David I. Pontin



Thesis submitted for the degree of Doctor of Philosophy of
the University of St Andrews

September 2nd, 2004

Th
E 720

Abstract

Magnetic reconnection is a fundamental process in many areas of plasma physics, whereby the magnetic field becomes restructured. It is a fundamentally non-ideal process, that is, it may occur only when the magnetic flux is allowed to break the ‘frozen in’ condition and ‘slip’ through the plasma in some finite region.

Much of the current understanding comes from two-dimensional theories, while little is known of the nature of reconnection in three dimensions. In this thesis, three-dimensional reconnection is described with the aid of a number of models, and particular attention is focussed upon the effect of the process on magnetic field lines and flux tubes. In each model, it is assumed that the reconnection takes place in a localised diffusion (non-ideal) region. It is found that the field line behaviour is very different from the two-dimensional case in a number of crucial ways.

Analytical solutions are presented which model steady kinematic reconnection at a three-dimensional null point. In these models the electric current lies parallel to either the spine or the fan of the null, and this current orientation is found to have a profound effect on the nature of the reconnection.

In order to test the results of kinematic models, a numerical experiment is performed, which solves the full equations of MHD, and models three-dimensional reconnection in the absence of a null point of the magnetic field.

One location where reconnection is very important is in the atmosphere of the Sun. The structure of the magnetic field there changes when *bifurcations* occur between different coronal *topologies*, and this requires reconnection. Here a classification of topologies due to three and four sources is described, as well as a model for predicting the occurrence of one such bifurcation.

Declaration

- (i) I, David I. Pontin, hereby certify that this thesis, which is approximately 38000 words in length, has been written by me, that it is the record of work carried out by me and that it has not been submitted in any previous application for a higher degree.

Name: David I. Pontin **Signature:**

Date: 7/10/04

- (ii) I was admitted as a research student in September 2001 and as a candidate for the degree of Doctor of Philosophy in September 2001; the higher study for which this is a record was carried out in the University of St Andrews between 2001 and 2004.

Name: David I. Pontin **Signature:**

Date: 7/10/04

- (iii) I hereby certify that the candidate has fulfilled the conditions of the Resolution and Regulations appropriate for the degree of Doctor of Philosophy in the University of St Andrews and that the candidate is qualified to submit this thesis in application for that degree.

Name: Eric R. Priest **Signature:**

Date: 7-10-04

- (iv) In submitting this thesis to the University of St Andrews I understand that I am giving permission for it to be made available for use in accordance with the regulations of the University Library for the time being in force, subject to any copyright vested in the work not being affected thereby. I also understand that the title and abstract will be published, and that a copy of the work may be made and supplied to any bona fide library or research worker.

Name: David I. Pontin **Signature:**

Date: 7/10/04

Acknowledgements

There are many people who deserve thanks for their contributions, direct or indirect, to this thesis.

Particular thanks must go to my supervisor, Eric Priest, for continual and invaluable advice and encouragement along the way. Various parts of the work contained within have been completed in collaboration with Gunnar Hornig and Klaus Galsgaard, to both of whom I am hugely grateful for their inspiration and most importantly patience. I am also grateful for many other useful discussions throughout my time in St Andrews, with various members (regular and guest) of ‘reco club’.

The completion of this thesis would not have been possible without a PhD scholarship from the Carnegie Trust. Furthermore, funding assistance to make the collaborations possible was provided by the European Community’s Human Potential Program, under the contract HPRN-CT-2000-00153, PLATON.

On a personal level, I would like to thank my family and friends for providing frequent welcome distractions from the equations. Last, but by no means least, I would like to thank my long-suffering office-mates over the three years, Rob, Danielle and Rhona, for participating in all of the nonsense, and sharing appreciation for the most important time of the week: Hammertime.

Contents

Contents	i
1 Introduction	1
1.1 Importance of magnetic reconnection	1
1.2 Equations of MHD	3
1.3 Two-dimensional reconnection	5
1.4 Structure of 3D null points	6
1.5 Flux and field line conservation	8
1.6 Aims and outline	9
2 Nature of reconnection	11
2.1 Introduction	11
2.2 2D kinematic reconnection solution	12
2.3 Reconnection with a local 3D region	16
2.4 Nature of 2D and 3D reconnection	20
2.4.1 Basic properties of 2D reconnection	20
2.4.2 Basic properties of 3D reconnection	22
2.5 3D reconnection in the absence of a null point	24
3 Kinematic reconnection at a magnetic null point: Spine-aligned current	27
3.1 Introduction	27
3.2 The model	29
3.3 Elementary solution	34
3.3.1 Induced flows	34
3.3.2 Reconnection rate	37
3.4 Composite solutions	39

3.4.1	$\varphi_0 > \varphi_{crit}$	40
3.4.2	$\varphi_0 < \varphi_{crit}$	42
3.4.3	Reconnection of flux tubes	44
3.5	Existence of perfectly reconnecting flux tubes and time dependence	46
3.6	Summary	51
4	Kinematic reconnection at a magnetic null point: Fan-aligned current	53
4.1	Introduction	53
4.2	The model	53
4.3	Nature and rate of reconnection	56
4.4	Non-existence of perfectly reconnecting field lines	60
4.5	Non-constant current	62
4.6	Summary	68
5	Numerical full MHD investigation of reconnection in the absence of null points	71
5.1	Introduction	71
5.2	The experiment	72
5.2.1	Numerical scheme	72
5.2.2	Experimental setup	75
5.3	Results of fixed- η runs	78
5.3.1	Electric current	79
5.3.2	Plasma flow	80
5.3.3	Field line behaviour	84
5.3.4	Importance of $E_{ }$	87
5.3.5	Full MHD runs	89
5.4	Results of current-dependent η runs	92
5.4.1	Electric current	92
5.4.2	Plasma velocity	95
5.4.3	Behaviour of flux and parallel electric field	98
5.5	Summary	101
6	A framework for understanding the topology of complex coronal structures	103
6.1	Introduction	103

6.2	Bifurcations	107
6.2.1	Euler characteristics	107
6.2.2	Local separator bifurcation	108
6.2.3	Tree diagram for three sources	109
6.2.4	Analytical model for local separator bifurcation	111
6.3	Three symmetric sources	113
6.3.1	Three positive sources	113
6.3.2	Two positive sources and one negative - Negative total flux	115
6.3.3	Two positive sources and one negative - Positive total flux	116
6.4	Three-source non-symmetric states	117
6.4.1	Zeros in the perpendicular field	117
6.4.2	Zeros in the parallel field	119
6.4.3	Bifurcation to touching state	122
6.4.4	Bifurcation to triangular state	124
6.5	More than three sources	125
6.5.1	Same-sign sources on bifurcation axis	126
6.5.2	Opposite-sign sources on bifurcation axis	126
6.5.3	Observed four-source locally-bifurcating states	129
6.5.4	More sources summary	129
6.6	Summary	131
7	Summary and future work	133
7.1	Summary	133
7.2	Future work	135
Appendix A	Flux and field line motion	139
A.1	Slippage with flux and field line conservation	140
A.2	Field line conservation without flux conservation	141
A.3	Field line and flux non-conservation	143
Appendix B	Diffusion of a toroidal flux tube	147
Appendix C	Non-existence of unique field line velocity in 3D	153
Appendix D	CD information	155

Appendix E	Maple commands	157
E.1	Input for maple worksheet <i>sp_rec_zsurf.mws</i>	157
E.2	Input for maple worksheet <i>fan_rec_jconst.mws</i>	161
E.3	Input for maple worksheet <i>fan_rec_spcross.mws</i>	166
E.4	Input for maple worksheet <i>fan_rec_fancross.mws</i>	168
Bibliography		175

Chapter 1

Introduction

“If we knew what it was we were doing it wouldn’t be called research, would it?”

Albert Einstein (1879 - 1955)

1.1 Importance of magnetic reconnection

Most of the matter in the universe is in the plasma state, and is threaded by a magnetic field, so that electromagnetic forces often have a significant effect on the dynamics of the plasma. In most of the universe, the magnetic field is ‘frozen into’ the plasma, and moves around with it. However, in some localised regions, the magnetic field lines are able to slip through the plasma, and may break and rejoin. This process of magnetic reconnection is a fundamental one in many areas of plasma physics.

Magnetic reconnection is responsible for many dynamic phenomena throughout the universe, as illustrated in our own heliosphere (for a comprehensive review, see Priest and Forbes (2000)). Reconnection is very important on the Sun, where it is thought to be at least partly responsible for heating the solar corona. Models for the generation of current concentrations in the corona have been put forward, such as *braiding* (Parker, 1979; Galsgaard and Nordlund, 1996) or *coronal tectonics* (Priest et al., 2002). The current concentrations, and thus the heating, are thought to accumulate at both *separatrix surfaces* and *separators* in the coronal magnetic field, leading to so-called *separatrix-surface reconnection*, such as *binary reconnection* between two adjacent flux sources (Priest et al., 2003b), and *separator reconnection* (e.g. Lau and Finn, 1990; Galsgaard et al., 2000; Parnell and Galsgaard, 2004). Reconnection is also thought to be the process which is behind many dynamic events on the Sun, such as *X-ray bright points* (see e.g. the

‘converging flux model’ of Parnell et al. (1994)), *explosive events* (e.g. Innes et al., 1997) and localised *compact flares* (see e.g. the ‘emerging flux model’ of Heyvaerts et al. (1977), Forbes and Priest (1984)), as well as large-scale *two-ribbon solar flares*, for which there are many different reconnection models, see for example Forbes (1988) or Priest and Forbes (2000) for a review. Furthermore, reconnection is crucial for the solar dynamo, which generates the Sun’s magnetic field in the solar interior (see Moffatt (1978) and Proctor et al. (1993) for comprehensive reviews).

Reconnection is also an important process closer to home in the Earth’s own magnetosphere. It may take place on the dayside of the magnetopause in a steady way in either *component merging* (Sonnerup et al., 1981) or *anti-parallel merging* (Crooker, 1979), as well as in *magnetospheric erosion* (Aubrey et al., 1970) and *flux transfer events* (e.g. Russell and Elphic, 1978). It is also thought to occur steadily at a distant nightside neutral point in the magnetotail, as well as closer to Earth on the nightside, causing *magnetospheric substorms* (e.g. Hones, 1973). For a review of these ideas, see Priest and Forbes (2000) and references therein.

Furthermore, reconnection is important in many astrophysical applications, see Mestel (1999) for a review. In particular, it is involved in models of *stellar flares* (see e.g. Mullan, 1986), in much the same way as in solar flares, as well as in models of *accretion disks* (Verbunt, 1982). In accretion disks, magnetic reconnection is invoked as a method of allowing the dissipation of angular momentum, and thus accretion, and the way in which this may occur has been modelled by, for example, Coroniti (1981) and Tout and Pringle (1992). Reconnection is also involved in models of *protostellar collapse* (Mestel and Strittmatter, 1967) and *extragalactic jets* (Romanova and Lovelace, 1992).

Finally, there are laboratory applications of reconnection theory. The principle application here is in nuclear fusion experiments, which it is hoped may some day provide a ‘clean’ sustainable energy source. In order to confine the plasma for the fusion to take place, a ‘magnetic bottle’ is used, where the plasma is contained within the fusion device with the aid of magnetic fields. In some such devices, for example *tokamaks* (see, e.g. Wesson (1997) for a review) magnetic reconnection, triggered by various different instabilities, is detrimental to the confinement process, and so is something to be avoided. In other devices, such as *reversed-field pinches* (e.g. Baker, 1984), *field-reversed configurations* (e.g. Milroy, 1984) and *spheromaks* (e.g. Finn and Guzdar, 1991), reconnection is essential in generating the confining magnetic field, by a kind of dynamo action. In addition, a large number of laboratory experiments, designed specifically to study the process of reconnection under various particular (often collisionless) plasma regimes, exist (see

e.g. Priest and Forbes (2000) and references therein).

1.2 Equations of MHD

In this thesis, the plasma will be assumed to obey the equations of magnetohydrodynamics (MHD). This MHD approximation is valid under certain assumptions, explained below. The equations of MHD are as follows: conservation of mass,

$$\frac{\partial \rho}{\partial t} + \nabla \cdot (\rho \mathbf{v}) = 0, \quad (1.1)$$

conservation of momentum (also known as the equation of motion),

$$\rho \frac{D\mathbf{v}}{Dt} = -\nabla P + \mathbf{j} \times \mathbf{B} + \mathbf{F}, \quad (1.2)$$

Gauss' law,

$$\nabla \cdot \mathbf{B} = 0, \quad (1.3)$$

Ampère's law,

$$\mathbf{j} = \frac{\nabla \times \mathbf{B}}{\mu}, \quad (1.4)$$

Faraday's equation,

$$\nabla \times \mathbf{E} = -\frac{\partial \mathbf{B}}{\partial t}, \quad (1.5)$$

Ohm's law,

$$\mathbf{E} + \mathbf{v} \times \mathbf{B} = \mathbf{R}, \quad (1.6)$$

the perfect gas law,

$$P = \mathcal{R}\rho T, \quad (1.7)$$

and finally an energy equation. In the above equations, \mathbf{B} is the magnetic field, \mathbf{E} the electric field, \mathbf{j} the current density, ρ the plasma density, P the pressure, μ the magnetic permeability, \mathcal{R} the gas constant and T the temperature. In Equation (1.2), \mathbf{F} denotes

other forces which may be present, for example the force of gravity, and in Equation (1.6), \mathbf{R} denotes a general *non-ideal* term, often taken to be \mathbf{j}/σ , where σ is the electric conductivity. In this case, Equations (1.6), (1.4) and (1.5) are often combined to give the induction equation

$$\frac{\partial \mathbf{B}}{\partial t} = \nabla \times (\mathbf{v} \times \mathbf{B}) + \eta' \nabla^2 \mathbf{B}, \quad (1.8)$$

where the magnetic diffusivity, $\eta' = 1/(\mu\sigma)$, is assumed to be constant. (In this thesis, η' will be used to denote the diffusivity, $1/(\mu\sigma)$, while η will be used to denote the electric resistivity, $1/\sigma$.)

The above equations are based upon a number of assumptions. Firstly, the plasma is assumed to behave as a single fluid, and is treated as a continuum, valid provided the typical length scales investigated are much larger than internal plasma lengths, such as the mean free path and the ion gyro-radius. It is also assumed that all speeds are non-relativistic, that is they are very much less than the speed of light. Furthermore, we assume quasi-neutrality, and that the magnetic permeability is equal to its vacuum value.

In the induction equation (1.8), the order of magnitude of the ratio of the first to the second term on the right hand side is known as the magnetic Reynolds number, given by

$$R_m = \frac{L_0 v_0}{\eta'}, \quad (1.9)$$

where L_0 is a typical length scale for variations and v_0 is a typical plasma velocity. In reality, R_m is typically very large, meaning that the magnetic field is frozen to the plasma, such that all plasma elements lying along a given field line at a given time will lie on the same field line for all subsequent time. The exception is in well localised regions where the length scales may collapse down to very small values. When this happens, the magnetic field lines may slip through the plasma. This leads to the concepts of conservation (or non-conservation) of flux and field lines, described in Section 1.5.

Derivations of the equations described in this section, as well as a more in-depth discussion of the conditions under which they are valid, may be found in, for example, Priest (1982) and Boyd and Sanderson (2003).

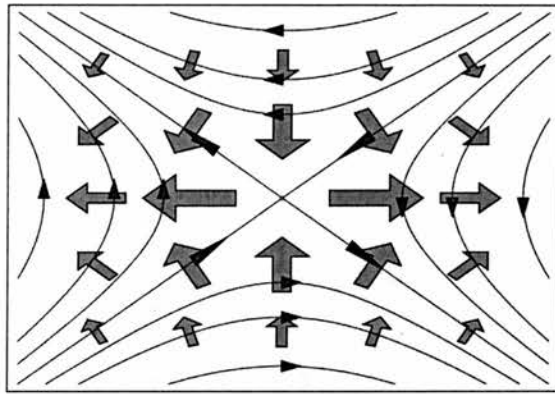


Figure 1.1: Two-dimensional reconnection at an X -point. The thin lines are magnetic field lines and the bold arrows indicate the direction of the plasma flow.

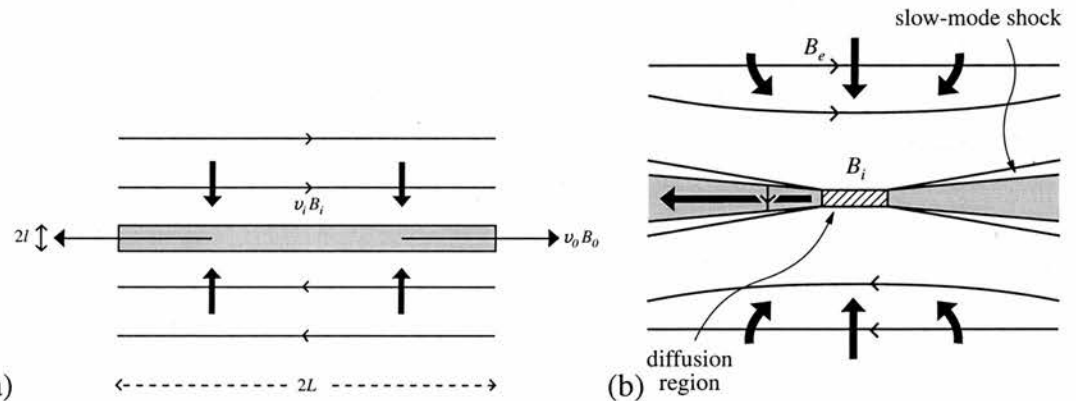


Figure 1.2: (a) The Sweet-Parker mechanism for 2D reconnection. (b) Petschek's mechanism for fast reconnection in 2D.

1.3 Two-dimensional reconnection

In two dimensions, reconnection occurs at hyperbolic null points of the magnetic field, commonly known as X -points (see Figure 1.1). A plasma flow transports magnetic flux towards the X -point, where the reconnection takes place, and the flow then transports the reconnected magnetic flux away from the X -point. The first model for such a process was the Sweet-Parker mechanism (Sweet, 1958), which provides an order-of-magnitude calculation of the energy which may be released when a current sheet is sandwiched between two regions of uniform oppositely-directed magnetic field (see Figure 1.2(a)). The inflow magnetic field and velocity are denoted by B_i and v_i . By considering simply the principles of conservation of mass into and out of the sheet, and a steady balance of advection and diffusion, it can be shown that a (dimensionless) reconnection rate of

$$M_i = \frac{1}{\sqrt{R_{mi}}} \quad (1.10)$$

is obtained, where $R_{mi} = Lv_{Ai}/\eta'$ is the magnetic Reynolds number based on the inflow Alfvén speed ($v_{Ai} = B_i/\sqrt{\mu\rho}$) and the sheet length (L). It can also be shown that half of the inflow magnetic energy is converted into kinetic energy, while the other half is released in the form of an ohmic heating.

The main shortcoming of the Sweet-Parker mechanism is that the energy released is insufficient to explain the energy release in solar flares, which was its main purpose. Consequently, numerous more sophisticated models have since been developed. Petschek (1964) proposed a model in which the Sweet-Parker diffusion region is very much smaller, and bifurcates at each end to form pairs of standing slow-mode shocks. Also, the magnetic field in the inflow region is now no longer exactly uniform (see Figure 1.2(b)). It is in the shocks that much of the extra energy conversion of Petschek's mechanism takes place. The smaller the size of the diffusion region, the more energy is released, and the more steeply-angled to the horizontal the shocks become. The reconnection rate thus varies depending on the geometry of the system, although there is a maximum allowable reconnection rate, given by

$$M_{e\ max} = \frac{\pi}{8 \ln R_{me}} \quad (1.11)$$

above which the mechanism chokes itself off since B_i becomes too small. Here, $M_{e\ max}$ is the ratio of the inflow and inflow Alfvén speeds $M_e = v_e/v_{Ae}$ and $R_{me} = L_e v_{Ae}/\eta'$ is the global magnetic Reynolds number based on the overall length scale (L_e). This maximum reconnection rate is typically considerably larger than the slow Sweet-Parker rate.

Many other models for two-dimensional reconnection have subsequently been proposed, including families of Almost Uniform (Priest and Forbes, 1986) and Non-Uniform (Priest and Lee, 1990) solutions. An in-depth review of 2D reconnection models can be found in Priest and Forbes (2000). Each of these models requires that an X-type null point of the magnetic field has collapsed to form a current sheet. Models for how this may occur are described, for example, by Imshennik and Syrovatsky (1967), Bulanov and Olshanetsky (1984), Klapper (1998) and Mellor et al. (2002). Each of these models however provides only a spatially linear analysis, describing the collapse only locally.

1.4 Structure of 3D null points

In three dimensions reconnection may either take place at a null point (at which $\mathbf{B} = 0$), as in 2D, or in the absence of a null point (Schindler et al., 1988; Lau and Finn, 1990).

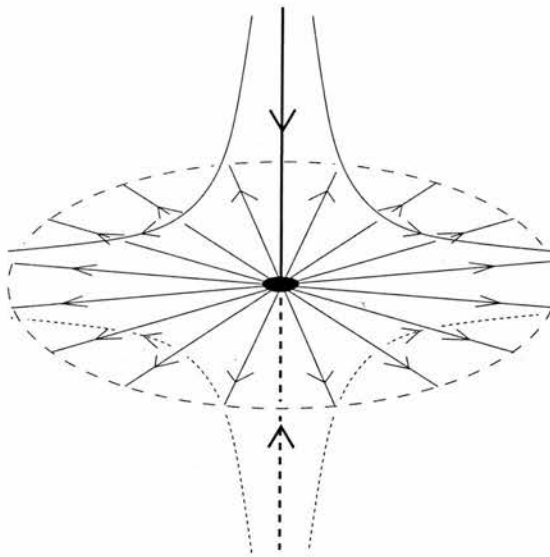


Figure 1.3: The basic structure of a 3D null point; the thick line is the spine field line, while the fan surface is marked out by the dashed circle.

In later chapters, reconnection at three-dimensional null points will be discussed, and so an introduction to them is given here. The local structure of the magnetic field around a three-dimensional null point is shown in Figure 1.3 (see also e.g. Cowley, 1973; Greene, 1988; Lau and Finn, 1990). The *skeleton* of the null point is made up of a pair of field lines directed into (or out of) the null from opposite directions, known as the *spine*, and a family of field lines which are directed out of (or into) the null lying in a surface, known as the *fan* plane (Priest and Titov, 1996).

A general mathematical formalism is given by Parnell et al. (1996), who classify nulls depending, amongst other things, on the size of the current, j , and its direction with respect to the spine axis and fan plane. If the current is zero then the null point is known as *potential*. In this case the null appears as in Figure 1.3; the spine and fan are perpendicular, and field lines in the fan point in a purely radial direction. However, when there is a current present directed *parallel* to the spine ($j = j_{||}$), the field lines in the fan form a spiral structure, while the fan and spine are perpendicular. In contrast, when the current is directed only *perpendicular* to the spine ($j = j_{\perp}$), the spine and fan are no longer orthogonal. In general, when the current has components in both directions, both of these effects are present, as well as further characteristics, depending on the relative magnitudes of $j_{||}$ and j_{\perp} . See Parnell et al. (1996) and Parnell et al. (1997) for a full description.

1.5 Flux and field line conservation

The idea of reconnection of magnetic field lines requires the concept of motion of those field lines (see e.g. Alfvén, 1950; Newcomb, 1958). In an ideal plasma (satisfying Equation (1.6) with $\mathbf{R} = 0$), a result of Alfvén's frozen flux theorem is that *magnetic flux conservation* and *magnetic field line conservation* hold. For the magnetic flux to be conserved, it is required that the magnetic flux through any closed loop which moves with the plasma (a loop made up of plasma elements) remains constant. Magnetic field line conservation, on the other hand, requires that any two plasma elements which are initially joined by a field line will remain connected by a field line for all time.

The process of magnetic reconnection, however, requires that non-ideal terms be present. In a non-ideal plasma the conservation of magnetic flux and field lines does not necessarily hold, although neither need it necessarily be broken. In general, for a plasma which obeys Ohm's law in the form given in Equation (1.6), the conditions under which flux and field line conservation still hold are as follows. If the condition

$$\nabla \times \mathbf{R} = 0 \quad (1.12)$$

holds then the flux is conserved. Similarly the condition

$$\mathbf{B} \times (\nabla \times \mathbf{R}) = 0 \quad (1.13)$$

implies field line conservation (see e.g. Hornig and Schindler, 1996; Priest and Forbes, 2000). From these two conditions it can be seen that flux conservation implies field line conservation, but not vice-versa. In a non-ideal plasma, three possible behaviours exist. Firstly, the magnetic field may slip through the plasma, though both flux and field line conservation may hold. Secondly, we may have slippage with field line conservation but no flux conservation, and lastly we may have a situation where neither the flux nor the field lines are conserved. Examples illustrating these concepts are included in Appendix A.

In this thesis, the breakdown of the magnetic connection of plasma elements, i.e. the violation of field line conservation, will be used as a definition of reconnection, as described by Schindler et al. (1988). For a full discussion of the concepts of flux and field line conservation, and their relation to the conservation of magnetic topology, see Hornig and Schindler (1996) or Priest and Forbes (2000).

1.6 Aims and outline

It is the aim of this thesis to provide a description of the fundamental process of three-dimensional magnetic reconnection. The contrast between the way in which reconnection takes place in 2D and in 3D is discussed. In particular, the behaviour of the magnetic flux in the reconnection, and the resulting restructuring of this flux, is focussed upon.

In Chapter 2 an introduction is given to the fundamental differences between the nature of reconnection in two and three dimensions. This is done with the help of new solutions for 2D reconnection and so called two-and-a-half-dimensional reconnection. Chapters 3 and 4 present models for kinematic reconnection taking place at magnetic null points and in the presence of localised non-ideal regions. In Chapter 3 the reconnection takes place at a null point with current directed parallel to the spine line. The solutions presented in Chapter 4 model kinematic reconnection at a null point with current directed locally parallel to the fan plane. The solutions given in these chapters are shown to confirm the properties described in Chapter 2. In Chapter 5 a numerical experiment is described which investigates the nature of 3D reconnection in the absence of a magnetic null point, but once again in the presence of a localised non-ideal region. This simulation, in which the full MHD equations are solved, is shown to confirm the results of the kinematic models described in previous chapters. In Chapter 6 an application of reconnection in the solar corona is explored. The magnetic charge topology approach to modelling coronal fields is introduced. In this model, states are classed according to the structure of their skeleton, describing the topology. This topology changes in bifurcations, and a model describing a way of predicting the necessary conditions for one of the fundamental bifurcations is presented. Finally, in Chapter 7 a summary and suggestions for further work are given.

Chapter 2

Nature of reconnection

*"The line it is drawn
The curse it is cast
The slow one now
Will later be fast
As the present now
Will later be past
The order is
Rapidly fadin'.
And the first one now
Will later be last
For the times they are a-changin'."*

Bob Dylan, The Times They are A-Changin'

2.1 Introduction

In this Chapter, the basic structure of reconnection in 2D and 3D is discussed. It transpires that the way in which the magnetic flux is restructured during the two processes is fundamentally different. These differences are illustrated by the solutions presented below. In this chapter, we focus on the implications of kinematic solutions; that is, we solve only Maxwell's equations (1.3, 1.4, 1.5) and a resistive Ohm's law,

$$\mathbf{E} + \mathbf{v} \times \mathbf{B} = \eta \mathbf{j}, \quad (2.1)$$

but we do not solve the equation of motion (1.2). Furthermore, a steady solution is assumed, so that Equation (1.5) implies that $\mathbf{E} = E \hat{\mathbf{z}}$ in 2D, while in 3D, $\mathbf{E} = \nabla\Phi$, where Φ is some scalar function. One further requirement which is imposed is that the non-ideal region, i.e. the region in which the term on the right-hand side of (2.1) is non-zero, must be localised. We consider a finite non-ideal region (D) as the generic situation for astrophysical plasmas, since these plasmas have extremely high magnetic Reynolds numbers, and dissipation is enhanced only in well localised regions, for example when the presence of strong electric currents may drive micro-instabilities.

In this and the following chapters, the effect of different types of reconnection on magnetic flux tubes will be described. Due to the simplicity of the magnetic fields used in the models, these flux tubes are all initially untwisted, although in general flux tubes with a finite amount of twist would be generic in three dimensions. The reconnection of isolated twisted and untwisted flux tubes has been investigated in a series of numerical experiments (Linton et al., 2001; Linton and Antiochos, 2002; Linton and Priest, 2003). The extreme case of a highly twisted flux tube would be a flux tube in which the magnetic flux is purely toroidal. In Appendix B the behaviour of such an isolated toroidal flux tube under diffusion is investigated. The magnetic field is taken to be initially $\mathbf{B}(t = 0) = B_0 \delta(r - R)\hat{\theta}$, where B_0 and R are constant, and it is shown that the toroidal flux all diffuses and annihilates at the origin.

2.2 2D kinematic reconnection solution

In order to contrast the new properties of three-dimensional reconnection with the familiar properties of reconnection in 2D, a two-dimensional solution is first described here. In order to obtain a physically acceptable solution, with all physical quantities continuous and smooth, the magnetic field and resistivity are first prescribed. The magnetic field is chosen to be a simple linear 2D X-point,

$$\mathbf{B} = (y, kx, 0), \quad (2.2)$$

where k is a constant, so that $\mathbf{j} = (k - 1)/\mu \hat{\mathbf{z}}$. The resistivity is defined as

$$\eta(x, y) = \eta_0 \begin{cases} ((k^2 x^2 + y^2) - 1)^2 & k^2 x^2 + y^2 < 1 \\ 0 & \text{otherwise,} \end{cases} \quad (2.3)$$

where η_0 is a constant. The profile of η is shown in Figure 2.1(a).

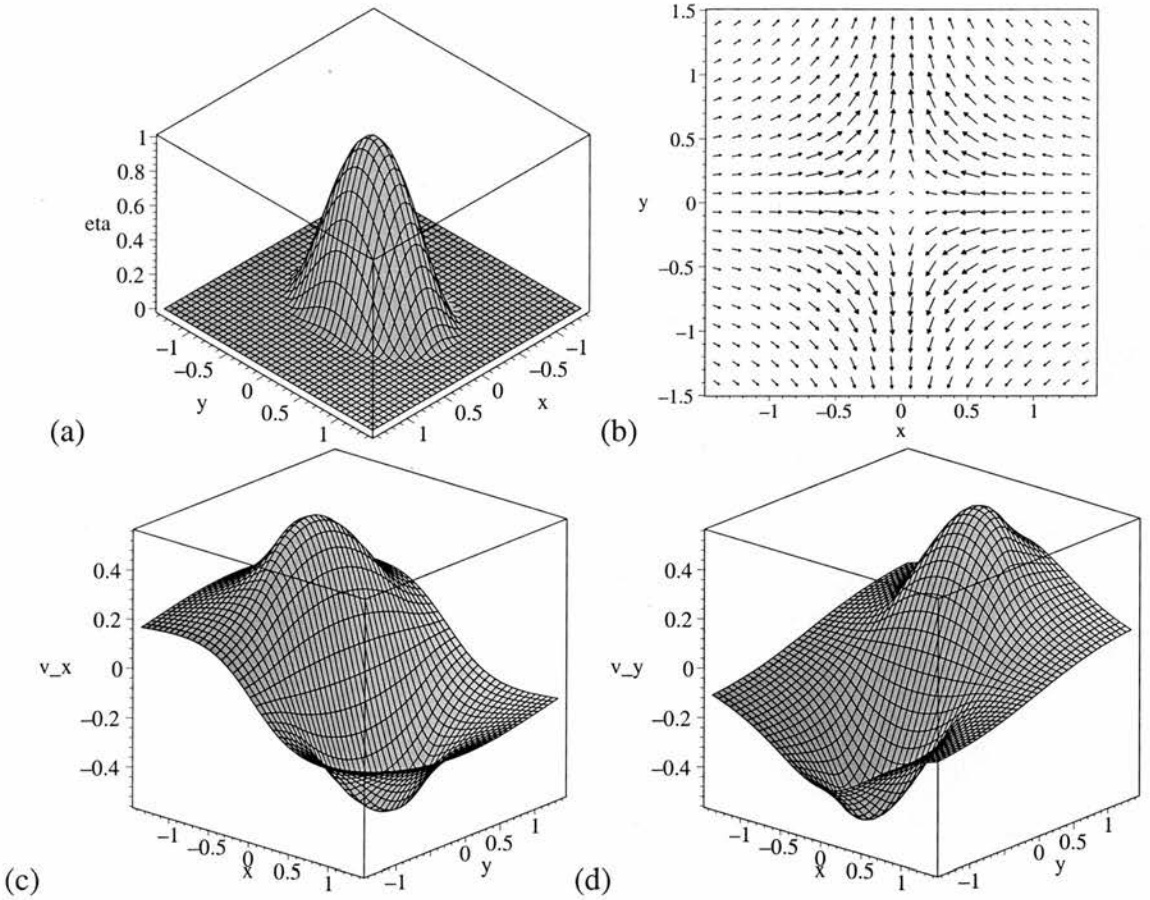


Figure 2.1: (a) Plot of η for parameters $\eta_0 = 1$, $k = 1.5$. (b), (c) and (d) show the plasma velocity for the same parameters.

In order to calculate the corresponding plasma velocity, or at least the component (v_{\perp}) of v perpendicular to B , take the vector product of Equation (2.1) with B to give

$$v_{\perp} = \frac{(\mathbf{E} - \eta \mathbf{j}) \times \mathbf{B}}{B^2} \quad (2.4)$$

$$= \frac{1}{R_1^2} \begin{cases} \left(E - \frac{\eta_0(k-1)}{\mu} (R_1^2 - 1)^2 \right) (-kx, y) & R_1^2 < 1 \\ E (-kx, y) & \text{otherwise,} \end{cases} \quad (2.5)$$

where $R_1^2 = k^2x^2 + y^2$. Notice that it is necessary that the value of E be chosen so as to keep the plasma velocity non-singular at the origin. To have $|v| = 0$ at the origin requires

$$E = \eta_0(k - 1)/\mu. \quad (2.6)$$

With this choice of E , the velocity takes the form of a smooth stagnation flow, shown in Figure 2.1(b-d).

In order to investigate the evolution of magnetic flux it is useful to define a flux trans-

porting velocity \mathbf{w} (Hornig and Schindler, 1996; Hornig and Priest, 2003) which satisfies

$$\mathbf{E} + \mathbf{w} \times \mathbf{B} = 0, \quad (2.7)$$

which is possible in two dimensions since the electric field (\mathbf{E}) is always perpendicular to \mathbf{B} . By comparison with an ideal Ohm's law, \mathbf{w} can be considered to be a flow within which the magnetic flux is frozen. The component of \mathbf{w} perpendicular to \mathbf{B} can be found from (2.7) to be

$$\mathbf{w}_\perp = \frac{\mathbf{E} \times \mathbf{B}}{B^2}. \quad (2.8)$$

The component of \mathbf{w} parallel to \mathbf{B} is usually assumed to be zero, so that the above gives an expression for \mathbf{w} itself. Note that for reconnection to take place, the flux transporting velocity \mathbf{w} must become singular at the null point, which is a signature of the breaking of the field lines (Hornig, 2001). Here, \mathbf{w} takes the form

$$\mathbf{w} = \frac{\eta_0(k-1)}{(y^2 + k^2x^2)\mu} (-kx, y, 0). \quad (2.9)$$

The evolution of the magnetic flux in this process is visualised as follows. Two flux tubes are picked out which initially lie in the inflow regions on opposite sides of the diffusion region. Each flux tube is then traced out at each time by integrating the field lines from two cross-sections, one at either end of each tube. These cross-sections are allowed to evolve in the ideal flow, and are chosen such that they never pass into the non-ideal region (see Figure 2.2). The cross-sections are chosen in this way so as to ensure that the same field lines are always traced at each time, because in the ideal region the field is frozen to the flow, so field lines may be identified by plasma elements there. The fact that each tube is traced from an ideal cross-section at each end will become important in later examples, which are described with the help of similar animations. Moreover, the flux tubes are chosen initially to be symmetric about $x = 0$.

The way in which the flux tubes evolve in the reconnection process is shown in Figure 2.3, which shows frames from the movie contained on the accompanying CD. Note that, although the non-ideal region (D) is of significant size within the box shown, the flux tubes traced from either end remain connected until they reach the X-point at $(0, 0)$. At the X-point the field lines which form the flux tubes are cut and rejoined, and finally two unique reconnected flux tubes move away from the X-point in opposite quadrants. Once again, while passing through the diffusion region and moving away from the X-point, the

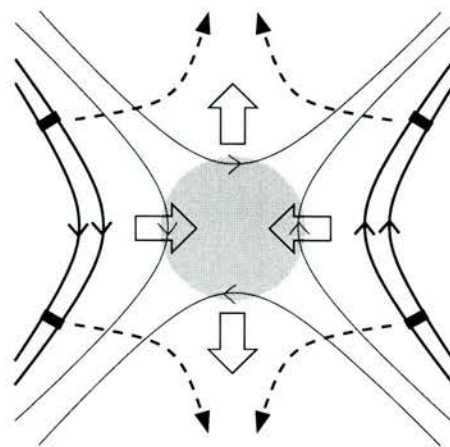


Figure 2.2: The choice of cross-sections (thick black bars) from which the flux tubes are traced ensures that the paths they follow (dashed lines), as they move in the ideal flow, never take them into the non-ideal region (shaded).

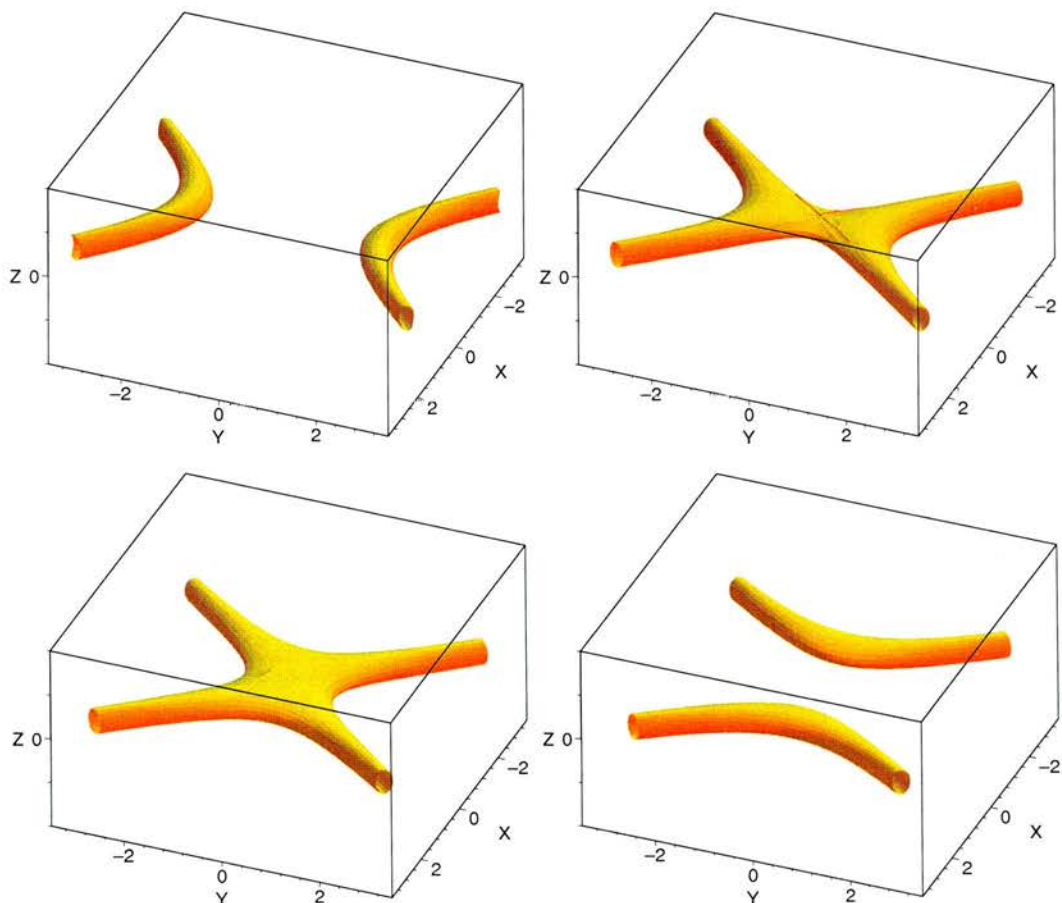


Figure 2.3: Flux tube reconnection in two dimensions (frames from the animation ‘2D.mpg’, contained on the accompanying CD).

flux tubes slip through the plasma, but remain connected. Finally they leave D and are carried away in the ideal flow.

2.3 Reconnection with a local 3D region

As a first step towards understanding the structure of magnetic reconnection in 3D, it is useful to consider so-called *two-and-a-half-dimensional* magnetic fields. Such a magnetic field has components in all three coordinate directions, but depends only upon two of those coordinates.

Consider a magnetic field which is the same as the familiar 2D X-point except within a small region close to the X-point. For example, let

$$\mathbf{B} = B_0 \left(y, kx, b_0 e^{-(x^2+y^2)/a^2} \right), \quad (2.10)$$

where B_0 , b_0 , a and k are constants, and a may be chosen so that B_z is localised within the non-ideal region. Now, suppose that within the 2D (ideal external) region there exists some solution for the plasma velocity which has a stagnation point structure as in the case where the magnetic field is 2D everywhere. If this is the case, then the nature of the reconnection may be investigated, as before, by simply tracing field lines which pass through cross-sections moving in the flow in the 2D region. The resulting evolution of the magnetic field lines is very different from the 2D case. This is shown in Figure 2.4 (the full animation is once again available on the CD), where the reconnection of flux tubes is shown for the magnetic field above. The magnetic field structure is chosen to be the same in the ideal region as the 2D case described in the previous section, and so the velocity with which the cross-sections are moved is taken to be the same as well. Note, however, that the nature of the motion of the field lines is independent of the exact flow, so long as this flow crosses the *quasi-separatrices* of the field. These *quasi-separatrices* (Priest and Démoulin, 1995) lie on the lines where separatrices would lie in the absence of a B_z component, i.e. along $y = kx$.

As the flux tubes move in the ideal 2D region the situation is as before- they are advected in towards the origin in the ideal flow. However, as soon as they enter the non-ideal region, each flux tube starts to split. This is because the paths traced along B from opposite cross-sections are no longer unique, for those field lines which have entered the non-ideal region. This splitting continues until all of the field lines have passed into the non-ideal region. When this happens the two initial flux tubes become completely

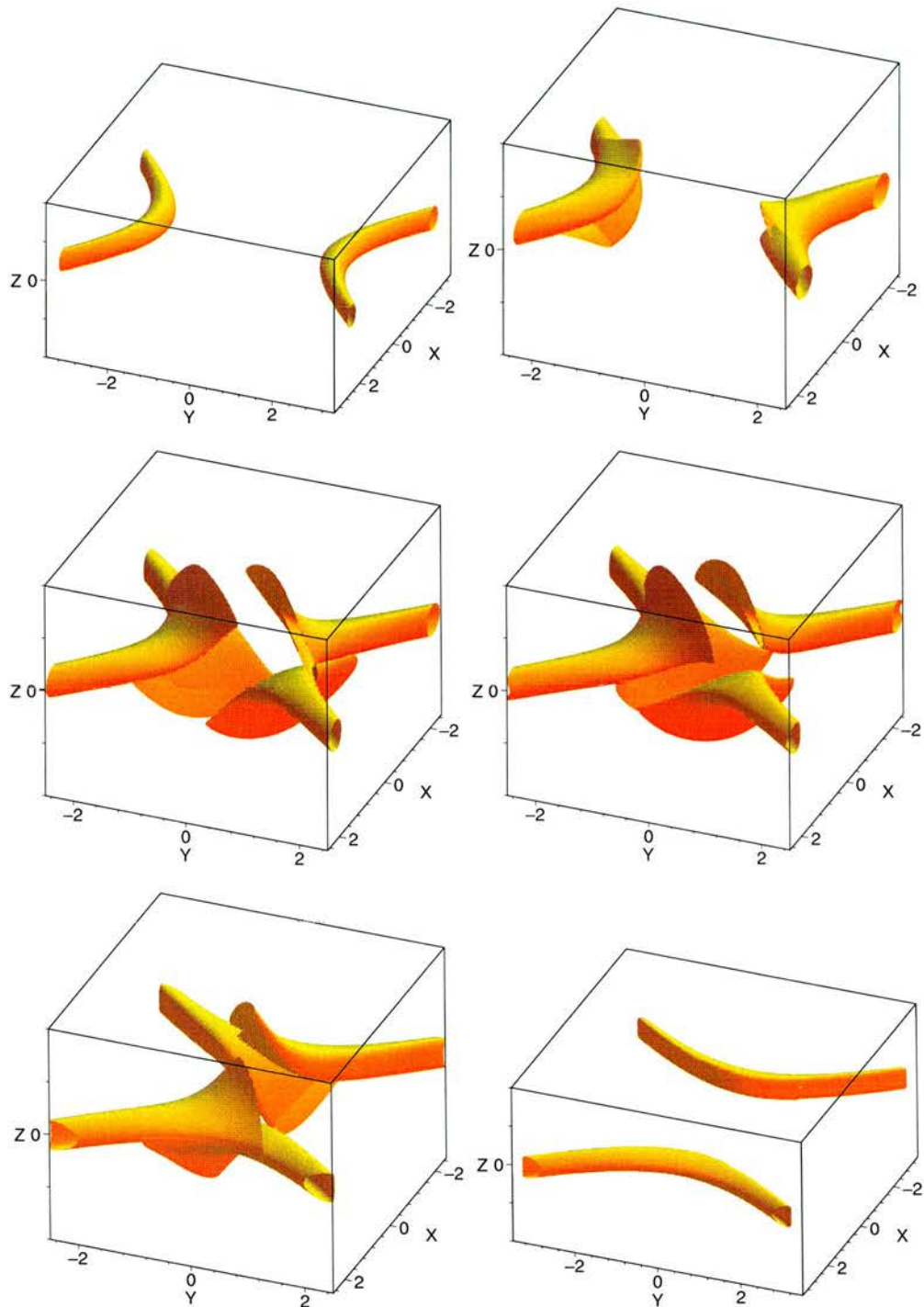


Figure 2.4: The behaviour of reconnecting flux tubes when a localised 3D region exists within the non-ideal region (see ‘*flip_loc.mpg*’ on the CD).

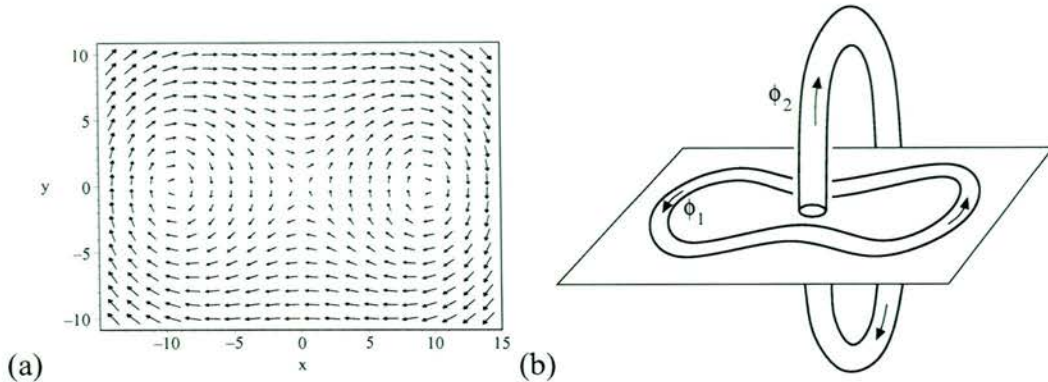


Figure 2.5: (a) Plot of \mathbf{B}_{glob} in the xy -plane, for $B_0 = 1$, $k = 1.5$. (b) Schematic of the global structure of the flux for a single closed flux tube before reconnection.

separated, and in fact the four cross-sections define four unique flux tubes. Note that, in the images in Figure 2.4, the tracing of field lines in towards the centre of the volume is only performed for a certain distance along the field. This is done simply for clarity, since, if the flux tubes were traced all the way through the box, then they would fan out across the top and bottom of the box and obscure the rest of the image. As the flux tube cross-sections are advected across the quasi-separatrices of \mathbf{B} , the ‘fans’ of the reconnecting flux tubes ‘flip’ quickly past each other. The four flux tubes then coalesce into two unique tubes once again as they leave the diffusion region.

Although the initial and final configurations for the two reconnection processes depicted in Figures 2.3 and 2.4 are the same, the behaviour of the magnetic flux during the processes is very different. This illustrates that, as soon as the symmetry of the 2D situation is broken, the reconnection is very different. A number of different properties of reconnection in 3D are described in the next section. It is instructive, however, to consider a couple of aspects of the present example, which show that in three dimensions the reconnection must actually be much more complicated.

Firstly, consider the effect of the reconnection process described above on the global magnetic field. Consider the magnetic field

$$\mathbf{B}_{\text{glob}} = B_0 \left(y + \frac{1}{2^7} (x^2 y + y^3), kx - \frac{1}{2^7} (x y^2 + 2x^3), b_0 e^{-(x^2+y^2)/a^2} \right), \quad (2.11)$$

where B_0 , k and b_0 are again constant. The structure of this magnetic field in the xy -plane is shown in Figure 2.5(a), and is approximately the same as the local magnetic field, described in the previous section, in the vicinity of the reconnection region, and where the flux tube cross-sections are situated. Allowing the flux tube cross-sections to once again evolve in the quasi-separatrix crossing flow has the effect on the flux tubes

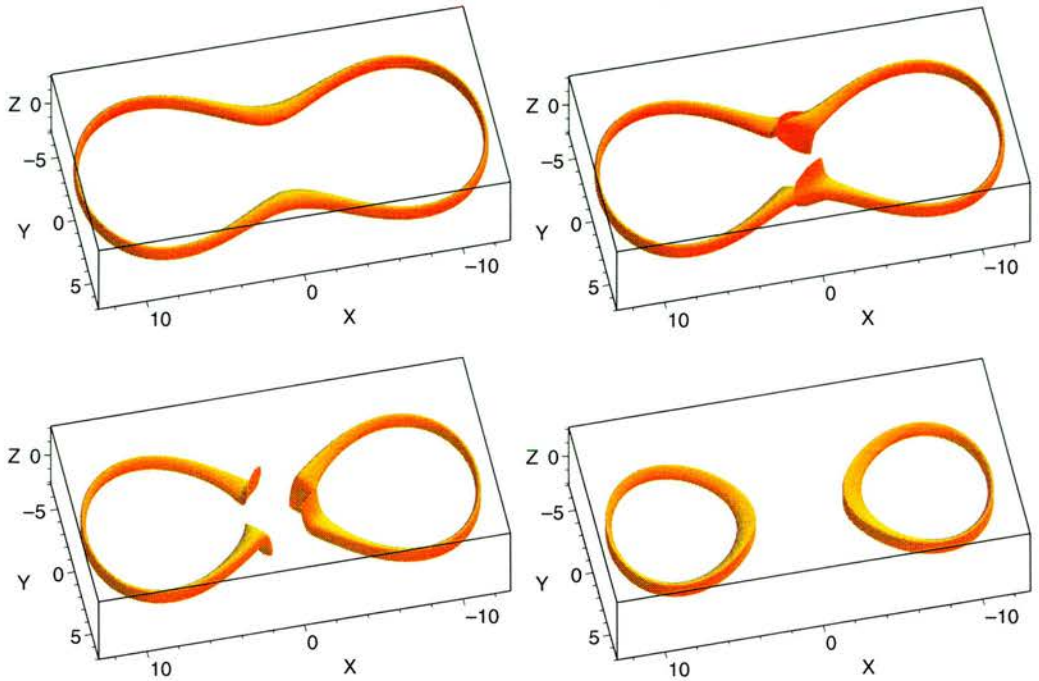


Figure 2.6: The global behaviour of the reconnecting flux tubes for a localised 3D region within the non-ideal region (see ‘*flip_glob.mpg*’ on the CD).

displayed in Figure 2.6. Once again a movie is shown on the accompanying CD.

First of all, it can be seen that the topology of the flux tube has changed, from being a single closed tube to two closed tubes. At a first glance it might appear that, as in 2D reconnection, there is no change of helicity in the process; since the field in the ideal region is 2D, the initial and final tubes are untwisted and lie in the same plane, and so their mutual and self helicities are all zero. However, since in fact there is a non-vanishing B_z component in the region of the z -axis, an analysis of the process should be completed by the inclusion of a flux tube running up the z -axis, which might be assumed to be closed at some distance from the reconnection region, as shown in Figure 2.5(b). Then, in fact, the helicity before the reconnection process is given by $2\phi_1\phi_2$, where ϕ_1 and ϕ_2 are the two magnetic fluxes, as shown in Figure 2.5(b), and the flux denoted by ϕ_2 is assumed to be untwisted. Once the field has reconnected in the plane, the vertical flux is still present in the vicinity of the z -axis, but there is now clearly no flux linkage, and so the helicity is zero. This violates the approximate conservation of helicity under reconnection (see e.g. Berger, 1984; Berger, 1999), since the fluxes ϕ_1 and ϕ_2 may be chosen to be arbitrarily large, and so is one indication that such a simple extension of 2D reconnection into 3D is not acceptable.

A further indication that the extension of 2D reconnection into three-dimensions is

not this simple can be seen by considering the nature of the field line velocity \mathbf{w} . If one naively assumes, as above, that a similar solution exists for the plasma velocity and field line velocity (\mathbf{w}), then unphysical effects are introduced in 3D. From (2.8), \mathbf{E} is given by $\mathbf{E} = -\mathbf{w} \times \mathbf{B}$. In 2D this results in a constant electric field (in the steady case) in the z -direction. However, if B_z is non-zero, then there are extra non-zero components in the electric field, for example $E_x = w_y B_z$, which is singular at the origin due to the singularity in \mathbf{w} . Clearly a singular electric field is unphysical.

Although the above two considerations illustrate the necessity for a more complicated reconnection process, and for a more sophisticated solution, in 3D, the basic nature of the field line motion found is still valid. In particular, in 3D reconnection, flux tubes break as soon as they enter the non-ideal region, and flip through the plasma as four unique flux tubes. This, as well as a number of other new properties of 3D reconnection, is described in the following section.

2.4 Nature of 2D and 3D reconnection

It can be shown, simply by considering the implications of Ohm's law, that there are a number of fundamental differences between the behaviour of the magnetic flux in 2D reconnection and 3D reconnection. These differences are described by Priest et al. (2003a), and are summarised below. In order to fully understand the differences between the two processes, it is instructive to first describe some of the basic properties of 2D reconnection. Although many of these properties may appear to be obvious, they are not usually explicitly stated, but rather implicitly assumed. It turns out that many of these underlying properties are not present for reconnection in three dimensions.

2.4.1 Basic properties of 2D reconnection

1. In two dimensions, a field line velocity (\mathbf{w}) always exists, satisfying

$$\frac{\partial \mathbf{B}}{\partial t} = \nabla \times (\mathbf{w} \times \mathbf{B}). \quad (2.12)$$

\mathbf{w} is the same as the plasma velocity (\mathbf{v}) in ideal regions, and is the velocity with which the field lines slip through the plasma in non-ideal regions. Also, \mathbf{w} is smooth and differentiable everywhere except at null points, where it has a hyperbolic singularity, signifying the breaking of magnetic field lines there. For an example, see

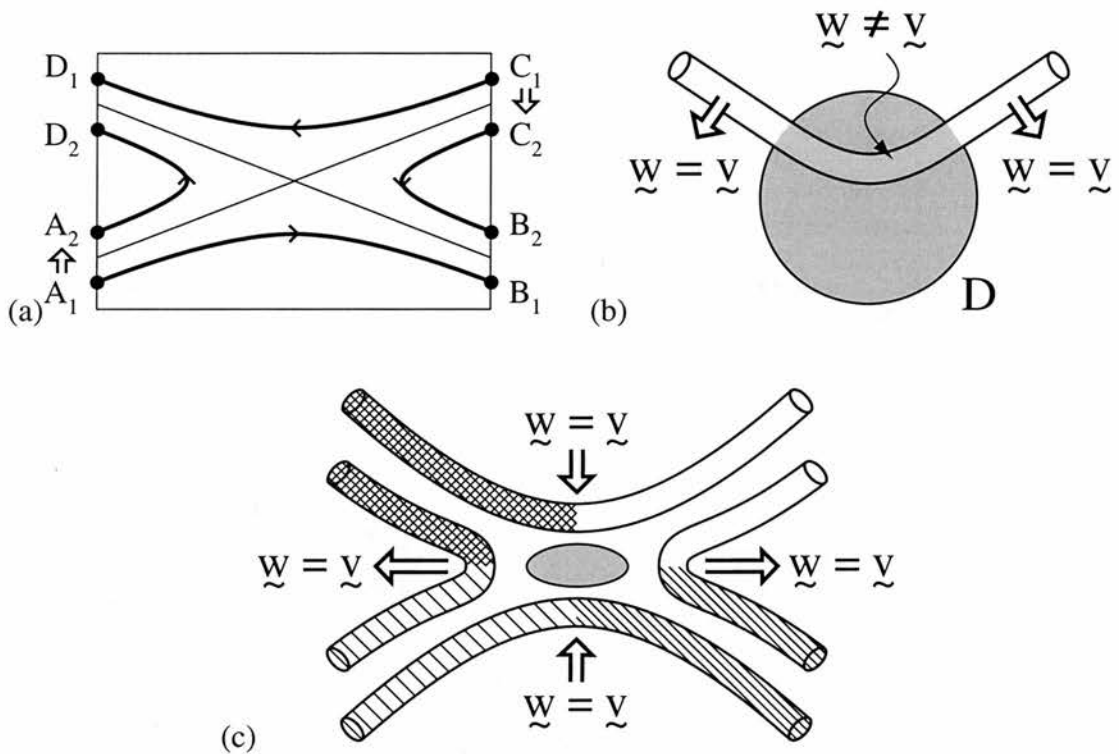


Figure 2.7: In two dimensional reconnection: (a) the mapping of field line footpoints, (b) motion of a flux tube passing through the non-ideal region, and (c) the breaking and rejoining of flux tubes.

Section 2.2.

2. While within a non-ideal region, field lines retain their connections until they reach the X-point. That is to say, field line conservation holds everywhere except at the separatrices of the null. Once the field lines lie on the separatrices of the null, they break and are rejoined at the null point, changing the connectivity.
3. The mapping between field line footpoints is discontinuous. Consider the schematic X-point shown in Figure 2.7(a). For example, as the field line anchored at footpoint A_1 moves towards the separatrix, it is connected to B_2 on the opposite boundary. However, as A_1 moves across the separatrix (to A_2) it suddenly becomes connected to a point D_2 on the same boundary as itself. This discontinuous mapping is a consequence of the fact the field lines break only at a single point.
4. A field line (or flux tube) which lies partly within the non-ideal region moves with the plasma velocity (v) everywhere outside the non-ideal region (see Figure 2.7(b)). Within the non-ideal region it slips through the plasma at the velocity w .
5. For every flux tube which is going to reconnect (in an inflow region of v), there

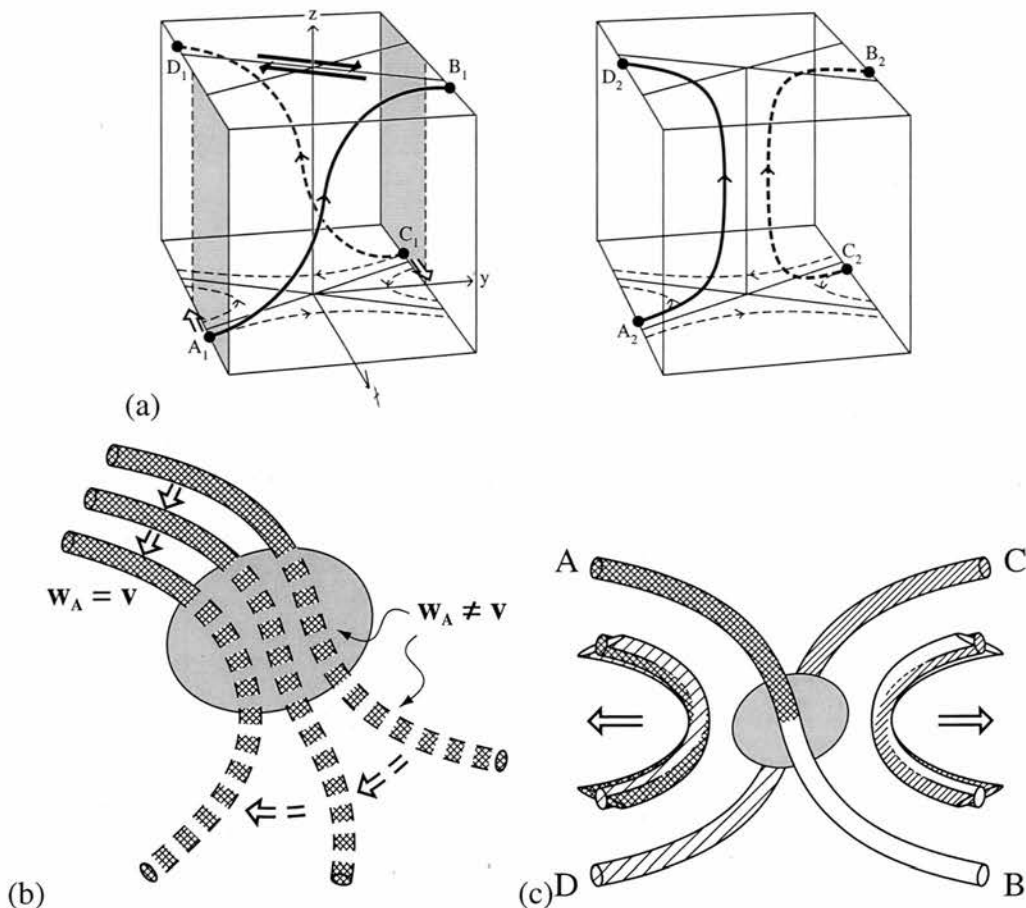


Figure 2.8: In three dimensional reconnection: (a) the mapping of field line footprints, (b) motion of a flux tube passing through the non-ideal region, and (c) the breaking and imperfect rejoining of flux tubes.

exists a corresponding flux tube on the opposite side of the X-point with which it will become perfectly rejoined after reconnection, such that two unique but differently connected flux tubes are produced (see Figure 2.7(c)). This will henceforth be referred to as ‘perfect reconnection’ of flux tubes.

2.4.2 Basic properties of 3D reconnection

In contrast, the behaviour of the magnetic flux does not obey any of the properties described above in three-dimensional reconnection. This means that it is necessary to completely overhaul the way in which we think about reconnection occurring when we move into 3D. Below, the behaviour in 3D is described, with the numbering corresponding to the numbering in the previous section.

1. In general, for 3D reconnection in an isolated non-ideal region, no unique field line

velocity (\mathbf{w}) exists. For a proof of this statement, see Appendix C. As a result, the behaviour of the magnetic field lines in 3D reconnection can be described by the following.

2. Field lines continually and continuously change their connections as they move through the non-ideal region, D . In other words, field line conservation is violated everywhere in the volume of space defined by all field lines which thread D . This means that a plasma element on one side of D is connected to a different plasma element on the opposite side of D at each instant in time.
3. As a result, the mapping between field line footpoints in 3D reconnection is in general continuous. As mentioned in Section 1.4, reconnection may occur in 3D either at null points or in their absence. In 3D, the mapping of field line footpoints is continuous everywhere except at separatrices of \mathbf{B} , i.e. at the fans or spines of null points. Figure 2.8 shows schematically the mapping of field lines in $B \neq 0$ reconnection. As in the 2D case, consider a field line anchored at the footpoint A_1 , which initially connects to a point B_1 on the opposite boundary. This time, as the footpoint A_1 is moved across the quasi-separatrix, the point B_1 flips rapidly across the top boundary of the box, to the point D_2 when A_1 reaches A_2 .
4. A flux tube which passes into the non-ideal region immediately splits into two separate tubes, one defined by the set of field lines traced from the initial tube cross-section on one side of D , and the other defined by the set of field lines traced from the other cross-section on the other side of D . This process is illustrated in Figure 2.4. The result of following the motion of one of these flux tubes, defined for example by a cross-section A , is shown in Figure 2.8(b). The motion of this flux tube is followed by tracing field lines from the cross-section in the ideal region at each time, and observing the evolution of the flux tube's position. The portion of the flux tube lying in the ideal region between the cross-section and D moves at $\mathbf{w} = \mathbf{v}$, as expected. Inside D , the flux tube moves at a velocity which is not equal to the plasma velocity, which is again what is expected by comparison with two dimensions. However, this velocity is not unique, but depends on the side of D from which the field lines are traced. It is therefore denoted by \mathbf{w}_A , to indicate that it is the field line velocity *associated with the cross-section A*. Furthermore, following the flux tube through to the far side of the non-ideal region, it does not move here at the ideal plasma velocity, in contrast with the 2D case. The fact that the field lines continually change their connections (point 2) means that the flux tube appears to evolve in a ‘virtual’ flow, \mathbf{w}_A .

5. In 3D steady reconnection, flux tubes do not perfectly reconnect in general (see Figure 2.8(c)). That is to say, for a given flux tube which is going to undergo reconnection, there is in general no corresponding counterpart flux tube on the other side of D with which it will become perfectly rejoined after reconnection. The net effect of the reconnection is to split each of the two initial flux tubes in two to form four unique flux tubes which never become rejoined, and so four flux tubes are produced by the process.

2.5 3D reconnection in the absence of a null point

The above properties of 3D reconnection are illustrated by a number of different solutions described in this thesis. In Chapters 3 and 4 solutions are described for kinematic reconnection at three-dimensional null points. Reconnection in the absence of a null point is illustrated in Figure 2.9, using the solution given by Hornig and Priest (2003). The reconnection takes place in a simple $2\frac{1}{2}$ -dimensional magnetic field. The field in the xy -plane has a hyperbolic X-type structure, while the field in the z -direction is taken to be uniform. \mathbf{B} takes the form

$$\mathbf{B} = B_0 \left(\frac{y}{L}, \frac{k^2 x}{L}, 1 \right), \quad (2.13)$$

where B_0 , L and k are constant. The non-ideal term is resistive, and the resistivity is assumed to be localised around the origin. The nature of the plasma flow in the ‘pure solution’ of Hornig and Priest (2003) is found to be rotational, with oppositely directed rotation, around the z -axis, above and below the diffusion region (D). The nature of the reconnection of magnetic flux is thus rotational as well, with field lines traced from foot-points anchored in the ideal region above D rotating in one sense, while those anchored below rotate in the opposite sense. Hence, in an arbitrarily short period of time, every field line which threads D changes its connection in this rotational fashion (except, because of symmetry, the field line lying along the z -axis). Composite solutions are also suggested, where an ideal stagnation flow is added to the pure solution, and it is one of these solutions which is illustrated in Figure 2.9. The cross-sections in the $z = 0$ plane of the flux tubes illustrated in Figure 2.9 are shown in Figure 2.10. As before, animations, of which the figures show snapshots, are contained on the CD.

The two figures (2.9 and 2.10) show the 3D reconnection properties described earlier. Firstly, it can be seen that as soon as they enter the diffusion region (marked out by the

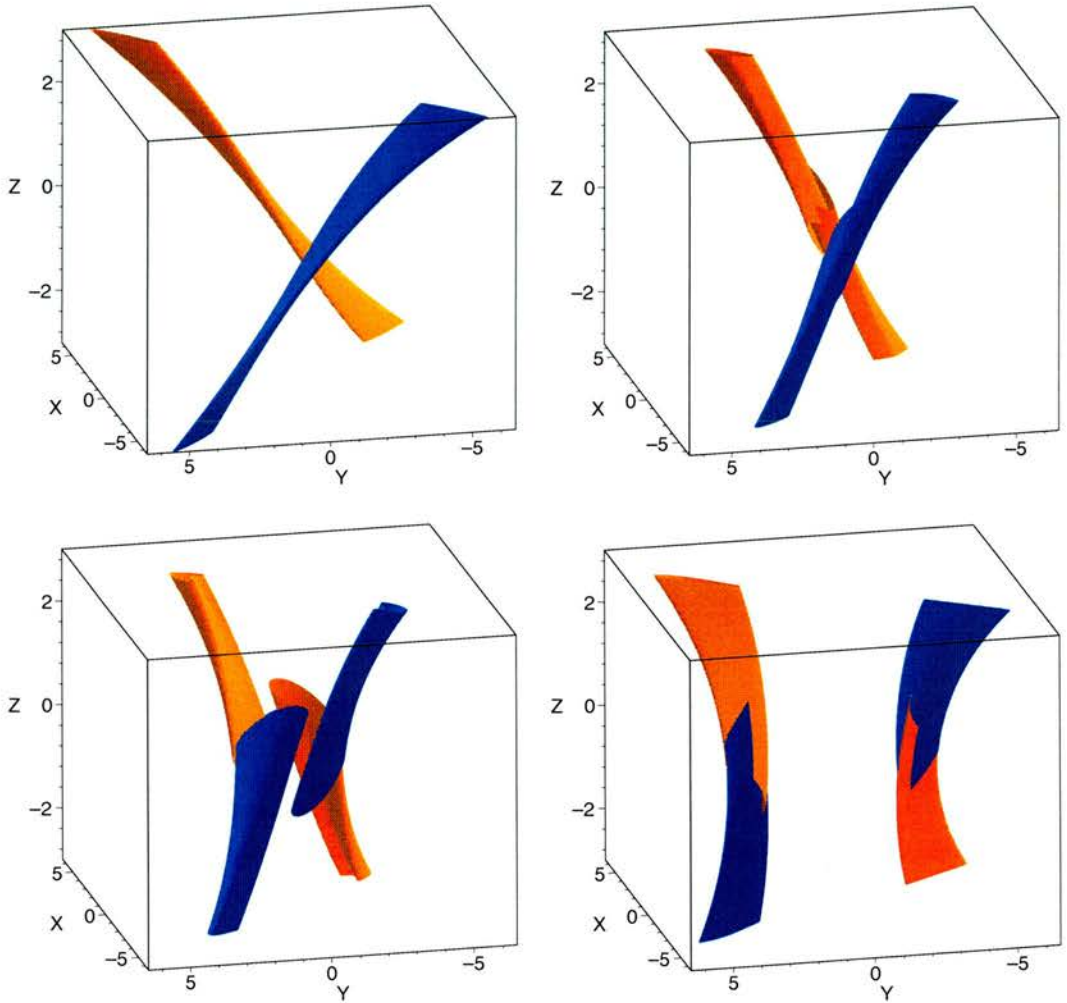


Figure 2.9: Reconnection of magnetic flux tubes in the field $\mathbf{B} = (y, 1.2x, 1)$. Note that the integration of the flux tubes through the volume is stopped at a certain point, for clarity (see ‘B nonzero.mpg’ on the CD).

beige disk in Figure 2.10) the flux tubes begin to split apart into four separate tubes. These four tubes then flip past each other through the diffusion region. In order to describe the motion of the flux in the process, it is necessary to define four separate velocities ($\mathbf{w}_i, i = 1 \dots 4$), which describe the motion of the four different tubes. The ‘imperfect’ rejoicing of the flux tubes can also be seen, particularly in the final frame of Figure 2.10. It can be seen that, although the four flux tubes which move away from the reconnection region intersect, they do not join to form two unique tubes. In fact each pair of tubes intersects at four points, indicating that they share four common field lines, since the flux tubes were chosen to intersect the $z = 0$ plane symmetrically about the z -axis (see the first frame of Figure 2.10). Note that the fact that the flux tubes do not rejoin perfectly after reconnection is not due to the choice of tubes. In fact, it is not possible to find a pair of perfectly rejoicing tubes.

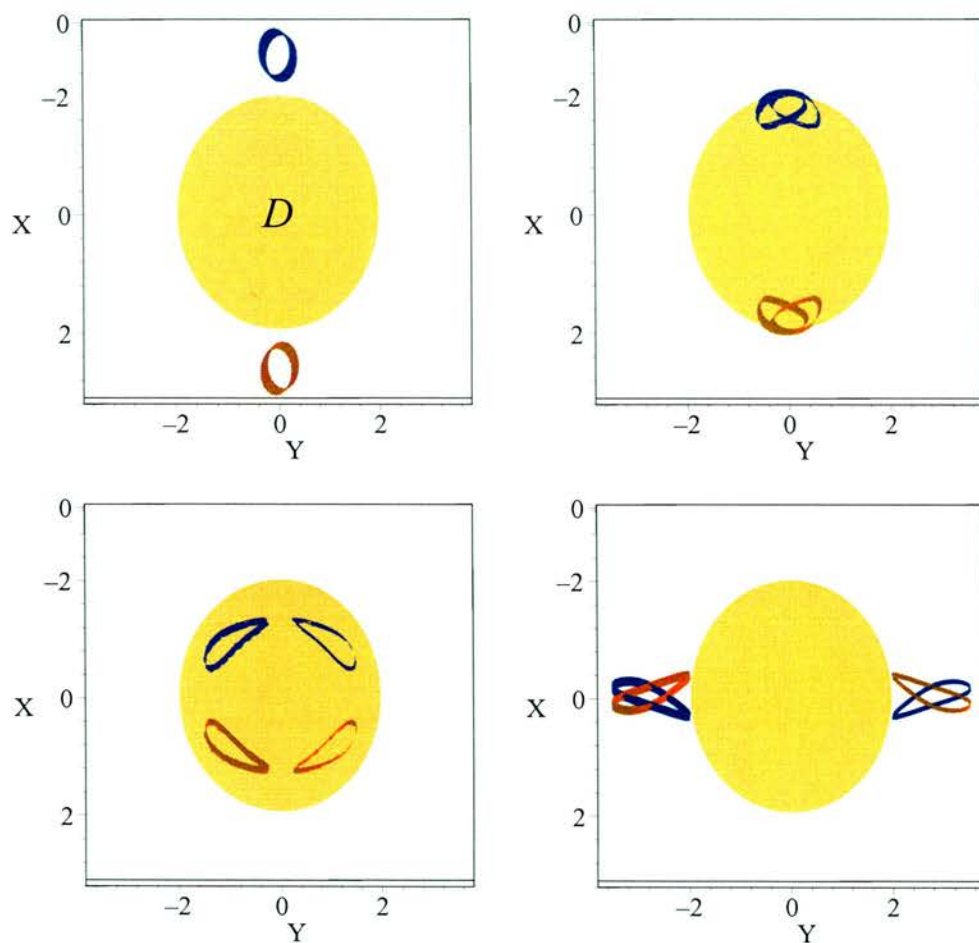


Figure 2.10: Cross-sections in the $z = 0$ plane of the reconnecting flux tubes shown in Figure 2.9. The beige disk shows the extent of the diffusion region (D) in that plane.

Chapter 3

Kinematic reconnection at a magnetic null point: Spine-aligned current

“On the planet Earth, man had always assumed that he was more intelligent than dolphins because he had achieved so much- the wheel, New York, wars and so on- whilst all the dolphins had ever done was muck about in the water having a good time. But conversely, the dolphins had always believed that they were more intelligent than man- for precisely the same reasons.”

Douglas Adams, *The Hitchhiker’s Guide to the Galaxy*

3.1 Introduction

As mentioned previously, reconnection can occur in three dimensions either at a null point or in the absence of a null point. In this chapter, a solution is described which models the behaviour of the magnetic flux in a reconnection process which takes place at a three-dimensional null point. The nature of this reconnection is of particular interest since a 3D null is the three-dimensional analogue of an 2D X-point. Three-dimensional null points are also of crucial importance in the topology and interaction of complex fields on the Sun. They are found in abundance in the solar corona (see e.g. Schrijver and Title, 2002; Longcope et al., 2003), where their associated separatrices and separators (special field lines which join two null points) are thought to be likely candidates for sites of coronal heating (Longcope, 1996; Antiochos et al., 2002; Priest et al., 2002). There is also evidence that null point reconnection may act as a trigger for at least some solar flares (Fletcher et al., 2001).

The local structure of the magnetic field around a three-dimensional null point is described in Section 1.4. The kinematics of steady reconnection at a 3D null have been studied previously by Priest and Titov (1996). They start off by discussing the ideal behaviour of the magnetic field lines in the vicinity of the simple potential null point given by

$$\mathbf{B} = (x, y, -2z). \quad (3.1)$$

The reconnection is classified as one of two types near an isolated null point, termed *spine reconnection* and *fan reconnection*. Reconnection associated with a separator joining two nulls is also discussed. Due to the fact that the configuration considered is ideal, the plasma velocity is necessarily singular at the null in order to achieve reconnection. During spine reconnection a flow is imposed across the fan ($z = 0$) resulting in singularities in \mathbf{E} and \mathbf{v} at the spine ($x = y = 0$). The field lines are advected through the fan, and when they reach the fan they flip down the spine, with the footpoint mapping being discontinuous at the fan surface. In fan reconnection the flow is imposed across the spine, resulting in singularities in \mathbf{E} and \mathbf{v} in the fan plane. Field lines are advected through and past the spine, and as they pass by the spine they flip quickly around in the fan plane. The effect of adding non-potential and diffusive terms is also considered in a preliminary manner. The aim of this chapter is to investigate the structure of reconnection when the null point is non-potential, with a current parallel to the spine, where a localised diffusion region is included in order to give a realistic model with no singularities in any physical quantities. The results described in the chapter can be found in Pontin et al. (2004b).

It is instructive to seek insight into the structure of the highly complex process of 3D reconnection by considering solutions to a reduced set of the MHD equations. We follow the method of Hornig and Priest (2003) and adopt the kinematic approximation, by solving the induction equation and Maxwell's equations, though not solving the equation of motion. In a fully dynamical situation we would expect to start from an initial field, which then forms a current sheet at which reconnection takes place. The way in which a current sheet may form by the collapse of a 3D null point is discussed by, for example Klapper et al. (1996), Parnell et al. (1997), Bulanov and Sakai (1997) and Mellor et al. (2003). It should be noted, however, that as in two dimensions, reconnection may be initiated in many different ways (see e.g. Priest and Forbes, 2000), such as by driving from boundaries, or as a result of instabilities of many different types, as well as by null point collapse (following response to external boundary motions).

In Section 3.2, the equations solved in the model are given, as well as the assumptions

made, and we detail our method of solution. The elementary solution is given in Section 3.3, before the result of adding a physically relevant ideal flow is described in Section 3.4. The existence of perfectly reconnecting flux tubes is discussed in Section 3.5, where the effect of adding a simple time-dependence to the model is described. Section 3.6 gives a summary of the main results.

3.2 The model

We seek a solution of the kinematic, steady, resistive MHD equations given by

$$\mathbf{E} + \mathbf{v} \times \mathbf{B} = \eta \mathbf{j}, \quad (3.2)$$

$$\nabla \times \mathbf{E} = \mathbf{0}, \quad (3.3)$$

$$\nabla \cdot \mathbf{B} = \mathbf{0}, \quad (3.4)$$

$$\nabla \times \mathbf{B} = \mu_0 \mathbf{j}. \quad (3.5)$$

The non-ideal term on the right-hand side of Equation (3.2) is assumed to be localised. The nature of reconnection in the vicinity of a simple spiral null point, where \mathbf{j} lies parallel to the spine, is investigated. In Chapter 4, we will go on to consider the case where \mathbf{j} is parallel to the fan. In general the field in the vicinity of a spiral null point can be written (Parnell et al., 1996) as

$$\mathbf{B} = B_0 \left(x - \frac{y}{2}, y + \frac{x}{2}, -2z \right), \quad (3.6)$$

where B_0 and j are constants, such that $\mathbf{j} = B_0 j / \mu_0 \hat{\mathbf{z}}$ (from Equation (3.5)) is directed along the z -axis, which is coincident with the spine. Due to the cylindrical symmetry of the field, it simplifies matters to work in cylindrical polar coordinates (R, θ, z) , in which \mathbf{B} has the form

$$\mathbf{B} = B_0 \left(R, \frac{jR}{2}, -2z \right). \quad (3.7)$$

It is crucial for the following analysis to be performed analytically that we are able to find analytical equations describing the field lines in terms of some initial starting

coordinates (\mathbf{x}_0). For \mathbf{B} defined as in Equation (3.7), this can be done by integrating

$$\frac{\partial \mathbf{X}(s)}{\partial s} = \mathbf{B}(\mathbf{X}(s)) \quad (3.8)$$

to find $\mathbf{X}(\mathbf{x}_0, s)$, given by Equations (3.9), as

$$R = R_0 e^{B_0 s}, \quad \theta = \theta_0 + \frac{B_0 j s}{2}, \quad z = z_0 e^{-2B_0 s}. \quad (3.9)$$

Note that the parameter s does not denote the distance (λ) along a field line, which is instead given by

$$d\lambda = |B|ds. \quad (3.10)$$

From Equation (3.3), \mathbf{E} can be written as the gradient of some scalar, Φ say, so that Equation (3.2) becomes

$$-\nabla\Phi + \mathbf{v} \times \mathbf{B} = \eta \mathbf{j}. \quad (3.11)$$

A solution to this equation for given \mathbf{B} may be found as follows. Firstly, since the non-ideal term is to be localised and since \mathbf{j} is constant, a localised resistivity (η) is prescribed. The component of Equation (3.11) parallel to \mathbf{B} is $-(\nabla\Phi)_{||} = \eta \mathbf{j}_{||}$, which may be integrated along field lines to give

$$\Phi = - \int \eta \mathbf{j}_{||} d\lambda + \Phi_0 = - \int \eta \mathbf{j} \cdot \mathbf{B} ds + \Phi_0. \quad (3.12)$$

Thus, if we can prescribe some function $\eta = \eta(\mathbf{x}_0, s)$ in such a way that, having substituted Equations (3.9) into \mathbf{B} and \mathbf{j} to find $\mathbf{B}(\mathbf{x}_0, s)$ and $\mathbf{j}(\mathbf{x}_0, s)$, Equation (3.12) is integrable, then we can deduce $\Phi(\mathbf{x}_0, s)$. From here it is possible to substitute the inverse of Equations (3.9) to find $\Phi(\mathbf{x})$. Then the electric field (\mathbf{E}) and the component of the plasma velocity perpendicular to \mathbf{B} , \mathbf{v}_{\perp} , can be found from

$$\mathbf{E} = -\nabla\Phi \quad (3.13)$$

and

$$\mathbf{v}_{\perp} = \frac{(\mathbf{E} - \eta \mathbf{j}) \times \mathbf{B}}{B^2}. \quad (3.14)$$

It is important to note, however, that the electric field is not fully defined until the function $\Phi_0(\mathbf{x}_0)$ is specified. Equations (3.12) and (3.13) with $\Phi_0 = 0$ describe the electric field resultant from the current and resistivity variation along the magnetic field only. The function $\Phi_0(\mathbf{x}_0)$, however, defines an extra component of \mathbf{E} perpendicular to \mathbf{B} . Since $\Phi_0(\mathbf{x}_0)$ is a constant of the integration, and therefore a function only of the field line starting points (\mathbf{x}_0) , it is constant along field lines, and so acts to add an ideal component to the flow, defined by Equation (3.19), as described below and in Section 3.4.

We now prescribe a physically reasonable profile for $\eta(\mathbf{x})$, that is, we require η to be smooth and continuous and to decay monotonically away from the null. We can then obtain an expression for η in terms of the field line coordinates (\mathbf{x}_0, s) with the help of the coordinate transformations (3.9). This expression can then be used for the integration (3.12). In order to have a unique coordinate transformation $\mathbf{x} \rightarrow (\mathbf{x}_0, s)$ we need to choose the initial points \mathbf{x}_0 on surfaces such that each field line passes through these surfaces exactly once. Two obvious choices which we will use in the following discussions are the planes $z = \pm 1$, or a cylindrical surface such as $R = 1$.

It is necessary for our method of solution to choose $\eta(\mathbf{x})$ in such a way that the integral in Equation (3.12) can be performed analytically, while still satisfying the above physical constraints. One analytically integrable form for $\eta(\mathbf{x})$ is a piecewise polynomial function, such as

$$\eta = \eta_0 \begin{cases} \left(\left(\frac{R}{a} \right)^2 - 1 \right)^2 \left(\left(\frac{z}{b} \right)^2 - 1 \right)^2 & R < a, z^2 < b^2 \\ 0 & \text{otherwise,} \end{cases} \quad (3.15)$$

where η_0 , a and b are constant and η_0 is the value of the resistivity (η) at the null point. This form of η gives a cylindrical diffusion region, of radius $R = a$, say, extending in the z -direction to $\pm b$. η is continuous and smooth everywhere. To proceed we need to perform the integration given by Equation (3.12). In order to do this we must choose the direction of integration along the magnetic field lines. That is, we may choose either to set $s = 0$ on some surface of $R = R_0$ (where R_0 is a constant, $R_0 > a$) and integrate in towards the null point and thus through D , or we may integrate down and up towards the null from $z = z_0$ and $z = -z_0$, respectively (z_0 constant, $z_0 > b$), setting $s = 0$ on these surfaces for each half-space. In the latter case the starting potentials (Φ_0) at $z = \pm z_0$ must be chosen such that Φ is continuous and smooth at the fan plane ($z = 0$). It is then necessary to set $s = 0$ on two different surfaces since each surface intersects only those field lines on the corresponding side of the separatrix (fan) surface, which splits the volume into two topologically distinct regions. The choice between the two

directions of integration is irrelevant provided we consider our model with respect to some chosen external/boundary conditions, equivalent to imposing some Φ on one boundary. The results from each case then are equivalent, and so we choose here to describe the result of setting $s = 0$ on $z = \pm z_0$, and point out any significant differences for the other case when they occur.

By the method described above, $\mathbf{E}(\mathbf{x})$ can be found. However, it turns out that for the choice of η given in Equation (3.15), \mathbf{E} is singular in the fan ($z = 0$). The reason is that the profile of η is not sufficiently flat near the null point, where the diverging field lines make the integration of Φ very sensitive to any variations of η . To obtain a smooth \mathbf{E} (for it to be physically acceptable in this local model), we find that the power of the variables in (3.15) must be greater than 4, and so take, for simplicity,

$$\eta = \eta_0 \begin{cases} \left(\left(\frac{R}{a} \right)^6 - 1 \right)^2 \left(\left(\frac{z}{b} \right)^6 - 1 \right)^2 & R < a, z^2 < b^2 \\ 0 & \text{otherwise,} \end{cases} \quad (3.16)$$

where η_0 , a and b have the same physical meanings as before. This form for η has essentially the same profile as that given by Equation (3.15).

It is now possible, via the method described at the beginning of this section, to calculate \mathbf{E} and \mathbf{v}_\perp , with the freedom of adding a perpendicular component of \mathbf{E} and \mathbf{v} as described above. The analytical expressions for these are too lengthy to present here, but can be calculated using a symbolic computation programme. These calculations, as well as subsequent ones described in this chapter, are contained on the accompanying CD (see Appendix D for details on how to access them), as well as in Appendix E.1. The resulting solution, with Φ_0 set to zero, described in detail in the following section, gives, in a sense, a local rearrangement of the flux within an envelope of field lines enclosing the diffusion region (D), see Figure 3.1. The rearrangement is local in the sense that Φ only changes on field lines which pass through D (see Equation (3.12)), and thus in a region of space threaded exclusively by field lines which have not passed through D , Φ is constant, and Equations (3.13) and (3.14) imply that \mathbf{E} and \mathbf{v}_\perp are zero.

Now, for a given magnetic field, Ohm's law (Equation (3.11)) may be decomposed into an ideal component (3.18) and a non-ideal component (3.17) as follows

$$-\nabla\Phi_{non-id} + \mathbf{v}_{non-id} \times \mathbf{B} = \eta \mathbf{j} \quad (3.17)$$

$$-\nabla\Phi_{id} + \mathbf{v}_{id} \times \mathbf{B} = \mathbf{0}. \quad (3.18)$$

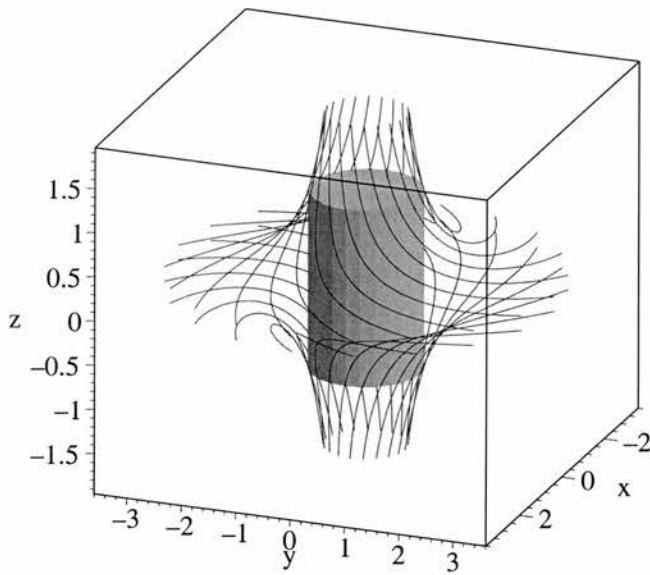


Figure 3.1: Field lines on the boundary of the envelope enclosing the diffusion region (cylinder), showing the region of influence of the local solution.

We have the freedom to add an ideal flow to the non-ideal solution since we do not solve the momentum balance equation here, which would otherwise determine the ideal part of the flow.

We can thus add an ideal flow to our ‘local’ solution by taking Φ_{id} to be our Φ_0 in Equation (3.12). Note that Φ_{id} should be constant with respect to the integration in Equation (3.12), i.e. $\Phi_{id} = \Phi_{id}(\mathbf{x}_0)$. The perpendicular component of the ideal flow $\mathbf{v}_{id\perp}$ may then be calculated, by taking the cross-product of Equation (3.18) with \mathbf{B} , as

$$\mathbf{v}_{id\perp} = \frac{-\nabla\Phi_{id} \times \mathbf{B}}{B^2}. \quad (3.19)$$

We may thus add an ideal flow to transport magnetic flux into and out of the local envelope shown in Figure 3.1, allowing us to see the global effect of the restructuring of the magnetic flux by the reconnection process. This will be discussed in Section 3.4, but first the elementary solution is considered in Section 3.3.

As mentioned previously, in general for reconnection in three dimensions $\mathbf{E} \cdot \mathbf{B}$ (or $\mathbf{j} \cdot \mathbf{B}$) is non-zero, and hence in general no unique field line velocity exists (Hornig and Schindler, 1996; Priest et al., 2003a, see Appendix C for a proof). Nonetheless, it is still possible to study the evolution of magnetic flux and field lines under certain circumstances. Consider the case of a resistive non-ideal term $\eta\mathbf{j}$, which is localised within some diffusion region, D . If no closed magnetic field lines exist within D , then it is still possible to follow the motion of individual field lines from each end, since in the ideal

region on either side of D they must remain attached to the same plasma elements for all time. On the boundary of D , field lines move at the velocity \mathbf{v}_\perp . Suppose the surface of D is split into two parts, through one of which magnetic flux enters D , and through the other of which it leaves. By reference to the ideal environment then, it is possible to define a velocity with which the field lines passing *into* D move, say \mathbf{w}_{in} , and another velocity \mathbf{w}_{out} at which the field lines passing *out of* D move, by tracing field lines into D which are anchored at the two boundaries. These two (pseudo-) field line velocities must each be identical to \mathbf{v}_\perp on the relevant section of the surface of D , but in contrast to the two-dimensional case, they are not identical to each other inside D , nor are they identical to \mathbf{v}_\perp on their continuations through D . This is a manifestation of the non-existence of a unique flux-conserving velocity, \mathbf{w} . The result is that following field lines with \mathbf{w}_{in} and \mathbf{w}_{out} , respectively, the field lines seem to split as soon as they are transported into the diffusion region, and inside D they continually change their connections (see Section 2). This is demonstrated in the following sections, where the above method is used to determine the motions of the field lines.

In order to calculate the velocities $\mathbf{w}_{in/out}$, we use the fact that they must match the plasma velocity on the relevant boundary of D , and they are thus given by

$$\mathbf{w}_{in/out} = \frac{-\nabla\Phi_{in/out} \times \mathbf{B}}{B^2}. \quad (3.20)$$

Assuming $B_0 > 0$, we can identify the surface through which flux enters D as $z = b$, and the surface through which flux leaves it as $R = a$, so that,

$$\mathbf{w}_{in} = \frac{-\nabla\Phi_{z=b} \times \mathbf{B}}{B^2}, \quad \mathbf{w}_{out} = \frac{-\nabla\Phi_{R=a} \times \mathbf{B}}{B^2}. \quad (3.21)$$

3.3 Elementary solution

3.3.1 Induced flows

We examine here the nature of the solution with $\Phi_{id} = 0$, i.e. just the local behaviour of the flux envelope enclosing D with no extra ideal flow. All physical quantities are completely symmetric about $z = 0$, and we will therefore describe the results only for $z > 0$. Choosing to integrate Equation (3.12) from $z = z_0$ we automatically start with Φ constant for $z > b$. Hence the electric field and plasma velocity are zero for $z > b$. The velocity for $z < b$ is a rotation within the flux envelope. (For integration from $R = R_0$,

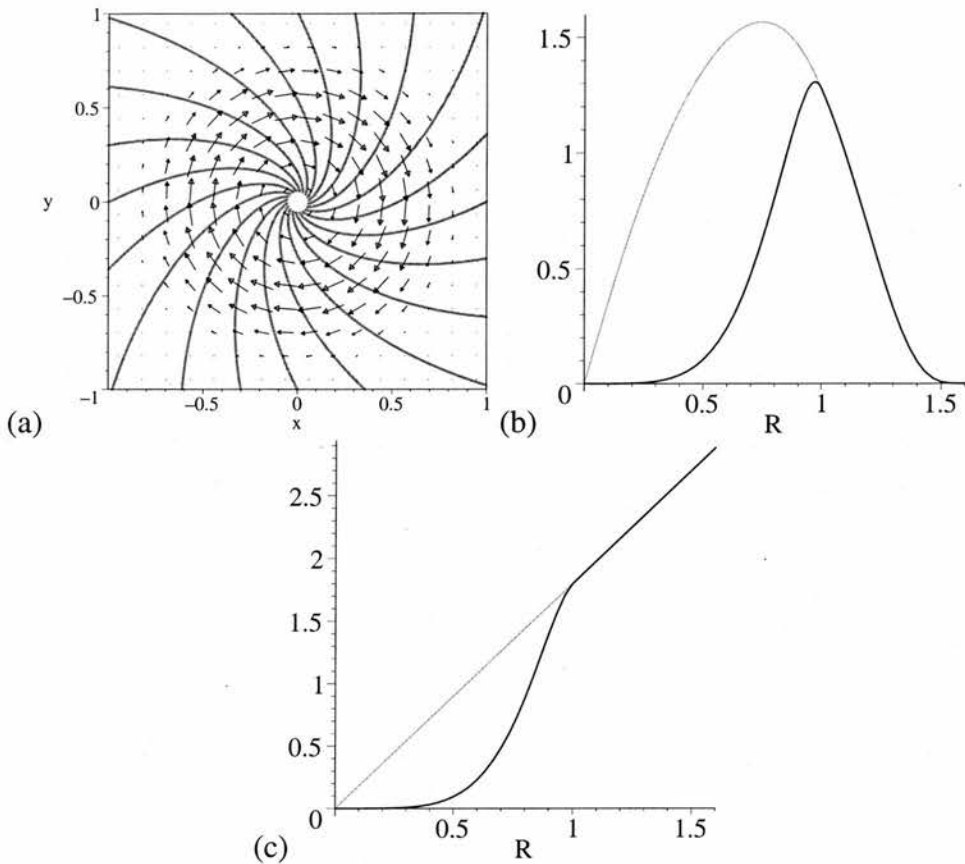


Figure 3.2: (a) Vectors of the plasma flow \mathbf{v} , along with a projection of the magnetic field lines in the plane $z = 0.4$, for the parameters $B_0 = 1$, $a = 1$, $b = 1$, $\eta_0 = 1$, $j = 2$. The corresponding radial variation of (b) the plasma velocity v_θ (black line) and field line velocity $w_{out\theta}$ (grey), and (c) the same plot for $z = 0$.

the plasma velocity (\mathbf{v}) vanishes for $R > a$, and we have a rotation within the remainder of the flux envelope.)

For the purposes of illustration of the results, it is at this stage convenient to add a component of \mathbf{v} parallel to \mathbf{B} such that $\mathbf{v}_z = 0$. This is achieved by defining

$$\mathbf{v} = \mathbf{v}_\perp - \frac{v_{\perp z}}{B_z} \mathbf{B}. \quad (3.22)$$

Our freedom to do this comes from the fact that Equation (3.11) determines only the perpendicular component of \mathbf{v} , since it is the part that affects the behaviour of the magnetic flux, and so for our purposes the parallel component is arbitrary. The resulting flow pattern of \mathbf{v} in a plane of constant z is shown in Figure 3.2(a). The radial component, as well as by definition the z -component, of \mathbf{v} is zero, so we have purely rotational flow, and the way that this varies with radius is shown in Figures 3.2(b) and (c). Note that here the angular plasma velocity is strongest in a ring centred on the spine. Note also that in the

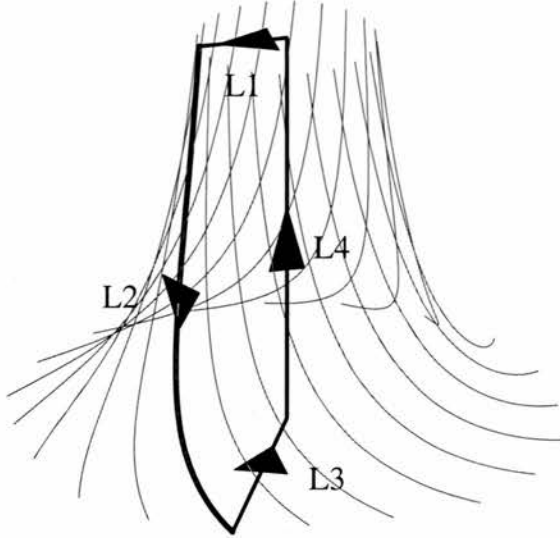


Figure 3.3: Closed loop made up of line sections. L_1 and L_3 are radial lines in planes $z = b$ and $0 < z < b$ respectively. L_2 is a field line lying on the surface of the flux envelope enclosing D , and L_4 lies along the spine ($R = 0$).

$z = 0$ plane the field lines in the fan itself rotate like a solid body, as does the plasma outside the diffusion region.

The source of the rotational flows can be explained as follows. We consider the case where Φ is integrated from $z = z_0$, and the argument can be easily adapted to the reverse integration. Consider the potential drop along sections of the closed loop illustrated in Figure 3.3. L_1 and L_3 are radial lines in planes $z = b$ and $z < b$, respectively, while L_2 is a field line on the surface of the envelope of flux threading D , and L_4 lies along the spine of the null. The potential drop around any closed loop must be zero. The potential drop along lines L_1 and L_2 must be zero, as L_1 lies at $z \geq b$ and L_2 lies on the boundary of the envelope, and so $\Phi = \Phi_0$ all along them. Thus

$$\Delta\Phi_{L_3} + \Delta\Phi_{L_4} = 0,$$

or

$$\Delta\Phi_{L_3} = -(\Phi_{spine} - \Phi_0) \neq 0, \quad (3.23)$$

where Φ_{spine} is the value of Φ at the vertex of L_3 and L_4 , which must be different from Φ_0 since \mathbf{E} is non-zero along the spine ($\mathbf{E} \cdot \mathbf{B} = \mathbf{j} \cdot \mathbf{B} \neq 0$ on spine). Since there is a potential drop along L_3 there must also be a non-zero electric field along it. The electric field induces a plasma flow perpendicular to such a radial line, i.e. a rotational flow. This rotation has the same sense for $z > 0$ and $z < 0$, and has maximum magnitude in the

$z = 0$ plane. Note that this argument is completely independent of the particular profile of η within D .

3.3.2 Reconnection rate

It is possible to calculate a reconnection rate for the flux in this reconnection process, although it is important to note that this has a very different physical meaning from the concept of a reconnection rate in two-dimensional reconnection. In 2D, flux is cut and rejoined at the null point, and the reconnection rate gives a measure of the amount of flux that undergoes this process in a given time. However, here we need a different definition since we have a localised flux envelope within which all of the flux continually changes its connections, so during an arbitrarily short length of time every field line is reconnected (except, for symmetry reasons, the spine field line).

Considering just the flux reconnected in the half-space $z > 0$, we define, by close analogy to Hornig and Priest (2003), the reconnection rate, F , as the integral over the parallel electric field along the spine axis,

$$\begin{aligned} F &= \int_{z=0}^{\infty} (\mathbf{E}_{\parallel})_{R=0} dl \\ &= \Phi(R = 0, z = b) - \Phi(R = 0, z = 0) \\ &= \frac{72}{91} B_0 j \eta_0 b. \end{aligned} \quad (3.24)$$

To obtain some idea of the meaning of this quantity, consider the difference between the velocities of the field lines anchored in the surfaces, $z = \pm b$ and $R = a$, of D through which flux passes in and out.

$\Phi = \Phi_0$ on $z = b$, and hence $\nabla\Phi_{z=b} = 0$ and $\mathbf{w}_{in} = 0$ from Equation (3.21), so field lines passing in through the top of D remain fixed and stationary there. Due to the rotational nature of \mathbf{v} , \mathbf{w}_{out} is also rotational, leading to a rotational mismatching between \mathbf{w}_{in} and \mathbf{w}_{out} . The value of F , given by Equation (3.24), provides an idea of the maximum difference between the rate of rotation of the inward flux bundle and outward flux bundle, or the maximum rate of relative slippage (see Hornig and Priest (2003) for a further pedagogic example). From Figures 3.2(b) and (c) it can be seen that the outward bundle of field lines rotates approximately like a solid body close to the spine, with the rotation falling off to zero at the edge of the flux envelope.

As mentioned above, $\Delta\mathbf{w} = \mathbf{w}_{out} - \mathbf{w}_{in}$, the rate of slippage between the inward and outward bundles of field lines, is purely rotational, so that it has a θ -component only. Thus

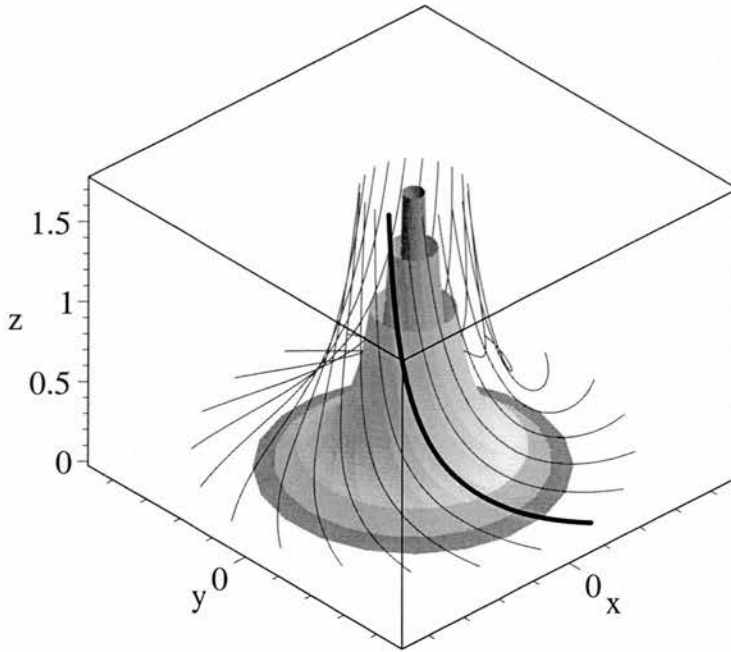


Figure 3.4: Flux surfaces of constant radius (for given z), within which field lines periodically reconnect exactly with themselves. For example, the highlighted (black) field line will split in the rotational flow, with the top ‘half’ remaining fixed, while the bottom ‘half’ reconnects with each of the grey field lines until eventually being reconnected again into the configuration shown after performing a rotation of 2π radians.

field lines are continuously reconnected in shells of constant radius (for a given value of z) only. These shells have the same 3D shape as, and are concentric with, our flux envelope, see Figure 3.4. An initial field line which splits into two will be periodically exactly reconnected with itself, every time the half embedded in $R = a$ performs a full rotation of 2π radians. Note, however, that this period is different for each shell, since it is not a rigid rotation. For this reason, if we consider a flux tube within the envelope with a finite radial extent, there will be no periodic return to the initial state.

It is important to note the implications the rotational slippage has for helicity production. If we imagine that some small flux tube within our flux envelope is closed somewhere far from D , then we can see that the relative rotation of the two ends of the tube would act to twist up the tube (i.e. the rotation of one ‘end’ of the tube around the spine while the other end remains fixed) and thus act as a source of self-helicity with respect to an initially untwisted tube.

3.4 Composite solutions

As discussed in Section 3.2, we may impose any ideal flow upon the solution described in the previous section, as shown in Equations (3.17) and (3.18). We would like to choose an ideal flow which shows the global effect of the local rotational slippage behaviour by transporting magnetic flux into and out of the local flux envelope. For this reason we choose to impose a stagnation-type ideal flow. Stagnation flows are also physically relevant flows to choose as they may perform the localisation of the quantities contained in the non-ideal term in Equation (3.2) (Priest and Forbes, 2000; Hornig and Priest, 2003), and are common in reconnection solutions, such as Craig and Fabling (1996).

The stagnation flow is chosen in such a way as to satisfy Equation (3.18) by imposing a suitable $\Phi_{id}(x_0, y_0)$ on the surface $z = z_0$, and then substituting the inverse of the field line Equations (3.9) to obtain $\Phi_{id}(x, y, z)$. The equivalents of Equations (3.13) and (3.14) can then be used to find \mathbf{E}_{id} and $\mathbf{v}_{id\perp}$, respectively. Again, for ease of analysis, we choose to set $(\mathbf{v}_{id\perp})_z = 0$, via Equation (3.22), to obtain \mathbf{v}_{id} . We choose to take

$$\Phi_{id}(x_0, y_0) = \varphi_0 x_0 y_0, \quad (3.25)$$

where φ_0 is a constant. The resulting flow (\mathbf{v}_{id}) takes the form of a stagnation-point flow, with separatrices coincident with the x - and y -axes in the plane $z = z_0$. For $z \neq z_0$, the flow separatrices are rotated with respect to this configuration, due to the spiralling of the field lines.

The total flow, obtained by adding this ideal flow to the elementary solution, and given by $\mathbf{v} + \mathbf{v}_{id}$, has the same stagnation-type structure outside the enclosing flux envelope, but inside we have a superposition of X -type and O -type flows (in planes of constant z). Which of these flows dominates is dictated by the nature of Φ near the spine ($R = 0$). If we consider all other parameters fixed, there is a critical value of φ_0 , (namely, $\varphi_0 = \varphi_{crit}$) at which the transition from O -type to X -type flow takes place. This can be determined by examining the total Φ at small R , which (in Cartesian coordinates) takes the form

$$\Phi = \beta + (x^2 + y^2) \gamma + (x^2 - y^2) \delta + \lambda xy + \mathcal{O}(x^3, y^3), \quad (3.26)$$

where

$$\begin{aligned}
 \beta &= \frac{B_0 j \eta_0}{91 b^{12}} z (-7z^{12} + 26z^6 b^6 - 91b^{12}), \\
 \gamma &= \frac{9 B_0 j \eta_0}{5 a^2} z, \\
 \delta &= \varphi_0 \left(\frac{z}{z_0} \right) \cos \alpha \sin \alpha, \\
 \alpha &= \frac{j}{4} \ln \left(\frac{z}{z_0} \right), \\
 \lambda &= \varphi_0 (\cos^2 \alpha - \sin^2 \alpha) \left(\frac{z}{z_0} \right),
 \end{aligned} \tag{3.27}$$

In a plane of constant z , Φ changes from a local maximum to a saddle point, and thus the flow changes from O -type to X -type, when

$$4\gamma^2 - 4\delta^2 - \lambda^2 = 0.$$

Substituting in the above expressions for γ , δ and λ and rearranging for φ_0 we find that

$$\varphi_{crit} = \frac{18 B_0 j \eta_0 z_0}{5 a^2}. \tag{3.28}$$

For $\varphi_0 > \varphi_{crit}$, the flow is of X -type at the spine axis, whereas for $\varphi_0 < \varphi_{crit}$ it is O -type. Note that φ_{crit} is independent of z , so the flow type is the same for all z for a given value of φ_0 .

3.4.1 $\varphi_0 > \varphi_{crit}$

For $\varphi_0 > \varphi_{crit}$, the stagnation flow dominates the rotational flow of the elementary solution everywhere, and hence \mathbf{v} , \mathbf{w}_{in} and \mathbf{w}_{out} all have a basic X -type structure. In order to analyse the effect the reconnection process has on rearranging the flux, we consider the mismatching of the two flux velocities \mathbf{w}_{in} and \mathbf{w}_{out} . The flow lines of these velocities are coincident with the contours of constant Φ_{in} and Φ_{out} , respectively. For clarity we examine the mismatching of these contours, and hence the flux velocities, in the plane $z = b$, without loss of generality. The two sets of contours are shown in Figure 3.5. Note that the flow \mathbf{w}_{in} is exactly the ideal plasma velocity (\mathbf{v}_{id}) since the associated elementary solution from the previous section vanishes on $z = b$. Note also that in the plane $z = b$, the boundary of the flux envelope associated with the elementary solution coincides with the boundary of the diffusion region, at $R = a$. The superposition of the flow lines of

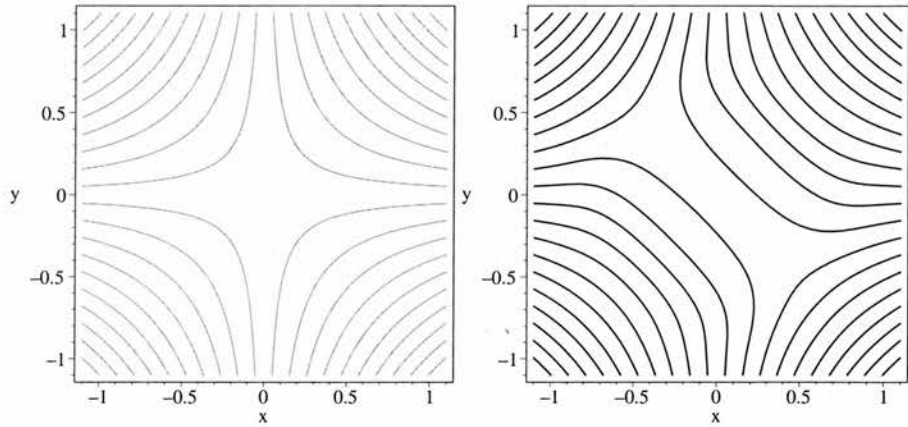


Figure 3.5: Flow lines in the plane $z = b$ of the field line velocities \mathbf{w}_{in} (left) and \mathbf{w}_{out} (right). The adopted parameter values are $B_0 = 1$, $a = 1$, $b = 1$, $\eta_0 = 1$, $j = 1$, $\varphi_0 = 4 > \varphi_{crit}$.

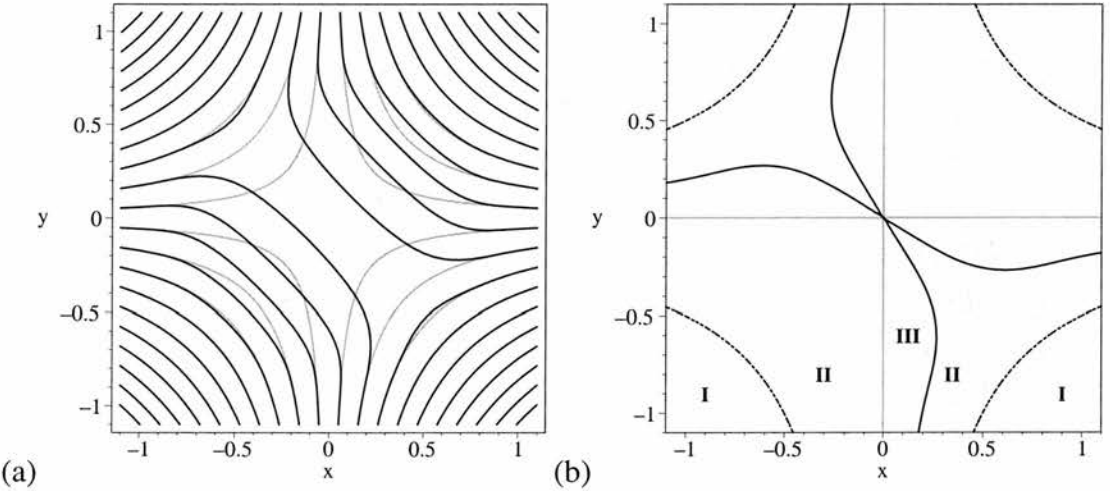


Figure 3.6: The superposition of the two sets of flow lines shown in Figure 3.5, highlighting the mis-matching. (b) Regions of different reconnective behaviour, distinguished by separatrices of \mathbf{w}_{in} (grey) and \mathbf{w}_{out} (black), as well as flow lines just touching the surface of D (dashed).

\mathbf{w}_{in} and \mathbf{w}_{out} is shown in Figure 3.6(a), which may be understood as follows. Consider a magnetic field line in an inflow region outside the diffusion region, whose intersection with the chosen plane ($z = b$) lies on one of the sketched flow lines. Outside D , the two sets of flow lines coincide (with each other and with \mathbf{v}), and the field line moves ideally. Once the field line is transported into D , the flux velocities \mathbf{w}_{in} and \mathbf{w}_{out} are no longer the same, and so the field line seems to split, with the ‘inward’ part following \mathbf{w}_{in} , and the ‘outward’ part following \mathbf{w}_{out} , if we trace the field line from both footpoints.

There are three distinct types of behaviour of the magnetic flux, which occur in different regions of the flows. These regions are separated by the separatrices of the \mathbf{w} -flows, as well as those flow lines which just touch (but do not enter) D , all of which are shown in Figure 3.6(b). Regions I show ideal behaviour everywhere. Here \mathbf{w}_{in} and \mathbf{w}_{out} coincide,

and so field lines always remain connected and frozen to the plasma. In regions II, the flow lines split inside D , and so an initially unique field line splits, with each footpoint becoming differently connected. Notice, however, that although any two flow lines separate when they enter D , the same two flow lines always come back together when they leave D . We can therefore think of these regions as slippage regions, since, although in general the two ‘halves’ of the initial field line will take different times to pass through D , and will hence not rejoin upon leaving D , they do move away from the reconnection region along the same flow line. Hence, after both ‘halves’ of the field line have left D , their separation remains constant in time.

Regions III are quite different. Here there is once again splitting of flow lines, and thus field lines, at the edge of D . In contrast to regions II, however, the flow lines in this case never rejoin, and in fact head off in opposite directions. Hence after we leave D each footpoint of our initial field line is now connected to a field line from a distinctly different region of magnetic flux. Regions III, then, can be thought of as more of a classical type of reconnection region, with the crucial characteristic being that initially joined field line footpoints continue to move away from each other for all time after leaving D . As φ_0 , and hence the strength of the ideal flow, is decreased, these classical reconnection regions grow in width, until we reach $\varphi_0 = \varphi_{crit}$.

3.4.2 $\varphi_0 < \varphi_{crit}$

When $\varphi_0 < \varphi_{crit}$, the rotational flow dominates \mathbf{w}_{out} near the spine, whereas \mathbf{w}_{in} retains the X -type structure, as it still coincides with \mathbf{v}_{id} . The two sets of flow lines and their superposition are shown in Figures 3.7 and 3.8(a). Again the different types of behaviour can be most clearly distinguished by studying the separatrices of these flows, which are shown in Figure 3.8(b). Regions I, II and III have essentially the same characteristic behaviours as before. Notice however that regions III, where the classical flux separation occurs, are now wider than when $\varphi_0 > \varphi_{crit}$ (if all other parameters are fixed). In addition we now have a region, marked IV in Figure 3.8(b), where the nature of the flux reconnection is different again. In this region the flow lines of \mathbf{w}_{out} are closed, and so following a field line anchored in this flow we find that it simply rotates round and round, never leaving the region or the local flux envelope. So we have a continuously rotating flux bundle moving at \mathbf{w}_{out} , which reconnects with a succession of different field lines, which are swept into and then out of the reconnection region at \mathbf{w}_{in} .

Note that the reconnection rate for both of the composite solutions described in this

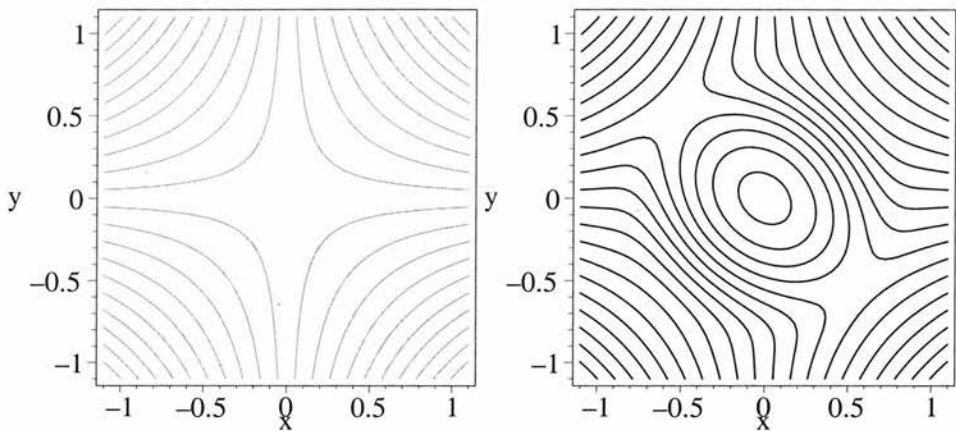


Figure 3.7: Flow lines in the plane $z = b$ of the field line velocities \mathbf{w}_{in} (left) and \mathbf{w}_{out} (right). The chosen parameters are $B_0 = 1$, $a = 1$, $b = 1$, $\eta_0 = 1$, $j = 1$, $\varphi_0 = 1 < \varphi_{crit}$.

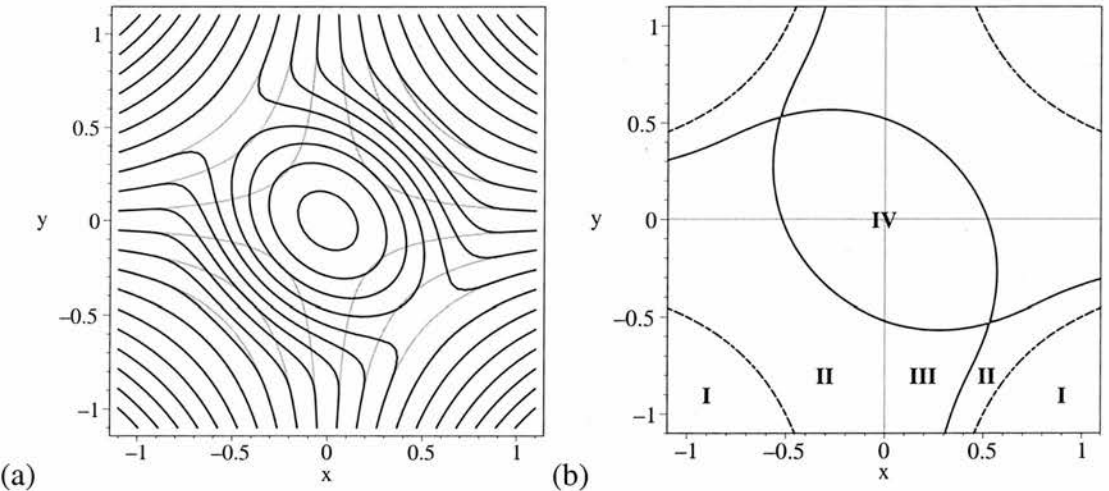


Figure 3.8: The superposition of the two sets of flow lines shown in Figure 3.7, highlighting the mis-matching. (b) Regions of different reconnective behaviour, distinguished by separatrices of \mathbf{w}_{in} (grey) and \mathbf{w}_{out} (black), as well as flow lines just touching the surface of D (dashed).

section is exactly the same as that given in Equation (3.24) for the elementary solution, since $\Phi_{id} = 0$ when $R = 0$, and so the calculation is unaffected. This reconnection rate now, however, summarises the combination of many different effects.

Lastly, note that the above analysis would follow through in exactly the same way had we chosen the option initially of integrating Φ from $R = R_0$. The only difference would be that flow lines of \mathbf{w}_{in} would become flow lines of \mathbf{w}_{out} and vice-versa.

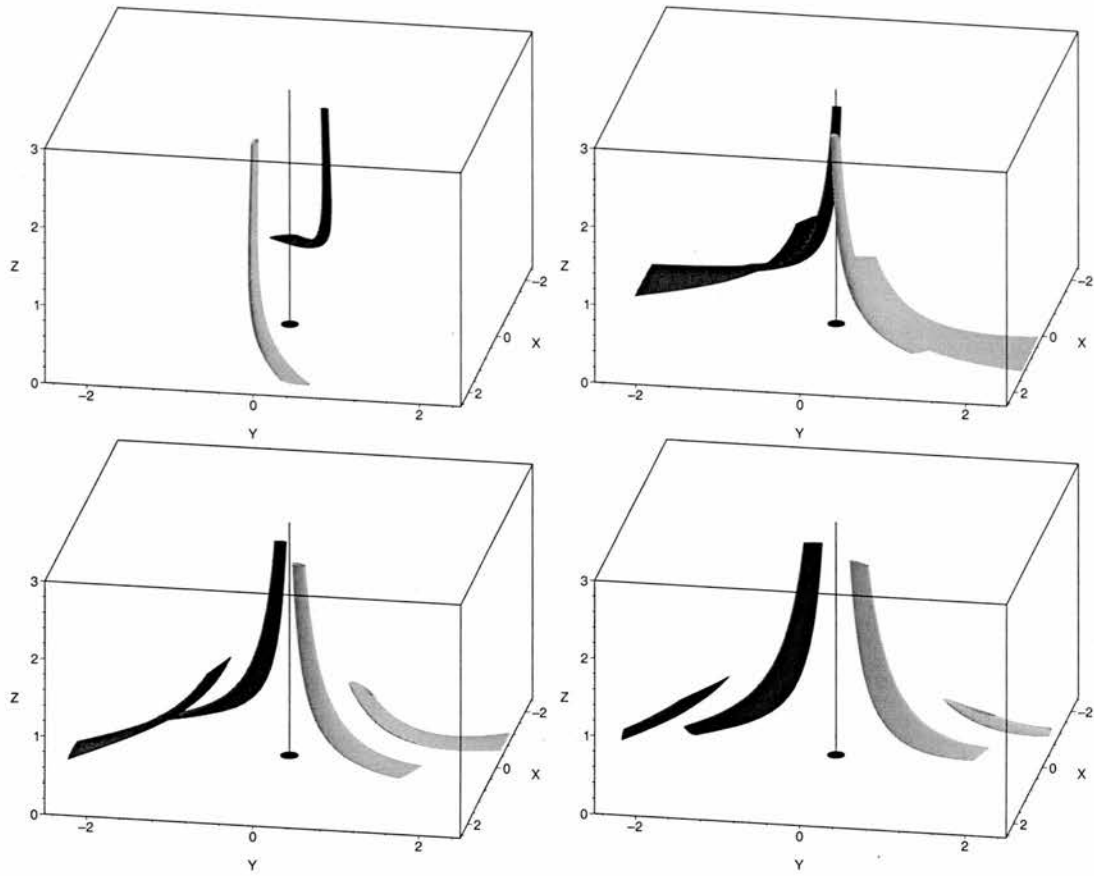


Figure 3.9: Evolution of a pair of flux tubes integrated from cross-sections lying in region II of the w -flows. As they enter the diffusion region each tube splits into two parts, which ‘slip’ apart, but on leaving D they move off in the same direction (the full colour animation, ‘*sp_rec_slip.mpg*’, is contained on the CD).

3.4.3 Reconnection of flux tubes

To visualise what effect the mismatching of the field line velocities has on the reconnection of flux tubes, we now describe two examples. In each case field lines are integrated from four arbitrary cross-sections chosen symmetrically about the spine such that initially we have two unique flux tubes on opposite sides of the diffusion region. The cross-sections are chosen so that they never pass into the diffusion region, and hence we can identify a set of field lines which remains frozen into these cross-sections for all time, defining our flux tubes (as described in Section 2.2). The resulting motion of the flux tubes is plotted, although we stop the field line integration at a chosen point to see more clearly what is happening.

When the flux tube cross-sections are chosen to lie in region II, the resulting flux tube behaviour is a slippage, as described in Section 3.4.1, and shown in Figure 3.9. We see that the flux tubes slip apart as they enter D , but the two sections of each initial flux

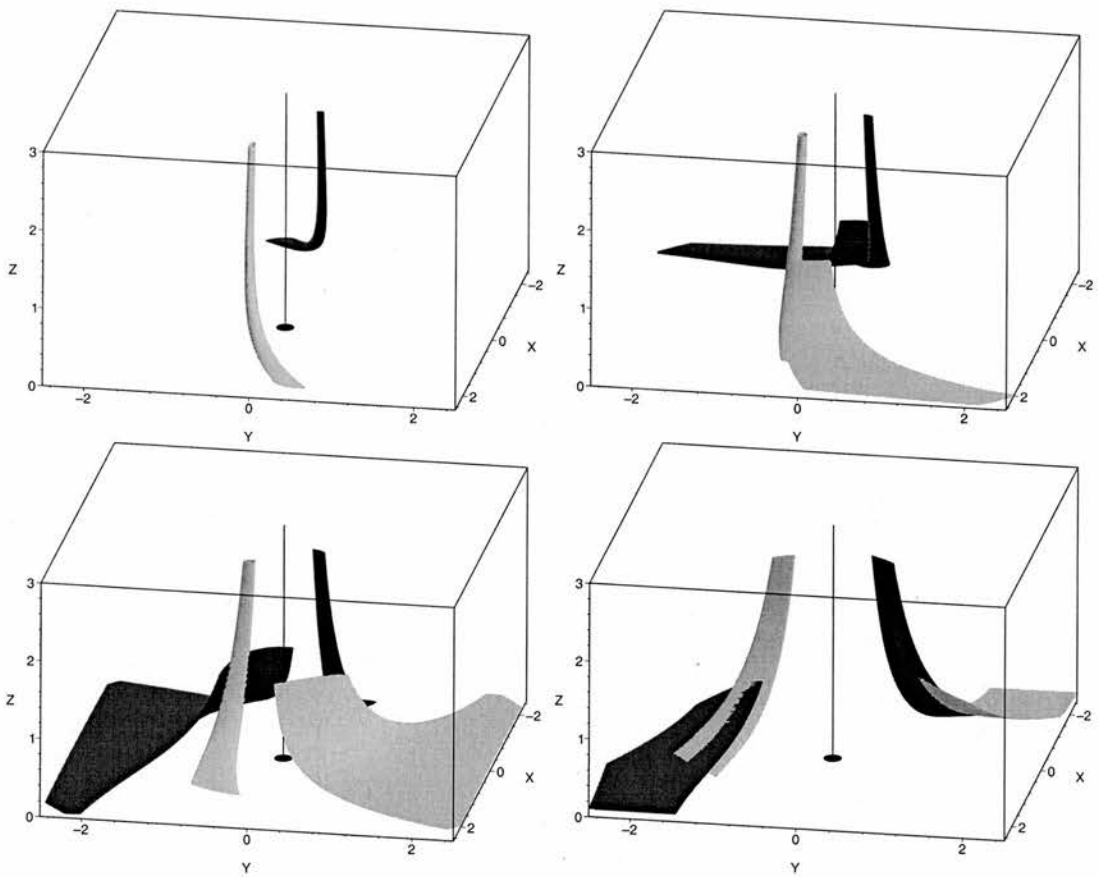


Figure 3.10: Evolution of a pair of flux tubes integrated from cross-sections lying in region III of the w -flows. As the tubes enter the diffusion region they split, with the two parts of each of the initial two tubes flipping around the spine in opposite directions. Notice in the final frame that after leaving D the four new tubes do not rejoin to form two unique tubes (again, the full animation, ‘*sp_rec.mpg*’, is contained on the CD).

tube leave the vicinity of the reconnection process in the same direction. The degree of slippage depends on the initial positions of the cross-sections, and the size of φ_0 .

The evolution of flux tubes whose cross-sections lie in regions III is shown in Figure 3.10. Now the two sections of each flux tube flip around the spine in opposite directions after splitting. They then leave the diffusion region in opposite directions, as described in Section 3.4.1. Notice, however, that the four flux tubes formed during the splitting process never rejoin cross-wise to form two unique flux tubes again as they do in 2D. They may share a few common field lines, although this need not necessarily be the case, depending on exactly where in region III the initial cross-sections are chosen.

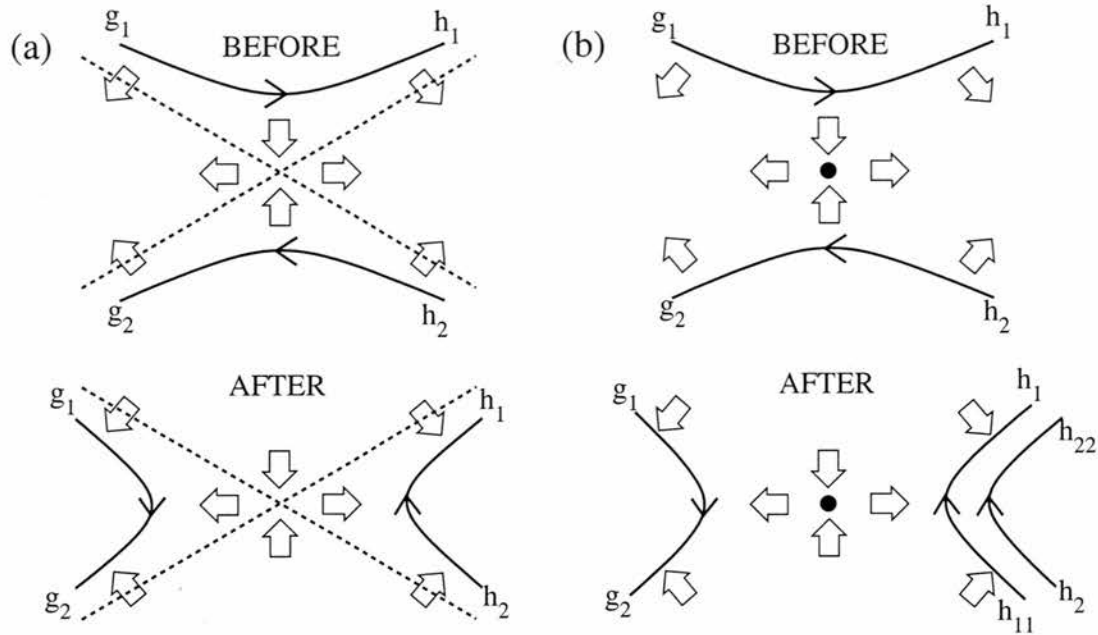


Figure 3.11: (a) The one-to-one reconnection of field lines in 2D. (b) Schematic picture of reconnection of field lines in 3D, e.g. top view of reconnection in region III of the composite solution of Section 3.4.

3.5 Existence of perfectly reconnecting flux tubes and time dependence

We now ask; is it possible to choose a pair of initial flux tubes which will perfectly rejoin after reconnection, such that we have two unique tubes before reconnection and two unique cross-wise differently connected tubes after reconnection. We have seen in the previous section that this is not generally the case, but perhaps with the right choice of initial cross-sections we can achieve this situation. In two dimensions things are relatively straightforward. If we choose to pick out one field line, in an inflow region of \mathbf{v} outside D , then it is always possible to find a corresponding field line, by simple symmetry through the X -point, with which it will perfectly reconnect. That is to say, if we label the two footpoints of field line 1 g_1 and h_1 , and of field line 2 g_2 and h_2 , then, if the field lines are chosen such that after reconnection g_1 is connected to g_2 , then h_1 will always be connected to h_2 (see Figure 3.11(a)). In three dimensions this is not generally the case, i.e., if g_1 maps to g_2 after reconnection then h_1 will in general *not* map to h_2 (see Figure 3.11(b) and Section 2.4.2). In this sense, there is no one-to-one reconnection of field lines, so a given field line has no unique counterpart with which it becomes uniquely rejoined.

This lack of a unique counterpart to a given field line can be illustrated for the present example as follows. Consider a field line starting in the classical reconnection region,

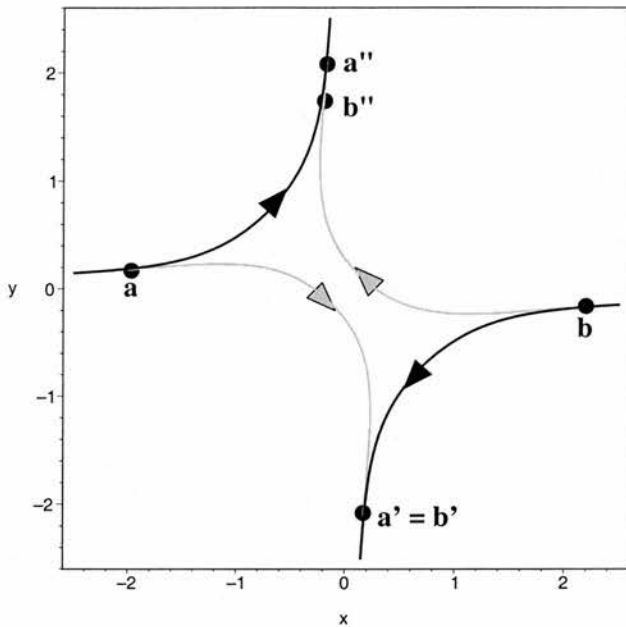


Figure 3.12: The non-existence of a unique counterpart to a given field line, shown for one circuit of flow lines of w_{out} (black) and w_{in} (grey). If field lines are chosen at a and b such that after reconnection $a' = b'$ then in general $a'' \neq b''$.

III, which initially intersects the flow line map (Figure 3.6 or 3.8) at a , outside D , see Figure 3.12. Allow this field line to move in the flow w_{in} for a time t' , where t' is large enough that a passes completely through the diffusion region to a point a' . Now, moving *backwards* in time from $t = t'$ to $t = 0$ along w_{out} we come to the point b , which corresponds to the field line (or its intersection with the plane $z = b$) with which a will join after the reconnection process. Next repeat this whole process starting from b ; i.e., move forwards $t = t'$ along w_{in} to b'' and then backwards $t = t'$ along w_{out} . In general we do *not* end up back at a as a result. The field lines corresponding to a and b before reconnection, which rejoin at $a' = b'$ on one side of D after reconnection do not rejoin on the other side of the diffusion region but instead end up at a'' and b'' , as shown. If a'' and b'' were coincident, then a would be the unique counterpart of b , in that their footpoints would become pairwise rejoined after the reconnection process at $a' = b'$ and $a'' = b''$, as in 2D. However, in general this is not the case in 3D, and so there is no unique counterpart to a given field line. The only exceptions for the present example are field lines which pass through one specific flow line circuit, for which the transit time through D on w_{in} and w_{out} is the same.

Nevertheless, if we can find two finite sets of field lines which reconnect with each other then we may still have perfect, or one-to-one, reconnection of these particular flux tubes. Iterating the procedure described above many times around the flow line circuit

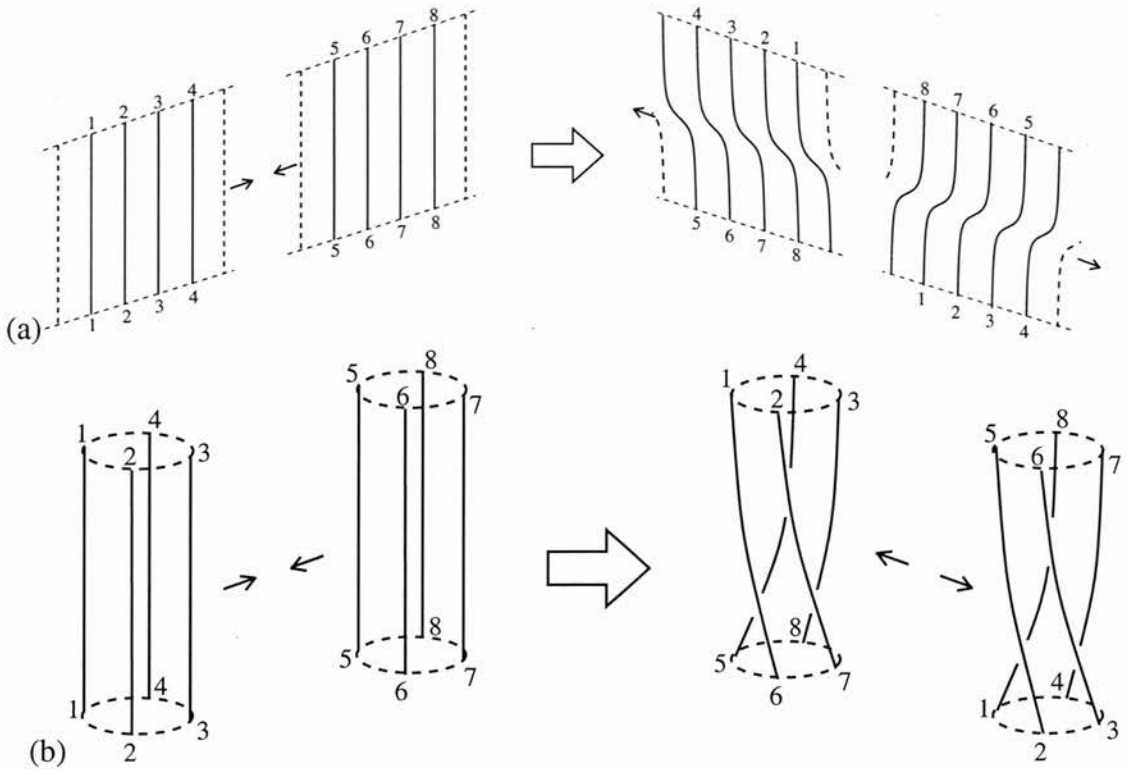


Figure 3.13: Schematic picture of reconnection of magnetic field lines in (a) a stationary state and (b) a time-dependent state, where there is one-to-one reconnection of flux tubes but not field lines.

(starting each subsequent circuit from the final point of the previous one) determines a set of field lines which reconnect with each other. If perfectly rejoining flux tubes existed, then their cross-sections would be mapped out by this iteration procedure, since every field line moving at w_{in} from one flux tube must reconnect with a field line moving at w_{out} in the other flux tube, and vice-versa. It turns out that the set of points we retrieve from the iteration all lie on the circuit of flow lines, and so they make up flux surfaces rather than flux tubes (see Figure 3.13(a)). Thus there is in general no unique counterpart to a given flux tube.

The fact that perfectly reconnecting flux tubes do not exist is a result of the fact that field lines are constrained to move around a single circuit of flow lines (as shown in Figure 3.12) or equivalently along contours of constant Φ . If, however, Φ were to be time-dependent, then these contours would change in time. We find that, if a simple time-dependence is introduced into η , as in Equation (3.29), then perfectly reconnecting flux tubes can be found, as follows. Let

$$\eta = f(t) \eta_0 \begin{cases} \left(\left(\frac{R}{a} \right)^6 - 1 \right)^2 \left(\left(\frac{z}{b} \right)^6 - 1 \right)^2 & R < a, z^2 < b^2 \\ 0 & \text{otherwise,} \end{cases} \quad (3.29)$$

where $f(t)$ is some arbitrary function of time only, and is thus effectively just a multiplicative constant in the calculation of Φ and \mathbf{E} described in Section 3.2. Hence $\nabla \times \mathbf{E}$ is still zero, and no extra magnetic field is induced. This time-dependence, then, shows up in Φ , \mathbf{E} , \mathbf{v} and thus \mathbf{w}_{in} and \mathbf{w}_{out} . By the same argument, a time-dependence could also be added to the ideal flow.

We will consider here the case where the ideal flow is still steady, and the diffusive process is localised in time via

$$f(t) = e^{-\frac{t^2}{T^2}}, \quad (3.30)$$

where T is a constant which controls the time-scale of the localisation. This time-dependence has little qualitative effect on the results described in the previous sections, other than to localise the effect of the reconnection process in time.

One reason why we found no unique reconnecting counterpart to a given field line in the previous section (as illustrated in Figure 3.12) was the difference in transit times through the diffusion region along \mathbf{w}_{in} and \mathbf{w}_{out} . This (in general large) difference, together with the fact that the ideal velocity outside the diffusion region grows quickly with radius, makes the iteration procedure for finding rejoining field lines numerically rather unstable. Thus, for the purpose of demonstrating the existence of perfectly reconnecting flux tubes for the present reconnection process, we use a modified ideal solution to add to the elementary solution. For the ideal potential we choose

$$\varphi_0 x_0 y_0 e^{-(x_0^2 + y_0^2)/4}, \quad (3.31)$$

so that the ideal solution is approximately the same as before near the diffusion region, but now the ideal velocity falls off with radius far away from the reconnection region. The separatrices of \mathbf{w}_{in} and \mathbf{w}_{out} associated with the new composite flow are shown in Figure 3.14(b), at $t = 0$.

We find that the result of adding the time dependence is that the flux surfaces of the stationary case close up to form flux tubes, as shown in Figure 3.13(b). Note that although these flux tubes do perfectly reconnect, there is still no one-to-one reconnection of field lines. For example, in the left-hand tube footpoint 1 is connected to footpoint 6 after reconnection, whereas in the right-hand tube footpoint 1 is connected to footpoint 8. The mapping of the field lines in the reconnected flux tubes shows a rotation, with respect to a one-to-one correspondence. This signifies the production of twist and hence a finite amount of self-helicity due to the rotation, consistent with the idea of the elementary

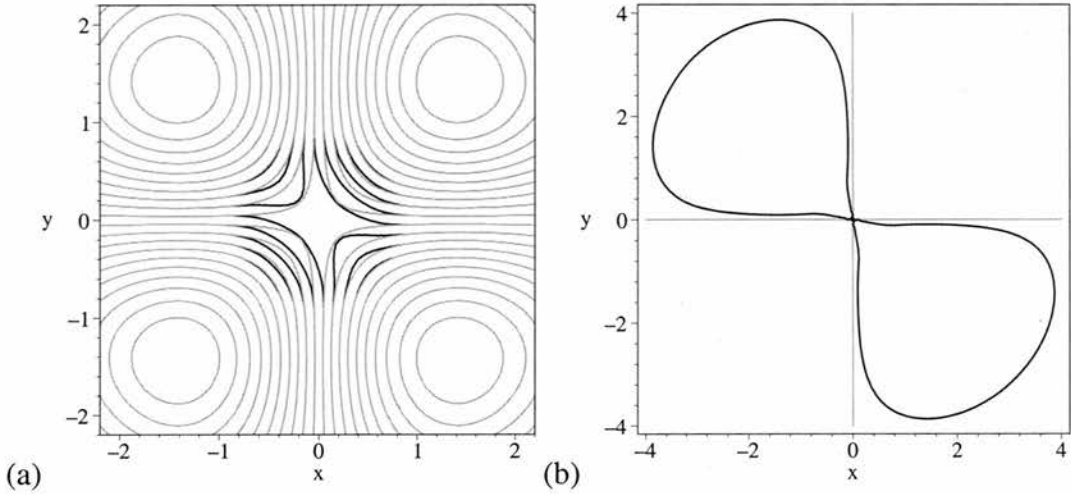


Figure 3.14: (a) Flow lines of \mathbf{w}_{in} (grey) and \mathbf{w}_{out} (black) for the modified time-dependent flow for $\varphi_0 > \varphi_{crit}$ and $t = 0$ and (b) the separatrices of these flows.

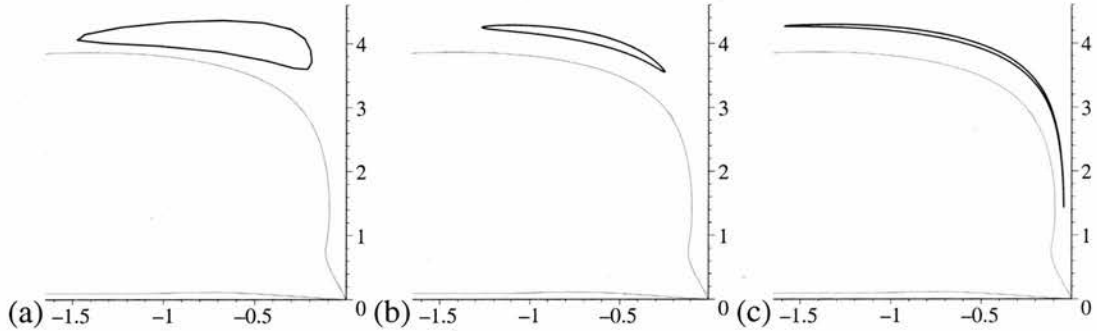


Figure 3.15: Perfectly reconnecting cross-sections in the time-dependent situation, in the plane $z = b$. For the parameters $a = 1$, $b = 1$, $B_0 = 1$, $\eta_0 = 1$, $j = 1$, $\varphi_0 = 1$, and (a) $T = 40$, (b) $T = 200$ and (c) $T = 800$. The grey lines are the separatrices of \mathbf{w}_{out} , while the separatrices of \mathbf{w}_{in} coincide with the x - and y -axes.

solution as a helicity source as described in Section 3.3.

For a given value of T and t' (the time for each step of the iteration) we trace out, via the iteration process, the cross-sections of perfectly reconnecting flux tubes. In Figure 3.15 we plot the shapes traced out by the points $a' = b'$ for each iteration. Precisely which cross-section we trace out depends on the starting point, a , of the iteration, with different cross-sections being concentric for fixed T, t' . The centres of these sets of cross-sections for all t' lie along the special flow-line circuit, described earlier, for which the transit time through D on \mathbf{w}_{in} and \mathbf{w}_{out} is the same. It should be noted that there is a maximum size for a cross-section centred on a certain point, as they cannot exist arbitrarily close to the separatrices of $\mathbf{w}_{in/out}$.

The effect of varying T , i.e. the localisation of the reconnection process in time, on the perfectly reconnecting cross-sections can be seen in Figure 3.15. When the process is

highly localised in time (T small) the cross-sections are fairly round, but as we increase T the cross-section becomes a thinner and thinner ellipse, whose major axis collapses towards the special time-symmetric flow line. When T is so large that we obtain a state which is numerically equivalent to the steady state, the iteration points (field lines) all lie along this flow line and we return again to a flux surface. It is important to note, however, that for this case the iteration leads to points inside D , and so these flux surfaces cannot simply be described as infinitely thin reconnecting flux tubes as they never exist wholly outside the diffusion region.

3.6 Summary

We have described here a steady solution of the kinematic resistive MHD equations, which exists in the vicinity of a spiral null point of the magnetic field, with a diffusion term localised around the null. A rotational type of flux reconnection is found, similar to that described in Hornig and Priest (2003) for reconnection in the absence of a null point. The reconnection of magnetic flux takes the form of a rotational slippage within an envelope of flux enclosing the diffusion region. We note that this rotational form of slippage is independent of the size and shape of the diffusion region.

In order to study the effect of the process on the global magnetic field structure an ideal flow was added which transports flux into and out of the local flux envelope. This results in different behaviours for field lines frozen into different regions of the ideal flow. In one region in particular, the rearrangement of the flux has some similar characteristics to 2D reconnection, where the two parts of any field line (mapped from initially-joined ends) separate, and the separation distance increases for all time. However, it is found that there is no simple one-to-one correspondence of reconnecting field lines after reconnection has occurred. As a result, there is also no splitting and one-to-one rejoicing of flux tubes in the steady time-independent case. The result is that the re-ordering of flux by the reconnection process is much more complicated than at a familiar two-dimensional null point.

Chapter 4

Kinematic reconnection at a magnetic null point: Fan-aligned current

“An expert is someone who learns more and more about less and less until they eventually know absolutely everything about absolutely nothing.”

Nicholas Murray Butler (1862 - 1947)

4.1 Introduction

In this chapter, as a complement to Chapter 3, we investigate the nature of reconnection at a 3D magnetic null point with fan-aligned current. There is once again assumed to be a localised non-ideal region in the vicinity of the null point itself, for the reasons described previously. The results of this chapter can be found in Pontin et al. (2004a).

In Section 4.2, the model is discussed, while the nature of the main solution is described in Section 4.3. In Section 4.4 the non-existence of perfectly reconnecting field lines is once again demonstrated, and Section 4.5 describes two further solutions in which the current is not spatially constant. The chapter is summarised in Section 4.6.

4.2 The model

As before, we seek a solution to the kinematic, steady, resistive MHD equations (3.2 - 3.5) in the locality of a magnetic null point. Whereas in Chapter 3 we examined the kinematic behaviour around a magnetic null point whose associated current was parallel

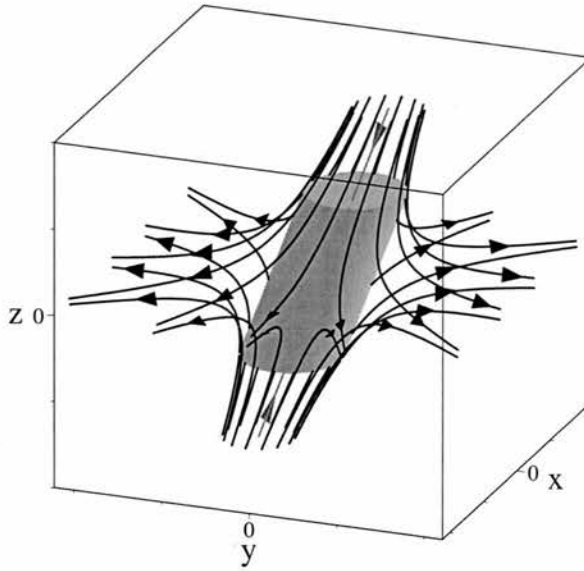


Figure 4.1: The basic structure of the 3D null point studied. The fan plane is in the $z = 0$ plane, while the spine line (grey) lies along $x = 0, y = jz/3$. The shaded cylinder shows the shape of the diffusion region.

with its spine axis, here we consider a null point with current directed parallel to the fan plane. We choose

$$\mathbf{B} = B_0 (x, y - jz, -2z), \quad (4.1)$$

such that, without loss of generality, the current lies in the x -direction, and is given by $\mathbf{j} = (\nabla \times \mathbf{B}) / \mu_0 = (B_0 j / \mu_0) \hat{\mathbf{x}}$, from Equation (3.5). The fan plane of this magnetic null point is coincident with the plane $z = 0$, while the spine is not perpendicular to this, but rather lies along $x = 0, y = jz/3$ (see Figure 4.1).

For the chosen magnetic field (4.1), analytical expressions for the equations of magnetic field lines can be found, as in Chapter 3, by solving

$$\frac{\partial \mathbf{X}(s)}{\partial s} = \mathbf{B}(\mathbf{X}(s)), \quad (4.2)$$

where the parameter s again runs along field lines. Solving Equation (4.2) we obtain

$$\begin{aligned} x &= x_0 e^{B_0 s}, \\ y &= \frac{jz_0}{3} e^{-2B_0 s} + \left(y_0 - \frac{jz_0}{3} \right) e^{B_0 s}, \\ z &= z_0 e^{-2B_0 s}. \end{aligned} \quad (4.3)$$

which describes the equations of the magnetic field lines in terms of some initial coordi-

nates $\mathbf{X}_0 = (x_0, y_0, z_0)$.

We proceed to solve Equations (3.2 - 3.5) by following the method described in Section 3.2 and defining a scalar potential Φ , so that

$$\mathbf{E} = -\nabla\Phi, \quad (4.4)$$

where

$$\Phi = - \int \eta \mathbf{j} \cdot \mathbf{B} ds + \Phi_0, \quad (4.5)$$

and Φ_0 is a constant with respect to the integration, i.e. $\Phi_0 = \Phi_0(\mathbf{X}_0)$, and so

$$\mathbf{v}_\perp = \frac{(\mathbf{E} - \eta \mathbf{j}) \times \mathbf{B}}{B^2}. \quad (4.6)$$

Here again Φ_0 is a free function of \mathbf{x}_0 , a constant with respect to the integration, although this time it must be set to a specific function to avoid singularities at the fan plane, as described below.

Now, for the simple magnetic field (4.1) described above, the electric current (\mathbf{j}) is constant, but we would like to consider a non-ideal region which is localised in space, so we must impose a localised resistivity. We must also choose the particular form of η such that the integration in (4.5) may be performed analytically. We therefore prescribe a resistivity of the form

$$\eta = \eta_0 \begin{cases} \left(\left(\frac{R_1}{a} \right)^2 - 1 \right)^2 \left(\left(\frac{z}{b} \right)^2 - 1 \right)^2 & R_1 < a, z^2 < b^2 \\ 0 & \text{otherwise,} \end{cases} \quad (4.7)$$

where $R_1^2 = x^2 + (y - \frac{iz}{3})^2$ and η_0 , a and b are constants. η_0 is the value of η at the null point, and the diffusion region is a tilted cylinder centred on the spine axis, extending to $z = \pm b$ and with radius a . This is shown, together with the structure of the magnetic field, in Figure 4.1. The diffusion region is chosen to be of this shape to simplify the calculations described above.

In order to perform the integration in Equation (4.5) we must choose a suitable surface on which to set $s = 0$ and so start the integration. The surface should be chosen such that it intersects every field line once and only once so that the mapping $(\mathbf{X}_0, s) \rightarrow (\mathbf{X})$, given by Equation (4.3), is one-to-one. With this in mind, we set $s = 0$ on $z = \pm z_0$.

Performing the integration of Equation (4.5) setting $s = 0$ on $z = z_0$ now gives an

expression for $\Phi(\mathbf{X}_0, s)$ for $z > 0$, and setting $s = 0$ on $z = -z_0$ gives $\Phi(\mathbf{X}_0, s)$ for $z < 0$. In order for these two expressions to match in the fan plane, that is for Φ to be smooth and continuous, and thus physically acceptable, we must set Φ at $z = \pm z_0$ (Φ_0) to

$$\Phi_0 = \frac{32}{21} \eta_0 B_0 j x_0. \quad (4.8)$$

This is equivalent to ensuring that when field lines in the fan plane converge on the null point, Φ approaches the same value along them, so that it is single-valued at the null. $\Phi(\mathbf{X})$, \mathbf{E} and \mathbf{v}_\perp can now be obtained from (4.5), (4.4) and (4.6) using (4.3) and (4.7), as described in Section 3.2. The mathematical expressions are too lengthy to show here, but can be calculated in a straightforward way using a symbolic computation package. These calculations are contained on the accompanying CD (see Appendix D for details on how to access them), as well as in Appendix E.2.

4.3 Nature and rate of reconnection

In order to study the effect of the reconnection on the magnetic flux, we examine the plasma velocity (\mathbf{v}_\perp) perpendicular to \mathbf{B} . This is the flux velocity in the ideal region, and is thus the component of the velocity that affects the flux transport. The nature of this flow in a plane of constant x is shown in Figure 4.2. The flow in the x -direction is zero across the spine, and is negligible for the reconnection process.

The plasma flow is non-zero across both the spine and the fan, having a stagnation point structure in the yz -plane, centred on the null point. Note that this is very different from the flow obtained in Chapter 3, where \mathbf{j} is parallel to the spine of the null point, and there is no flow across either the spine or the fan. The result of the plasma flows across the spine and fan is that the nature of the field line behaviour under the reconnection is qualitatively the same as described by Priest and Titov (1996) in the ideal analysis, with field lines advected across the spine having a behaviour like the *fan reconnection*, and those advected across the fan having a *spine reconnection* type behaviour.

Consider following field lines, with footpoints anchored in the ideal region, which pass across the top of the diffusion region (D) such that they pass down through D . These field lines can be seen to flip around the spine in the fan plane, as illustrated in Figure 4.3, with a behaviour analogous to the fan reconnection of Priest and Titov (1996). By contrast, following field lines anchored in the flow across the fan plane we see these field

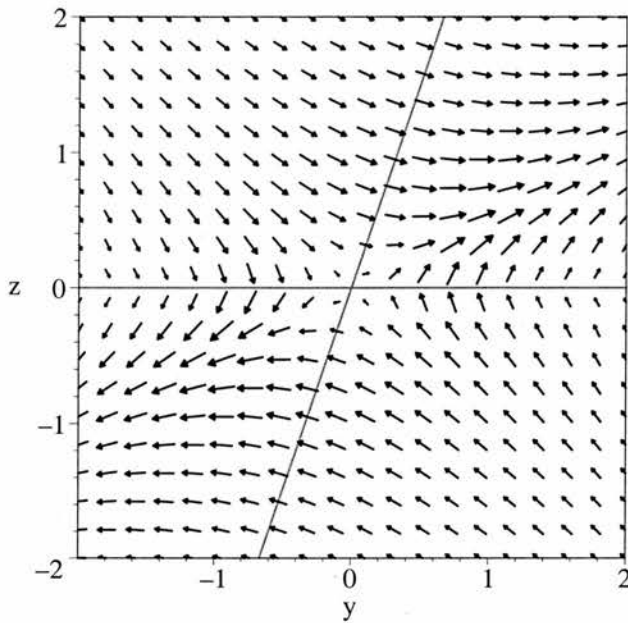


Figure 4.2: The structure of the plasma flow, along with the fan and spine (black lines) in a typical plane of constant x , for parameters $\eta_0 = B_0 = j = a = b = 1$.

lines move towards the fan until they lie in the fan plane, at which point they flip down the spine, and then move away from the null on the opposite side of the fan (analogous to spine reconnection).

Although a continuous stream of field lines is reconnected through the spine, no finite amount of flux is reconnected at it, since it is a single line. A finite amount of flux *is*, however, transported across the fan plane in an arbitrary time. This can be very important, since if we consider our null point to be surrounded by a global field, for example in the solar corona, then the fan plane is a separatrix surface of this magnetic field, which separates distinct regions of magnetic topology. The topology of this field changes when flux is transported across a separatrix surface. As described previously, in the solar atmosphere separatrices are thought to be very important locations for coronal heating.

It is possible to calculate the amount of flux transported across the fan surface by evaluating

$$F = \int_{C1} \mathbf{v} \times \mathbf{B} \cdot d\mathbf{l}, \quad (4.9)$$

where $C1$ is the curve shown in Figure 4.4, which lies in the fan plane. Note that, since the flux is transported across the fan in opposite directions for positive and negative y , the total amount transported across the fan plane is double this amount, with equal amounts transported in either direction.

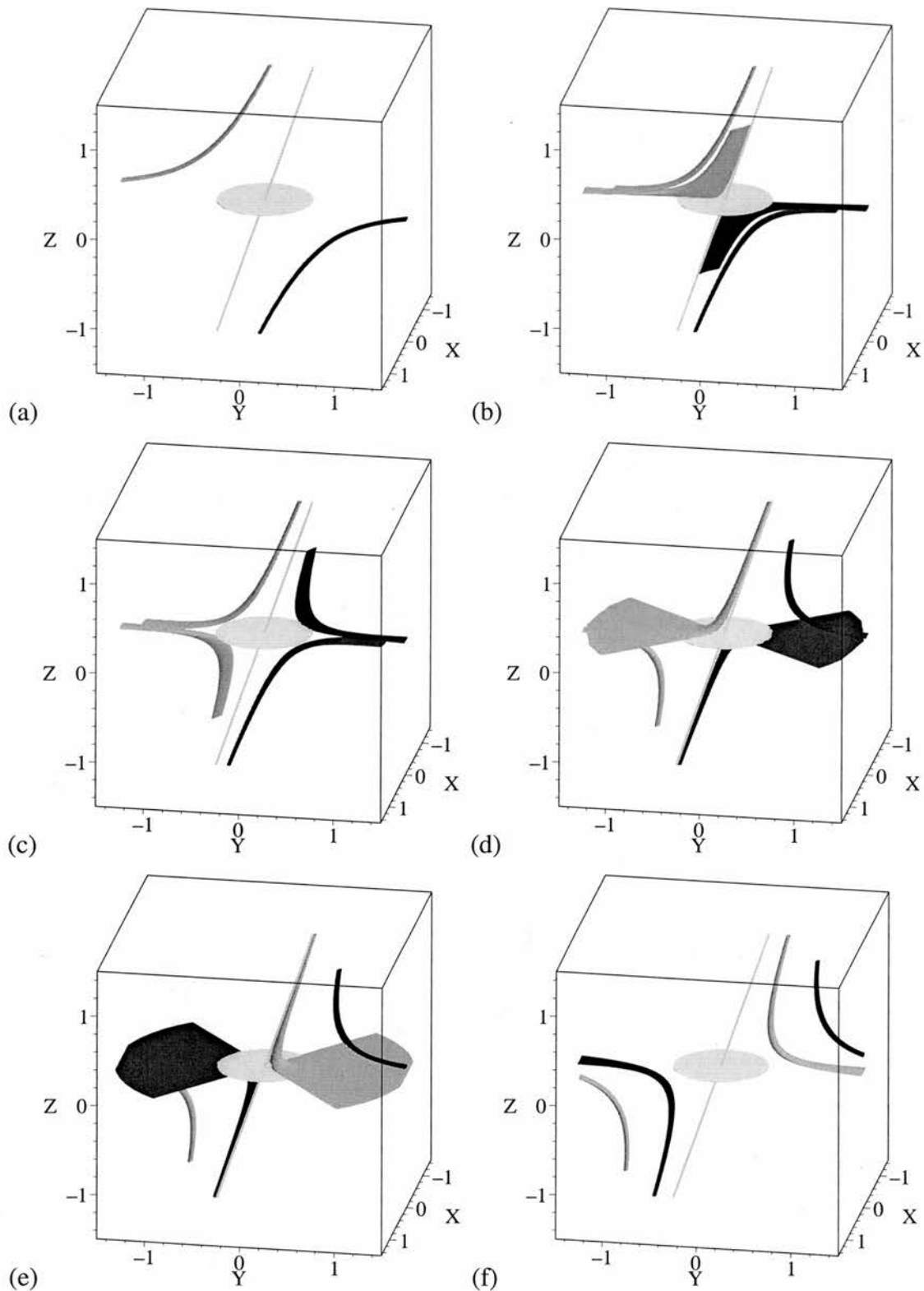


Figure 4.3: Sequence of snapshots showing the reconnection of two thin flux tubes, initially chosen to be symmetric about the null. Field lines traced from footpoints anchored in the fan-crossing flow flip up the spine. Field lines traced from the top/bottom of the box (anchored in the spine-crossing flow) flip around the spine in the fan plane. The grey line is the spine and the grey disc shows the location of the fan plane. (See ‘fanrec.mpg’ on the CD.)

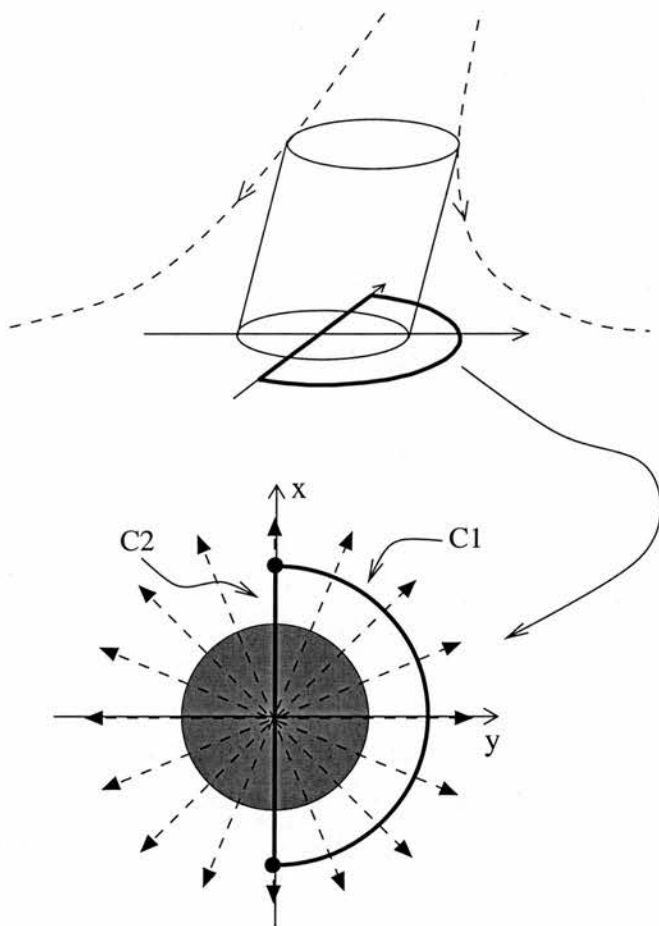


Figure 4.4: The curves C_1 and C_2 joining two points on the x -axis, on opposite sides of the diffusion region, in the fan plane. The curve C_1 is semi-circular and therefore perpendicular to \mathbf{B} .

Now, since the curve C_1 lies outside D , and therefore along it $\mathbf{v} \times \mathbf{B} = -\mathbf{E}$, we can write $F = - \int_{C_1} \mathbf{E} \cdot d\mathbf{l}$. Furthermore, since \mathbf{E} is conservative this integral is independent of the path, so we may write

$$F = - \int_{C_2} E_{||} dl, \quad (4.10)$$

where the curve C_2 , as shown in Figure 4.4, runs along a pair of field lines coincident with the x -axis. Due to the form of Equation (4.10), and the fact that C_2 passes through the null, we define F as the reconnection rate. From Equation (4.10),

$$F = - \int_{-a}^a E_x dx = \frac{16}{15} B_0 j \eta_0 a. \quad (4.11)$$

The physical interpretation of this reconnection rate is as follows. Firstly, it is similar to the reconnection rate of Chapter 3, in that it is calculated by integrating the parallel

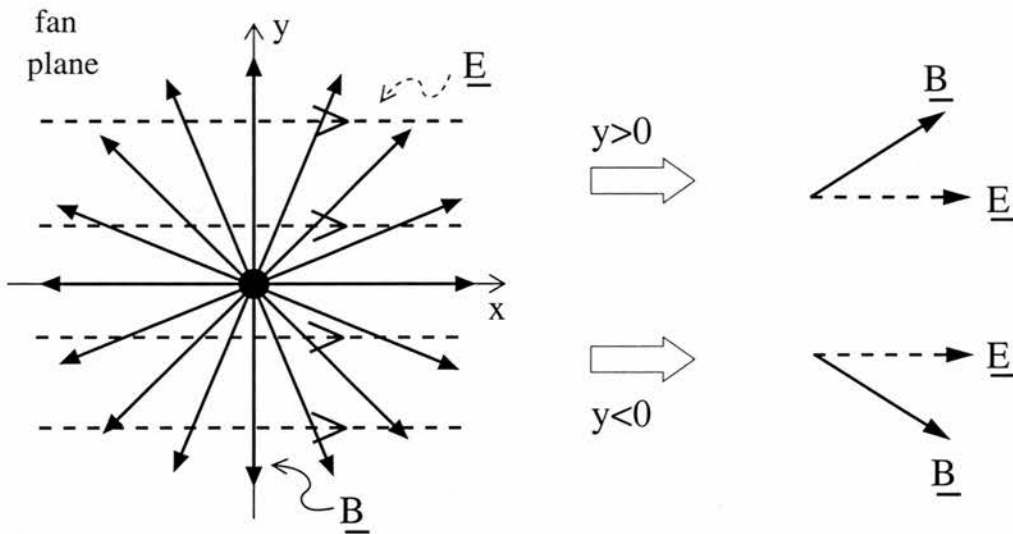


Figure 4.5: The structure of the magnetic field (\mathbf{B}) and electric field (\mathbf{E}) in the fan plane. The non-zero vector product between the two implies a flow across the fan, in opposite directions for $y > 0$ and $y < 0$.

electric field along the direction parallel to \mathbf{j} . Moreover, there are also similarities to the case of 2D reconnection with an invariant third direction, since the reconnection rate gives a measure of the amount of flux transported across the separatrix surface(s) of the null.

The plasma flow across the fan plane is very important for topological considerations, and is a major difference between this solution and the one described in Chapter 3. The cause of the fan-crossing flow can be understood as follows. Consider simply the structure of \mathbf{B} and \mathbf{j} , in the vicinity of the x -axis, in the fan plane. $\mathbf{j} \cdot \mathbf{B}$ has opposite sign for $x > 0$ and $x < 0$, since \mathbf{j} and \mathbf{B} are parallel on the x -axis for $x > 0$ and anti-parallel for $x < 0$. So $\Phi = -\int \eta \mathbf{j} \cdot \mathbf{B} ds$ has opposite sign for $x > 0$ and $x < 0$. Hence, in the fan plane close to the x -axis, $\mathbf{E} = E_x$ is uni-directional across the spine, as shown in Figure 4.5. Since $\mathbf{E} \times \mathbf{B}$ is non-zero in the fan plane, we obtain a plasma flow in the z -direction, across the fan. Note that v_z must have different signs for $y > 0$ and $y < 0$ due to the different handedness of the vector products in these two regions (see Figure 4.5). This argument is completely independent of the profile of η , and relies only upon the structure of \mathbf{B} (and thus \mathbf{j}) and the fact that η is localised.

4.4 Non-existence of perfectly reconnecting field lines

A major result of Hornig and Priest (2003) and also of Pontin et al. (2004b) (as described in Chapter 3) is that in three dimensions there is no simple one-to-one correspondence of

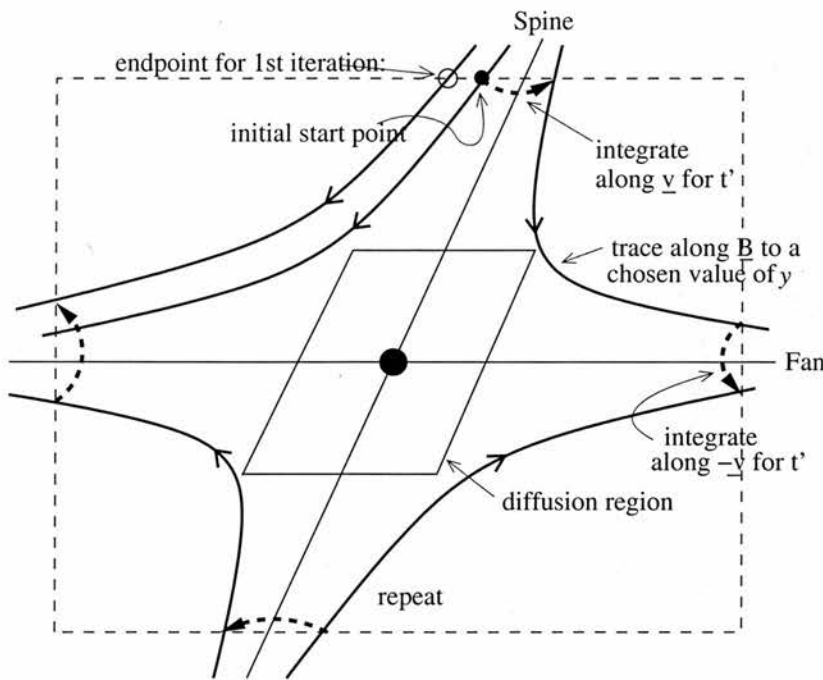


Figure 4.6: Circuit of magnetic field lines (solid black) and plasma flow lines followed by the corresponding field line footpoints (dashed black). In general the start and end points of the circuit lies on different field lines, implying no one-to-one correspondence of reconnecting field lines. We define quadrant 1 as the top left area bounded by the fan and spine, and number the other quadrants clockwise.

reconnecting field lines. That is, for any field line which undergoes reconnection, there is in general no corresponding field line with whose two footpoints the original footpoints will become pairwise reconnected. As a result there is also no one-to-one correspondence, or perfect reconnection, of reconnecting flux tubes in the time-independent case.

It turns out that, by tracking the change of connections of field lines for the solution described in the previous section, it can be shown that once again no one-to-one field line reconnection occurs. This can be shown explicitly by following the procedure shown in Figure 4.6. To find reconnecting field lines we consider starting from an initial point (or plasma element) outside the diffusion region on a given field line. Start from a point close to the spine axis, in the ‘first quadrant’, as shown in Figure 4.6. We allow this point to evolve in the ideal flow for a time $t = t'$, where t' is large enough that the plasma element crosses the spine. On the new field line (in quadrant 2) on which our plasma element now lies, choose a point (outside D) in the fan-crossing region of the flow and follow this point backwards in v from $t = t'$ to $t = 0$ to find the reconnecting field line in quadrant 3. Now repeat these two steps. Note that performing this procedure is analogous to performing a step of the iteration procedure described by Hornig and Priest (2003), or equivalently that described in Section 3.5. In this case, the procedure is performed in the constant- x plane

(shown in Figure 4.6) which is the analogue of the constant- z plane, also perpendicular to \mathbf{j} , in Hornig and Priest (2003) and Section 3.5.

If field lines were to reconnect in a one-to-one fashion, then after completing the circuit and returning to quadrant 1, we would return to a point lying on the initial field line. However, performing this routine for our solution we find that we never end up back on the same field line, and hence there is no field line with which our initial magnetic field line will perfectly reconnect, such that their footpoints become pair-wise oppositely connected after the reconnection process. As a consequence of this, there is no simple one-to-one reconnection of magnetic flux tubes either, as illustrated in Figure 4.3.

4.5 Non-constant current

It is possible to perform the same analytical analysis as described in Section 4.2 for certain slightly more complex magnetic fields, whose associated currents (\mathbf{j}) are not constant. It is instructive, in particular, to consider situations in which the magnetic current vanishes at the null point itself. We consider first the magnetic field

$$\mathbf{B} = B_0 (x, y - jz^3, -2z), \quad (4.12)$$

so that the current is now $\mathbf{j} = (3B_0/\mu_0) z^2 \hat{x}$. The fan of the null point again lies in the $z = 0$ plane, although now the spine curves away from the z -axis. We note that the current is zero at $z = 0$, in the fan.

Solving Equation (4.2), the equations for the magnetic field lines are

$$\begin{aligned} x &= x_0 e^{B_0 s}, \\ y &= \frac{jz_0^3}{7} e^{-6B_0 s} + \left(y_0 - \frac{jz_0^3}{7} \right) e^{B_0 s}, \\ z &= z_0 e^{-2B_0 s}. \end{aligned} \quad (4.13)$$

Once again, s is set to zero on the surfaces $z = \pm z_0$ for the purpose of performing the integration (4.5). It remains to impose a suitable form for the resistivity, and for analytical simplicity we choose the profile of η to again be described by Equation (4.7), where this time $R_1^2 = x^2 + \left(y - \frac{jz^3}{7} \right)^2$.

We now proceed by repeating the analysis described in Section 4.2, solving (4.5), (4.4) and (4.6) to find Φ , \mathbf{E} and \mathbf{v}_\perp . We find this time that, in order to ensure that Φ is

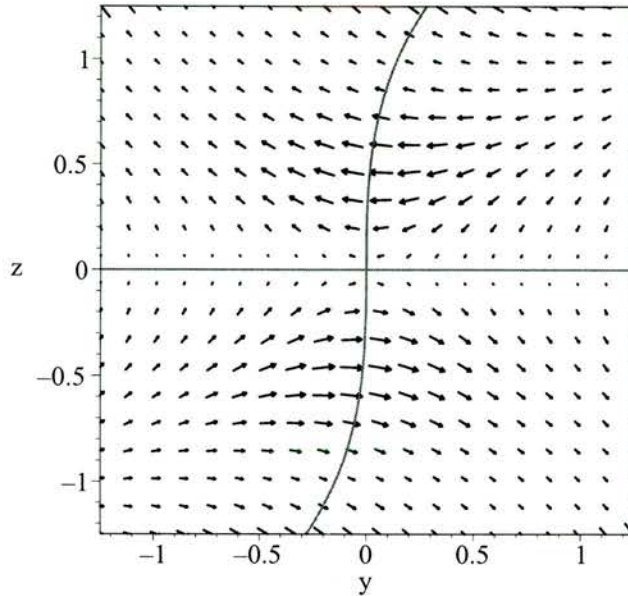


Figure 4.7: The plasma flow and magnetic skeleton in a plane of constant x when $|\mathbf{j}| \propto z^2$, for the same choice of parameters as Figure 4.2.

smooth at the fan, the constant of integration (Φ_0) in Equation (4.5) must be set to

$$\Phi_0 = -\frac{32}{77} \eta_0 B_0 j x_0 z_0^2. \quad (4.14)$$

The calculations are again given on the CD, as well as in Appendix E.3.

The resulting plasma flow is shown in Figure 4.7. As before, the flow crosses the spine of the null point, but this time there is no flow across the fan, $v_z(z=0) = 0$. The effect on the reconnection of magnetic field lines is that we have a slippage-type behaviour of field lines which pass through the diffusion region. Both ends of a given field line, passing through D , move, outside D , at the ideal plasma velocity. This plasma velocity is, as shown in Figure 4.7, largely in the y -direction, and thus the field line is moved through D in this direction, with each ‘half’ of the field line slipping relative to the other during the time they are in D . The result is that, after leaving D , the two footpoints are differently connected, but continue to move in the same direction. Note also that, by analogy with our previous argument (considering the structure of \mathbf{B} and \mathbf{j} in the fan), it is no surprise that we now have no flow across the fan, since \mathbf{j} is now zero in the fan plane.

The effect of the reconnection process described by this solution on a pair of magnetic flux tubes is shown in Figure 4.8. The flux tubes are chosen, as before, to be centred on the $x = 0$ plane, and as a result, both ends of each tube are swept through the spine by the plasma. The tubes are seen to split as they enter the diffusion region, as before, and flip

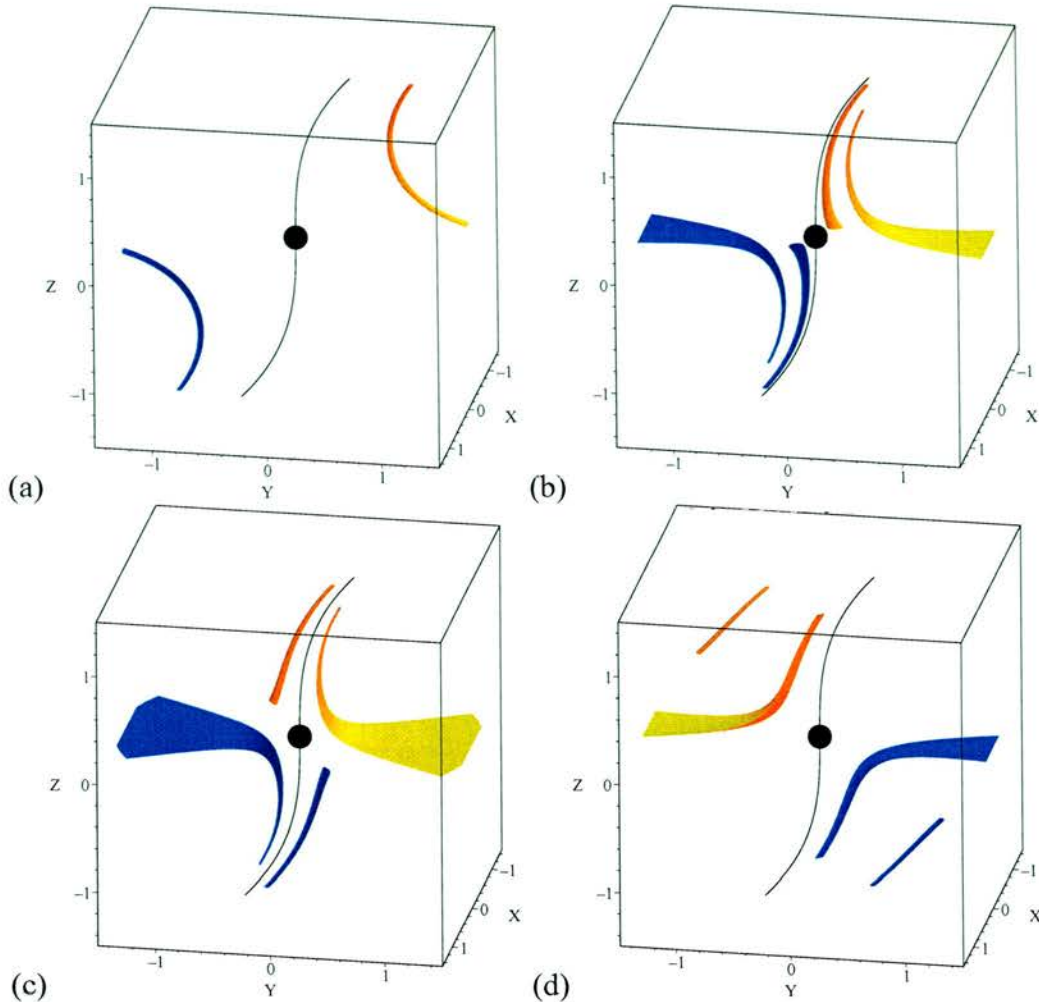


Figure 4.8: Snapshots of the reconnection of magnetic flux tubes in the field $\mathbf{B} = B_0(x, y - jz^3, -2z)$, where the corresponding plasma flow crosses the *spine* but *not the fan* of the null point. The black sphere marks the null, while the black line is the spine. The full animation is contained on the CD; ‘spinecross.mpg’.

through the spine in a fashion very much like that of the fan reconnection of Priest and Titov (1996). Note, however, that the cross-sections close to the fan plane from which two of the final tubes are traced (each initial tube is traced from one cross-section at the top/bottom of the box, and one close to the fan plane) actually pass into the diffusion region as these tubes flip around the spine. This is due to the positioning of the tubes about the $x = 0$ plane, and means that the second pair of tubes which flip through the spine are not really flux tubes, in the sense that, once they cease to be traced from the ideal environment, we no longer be sure that *the same field lines* are plotted at each time. The basic nature of the reconnection described by this solution is nonetheless illustrated by the images (Figure 4.8).

The motion of the magnetic field lines under the process described above is very

similar to the field line behaviour associated with the fan reconnection of Priest and Titov (1996). This behaviour is obtained by considering a situation in which the electric current is zero in the fan plane of the null point. Is it possible, then, to find a configuration in which the field line behaviour is analogous to *spine reconnection*, such that there is a plasma flow across the fan of the null point but not the spine? In order to answer this question, we consider a null point where the current is zero on the spine.

Consider the magnetic field

$$\mathbf{B} = B_0 \left(x, y, -2z + \frac{jy^3}{3} \right), \quad (4.15)$$

whose spine lies along the z -axis, and whose fan is the surface $z = jy^3/15$. The resultant current is given by $\mathbf{j} = (B_0 j / \mu_0) y^2 \hat{\mathbf{x}}$, which again lies parallel to the fan plane. We repeat once more the analysis previously described, where this time η is prescribed, for analytical simplicity, as

$$\eta = \eta_0 \begin{cases} \left(\left(\frac{R}{a} \right)^2 - 1 \right)^2 \left(\left(\frac{z_1}{b} \right)^2 - 1 \right)^2 & R < a, z_1^2 < b^2 \\ 0 & \text{otherwise,} \end{cases} \quad (4.16)$$

where $R = \sqrt{x^2 + y^2}$ and $z_1 = z - jy^3/15$. Solving Equation (4.2) once again, the magnetic field lines are described by

$$\begin{aligned} R &= R_0 e^{B_0 s}, \\ z_1 &= z_{10} e^{-2B_0 s}. \end{aligned}$$

For simplicity we choose to this time set $s = 0$ on $z_1 = \pm z_{10}$. In this case, the potential Φ is smooth at the fan for $\Phi_0 = 0$. The calculations are again given on the CD, as well as in Appendix E.4.

The resulting plasma flow in this case is shown for a typical plane of constant x in Figure 4.9(a). As can be seen, there is a plasma flow in this case across the fan, but not across the spine, and so we have a field line behaviour similar to the spine reconnection of Priest and Titov (1996), where flux is continually transported across the fan of the null point. However, the nature of the flow across the fan is not as simple in this case as in the constant-current solution. In the constant-current solution the plasma velocity is qualitatively the same for all planes of constant x , and so there is little variation in the nature of the reconnection process. Flux is simply transported across the fan in one direction for $y > 0$ and the other direction for $y < 0$. However, when we move to this situation where $|\mathbf{j}| \propto y^2$, the structure is not quite so simple. The difference can be clearly

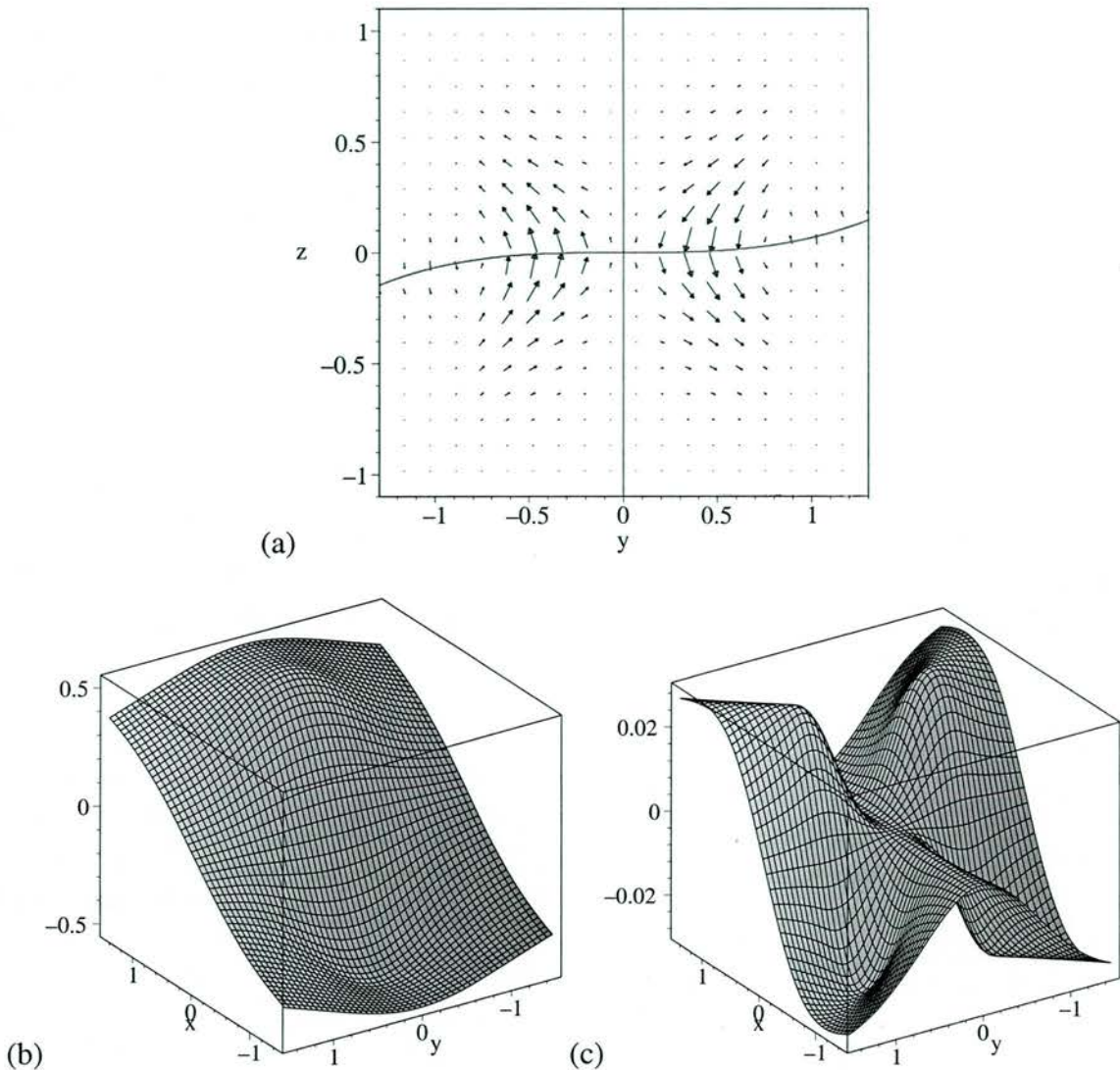


Figure 4.9: (a) The plasma flow and magnetic skeleton in a plane of constant x when $|j| \propto y^2$, for the same choice of parameters as Figure 4.2. (b) Surface of the electric potential, Φ , in the fan plane for the constant current solution and (c) for the solution with $|j| \propto y^2$.

seen by considering surfaces of Φ in the fan plane for each solution (see Figure 4.9). In the constant current solution, Φ decreases monotonically along, as well as away from, the x -axis (see Figure 4.9(b)), resulting in the simple flux transport described. However, when $|j| \propto y^2$, the potential, Φ , is zero along the x -axis, and there are two positive peaks and two negative (see Figure 4.9(c)). (The disparity between the peak Φ values for the two solutions is due to the extra term (Φ_0) required in the constant-current solution to ensure smooth variation of physical quantities across the fan plane.) The resulting plasma flow also has a different structure. While there is a strong plasma flow across the fan within the diffusion region, the flow across the fan outside the diffusion region is actually in the opposite direction (see Figure 4.9(a)).

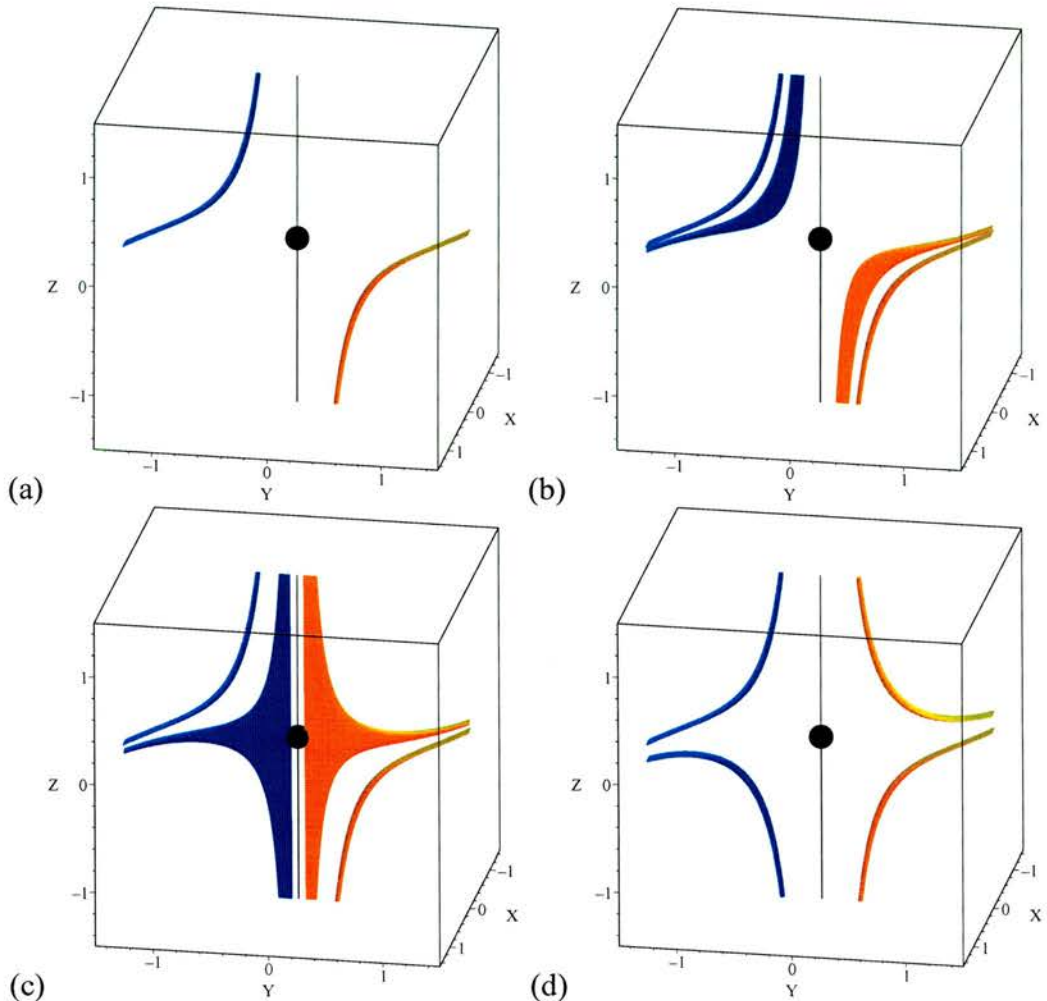


Figure 4.10: Snapshots of flux tube reconnection in the field $\mathbf{B} = B_0 \left(x, y, -2z + \frac{iy^3}{3} \right)$, where the corresponding plasma flow crosses the *fan* but *not the spine* of the null point. The full animation is contained on the CD; ‘fancross.mpg’.

This reconnection process has two different possible interpretations. Consider performing the same analysis as performed in Section 4.3 in order to find the reconnection rate. Performing the integration $F = - \int_{-a}^a E_x dx$, should again provide us with a reconnection rate, with physical interpretation being the rate of flux transport across the fan. However, in this case, evaluating this integral we obtain the answer $F = 0$. Alternatively, the integral (4.9) can instead be evaluated around only a quarter circle, to give $4\sqrt{2} \eta_0 B_0 j a^3$. The reconnection rate can thus be thought of as zero, due to two reconnection processes cancelling each other, or as $16\sqrt{2} \eta_0 B_0 j a^3$, if the two processes are envisaged to complement each other.

As before, the process is illustrated (see Figure 4.10) by tracing out reconnecting magnetic flux tubes. It can be seen that field lines traced from cross-sections near the

fan plane are advected across it (in the opposite direction to the plasma, near the null), flipping up the spine as in *spine reconnection* (Priest and Titov, 1996). Note that, due to the fact that Φ is integrated from surfaces of $z_1 = \pm z_{10}$, and $\Phi_0 = 0$, the flow is zero for $|z_1| > |z_{10}|$, so that the flux tubes anchored there remain stationary. Furthermore, $\Phi_0 = 0$ also implies that $\Phi = 0$ outside the envelope of field lines which thread the diffusion region (as in the ‘pure solution’ of Chapter 3). This implies that there must be a circulation of the flux which is transported across the fan surface, so that it will later be transported back across the fan in the opposite direction at some other location, in order to maintain the steady magnetic field. Such a circulation is in fact present, with closed circulation ‘cells’ present in each xy -quadrant.

In order to test the solution, it is important to check that an equal amount of flux is transported in each direction across the fan in each of these regions of circulation. By the same argument as for Equation (4.10), the flux transported across the fan in each xy -quadrant can be found by integrating E_{\parallel} along the axes in the fan plane enclosing that quadrant. This is the same as taking the difference between the values of Φ on the boundary of D on each axis, since fan field lines are radial and so lie along these directions. Since $\Phi = 0$ along the x - and y - directions in the fan plane (see Figure 4.9(c)), this is automatically the case.

4.6 Summary

We have described here steady solutions of the kinematic resistive MHD equations, which exist in the vicinity of a magnetic null point with fan-aligned current, with a diffusion term localised around the null. In contrast to what was found in Chapter 3, the result of the fan-aligned current is that flows are present across both the spine line and the fan plane of the null. The flow across the fan plane is of particular interest, since in a global field, for example in the solar corona, the fan surface is a separatrix of the field, and thus a transfer of flux across it constitutes a change in the magnetic topology. A further solution is found in which the current drops to zero at the null point itself, resulting in flow across the fan only, as well as a solution with a solely spine-crossing flow.

Although the nature of the reconnection discovered here is very different from the case where the current lies parallel with the spine (see Chapter 3), a number of key properties are still present. In particular, no unique field line velocity exists, and so the process must be described by two separate flux velocities, w_{in} and w_{out} , which do not coincide within the non-ideal region. Furthermore, it is found that there is no simple one-to-one

correspondence of reconnecting field lines after reconnection has occurred. The result is that the re-ordering of flux by the reconnection process is much more complicated than at a familiar two-dimensional null point.

Chapter 5

Numerical full MHD investigation of reconnection in the absence of null points

“The most exciting phrase to hear in science, the one that heralds new discoveries, is not ‘Eureka!’ (I’ve found it!), but ‘That’s funny....’ ”

Isaac Asimov (1920 - 1992)

5.1 Introduction

In this chapter, a numerical experiment is described which investigates the nature of 3D reconnection, in the absence of magnetic null points, at an isolated non-ideal region. We focus on the resulting behaviour of the magnetic flux, which has been shown in previous chapters to be fundamentally different in the kinematic regime from the familiar two-dimensional behaviour. The aim of this numerical experiment is to test whether the new properties of 3D kinematic reconnection, described in Chapter 2, follow through to the dynamical regime where the full set of MHD equations are solved. We aim also in particular to verify (or otherwise) the solution of Hornig and Priest (2003) for kinematic 3D reconnection in the absence of a magnetic null point. The importance of a component of \mathbf{E} parallel to \mathbf{B} in reconnection has been described by, for example Schindler et al. (1988) and Hornig (2001). The role of this parallel electric field in our experiment is described in detail.

There are now very many 3D numerical experiments into various applications of re-

connection. Of those 3D MHD simulations which are intended to focus on the reconnection process itself, there are a number of studies of the interaction of isolated magnetic flux tubes in various different 3D configurations (e.g. Yamada et al., 1990; Lau and Finn, 1996; Dahlburg et al., 1997; Linton et al., 2001; Linton and Priest, 2003). Simulations have also been made of 3D reconnection in magnetic fields containing null points (e.g. Galsgaard and Nordlund, 1997; Galsgaard et al., 1997) as well as when no null points are present (e.g. Galsgaard and Nordlund, 1996; Milano et al., 1999; Kliem and Schumacher, 2001), where in general a lot of the focus has been on determining at which locations currents preferentially grow. In the experiment described in this chapter, we consider such a configuration in which the current is known to grow (see the following section), and focus on the behaviour of the magnetic flux when a resistivity is introduced to facilitate reconnection.

In Section 5.2 we describe the numerical scheme, as well as the initial configuration and boundary conditions. In Section 5.3, the results of the experiment are presented for reconnection at a fixed isolated diffusion region. Section 5.4 describes the effect of instead allowing the resistivity to depend on the current, in such a way that the resistivity is non-zero in regions where the modulus of the current exceeds a chosen threshold value. In Section 5.5 a summary is given. A number of additional images and plots for various runs of the experiment are provided on the CD which accompanies the thesis (see Appendix D for details on how they can be accessed).

5.2 The experiment

5.2.1 Numerical scheme

In order to perform the experiment we employ a parallel numerical code to solve the dimensionless equations of MHD in the form;

$$\frac{\partial \mathbf{B}}{\partial t} = -\nabla \times \mathbf{E}, \quad (5.1)$$

$$\mathbf{E} = -(\mathbf{v} \times \mathbf{B}) + \eta \mathbf{j}, \quad (5.2)$$

$$\mathbf{j} = \nabla \times \mathbf{B}, \quad (5.3)$$

$$\frac{\partial \rho}{\partial t} = -\nabla \cdot (\rho \mathbf{v}), \quad (5.4)$$

$$\frac{\partial}{\partial t} (\rho \mathbf{v}) = -\nabla \cdot (\rho \mathbf{v} \mathbf{v} + \underline{\tau}) - \nabla P + \mathbf{j} \times \mathbf{B}, \quad (5.5)$$

$$\frac{\partial e}{\partial t} = -\nabla \cdot (e \mathbf{v}) - P \nabla \cdot \mathbf{v} + Q_{visc} + Q_{Joule}, \quad (5.6)$$

where \mathbf{B} is the magnetic field, \mathbf{E} the electric field, \mathbf{v} the plasma velocity, η the resistivity, \mathbf{j} the electric current, ρ the density, $\underline{\underline{\tau}}$ the viscous stress tensor, P the pressure, e the internal energy, Q_{visc} the viscous dissipation and Q_{Joule} the Joule dissipation. An ideal gas is assumed, and hence $P = (\gamma - 1) e = \frac{2}{3}e$.

Note that the equations above have been non-dimensionalised by setting the magnetic permeability $\mu_0 = 1$, and the gas constant equal to the mean molecular weight. The result is that, for a cubic domain of unit size (as described in the following experiment), if $|\rho|$ and $|\mathbf{B}| = 1$, then the time is measured in units of the Alfvén travel time across the domain ($\tau_A = L\sqrt{\mu\rho_0}/B_0$, where L is the size of the domain, and ρ_0 and B_0 are typical values of the density and magnetic field respectively).

We perform two sets of runs of the experiment, in the first of which we assume the *cold plasma* approximation, that the density and internal energy are constant, and in the second of which the full set of equations above are solved with all variables free to evolve. A number of runs are performed of different numerical resolution, with the equations solved on Cartesian grids of size 64^3 , 128^3 and 256^3 . The variables are evaluated on staggered meshes; with respect to a unit cube, ρ and e are calculated in the body centre, \mathbf{B} and $\rho\mathbf{v}$ are calculated at face centres, and \mathbf{E} and \mathbf{j} are calculated at edge centres. Spatial derivatives are evaluated using a sixth-order accurate finite difference method. This method involves the six nearest-neighbour points in the relevant direction, and the formulae for calculating derivatives are obtained by simple permutation of the indices in the expression below. The six operators $\partial_{[xyz]}^\pm$ give a value for the derivative evaluated at $\pm\frac{1}{2}$ gridpoint in the relevant direction and, for example, ∂_x^+ is given by

$$\begin{aligned}\partial_x^+(f_{i,j,k}) &= f'_{i+\frac{1}{2},j,k} \\ &= \frac{a}{\Delta x} (f_{i,j,k} - f_{i+1,j,k}) + \frac{b}{\Delta x} (f_{i-1,j,k} - f_{i+2,j,k}) \\ &\quad + \frac{c}{\Delta x} (f_{i-2,j,k} - f_{i+3,j,k})\end{aligned}\tag{5.7}$$

where

$$a = 1 - 3b + 5c, \quad b = -\frac{1}{24} - 5c, \quad c = \frac{3}{640}.\tag{5.8}$$

It is often the case that, due to the staggered mesh, this value of the derivative is returned in exactly the position it is needed. When this is not the case, the values are interpolated with a fifth-order interpolation method using one of six ‘shift’ operators ($T_{[x,y,z]}^\pm$), which interpolate the value of the chosen function at $\pm\frac{1}{2}$ gridpoint in the relevant direction. For

example, T_x^+ is given by

$$\begin{aligned} T_x^+(f_{i,j,k}) &= f_{i+\frac{1}{2},j,k} \\ &= a(f_{i,j,k} + f_{i+1,j,k}) + b(f_{i-1,j,k} + f_{i+2,j,k}) \\ &\quad + c(f_{i-2,j,k} + f_{i+3,j,k}) \end{aligned} \quad (5.9)$$

where

$$a = \frac{1}{2} - b - c, \quad b = -\frac{1}{16} - 3c, \quad c = \frac{3}{256}. \quad (5.10)$$

For further explanation of the choice and implementation of these operators, see Nordlund and Galsgaard (1997).

A third-order predictor-corrector method is employed for time-stepping. It is a modification of that by Hyman (1979), altered to allow for variable time-stepping, and the predictor step is given by

$$f_{n+1}^* = a_1 f_{n-1} + (1 - a_1) f_n + b_1 \dot{f}_n, \quad (5.11)$$

while the corrector step is

$$f_{n+1} = a_2 f_{n-1} + (1 - a_2) f_n + b_2 \dot{f}_n + c_2 \dot{f}_{n+1}^*, \quad (5.12)$$

where

$$\begin{aligned} a_1 &= r^2, \\ b_1 &= \Delta t_{n+\frac{1}{2}} (1 + r), \\ a_2 &= 2(1 + r)/(2 + 3r), \\ b_2 &= \Delta t_{n+\frac{1}{2}} (1 + r^2)/(2 + 3r), \\ c_2 &= \Delta t_{n+\frac{1}{2}} (1 + r)/(2 + 3r), \\ r &= \Delta t_{n+\frac{1}{2}} / \Delta t_{n-\frac{1}{2}}, \\ \Delta t_{n+\frac{1}{2}} &= t_{n+1} - t_n, \\ \Delta t_{n-\frac{1}{2}} &= t_n - t_{n-1}. \end{aligned} \quad (5.13)$$

Information regarding the implementation of this scheme in the code is given by Nordlund and Galsgaard (1997). In the code, artificial diffusion and viscosity terms are included which have been carefully chosen so as to provide a very limited effect in situations where dissipative effects are negligible, but which are also capable of providing sufficient localised dissipation where necessary to handle the development of numerical instabilities.

ties. The choice of these terms is based on a number of tests for model situations, as described once again by Nordlund and Galsgaard (1997). In addition, for different runs of the experiment, extra resistive terms are added, as described in the following section.

5.2.2 Experimental setup

The aim of the experiment is to study the evolution of magnetic flux in a reconnection process involving no null point of \mathbf{B} , in order to test the assertions of Priest et al. (2003a) and Hornig and Priest (2003). They chose to study the simple magnetic field $\mathbf{B} = B_0 \left(\frac{y}{L}, \frac{k^2 x}{L}, 1 \right)$, where B_0 , k and L are constant, as described in Chapter 2. It is with this in mind that we choose our initial magnetic field configuration to have the basic form of a hyperbolic X-type structure in one plane, with a uni-directional field in the perpendicular direction. Such a field structure is termed a *hyperbolic flux tube* (HFT) (Titov et al., 2002), which in general can be considered as the intersection of two *quasi-separatrix layers* (QSLs, Priest and Démoulin, 1995).

A QSL is the generalisation of a separatrix surface, in that such a surface is a limiting case of a QSL (Titov et al., 1999). Across a separatrix surface, there is a discontinuous ‘jump’ in field line connectivity. In a QSL however, the connectivity is continuous but shows a large spatial variation, so that a ‘small’ change of footpoint position at either end maps to a ‘large’ change at the opposite end. In order to quantify this, the *degree of squashing* of elemental flux tubes may be introduced (Titov et al., 1999). It has been shown that these QSLs are sites where current layers may form for particular types of imposed footpoint motions (Inverarity and Titov, 1997; Galsgaard, 2000). Since an HFT is essentially the intersection of two QSLs (Titov et al., 2002), it is interesting to consider whether it too may be a favourable site for current growth, in a magnetic field with simple topology (i.e. no nulls or separatrices). The growth of currents in HFTs has been investigated in a series of papers by Titov et al. (2003), Galsgaard et al. (2003) and Neukirch et al. (2004). It is found that a strong current grows in the centre of the HFT, due to the geometry of the field, if a shearing motion is applied to the footpoints which is in such a sense as to rotate (‘twist’) either end of the tube in opposite directions. This is termed *magnetic pinching* of the HFT. This is in contrast to the effect of a ‘turning’ motion, which is achieved by rotating either end of the HFT in the same direction, and results in minimal current growth (see Figure 5.2(a)).

In order to set up such an initial magnetic field we follow Galsgaard et al. (2003) in calculating first the potential field resulting from a magnetic field imposed normal

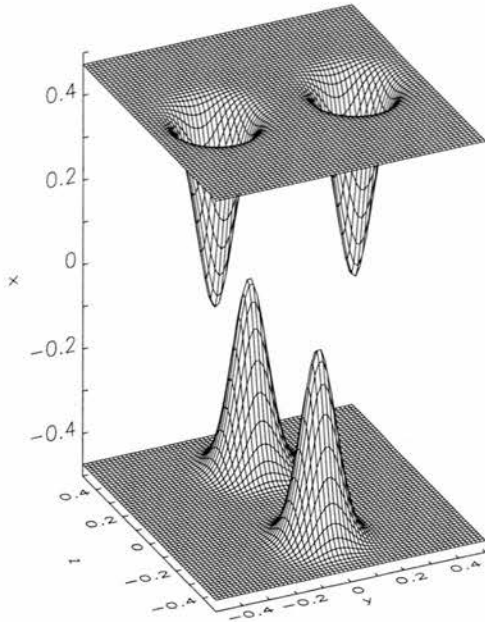


Figure 5.1: The boundary conditions on B_x at the start of the simulation. Two flux patches of opposite polarity are superimposed upon weak background fields of opposite polarity on opposite x -boundaries.

to two opposite boundaries. The x -component of the magnetic field is imposed upon the two x -boundaries, $x = \pm 0.5$, and in each case takes the form of two flux patches and a background field, with opposite polarity on each boundary. The flux patches each have a symmetric Gaussian profile, and are centred on $(x, y, z) = (-0.5, \pm y_0, 0)$ and $(0.5, 0, \pm z_0)$, where the numerical domain runs from -0.5 to 0.5 in each direction (see Figure 5.1). Note that the configurations of the flux patches on each boundary are the same, except that the two are rotated by 90° with respect to one another. The peak strength of the magnetic field within the patches is 0.5 , while the background field is 10 times weaker. The flux from these patches spreads out to fill the domain, and at the central plane of the domain ($x = 0$), the field is approximately uniform, and has a strength of ~ 0.072 . In planes of constant x , the field has a hyperbolic X-type structure.

It is important to note that, in order to achieve this numerical setup, the boundary conditions in the y - and z -directions are periodic. This means that, although the initial magnetic field is relatively simple, once the system is disturbed and stressed secondary effects will develop, such as the build-up of current concentrations, due to the interaction of adjacent systems. In general though, these effects are dominated by those of the stress on the individual system. Driven boundary conditions are applied on the x -boundaries, as described below.

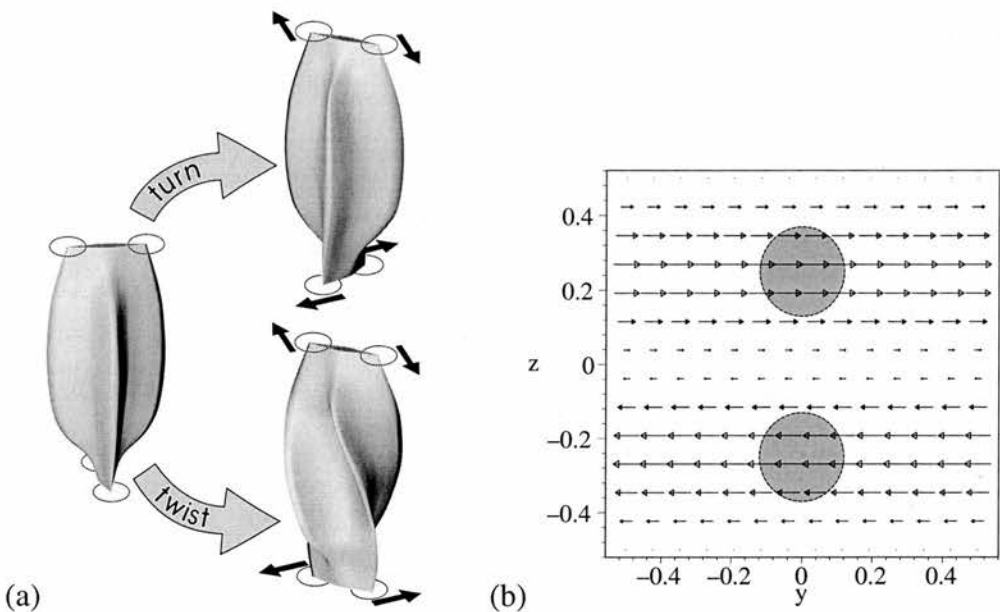


Figure 5.2: (a) The effect of rotating the opposite ends of an HFT in the same sense ('turn') and in the opposite sense ('twist'), after Galsgaard et al. (2003). (b) The imposed plasma velocity on the boundary $x = -0.5$; the discs represent the flux patches.

The driving velocity on the x -boundaries is a shear motion, and is chosen to be in the 'twisting' sense, so as to form a current layer along the central axis of the HFT, as described by Galsgaard et al. (2003). The shear has a sinusoidal dependence, and is again different on the two boundaries by a rotation of 90° . On each boundary, it acts to advect the flux patches in opposite directions perpendicular to the line that initially joins them (see Figure 5.2(b)). Specifically, we impose

$$\mathbf{v}_{yz}(x = -0.5) = (-v_0 \sin 2\pi z, 0), \quad \mathbf{v}_{yz}(x = 0.5) = (0, v_0 \sin 2\pi y), \quad (5.14)$$

where v_0 rises from zero over a time t_0 to a steady value, at which it remains for the rest of the simulation. The gradual rise is included to minimise the effect of Alfvén waves which propagate into the domain when the boundary motion is initiated. These waves cause undesirable effects, such as an oscillation of the field lines, which complicates the evolution of the magnetic flux that we intend to study. They also create weak current concentrations at their fronts. The time, t_0 , over which the driving velocity grows to its maximum value is chosen to be 0.5, which is found to give a reasonable reduction of these undesirable effects, while further increase in t_0 seems to be of little help.

The plasma parameters for the simulation are as follows. The density and thermal energy are both initially uniform, and take values 0.1 and 0.01 in our normalised units respectively. This means that the sound speed ($c_s = \sqrt{\frac{\gamma P}{\rho}}$) is uniform at 0.33, while

the plasma beta ($\beta = \frac{2\mu P}{B^2}$) and Alfvén speed ($v_A = \frac{|B|}{\sqrt{\mu\rho}}$) take values of approximately 2.57 and 0.23, respectively, at the centre of the domain and 0.04 and 1.58, respectively, at the centres of the flux patches. Hence the Alfvén crossing time is around 4 time units. The eventual steady value for the driving velocity (v_0) is 0.02, which is 13% of the local Alfvén speed in the region of background field and 1.3% of the Alfvén speed at the flux patches.

Finally, in order to achieve our goal of investigating the behaviour of magnetic flux being reconnected at an isolated non-ideal region, we impose a resistivity (η). We have made two classes of run with differently prescribed resistivity. In the first (described in Section 5.3), η is imposed to have a spherically-symmetric exponential dependence of the form

$$\eta = \eta_0 e^{-(r/r_0)^2}, \quad (5.15)$$

where η_0 is chosen to be 1×10^{-3} and r_0 is chosen to be 0.06, so that non-ideal processes are localised within a small region centred on the origin. In the second set of runs, η is prescribed to depend on the modulus of the current, so that η is zero everywhere that the current is below a threshold value J_0 , while in regions where $|\mathbf{j}|$ exceeds J_0 , η is given by

$$\eta = \eta_0 \sqrt{\frac{|\mathbf{j}|^2 - J_0^2}{|\mathbf{j}|^2}}, \quad (5.16)$$

where η_0 is now chosen to be 5×10^{-4} , so that η grows quickly where $|\mathbf{j}|$ increases above J_0 . The results of these runs are described in Section 5.4.

5.3 Results of fixed- η runs

We describe first the results of the runs with a fixed region of resistivity in the centre of the domain. The initial set of experiments was done in the cold plasma limit (setting $\frac{\partial \rho}{\partial t} = \frac{\partial e}{\partial t} = 0$), so that only Equations (5.1), (5.2), (5.3) and (5.5) were solved. The results of this experiment are qualitatively very similar to those of the later full MHD runs, and so we present the cold plasma results here first. The few differences between the two sets of runs are described in Section 5.3.5.

Runs were made in the cold plasma limit at three different resolutions, on 64^3 , 128^3 and 256^3 Cartesian grids. It was found that no new qualitative features appear with higher resolution runs, and so, as a compromise between clarity and computational cost, the

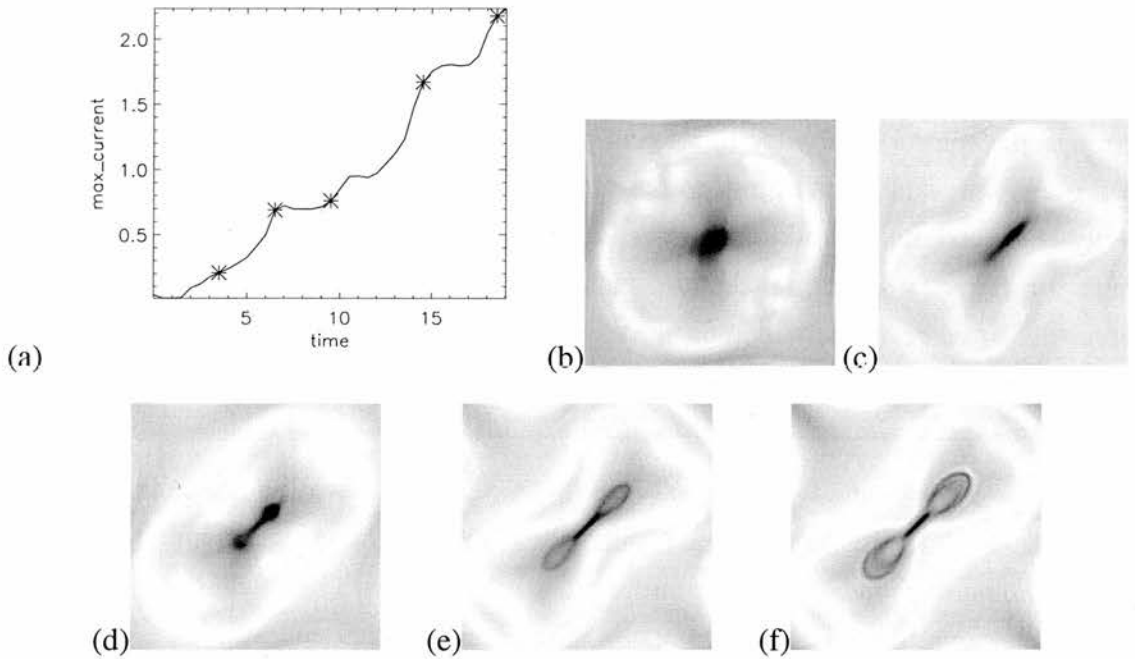


Figure 5.3: (a) Growth of the maximum value of $|j|$ in the $x = 0$ plane, and (b)-(f) shaded scaled images showing $|j|$ at intervals throughout the run (in each image the intensity is scaled to the maximum in that image, where white is zero current density and dark is high). The asterisks in (a) mark the times of the images (b)-(f).

standard run resolution hereafter is 128^3 . Differences between the different resolution cold plasma runs are described as and when they occur in the following sections. Each of the experiments described is run from time $t = 0$ to time $t \approx 19$.

5.3.1 Electric current

At the beginning of the simulation, the magnetic field is potential and the plasma is at rest, and so there are no currents and no reconnection. As the simulation progresses, and the boundary flux concentrations are sheared, the QSLs of the field structure fold up from their initial orthogonal configuration. An associated growth of the current focusses at the centre of the domain due to the geometric structure of the magnetic field. The peak current in the centre of the domain lies in the negative x -direction, anti-parallel to the magnetic field on the x -axis. Note, however, that the maximum current within the domain by the end of the run is actually around the flux sources on the x -boundaries, as there is no resistivity here to allow the current to dissipate.

The growth of $|j|$ in the $x = 0$ plane is shown in Figure 5.3. It grows approximately linearly as time progresses, although there are regular fluctuations away from the lin-

ear growth (Figure 5.3(a)). The cause of these fluctuations is described by Mellor et al. (2004), who perform a similar experiment. The current essentially increases in a step-like fashion due to the Alfvén waves set off by the boundary motion, which periodically pass through the central plane, due to reflections off opposite boundaries. Here the damping process is not as obvious as in the analytical model of Mellor et al. (2004), as the resistivity is only significant in a small portion of the domain. One difference between the runs of different resolution is that the peak current in the central plane is actually higher in runs of lower resolution, by a factor of around 30% for each change in resolution. This is probably because the dissipation is closer to properly resolved in the higher resolution runs since there are more gridpoints within the effective non-ideal region.

Figures 5.3(b-f) show the evolution of the current concentration in the central plane, where the shading intensity is normalised to the maximum value in each individual frame. These maximum values can be seen from the graph in Figure 5.3(a), where the data points corresponding to the times of the images 5.3(b-f) are marked with asterisks. The current concentration gradually collapses towards the $y = z$ line, from an initial approximate circle shape, as the field becomes more twisted. This current concentration remains well resolved throughout the simulation, since the resistivity eventually acts to stop the collapse, by allowing the current to diffuse outwards (from the X-line, where ‘X-line’ shall henceforth be used to refer to the x -axis, along which \mathbf{B}_{yz} has an X-point structure). It is possible to be sure that the current concentration remains well resolved since its width remains approximately constant for runs of different resolution, and is around 16 gridpoints (full-width at half-maximum) in the 256^3 run (see images on CD).

Note also from Figure 5.3 that the profile of $|\mathbf{j}|$ has a ‘bow-tie’ type shape, with loops extending from either end of the elongated concentration later in the simulation. An explanation of the effect is offered in the following section. Since there is a diffusion region in the centre of our domain, and since the current grows strongly here, we expect non-ideal processes to have a significant effect, and reconnection to occur.

5.3.2 Plasma flow

Although a shear plasma flow is imposed upon the x -boundaries of the domain, the flow within the volume is not imposed, and so evolves freely, although it is of course influenced by the boundary motion. Examining once again the $x = 0$ plane, in which the magnetic field has a hyperbolic structure, we find that the plasma flow develops a stagnation-point structure, as shown in Figure 5.4. The background shading in the image shows the mod-

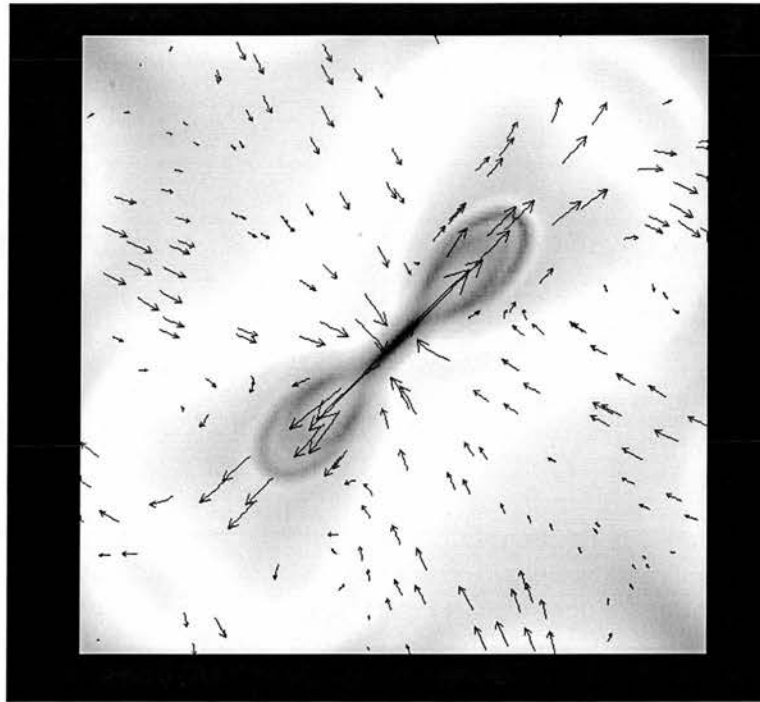


Figure 5.4: The plasma velocity in the $x = 0$ plane at $t = 19$ (the end of the run). The vectors indicate the strength and direction of \mathbf{v}_{yz} , while the background is shaded to show $|\mathbf{j}|$.

ulus of the current in the same plane. There is also of course some plasma flow in the x -direction, along the HFT. However, this flow is likely to be of only secondary importance when it comes to the restructuring of the magnetic flux, since it is in a direction largely parallel to the magnetic field, and in any case is less than half of the strength of the flow in the yz -plane (in both peak and average value). In addition, examination of the structure of v_x with respect to the magnetic field lines shows that in fact the regions of significant v_x are found around field lines which do *not* reconnect.

Closer to the x -boundaries, away from the diffusion region, the flow exhibits a superposition of the stagnation point and shear characteristics in constant- x planes. However, the dominant plasma flow in the vicinity of the diffusion region is the stagnation point flow. The presence of a stagnation flow, co-centred with the X-point of \mathbf{B}_{yz} , coupled with the presence of the non-ideal region, is a strong indication that reconnection is occurring there. Stagnation point flows are characteristic of reconnection solutions (e.g. Craig and Fabling, 1996) and are favourable for reconnection as they are efficient at localising physical quantities into small scales (see references in Priest and Forbes (2000), Biskamp (2000)).

We note that the stagnation flow is particularly strong in the outflow directions, corresponding to the direction along which the current concentration is stretched. In the strong

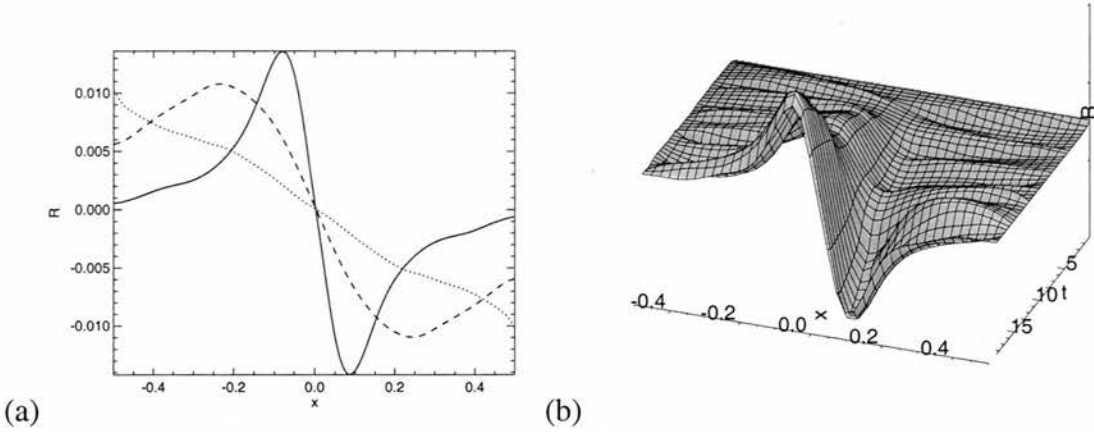


Figure 5.5: (a) Rotation as a function of x , calculated for circular circuits of radius 0.01 (solid line), 0.1 (dashed) and 0.2 (dotted), and normalised by $2\pi R_0$, where R_0 is the circuit radius. (b) Growth of rotation in time for the circuit of radius 0.01.

outflow regions, the plasma velocity reaches over a quarter of the local Alfvén speed, whereas in the inflow regions the ratio is typically less than a tenth. This strong outflow from the reconnection region is driven by the magnetic tension in the newly-reconnected field lines. The outflow ‘jets’ are characteristic of reconnection (see e.g. Priest and Lee, 1990), and they are responsible for the loop-like spreading of the current concentration at its ends. This can be seen by comparison of the flow and current since the ‘wings’ of the current structure mark out the regions of the outflow jets (see Figure 5.4).

One of the major results of Hornig and Priest (2003) was the discovery in their ‘pure reconnection’ solution of rotational flows centred on the X-line, of an opposite sense on either side of the diffusion region. When an ideal stagnation point flow was added to form the ‘composite solution’, it was found to dominate the flow structure and completely mask the rotation if its strength was above a certain value. Although there is no rotational plasma flow obvious in our solution, it is still possible to search for a background rotation. In order to do this we examine

$$R = \frac{1}{2\pi R_0} \oint \mathbf{v} \cdot d\mathbf{l}, \quad (5.17)$$

for closed curves (in this case we choose circles of radius R_0 in planes of constant x for simplicity) centred on the X-line (x -axis). If there is a rotation associated with the flow in a particular region, then this should result in a non-zero value of R . As shown in Figure 5.5(a), there is in fact a rotation present in the flow. The rotation is indeed found to be oppositely directed on either side of the diffusion region (x positive or negative), and has

the correct sense on each side predicted by Hornig and Priest (2003), with respect to the direction of the electric current.

Although we expect the shear flows at the x -boundaries to give a non-zero contribution to R , the rotation actually increases away from the boundaries, implying that there is some other mechanism acting within the volume to incite the rotation. Note also that, after normalising R by $2\pi R_0$, where R_0 is the radius of the path of integration, we get stronger rotation closer to the X-line (in fact, this is not strictly the case, as shown in Section 5.4). By contrast, for circular paths of large radius there is essentially no extra rotation (above the shear boundary contribution) incited within the volume, with R having its maxima at $x = \pm 0.5$. This is consistent with the idea of the rotation falling to zero at the boundary of an envelope of space defined by the bundle of field lines which thread through the diffusion region, as described by Hornig and Priest (2003). Note finally that the rotational flow grows approximately steadily in time (Figure 5.5(b)), as the current grows. Moreover this growth does seem to accelerate quite significantly around $t = 12$, as in the current growth, when the reconnection appears to speed up.

As a test of this analysis, we check the order of magnitude of the background rotation found. As described by Hornig and Priest (2003), the magnitude of this rotation gives a measure of the reconnection rate, which may also be defined as $\int \mathbf{E} \cdot d\mathbf{l}$ along the X-line (Schindler et al., 1988; Hornig, 2001). So evaluating

$$\Omega = \frac{1}{2B_x x_0} \int_{y=z=0} \mathbf{E} \cdot \mathbf{B} dx, \quad (5.18)$$

where B_x is the average magnetic field along the x -axis within the diffusion region, and x_0 is the approximate extent of the non-ideal region in the x -direction, ought to give approximately the same values (to order of magnitude) as those found for the rotation, R . A typical value of $\Phi = \int \mathbf{E} \cdot \mathbf{B} dx$ along the x -axis is around 2.5×10^{-4} (see Figure 5.8(c)), a typical value for B_x is 0.085, and x_0 is approximately 0.1 (at $x = 0.1$, η is $\sim 5\%$ of η_0). Substituting these values into (5.18) gives

$$\Omega \approx 0.015,$$

which is in good agreement with the value of the peak rotation as shown in Figure 5.5(a).

In summary, even before investigating the behaviour of the magnetic field lines, as we will go on to do in the follow section, there is good evidence that reconnection is taking place in the centre of the hyperbolic flux tube. A well localised, well resolved current concentration is present along the HFT axis, in agreement with the ‘pinching’ described

in Titov et al. (2003) and Galsgaard et al. (2003). In addition, a stagnation point flow is present in planes in which \mathbf{B} is hyperbolic, with the flow having very strong outflow regions, which are also highlighted in the current profile by strong wavefronts. Furthermore, in common with the results of Hornig and Priest (2003) (described in Chapter 2) a background rotation is found to be present in the flow, which has opposite sense above and below D , and whose maximum magnitude may be closely predicted by calculating $\int \mathbf{E} \cdot d\mathbf{l}$ along the X-line.

5.3.3 Field line behaviour

We want to investigate the behaviour of magnetic field lines which undergo the reconnection process, and in particular to investigate the assertion of Priest et al. (2003a) that field lines continually and continuously change their connections throughout the non-ideal region due to the non-existence of a unique field line velocity. In order to do this we pick out some particular field lines at the start of the simulation which lie in what will become the inflow region. That is, we choose to follow field lines which intersect the $x = 0$ plane in the vicinity of the line $y = -z$, and which at the start of the simulation are situated suitably far from the diffusion region.

It is important to be sure that we fully describe the evolution of the chosen field lines, and also to be sure that we in fact trace always the same field lines. So that this is the case, we trace field lines from footpoints which are advected in the ideal flow, where the magnetic flux is frozen into the plasma. This is achieved by tracing field lines at each instant in time from their intersections with the x -boundaries, where the value of the resistivity is extremely small. We trace every field line from both boundaries into the centre of the domain. While they remain wholly in the ideal region, the field lines that are traced from each boundary are the same, and can be thought of as unique field lines. However, once non-ideal processes become important, and the field lines that are traced out from corresponding pairs of footpoints are no longer co-spatial, then we can say that the two footpoints have become differently connected, or that the original field line has undergone reconnection. This procedure for tracking the magnetic field lines is the same as that used to model the evolution of flux in the kinematic models in earlier chapters.

The effect of the reconnection process on such a set of field lines is illustrated in Figure 5.6, and the full animation can be found on the CD. The field lines are traced from points at regular intervals around initially circular cross-sections on the boundaries (marked black). While the field lines remain in the ideal region, we see that corresponding

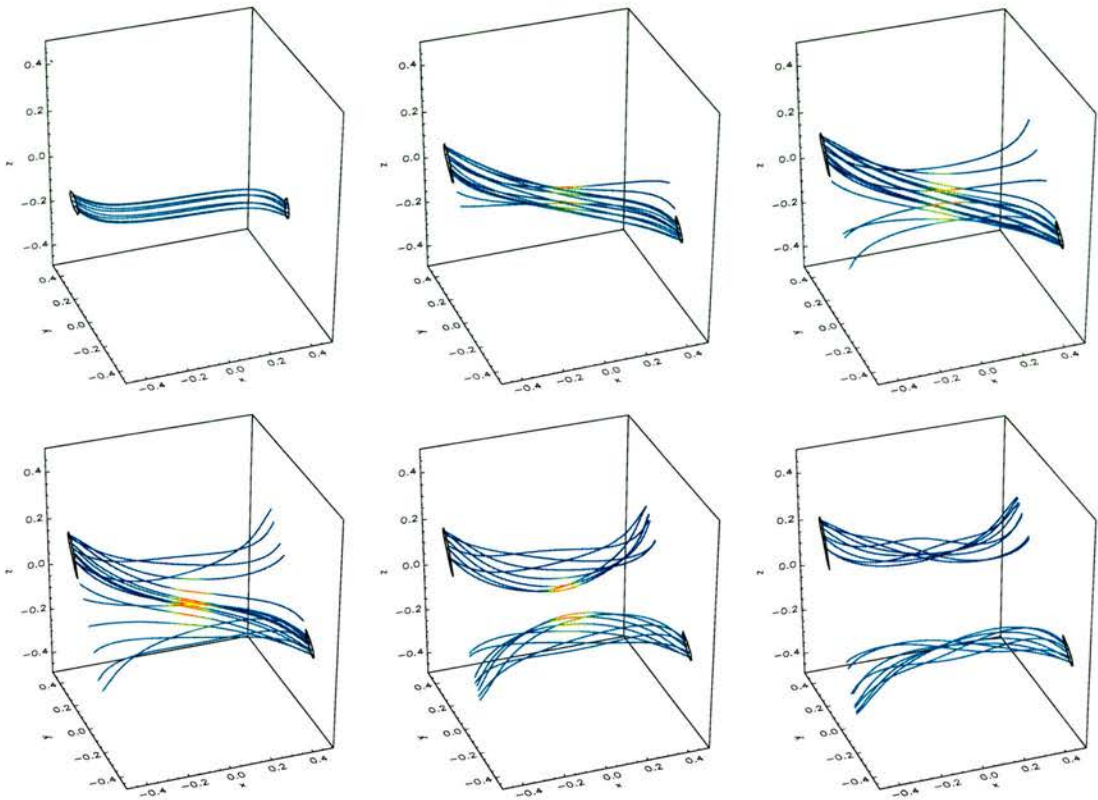


Figure 5.6: Reconnection of field lines, coloured to show the local parallel electric field, with blue being zero and red/yellow being high. The black rings mark the regions from within which field lines are traced on each boundary. (Note the change in orientation of these images from that in Figure 5.1; the vertical axis is now the z - rather than x -direction, so that the imposed flux patches are to left and right of the displayed volume.)

pairs of footpoints remain (approximately) connected. Note that the angle of the field lines with respect to the x -axis increases as they are advected towards the X-line (x -axis). This is due to the increasing shearing on the boundaries.

As the magnetic field lines begin to enter the non-ideal region (see the second frame in Figure 5.6), they start to change their connections, as field lines traced from initially connected points now intersect the opposite boundaries far from the position of their opposite footpoints. (The significance of the colouring of the field lines is described in the next subsection.) As they continue to pass through the non-ideal region (D), it can be seen that the traced field lines flip through the volume, before becoming everywhere anchored in the ideal flow once more after they exit D . This flipping behaviour demonstrates the continual reconnection of field lines throughout the non-ideal region, since a given plasma element (footpoint) in the ideal region on one side of D is connected to a different plasma element in the ideal region on the other side of D for each instant in time throughout the flipping motion. Once the field lines have fully reconnected (i.e. passed wholly out of

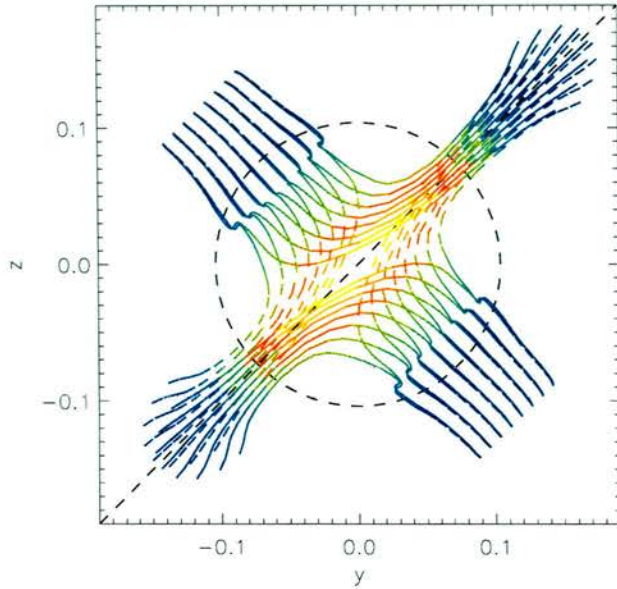


Figure 5.7: Flow lines of \mathbf{w}_{in} (dashed) and \mathbf{w}_{out} (solid) in the $x = 0$ plane, coloured at each point to show the integrated parallel electric field along the corresponding field line at the corresponding time. The dashed circle shows the radius at which $\eta \sim 0.05 \eta_0$.

non-ideal region again), we note that the final sets of field lines appear twisted around themselves, where originally there was no twist. This indicates the presence of self-helicity within the plotted sets of field lines in the outflow region. This may be obtained by conversion of the initial helicity of the angled inflow field lines on either side of D (which are twisted and wrapped around each other due to the boundary driving), and also possibly created by the rotational motion within the reconnection flow, as described by Hornig and Priest (2003).

The continual reconnection of field lines passing through the non-ideal region signifies the different field line velocities for field lines traced from points anchored on either side of the non-ideal region. The nature of the mismatching of these two velocities is shown more clearly by plotting the motions of the field line footpoints in a plane which all field lines intersect. We choose to follow the intersections of sets of field lines with the $x = 0$ plane for symmetry reasons, although the picture is qualitatively the same for other such planes. We denote the velocity of field lines traced from $x = -0.5$ as \mathbf{w}_{in} , since this is the direction from which magnetic flux passes *into* D . Similarly, the velocity of field lines traced from $x = 0.5$ is denoted by \mathbf{w}_{out} .

The flow lines of the two velocities, \mathbf{w}_{in} and \mathbf{w}_{out} , i.e. the paths of the footpoints in

the plane, are shown in Figure 5.7. Two sets of field lines are traced, this time starting from two rows of footpoints in the $x = 0$ plane which are parallel with the long axis (in $x = 0$) of the current concentration ($y = z$), and are symmetric about this line. The flow lines of w_{in} are the dashed lines, while those of w_{out} are solid (again the significance of the colouring is described in the next subsection).

The flow lines remain approximately coincident in the inflow region as the field lines are brought towards the reconnection region. The slight discrepancy is due only to the small non-idealness here (due partly to numerical effects) and to numerical errors in the field line tracing. One further undesirable effect which causes extra splitting of the flow lines is the ‘kinking’ which they undergo about half way in towards the origin. This is due to the Alfvén wave set off by the initial boundary motion, and had been reduced as much as possible, as described previously. Once they reach the central region where reconnection is taking place, the flow lines of w_{in} and w_{out} diverge very strongly, and carry the field lines out into opposite outflow regions (as can be seen by comparison of Figures 5.7 and 5.4). Within this central region the two sets of flow lines regularly cross, showing that individual magnetic field lines traced from either side of D become instantaneously connected (at the point of crossing), before becoming immediately disconnected again. In the outflow regions, the flow lines, once they have met, remain closely matched again, indicating that the field lines are now once again retaining their connections.

In summary, the mismatching of the flow lines of w_{in} and w_{out} illustrates clearly the continual and continuous reconnection of field lines within the non-ideal region, and the non-existence of a unique velocity describing the motion of the field lines. The pattern that we see here is very similar to that of the ‘composite solution’ of Hornig and Priest (2003).

5.3.4 Importance of E_{\parallel}

In order for fully three-dimensional reconnection to occur, it is necessary that the electric field (E) have some component parallel to the magnetic field (B), denoted by E_{\parallel} . The importance of E_{\parallel} for the present reconnection process can be seen in Figure 5.6. Here the field lines are coloured to show the local value of E_{\parallel} . The quantity is highly localised within the reconnection region, and is always present along the corresponding section of field lines which are flipping and changing their connections.

The dependence of the reconnection on E_{\parallel} is shown even more clearly in the flow

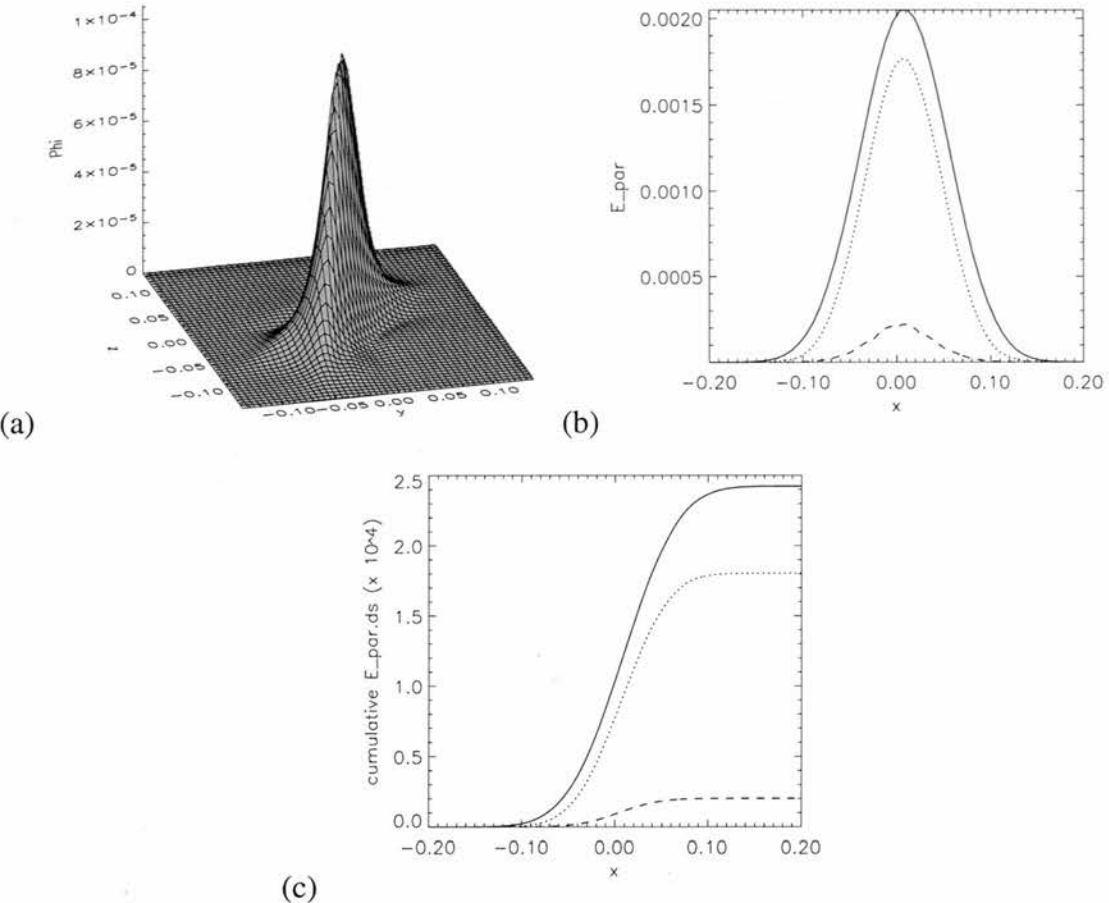


Figure 5.8: (a) Surface plot of Φ in the $x = 0$ plane, at the end of the simulation. (b) Plots of E_{\parallel} along three magnetic field lines at the end of the simulation. The field lines intersect the $x = 0$ plane at $(0, 0)$ (solid line), $(0.2, 0.2)$ in the outflow region (dotted) and $(-0.2, 0.2)$ in the inflow (dashed). (c) Cumulative plot of $\mathbf{E} \cdot d\mathbf{s}$ along the same three field lines (starting from $x = -0.5$).

lines of Figure 5.7. Define

$$\Phi = \int E_{\parallel} ds, \quad (5.19)$$

where s is a parameter along the magnetic field lines, and the integral is calculated between the boundary from which the field line is traced and the $x = 0$ plane. The flow lines in Figure 5.7 are coloured at each point according to the value of Φ along the relevant magnetic field line at the corresponding time. It is clear that Φ is largest in the region where the field lines are becoming reconnected most quickly, and is zero for field lines which are retaining their connections.

The strong localisation of the quantity E_{\parallel} is illustrated by the plots in Figure 5.8. Figure 5.8(a) shows the localisation of Φ in the $x = 0$ plane. Figure 5.8(b) displays

$E_{||}$ plotted as a function of x along a selection of field lines, showing that there is also localisation in the x -direction. It is important to notice the simple monotonic decay of the parallel electric field away from the centre of the reconnection region (the origin). The proof given by Priest et al. (2003a) (and in Appendix D) for the non-existence of a unique field line velocity requires that the quantity Φ (in the stationary case the electric potential) be non-zero when the integral is calculated from one side of the non-ideal region to the other. In theory this might not be the case even if $E_{||} \neq 0$ in D , if the integrand were to have equal positive and negative contributions. The plots in Figure 5.8 clearly show that this is not the case for the present simulation, and that in fact Φ is non-zero for field lines in a localised region in the centre of the domain.

5.3.5 Full MHD runs

In this section we discuss a run of the experiment in which the full set of MHD equations (5.1-5.6) were solved, and focus on the aspects of this run which show differences to the experiments made in the cold plasma limit.

The effect of solving the full set of equations is that the density and pressure are no longer uniform throughout the domain. By the end of the run (once again at $t \approx 19$) the density shows fluctuations of up to 13% about the average (0.1), with the lowest density being within the current concentration in the central plane, while the highest density is in the extreme corners of the volume. The pressure shows fluctuations of up to 15%, with the regions of high pressure being in the corners of the domain and in the current concentration, meaning that the pressure gradient force acts to maintain the width of the current concentration. The result is that the plasma beta (β) in the vicinity of the reconnection (non-ideal) region varies between approximately 1.5 and 3.1, being lowest in the region immediately surrounding the current concentration. Further quantitative information on ρ , P and β is given on the CD.

The current within the HFT develops in much the same way in the full MHD run. The pattern of the current concentration, with the development of the wings, is exactly the same, and the width (in the $y = -z$ direction) to which it collapses is also the same. Moreover, the evolution of $|\mathbf{j}|_{max}$ in the $x=0$ plane is very similar, although the maximum current at the boundaries does grow a little quicker in the full MHD run (see Figure 5.9). This may be due to the fact that here the plasma density and pressure are reduced in the centres of the flux patches, so that the pressure gradient force acts to collapse current concentrations which develop there.

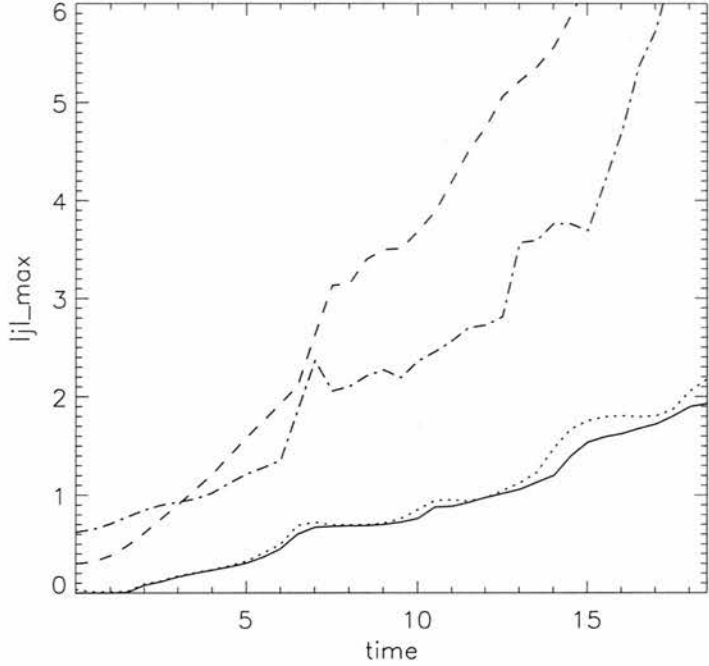


Figure 5.9: Comparison of the growth of the maximum current in the cold plasma and full MHD runs. $|j|_{max}$ is plotted as a function of time in the volume for cold plasma (dot-dashed) and full MHD (dashed) runs, as well as in the $x = 0$ plane for cold plasma (dotted) and full MHD (solid line).

The pattern of the plasma velocity induced within the volume is also very similar. A stagnation flow is again present in the central plane, with $|\mathbf{v}| \sim v_A/10$ in the inflow and $|\mathbf{v}| \sim v_A/4$ in the outflow regions. Furthermore, repeating the search for rotation in the flow described earlier, a very similar pattern emerges, as shown in Figure 5.10.

In relation to the behaviour of the magnetic field lines in the reconnection (shown in Figure 5.6), and the pattern of the velocities of these field lines (Figure 5.7), there is no qualitative difference for the full MHD run, and so the very same overall conclusions may be reached.

Finally, the parallel electric field shows a similar localisation here, and also a similar monotonic decay away from the origin. The integrated parallel electric field along the X-line (or the reconnection rate, as described earlier) grows slightly more slowly, as shown in Figure 5.11, in the run with full MHD, although again the difference is very small.

In summary, the inclusion of the full MHD equations makes very little qualitative difference to our experiment, in particular with respect to the behaviour of the magnetic flux in the process. More plots and information for each of the aspects discussed briefly

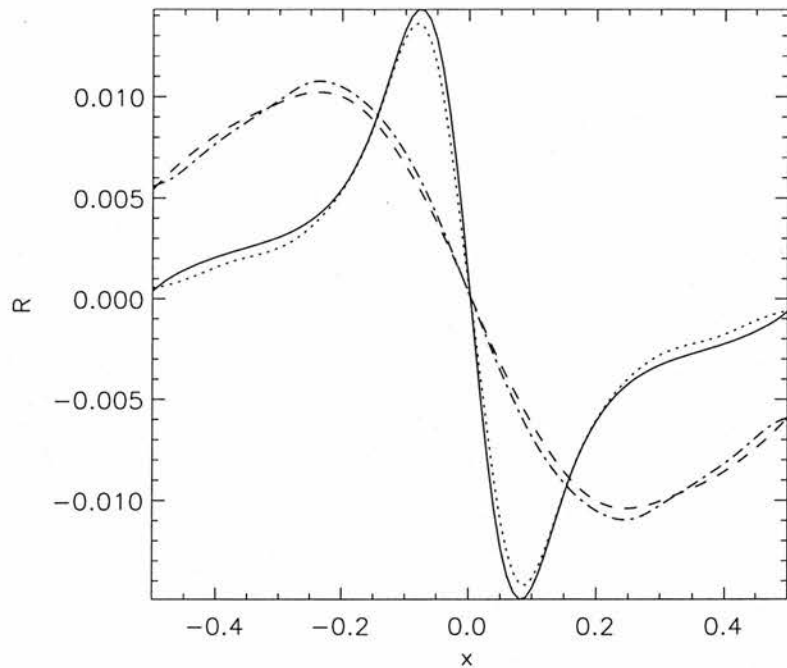


Figure 5.10: Comparison of the rotational flows present at the end of the simulation for cold plasma and full MHD runs. Shown are the rotation for circuits of radius 0.01 (cold plasma dotted, full MHD solid) and radius 0.1 (cold plasma dot-dashed, full MHD dashed).

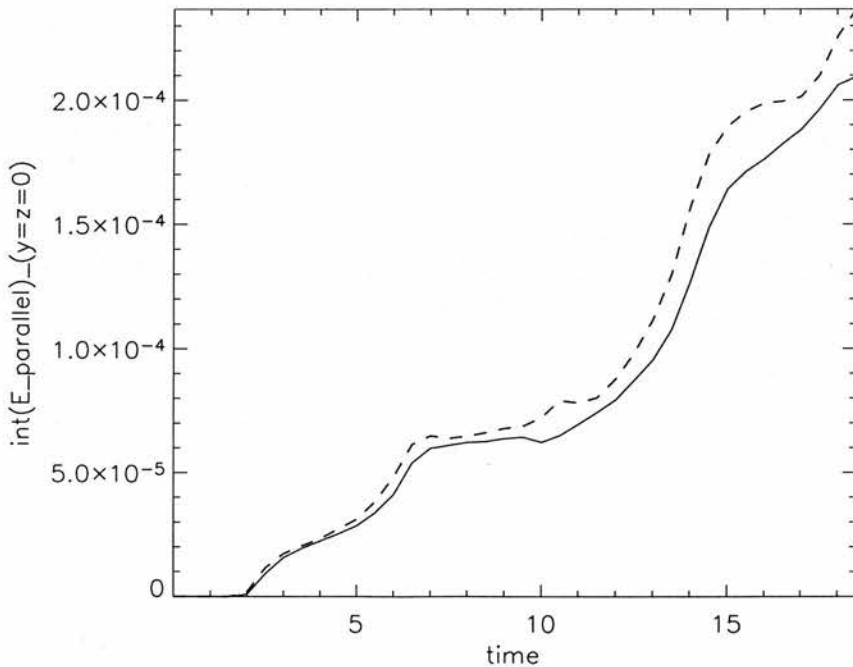


Figure 5.11: Comparison of the evolution of the reconnection rate (integral of $E_{||}$ along the X-line) for the cold plasma run (dashed) and the full MHD run (solid).

above may be found on the CD.

5.4 Results of current-dependent η runs

All of the results described in previous sections are based upon reconnection in the vicinity of an isolated non-ideal region which is arbitrarily imposed, with a fixed shape and size. In many astrophysical plasmas, the classical Spitzer resistivity is far from sufficient to explain fast reconnection processes such as those in solar flares. An ‘anomalous resistivity’ is often invoked, in order to give enhanced dissipation in small regions, where microscale processes may play an important role. The idea is that when field structures collapse down to very small scales, the fluid approximation of MHD breaks down, as the length scales become comparable to the internal plasma length scales. Micro-instabilities may then be excited which act to scatter the electrons and ions which carry the current, and so impede that current (see Priest and Forbes (2000) for a summary). These instabilities may be current-driven, and so an enhanced resistivity within regions of large current is often assumed.

In the experiments described in this section, the resistivity (η , equivalent to the diffusivity since $\mu = 1$) is chosen to depend on the current, and takes the form

$$\eta = \eta_0 \begin{cases} 0 & |\mathbf{j}| < J_0 \\ \sqrt{\frac{|\mathbf{j}|^2 - J_0^2}{|\mathbf{j}|^2}} & |\mathbf{j}| \geq J_0, \end{cases} \quad (5.20)$$

so that η grows quickly when $|\mathbf{j}|$ exceeds J_0 . Three runs of the experiment have been made, with $J_0 = 1.5$, $J_0 = 2.5$ and $J_0 = 3.5$. Other than the form of the resistivity, the experiments described in the following are exactly the same as that described in Section 5.3.5. The only difference is that each run is continued until time $t \approx 27$ (as opposed to $t \approx 19$), for the reasons outlined below.

More images and information for all of the aspects discussed in the following sections are provided on the CD.

5.4.1 Electric current

The magnetic field configuration and driving in these runs is the same as before, so that the initial development of the electric current in the HFT is also the same. However, due to the different form of the resistivity here, the later evolution of the current is different.

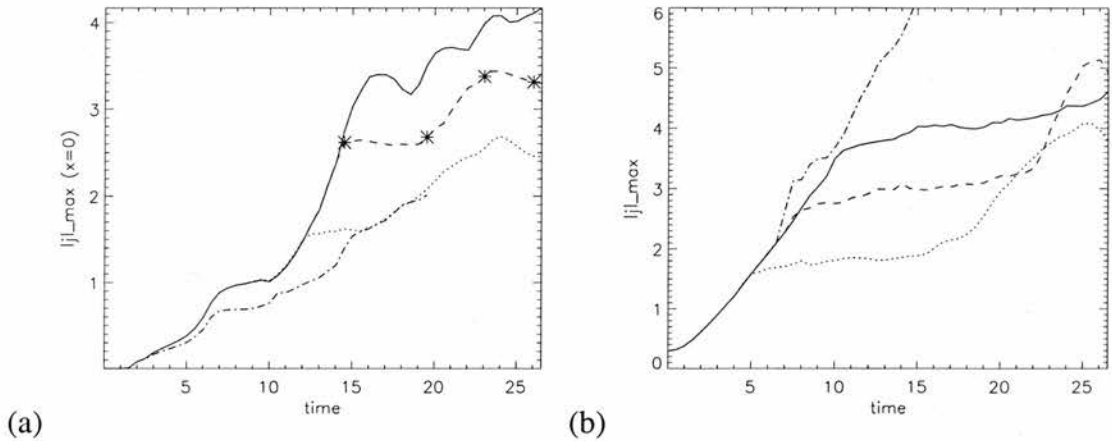


Figure 5.12: Comparison of the evolution of the maximum current between the full MHD fixed- η runs and the different runs with η dependent on j , in (a) the $x = 0$ plane and (b) the whole volume. The growth for $J_0 = 3.5$ is indicated by the solid line, $J_0 = 2.5$ is dashed, $J_0 = 1.5$ is dotted, and the full MHD fixed- η run is shown dot-dashed. The asterisks in (a) show the times of the frames shown in Figure 5.13.

Examining the growth of $|j|$ along the X-line (x -axis) in each experiment shows that the current first reaches the value J_0 in the vicinity of the origin. The resistivity then consequently ‘switches on’ there, and so the current begins to dissipate. As this happens, the continued twisting of the HFT results in $|j|$ increasing to a value of around J_0 along most of the length of the X-line. Only once the system can take up no more stress in this way does the current modulus grow significantly above J_0 , around the centre of the domain (an animation of this process can be seen on the CD). The result is that the region in which non-ideal processes take place is very much less localised in the x -direction (along the HFT axis) than in previous experiments.

The growth of the current modulus in each run is shown in Figure 5.12, where it is illustrated that once $|j|$ reaches J_0 in the central plane, the growth here is indeed halted in each run for a time before picking up again a few time units later. Note that the length of time over which the current growth is slowed in this way is roughly the same, implying that the current maximum takes a similar length of time to extend along the length of the HFT axis (x -axis) in each case. One consequence of the delay before the current exceeds J_0 is that the initiation of the reconnection process is delayed, by a longer time for larger J_0 . This is signified by the late appearance of the current ‘wings’, marking the outflow plasma jets from the reconnection. In fact, the current profile starts to develop these wings at $t \approx 17.5$ for $J_0 = 1.5$, $t \approx 20$ for $J_0 = 2.5$, and $t \approx 25$ for $J_0 = 3.5$.

In each run the width of the current concentration is similar to that observed before, both during the reconnection, and throughout the period beforehand when the current is

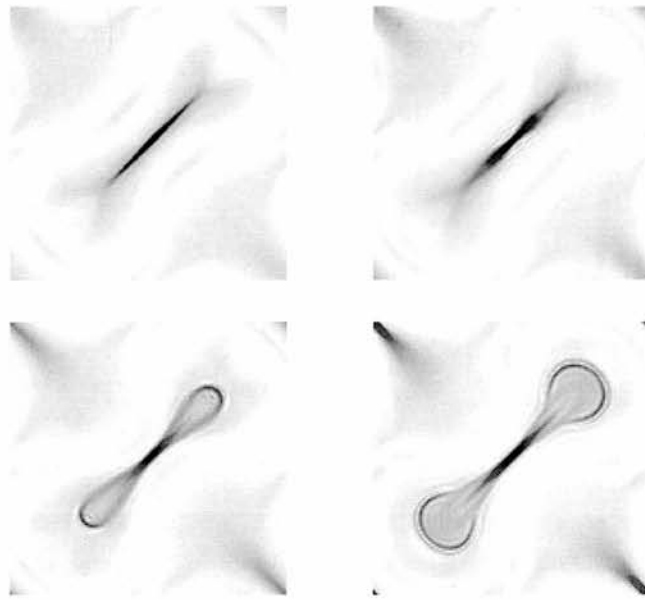


Figure 5.13: Evolution of the current concentration in the $x = 0$ plane for $J_0 = 2.5$. The shading indicates the value of $|\mathbf{j}|$, which is scaled in each frame to the maximum value at that time (shown in Figure 5.12(a)). The first frame shows $t = 15$ (corresponding to a time close to that of Figure 5.3(e)) at which point the reconnection proper is just beginning, while the other frames show $t = 20$ (corresponding approximately to the end of the fixed- η runs, Figure 5.3(f)), $t = 23.5$ and $t = 26.5$ respectively.

growing. The exception to this is the run with lowest J_0 ($J_0 = 1.5$). Here the current profile in the central plane is wider than in the other runs during the build-up phase (from $t = 0$ until $|\mathbf{j}|$ begins to significantly exceed J_0), although the basic pattern is the same.

The extent of the current structure in the $y = z$ direction is significantly different in these runs. The evolution of the current profile once reconnection has been initiated in the run with $J_0 = 2.5$ is shown in Figure 5.13. This time, once the wings develop in the current profile, they quickly expand out towards the edges of the domain. This appears to be due to the fact that the current concentration has a greater length before the reconnection starts, due to the large amount of stressing that precedes reconnection, so that the diffusion acts on a greater length of current concentration, in the $y = z$ direction as well as in the x direction. Also, at the very ends of the current concentration and beyond, the resistivity is exactly zero, so that the wings remain as sharp wavefronts. The fact that they are longer and wider may be also due to the increased outflow speed, as described in the following section.

The effect of the different form of the resistivity on the shape and dimensions of the non-ideal region is severe, and is illustrated in Figure 5.14. Isosurfaces of the non-ideal term $\eta \mathbf{j}$ are shown, which clearly demonstrate that the non-ideal region is squashed and

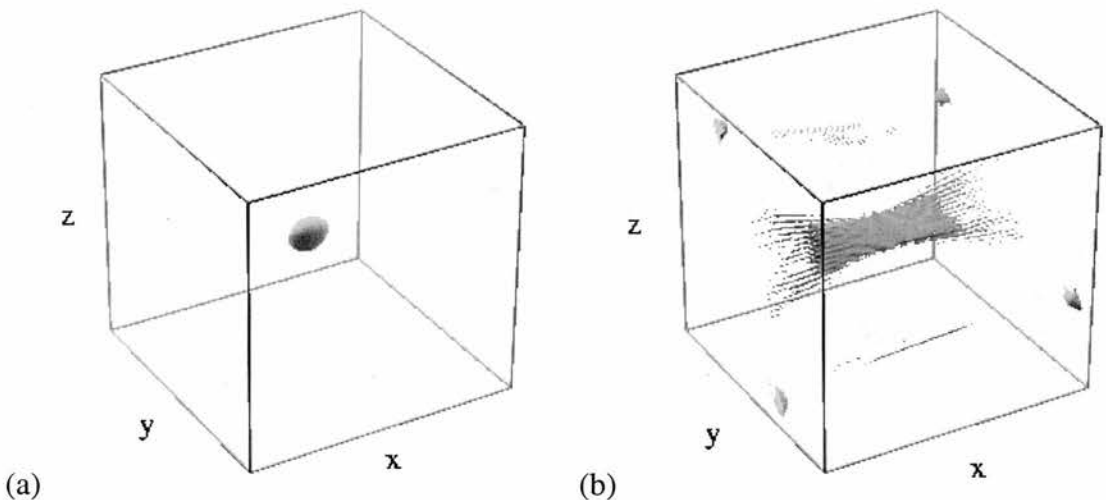


Figure 5.14: Isosurfaces of $\eta|j|$ at 25% of the maximum value for (a) the fixed- η full MHD run and (b) the current-dependent η run with $J_0 = 2.5$, illustrating the different shapes and sizes of the non-ideal regions. The images are plotted at the end of each experiment.

stretched in these runs compared to those with a fixed ‘blob’ of resistivity. This is to be expected from the structure of the current driven by the pinching of the HFT.

5.4.2 Plasma velocity

The plasma velocity, like the current, shows many similarities to previous runs, as well as some important differences. There is once again a stagnation point flow, centred on the origin in the $x = 0$ plane, although for the early portion of the run the inflow and outflow speeds of the stagnation point are very similar (see Figure 5.15(a)). At approximately the same time as the current wings develop, we also see strong outflow jets begin to appear (see Figure 5.15(b)). Furthermore, the current wings again expand with the regions of strong outflow, indicating once again that they mark some type of boundary of the outflow jets. The inflow and outflow velocities once the jets appear are similar fractions of the local Alfvén speeds as before.

The pattern of rotational flow in these runs is also similar to that seen previously. It is difficult to compare the magnitudes of the rotations with the fixed-resistivity runs, since the reconnection proceeds differently, but the rotational pattern does confirm the assertion made above that the reconnection region has a greater extent here, since the rotational flows are present further out from the X-line in these runs (see Figure 5.16).

One fact which should be noted about the outflow jets is that they are stronger for

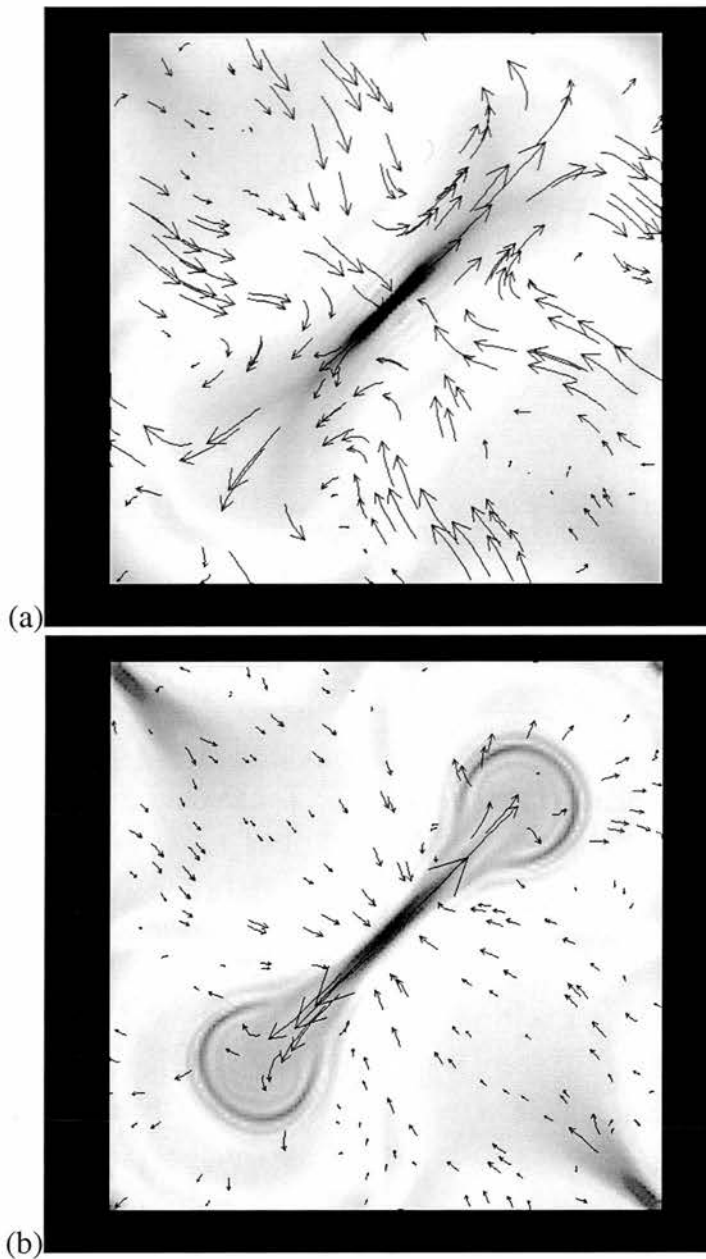


Figure 5.15: Plasma velocity in the $x = 0$ plane for $J_0 = 2.5$, for time (a) $t = 19$ (the end of the fixed- η runs) and (b) $t = 27$. The lengths of the velocity vectors are scaled to the maximum in the individual frame. The background shading shows $|j|$.

runs with higher J_0 , as shown in Figure 5.17. This is probably not too surprising, since a greater stress has to be built up in the system for reconnection to properly get going at higher J_0 , and so a greater release would be expected. It is not clear, however, whether once the reconnection becomes more steady (after this initial release), the outflow jets would settle down to the same speed or whether they would remain ordered, according to their respective values of J_0 , as they are at the end of the runs described. In order to determine this, each experiment would have to be run for significantly longer.

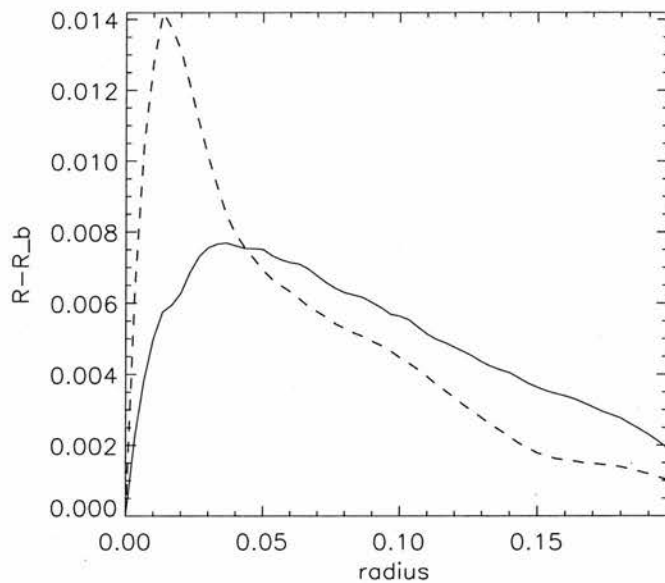


Figure 5.16: Comparison of the radial extent of the rotational flow pattern for $J_0 = 2.5$ (solid line) and the full MHD run with fixed- η (dashed), at the end of each experiment.

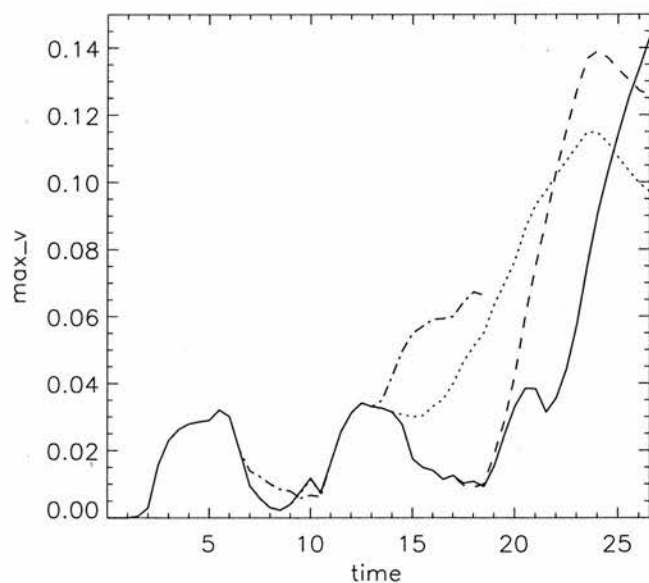


Figure 5.17: Comparison of the evolution in time of the maximum flow speed in the outflow region for runs of different J_0 . $J_0 = 3.5$ is the solid line, $J_0 = 2.5$ is dashed, $J_0 = 1.5$ is dotted, and the dot-dashed line shows the same quantity for the fixed- η run, for reference.

A further point to note is that the main (initial) acceleration of the jets by the tension of the magnetic field lines, given by the slope of the plots shown in Figure 5.17 is of roughly the same magnitude. This acceleration looks to be slightly greater for the $J_0 = 2.5$ and $J_0 = 3.5$ runs than the other two, but it is interesting to note that the acceleration for $J_0 = 1.5$ and fixed- η are very similar.

5.4.3 Behaviour of flux and parallel electric field

The behaviour of the magnetic flux too shares many similarities with the fixed- η runs. Field lines starting at some distance outside the diffusion region in the inflow region (like those shown in the first frame of Figure 5.6) are advected slowly toward the X-line, where the flux slowly ‘piles up’ until the reconnection kicks in (as described in the previous subsections). Once the reconnection begins in earnest, the sets of footpoints are disconnected, and the field lines are ejected out of the reconnection region in opposite directions, as shown in Figure 5.18 (an animation of these reconnecting field lines is contained on the CD). The field lines in the images are coloured, as before, to show the parallel electric field, and it can be seen that, while the localisation in time on the reconnecting field lines is still present, the localisation in the x -direction is not. That is, it is still the case that only field lines which are passing through the small reconnection region show significant values of $E_{||}$, but at this time $E_{||}$ is very much less localised *along* these field lines, i.e. in the x -direction. Examining the profile of $E_{||}$ on the x -axis backs up this point, as shown in Figure 5.19, where it should be noted that, unlike in Figure 5.8(b), the whole of the domain in the x -direction is plotted. (It may also be understood by considering Figure 5.14.)

As before the nature of the field line reconnection can be more clearly visualised by plotting the flow lines (of \mathbf{w}_{in} and \mathbf{w}_{out}) which the field lines follow as they are reconnected. We choose again to plot the flow lines, which are shown in Figure 5.20, in the $x = 0$ plane. Corresponding pairs of flow lines are seen to drift apart as they are brought in towards the current sheet, although the splitting is slow, and due simply to numerical effects. At the point in time when the reconnection kicks in, the flow lines bend very sharply, with field lines anchored in \mathbf{w}_{in} and \mathbf{w}_{out} being accelerated along the current sheet in opposite directions. Note that the reconnection region (i.e. the region within which \mathbf{w}_{in} and \mathbf{w}_{out} show large splitting) is very much thinner, since η is zero, and so the evolution is ideal, everywhere except in the main body of the current concentration itself.

The flow lines in Figure 5.20 are again coloured with the corresponding value of

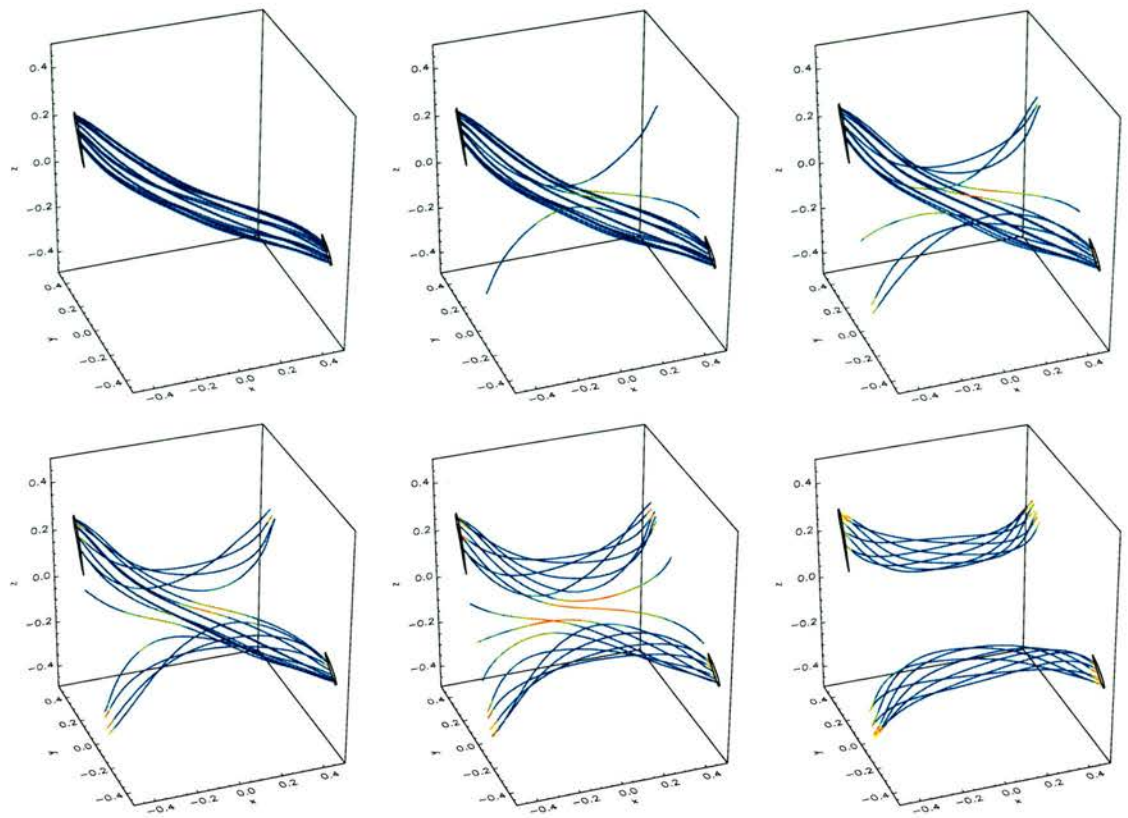


Figure 5.18: Reconnection of field lines in the run with $J_0 = 2.5$. The shading of the field lines shows the local parallel electric field. The black rings indicate the regions on each boundary from which the field lines are traced.

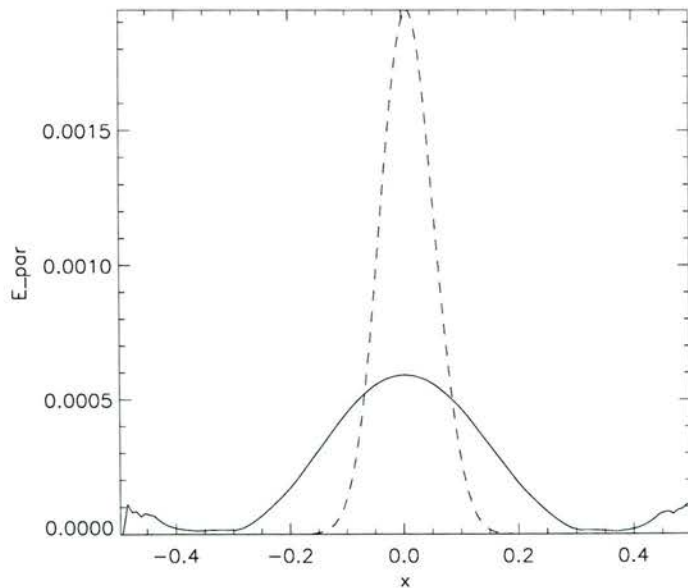


Figure 5.19: The parallel electric field along the X-line, at the end of the run with $J_0 = 2.5$. For reference, the dashed line shows the same thing at the end of the fixed- η run.

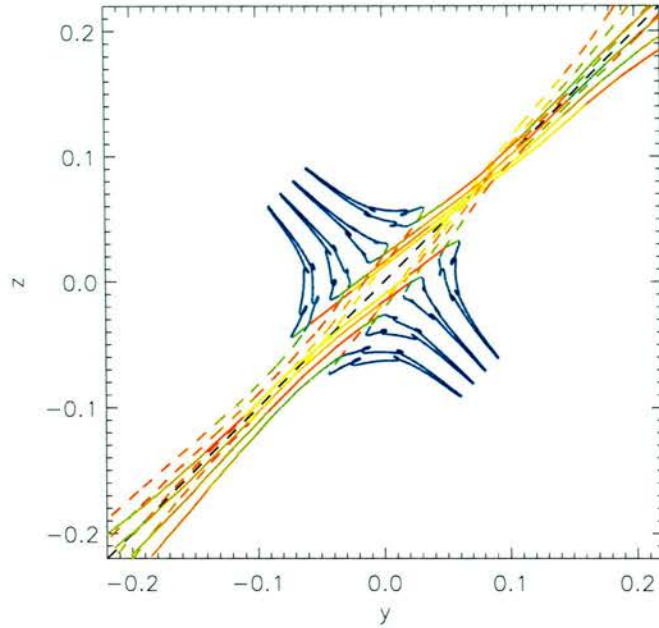


Figure 5.20: Flow lines in the $x = 0$ plane of \mathbf{w}_{in} (dashed) and \mathbf{w}_{out} (solid) for the run with $J_0 = 2.5$. The colouring shows the integrated parallel electric field along the relevant field line at the relevant time.

$\Phi = \int E_{||} ds$. From this image, it is evident that not only is $E_{||}$ localised within a much thinner region in the $y = -z$ direction, but it is also *less* well-localised *along* the current concentration ($y = z$ direction), since η is non-zero for a greater portion of its length in this direction.

Finally, in order to compare the pattern of the changing reconnection rate in each of the runs, the evolution of the value of the integrated parallel electric field along the X-line is shown in Figure 5.21(a). It can be seen that the highest value of the reconnection rate between the runs is achieved in the run with $J_0 = 1.5$. However, if the approximate linear growth in the fixed- η run were maintained, then it would be higher than any of the switch-on η runs by the time they end. Also, because the growth of the reconnection rate with fixed- η is more steady from the beginning, a greater total amount of flux is reconnected in this case, as shown in Figure 5.21(b), where

$$\int_{\tau=0}^{\tau=t} \int_{y=z=0} E_{||} ds d\tau$$

is plotted for each run.

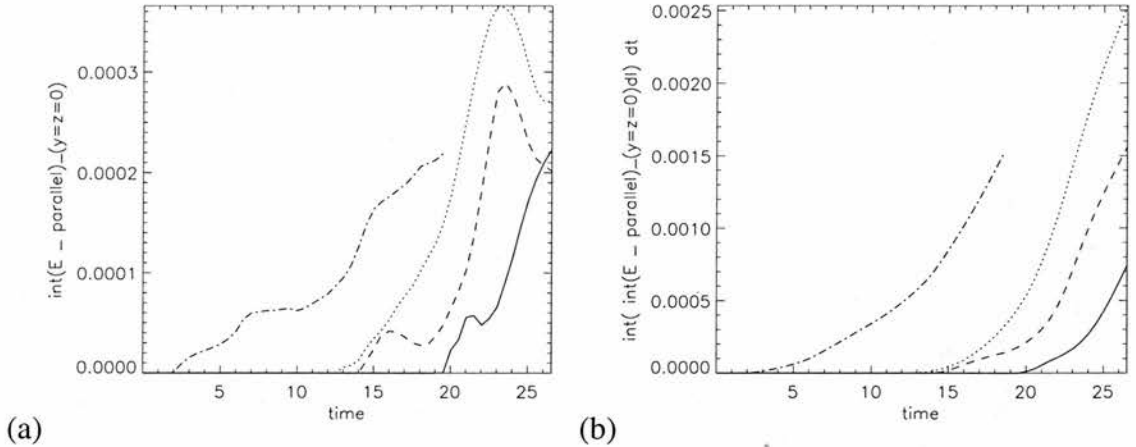


Figure 5.21: (a) Comparison of the evolution of the reconnection rate between the runs, and (b) the time integral of this quantity showing the total reconnected flux. The solid line is for $J_0 = 3.5$, $J_0 = 2.5$ is dashed, $J_0 = 1.5$ dotted and the full MHD fixed- η run is dot-dashed.

5.5 Summary

The main aim of our experiment was to investigate the evolution of magnetic flux in a reconnection process described by the full equations of MHD. The reconnection studied took place at an isolated diffusion region in a magnetic field structure known as a hyperbolic flux tube. This field structure was chosen as it is of essentially the same form as that studied in the kinematic work of Hornig and Priest (2003), in that it has an X-type structure in one plane with a uni-directional field component in the third direction. Such a magnetic field structure has also been shown to be a preferential site for current growth under certain footpoint motions.

Three main sets of experiments were run, in the first of which the cold plasma limit was assumed. In the second and third sets of experiments the full MHD equations were solved, with different forms for the resistivity. In one set the resistivity was fixed and localised around the origin, while in the other an ‘anomalous resistivity’ dependent on the current was prescribed. The latter case nonetheless contained a localised non-ideal region, albeit with a very different localisation. The qualitative behaviour of the system was shown to be largely invariant between the different sets of experiments.

The plasma flow is found to develop a stagnation-point structure in planes perpendicular to the HFT axis, as was seen by Galsgaard et al. (2003). The result is that magnetic flux is swept towards the non-ideal region, where a reconnection process takes place before the flux is ejected in strong outflows. The boundary driving which twists the HFT also induces the growth of a current concentration which collapses towards the HFT axis

(the X-line). The current profile is shown to develop ‘wings’ on the sides of this current concentration corresponding to the reconnection outflow direction.

A number of the basic characteristics of the kinematic model described by Hornig and Priest (2003) (and in Chapter 2) are reproduced in the simulation. In particular, although the plasma flow is dominated by the stagnation flow of the HFT pinching, a rotational background component is found in the flow, which has opposite sense on either side of the diffusion region, in agreement with the kinematic model. This rotation is shown to fall off with distance away from the X-line. The nature of the flux velocities for field lines traced from above and below the diffusion region has also been demonstrated to be similar to that found in the kinematic solution.

Furthermore, the importance for the reconnection process of a component of \mathbf{E} parallel to \mathbf{B} is demonstrated. The quantity E_{\parallel} is shown to have a simple structure in that it decays monotonically away from the centre of the non-ideal region.

The major result of the simulation is the verification of the basic results of the kinematic models. In particular, it was shown that no unique field line velocity exists even in the dynamical regime. The behaviour of field lines anchored in the ideal region on each side of the diffusion region is demonstrated to be different, signifying the continual and continuous reconnection of field lines throughout the non-ideal region. To describe the motion of magnetic flux within the domain, it is thus necessary to use two field line velocities, \mathbf{w}_{in} and \mathbf{w}_{out} .

Chapter 6

A framework for understanding the topology of complex coronal structures

“Far out in the uncharted backwaters of the unfashionable end of the Western Spiral Arm of the Galaxy lies a small unregarded yellow sun.....”

Douglas Adams, The Hitchhiker’s Guide to the Galaxy

6.1 Introduction

In this chapter, we explore a particular aspect of the topology of the magnetic field in the atmosphere of our Sun, and the results of this study can be found in Pontin et al. (2003). The Sun is made up of many different layers, starting at the centre with the *core*, then the *radiative zone*, *convection zone*, *photosphere* (the visible surface), *chromosphere*, and finally the *corona*, extending out into interplanetary space (for an in-depth description of the properties of all of these regions, see, for example, Golub and Pasachoff (2001) or Priest (1982)). The mechanism discussed in this chapter models a process which takes place in the solar corona, a region in which most of the processes are dominated by the magnetic field. This magnetic field emerges into the corona through the photosphere in a multitude of discrete flux patches. The pattern of these flux patches continually changes due to their emergence, cancellation, fragmentation and coalescence. The resulting coronal magnetic field, or in other words the connectivity of field lines between the patches, is thus very complex (see, e.g. Berger, 1986; Longcope, 1996). The connectivity, however, can be described more simply by the so-called *topological skeleton* of the field (Priest et al., 1997). A topological skeleton includes the set of photospheric flux sources that

produce the magnetic field, together with the null points and their spines, fans and separators.

We model the corona using a potential magnetic field, following the *magnetic charge topology* approach of Longcope (1996) (for further discussion of modelling coronal fields, see, e.g. Lothian and Browning (1995), Brown and Priest (2000), Schrijver and Zwaan (2000), Title (2000)). The flux patches in the photosphere are represented by point sources, so that, although magnetic monopoles do not exist in nature, they are used here to model the locations where the magnetic flux breaks through the photosphere into the corona. In fact, the magnetic field due to a flux patch of radius δ , say, is fairly well modelled by a point source at distances greater than δ from the patch (Brown and Priest, 2001). So, it is assumed here that the flux patches modelled are separated by distances which are large compared with their radii. Furthermore, it is assumed that the size of the region that is modelled is much smaller than the solar radius, so that the photosphere may be treated locally as a plane (chosen to be $z = 0$).

The potential field approximation greatly simplifies the modelling of the coronal magnetic field, although care must be taken when it is applied, as it relies upon a number of assumptions. Firstly, it is assumed that the plasma flows are much slower than the Alfvén or sounds speeds ($v \ll v_A, c_s$), so that the field evolves through a series of equilibria. Moreover, typical vertical length scales are assumed to be much less than the pressure scale height, and the plasma beta ($\beta = 2\mu p_0/B_0^2$) is assumed to be much less than 1 (i.e. the pressure gradient force is negligible compared with the Lorentz force) so that the equation of motion (1.2) becomes

$$\mathbf{j} \times \mathbf{B} = 0. \quad (6.1)$$

This results in a *force-free* magnetic field satisfying $\nabla \times \mathbf{B} = \alpha \mathbf{B}$, where α is a constant along individual field lines. The special case where $\alpha = 0$ everywhere gives a potential field (which satisfies $\nabla \times \mathbf{B} = 0$), where it is assumed that the currents are negligible. Note that the fact that the currents are assumed never to grow to non-negligible strengths is equivalent to assuming that reconnection occurs unimpeded as the flux sources are moved.

The strength (q) of our point sources is given by the magnetic flux through any dome within which the source lies, divided by 2π . Then the total magnetic field at a point \mathbf{r} due

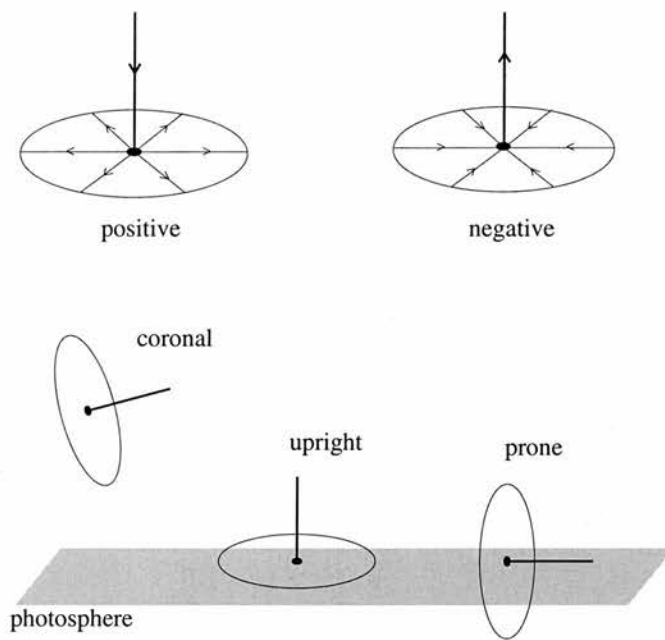


Figure 6.1: The spines (thick lines) and fans (discs) for the different types of null point which may be present in a potential coronal magnetic field.

to sources of strength q_i at position \mathbf{r}_i is given by

$$\mathbf{B}(\mathbf{r}) = \sum_i \frac{q_i (\mathbf{r} - \mathbf{r}_i)}{|\mathbf{r} - \mathbf{r}_i|^3}. \quad (6.2)$$

Other than flux sources, the main components of a topological skeleton are the null points of the field and their associated spine field lines and fan planes. The local structure of 3D null points is described in Section 1.4, and they can be classified in the magnetic charge topology model according to their position and orientation. If all flux sources lie in a plane, a null which is present outwith the source plane (the photosphere) is known as a *coronal* null. Nulls which occur in the photosphere can be split into two types depending on whether their spines locally lie perpendicular or parallel to the photospheric plane (these are the only two possibilities for nulls in the photosphere if the field is potential and all the sources lie in the photosphere). Nulls whose spines are perpendicular to the photosphere are said to be *upright*, whereas those whose spines lie parallel to it are said to be *prone*. We can further classify these nulls by giving them signs. They are termed positive or negative according to whether the field lines in the fan point away from the null or towards it, respectively (Figure 6.1).

In the analysis which follows, we shall first consider the topologies due to three photospheric sources, which have all been classified by Brown and Priest (1999b). The eight distinct topologies are shown in Figure 6.2. The question is; can we understand why these

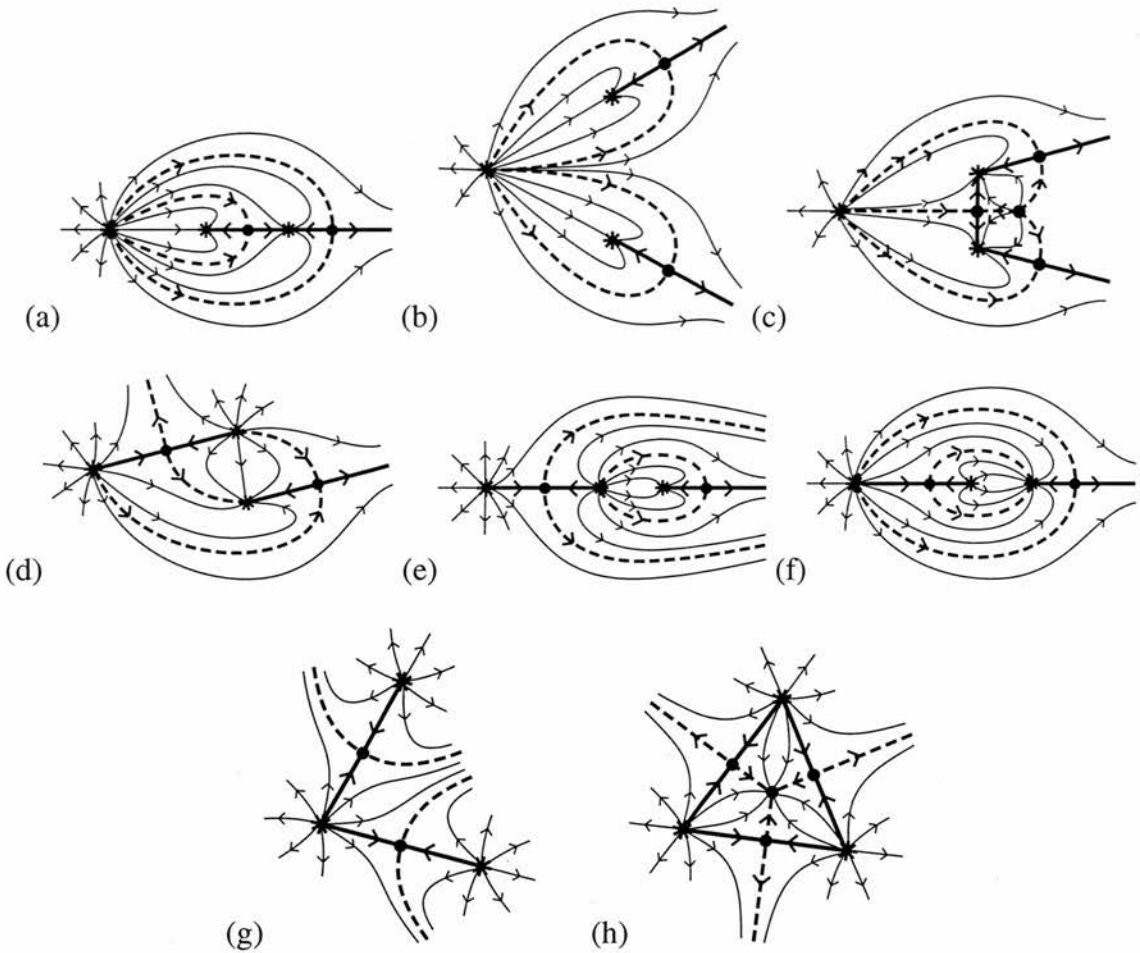


Figure 6.2: The intersections with the photosphere made by the eight topologies due to three photospheric sources (Brown and Priest, 1999b). (a) Enclosed, (b) Separate, (c) Touching (d) Intersecting, (e) Detached, (f) Nested, (g) Divided and (h) Triangular States. Here the sources are shown as stars, the nulls by large dots, the spines by thick curves, the separatrix fans by dashed curves and additional field lines in each domain by thin curves.

topologies occur, in particular why some sets of sources allow local bifurcations from their basic states to more complex ones (touching, triangular) whereas others do not? If we can understand this, then we will be well-equipped to predict allowed topologies for larger numbers of sources, where manually searching the parameter-space is impossibly time-consuming. In this way we can develop a tool for modelling real coronal fields.

We start by giving a brief description of Euler characteristics and an overview of the behaviour of the nulls which take part in a particular type of local bifurcation. We then go on to describe three-source topology, which leads to the question of how we might go about understanding why the observed topological states occur. In Section 6.2.4 we propose an analytical model for the local separator bifurcation. Section 6.3 compares the bifurcation model with the three-source states which are observed to bifurcate in this

way, and puts forward an explanation as to why the other states may not do so. In Section 6.4 the explanation is confirmed to follow through to general three-source configurations. Section 6.5 describes the extension to higher numbers of sources, while Section 6.6 gives a summary.

6.2 Bifurcations

6.2.1 Euler characteristics

The numbers of positive/negative sources and nulls in a potential vector field are related by Euler characteristics (or Poincaré indices) (Seehafer, 1986; Gorbachev, 1988; Dubrovin et al., 1990). In the limit of infinite contour/surface radius in the calculation of these characteristics (which is appropriate for an isolated system), they become, in 2D (Inverarity and Priest, 1999);

$$S_+ + n_{u+} + S_- + n_{u-} = n_{p+} + n_{p-} + \begin{cases} 1 & \sum q \neq 0 \\ 2 & \sum q = 0 \end{cases} \quad (6.3)$$

and in 3D;

$$S_+ - S_- = n_{u+} + n_{p+} + n_{c+} - n_{u-} - n_{p-} - n_{c-} + \begin{cases} sign(\sum q) & \sum q \neq 0 \\ 0 & \sum q = 0 \end{cases} \quad (6.4)$$

where

$$\begin{cases} S_{+-} & \text{is the number of positive/negative sources} \\ n_{p+-} & \text{is the number of positive/negative prone nulls} \\ n_{u+-} & \text{is the number of positive/negative upright nulls} \\ n_{c+-} & \text{is the number of positive/negative coronal nulls} \\ \sum q & \text{is the sum of the source fluxes} \end{cases}$$

The 2D characteristic is calculated for the photosphere, and the 3D characteristic for all space. In this chapter we verify that the constraints inferred from these characteristics are indeed satisfied when new states arise due to the addition of new sources or the bifurcation of nulls. More generally, when dealing with a large number of sources (e.g. Inverarity and Priest, 1999), the characteristics provide a useful check on whether or not

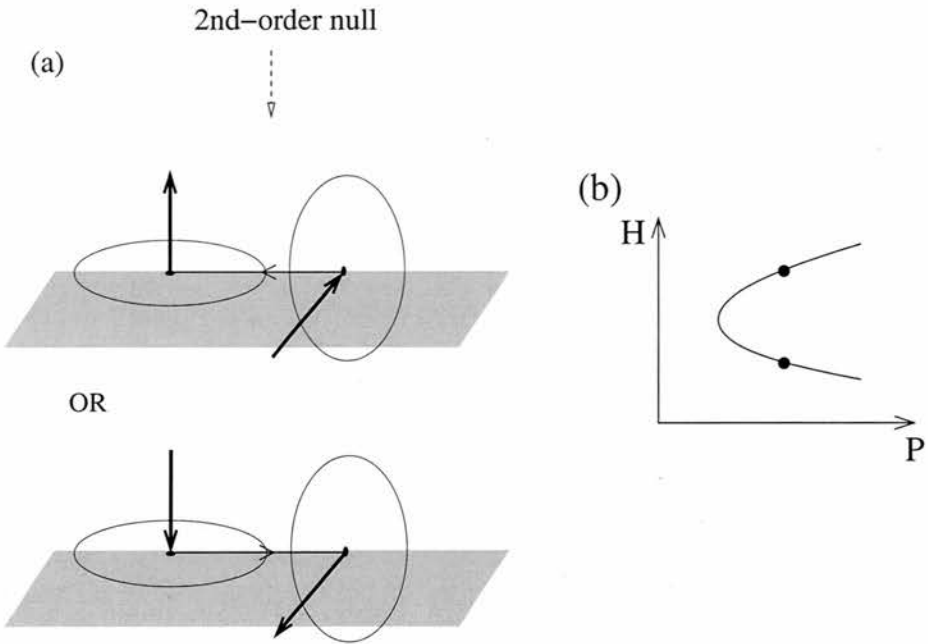


Figure 6.3: (a) The structure of the nulls created in a local separator bifurcation. (b) Schematic representation of a saddle-node bifurcation, where H is the horizontal position of the null and P is a control parameter.

all the null points have been detected.

6.2.2 Local separator bifurcation

A *local bifurcation* is a bifurcation in which nulls are created or destroyed, and thus the local fieldline connectivity is changed (Hornig and Schindler, 1996). A *local separator bifurcation* (Brown and Priest, 1999b) is a saddle-node bifurcation in which either a second-order null is created and splits into two new first-order nulls, or the reverse occurs and two first-order nulls coalesce to form a second-order null which is subsequently annihilated (see Figure 6.3). All of this happens in the photosphere for our set of potential sources placed in the photosphere. Of the two first-order nulls, one is positive and one is negative, while one is upright and one is prone (see Figure 6.3(a)). The skeletal structure of the field around such a pair of null points is shown in Figure 6.4. Note that this bifurcation always ensures that the system continues to satisfy the Euler characteristics, since increasing n_{u+} and n_{p-} , say, by 1 does not produce a net change in the terms in both Equations (6.3) and (6.4).

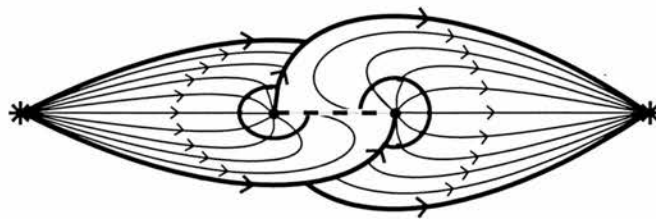


Figure 6.4: The Skeletal field structure near a pair of null points (large dots) created in a local separator bifurcation. The discs represent the fans of the two nulls and the thick lines the spines. The dotted line is a separator and the stars are sources.

6.2.3 Tree diagram for three sources

The analysis which follows involves performing a thought experiment where we start with a known (allowed) configuration of sources and nulls and consider the effect of adding further sources. If the new source is very weak compared to the existing source(s), then close to the new source there appears also a prone positive (or negative) null if the source is positive (or negative, respectively). The source strength can then be increased, and local bifurcations to new states may eventually occur. Note that we will always continue to satisfy the Euler characteristics in this way, since adding a small source increases both S_+ and n_{p+} , say, by 1. Indeed, neither adding a small source nor allowing a local bifurcation has a net effect on Equations (6.3) and (6.4). New states may also be created by global bifurcations, in which there is a global change of connectivity, but the number and nature of the nulls are unchanged. However, global bifurcations are outside the scope of our treatment here. Furthermore, as we consider only sources in the plane and the local separator bifurcation, we will here concentrate on nulls that lie in the photospheric plane.

The different sets of sources and nulls that we arrive at are shown in Figure 6.5. Consider starting with a single positive (say) source on the extreme left of the Figure. Adding another positive source to this simply gives two positive sources and one positive prone null (p_+). This remains the case regardless of the source positions and strengths. Let us call this the *two-source wall* state. Adding a weak negative source (S_-), on the other hand, produces a negative prone null (p_-), so we have one source of each sign with a negative prone null. This state will remain in existence as long as the negative source is weaker than the positive source. In the topological skeleton of this state the weaker source is enclosed within the fan of the null point, so we call it a *dome* state with positive total flux. However, if the negative source becomes stronger, a global bifurcation will occur to a new dome state with a positive prone null instead of a negative one and a negative total flux.

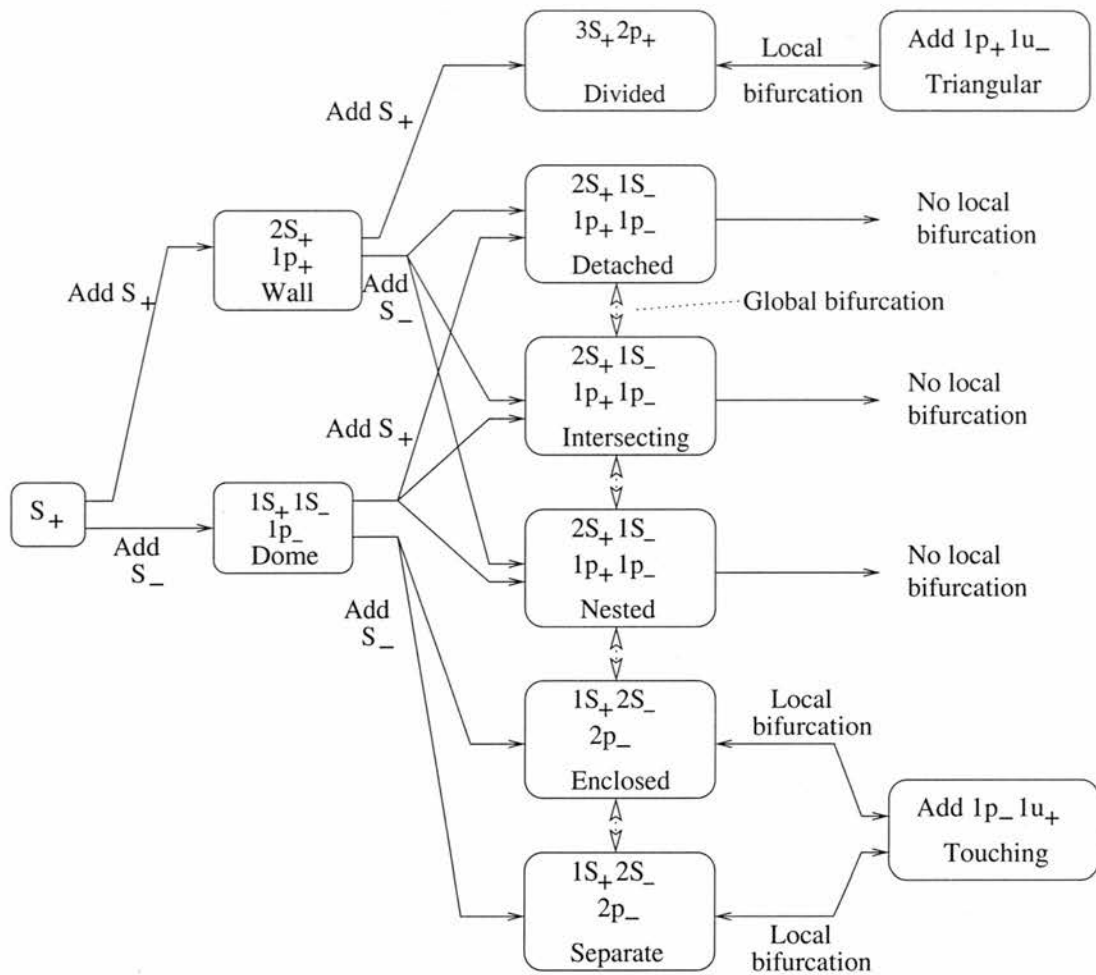


Figure 6.5: Diagram showing how the different three-source topologies with positive total flux can be built up by starting with one positive source (S_+) and adding further weak sources of positive (S_+) or negative (S_-) polarity. The presence of prone positive (p_+) and negative (p_-) nulls is indicated, together with the effects of global and local bifurcations, which sometimes involve the creation of upright nulls (u_+ or u_-).

For clarity and without loss of generality, we consider here only states with positive total flux. All of the topologies described also occur with negative total flux and reversed polarity. These negative flux states can be reached by global bifurcations from the two- or three-source states with positive total flux, by increasing the strengths of their negative sources.

Consider now the effect of adding more weak positive or negative sources to the wall and dome states with positive total flux. From the wall state if we add a further positive source then we will obtain the *three-source divided* state. As the strengths and positions of the three sources are changed, a local separator bifurcation may occur to the *triangular* state, in which, in addition to the original two positive prone nulls there is an extra positive

prone null (p_+) and an upright negative null (u_-). The reasons for the presence of such a bifurcation will be discussed in Section 6.3.

Consider next the addition of a negative source to the wall state with positive total flux. As discussed above, this will give birth to a negative prone null, in addition to the positive one which is already present. We can obtain the same state by instead adding a positive source to the two-source dome state with positive total flux. In this case we gain a positive prone null and again end up with two positive sources, one negative source, and positive total flux, and therefore one positive and one negative prone null. Depending on the source positions and strengths, the topology may be either *detached*, *intersecting* or *nested*, with global bifurcations possible between these topological states. No local bifurcations occur from them, for reasons discussed in Section 6.3. When the total flux is close to zero, the state has the nested topology. From this state, if the strength of the negative source is increased so as to make the total flux negative, a global bifurcation takes place into the enclosed state.

Finally, suppose we add a negative source to the dome state with positive total flux. In doing so, we arrive at either the enclosed state or the separate state, and again global bifurcations between these states may occur. For the right source configuration, we may have a local bifurcation from either of these states into the *touching* state, in which an extra positive prone null and an extra upright negative null are present. A state which has the touching topology may locally bifurcate into either the enclosed or the separate state.

6.2.4 Analytical model for local separator bifurcation

The crucial field structure required for a local separator bifurcation is a second-order null point, as described in Section 6.2.2. Consider the field

$$\mathbf{B} = (x(1+2y), \lambda + x^2 - y^2, -z), \quad (6.5)$$

where λ is a constant, which is the simplest example of a potential field which exhibits second-order behaviour (while still satisfying $\nabla \cdot \mathbf{B} = 0$ and $\nabla \times \mathbf{B} = 0$).

When $\lambda < 0$, no nulls are present. When $\lambda = 0$, a second-order null appears at the origin. When $\lambda > 0$ there are two first-order nulls at $(0, \sqrt{\lambda}, 0)$ and $(0, -\sqrt{\lambda}, 0)$, (see Figure 6.6(a)). As we can see from Equation (6.5), the structure of the field near a second-order null is as follows. In one plane (here the xz -plane) it has the hyperbolic topology of an X-type null point. In a direction perpendicular to this plane the field is everywhere

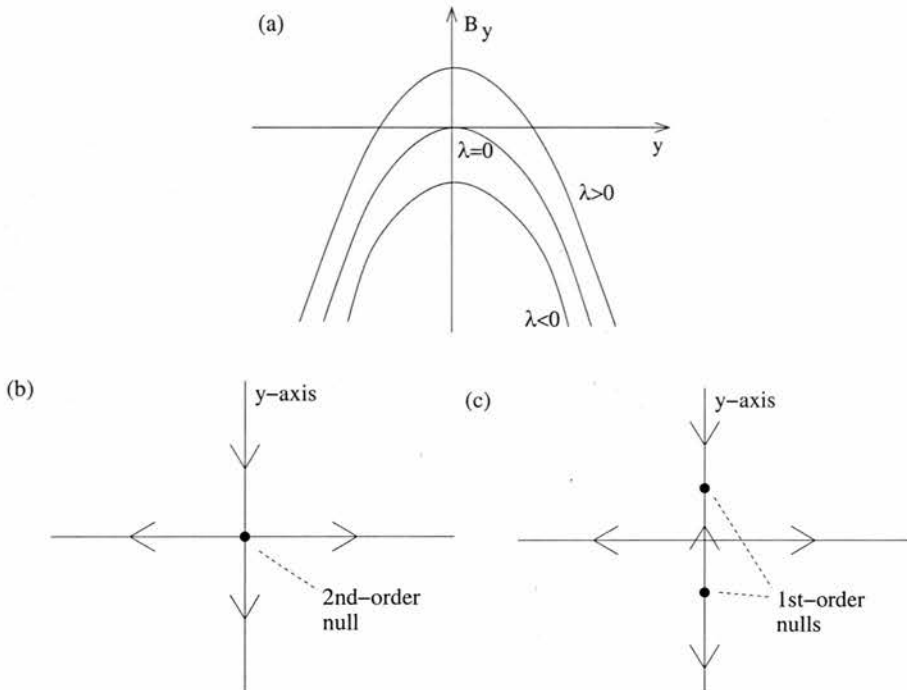


Figure 6.6: (a) The variation with y of the magnetic field component B_y along the y -axis for the field $\mathbf{B} = (x(1 + 2y), \lambda + x^2 - y^2, -z)$ when λ is positive, zero and negative. (b) and (c) show schematic diagrams of the field structure during a local separator bifurcation when (b) a second-order null splits into (c) two first-order nulls or vice versa.

in one direction, but falls in magnitude to zero at one point. If we perturb such a field by adding a small positive λ , the second-order null will split into two first-order nulls. Note that to each side of this newly-created pair of first-order nulls the field (B_y) retains its original direction, while this direction is reversed between them. The skeletal structure of the field between such a pair of null points is shown in Figure 6.4.

In the xz -plane, close to the y -axis, the field behaves like a typical 2D hyperbolic null, so that the field is directed everywhere away from the y -axis in the photosphere (or towards it if $(1 + 2y)$ is replaced by $(-1 + 2y)$ in the x -component of \mathbf{B} in Equation (6.5), whereupon the z -component must become $+z$). From the above analysis, we might expect the local behaviour near a second-order null point during bifurcation to have the structure shown in Figures 6.6(b) and (c).

Note that the magnetic field given by Equation (6.5) also possesses zeros located at $(\sqrt{\frac{1}{4} - \lambda}, -\frac{1}{2}, 0)$ and $(-\sqrt{\frac{1}{4} - \lambda}, -\frac{1}{2}, 0)$, when $\lambda < \frac{1}{4}$. As λ increases towards $\frac{1}{4}$ the nulls approach along the line $y = -\frac{1}{2}$, $z = 0$. They coalesce at $\lambda = \frac{1}{4}$ and no longer exist when $\lambda > \frac{1}{4}$.

6.3 Three symmetric sources

Now let us try to understand why a divided, enclosed or separate state can undergo a local bifurcation through the creation of a second-order null, whereas a detached, intersecting or nested state cannot. Consider two positive (say) sources in a region of the photosphere with no ambient field. Between such sources a null is present, whose spine connects them and whose fan is a separatrix wall. The intersection of the fan with the photosphere is a straight line if the two sources are of equal strength, but in general for unequal sources the wall curves around the weaker source. In the photosphere, the magnetic field lies along the direction of the separatrix curve since it is a field line. Across the curve there is an opposition of the field from the two sources, and in a plane perpendicular to it the field looks like the hyperbolic null structure described in the previous section. Now consider adding a third (photospheric) source to this configuration.

For a configuration of three sources, there are three distinct situations which exhibit quite separate behaviour with respect to the topologies that they form and the bifurcations between these topologies. Firstly, there is the case of three positive (say) sources. Secondly, we may have two positive sources and one negative source with the total flux being negative and, thirdly, the same set of sources but with a total positive flux. (These situations are equivalent to those with reversed polarity, i.e., three negative sources or two negative sources and one positive source, which do not therefore need to be considered separately.)

6.3.1 Three positive sources

Consider a situation where we already have a symmetric two-source wall state with two balanced sources, as described above, and add a third source to this configuration. If the added source (source 1 in Figure 6.7) is of a suitable strength, then the two nulls that are formed join this new source, via their spines, to the other two sources (2 and 3). (If not, the configuration will be an equivalent rotation of this, so long as the sources are placed in a roughly triangular shape.) The separatrix fans of these nulls run up between the two original sources as shown in Figure 6.2(g).

The simplest case is the symmetric case when q_2 (the strength of source 2) is equal to q_3 (the strength of source 3), and source 1 is placed on the perpendicular bisector of the line between sources 2 and 3, which we refer to as the *bifurcation axis* (see Figure 6.7). The field (B_1) due to source 1 is parallel to the bifurcation axis, and, due to the symmetry

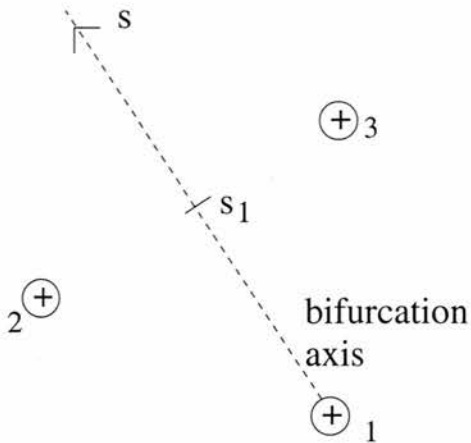


Figure 6.7: The parameterisation used for constructing the bifurcation axis argument. The dashed line is the bifurcation (s -) axis. $s=0$ at source 1 and s_1 is the point midway between sources 2 and 3.

of the situation, the components perpendicular to this axis of the fields of sources 2 and 3 cancel one another. If we take a cross-section through the bifurcation axis, the field in this plane has a hyperbolic null structure. It is likely, therefore, that this axis may be a good candidate to act as the y -axis in the analysis of Section 6.2.4.

Along the bifurcation axis B_1 decays in the usual inverse-square law fashion. Consider the parameterisation shown in Figure 6.7, where s is the distance along the bifurcation axis from source 1 and s_1 marks the point midway between sources 2 and 3. For small s ($s/s_1 \ll 1$), the field (B_s) along the bifurcation axis is in the direction of increasing s , i.e., $B_s > 0$, since B_1 dominates. For $s > s_1$, $B_s > 0$ always, since B_1 , B_2 and B_3 are all in the positive s -direction. However, for $s < s_1$ the field (B_{2+3}) along the bifurcation axis due to sources 2 and 3 combined opposes B_1 . If B_1 and B_{2+3} are equal and opposite at some point, then there will be a null there. The variation of B_{2+3} with s is shown schematically in Figure 6.8.

Three possible composite profiles for B_s are shown in Figure 6.8. As the strength of source 1 is decreased, the B_1 curve drops until it touches (dashed line) and then cuts (solid line) the curve $-B_{2+3}$, thus creating two first-order nulls. The transition between the dot-dashed and solid B_1 curves in Figure 6.8 is analogous to increasing λ from $\lambda_1 < 0$ to $\lambda_2 > 0$. They correspond, respectively, to the divided and triangular topological states shown in Figure 6.2(g) and (h).

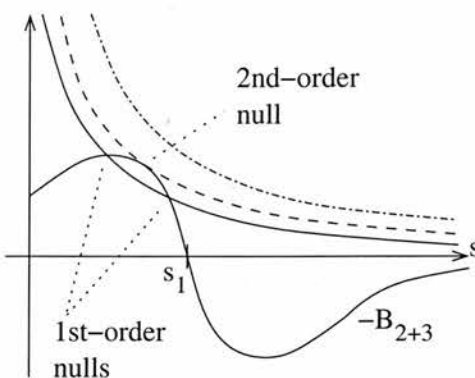


Figure 6.8: The field profiles along the bifurcation axis for three positive sources due to source 1 (B_1) and sources 2 and 3 (B_{2+3}). B_1 profiles are shown dot-dashed before bifurcation, dashed at the point of appearance of the second-order null, and solid after bifurcation.

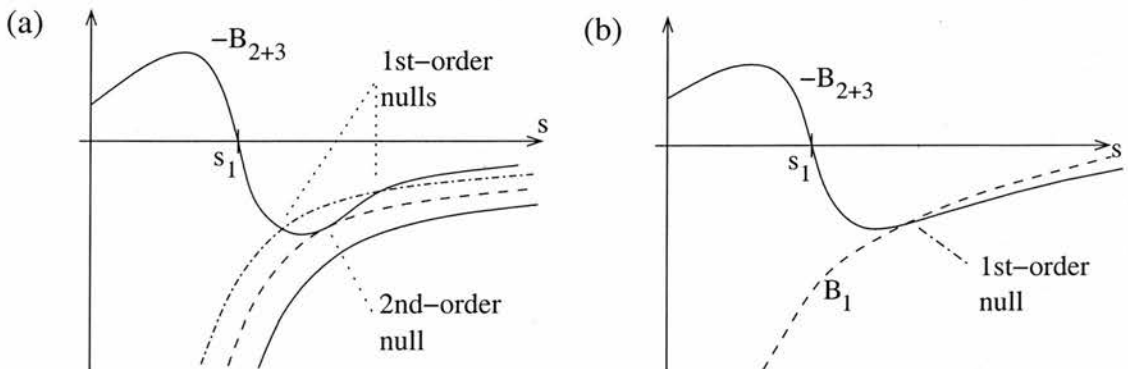


Figure 6.9: (a) Field profiles along the bifurcation axis for one negative and two positive sources with negative total flux. B_1 is shown solid before, dashed during, and dot-dashed after bifurcation. The case when the total flux is positive is shown in (b).

6.3.2 Two positive sources and one negative - Negative total flux

Now consider the case of two positive sources and one negative source, keeping to a symmetric configuration for simplicity. We want to look for the possibility of having a second-order null, so consider the case where the positive sources have equal strength and the negative source lies on their perpendicular bisector. Call this line, once again, the bifurcation axis (we replace the positive source 1 in Figure 6.7 with a negative source). A hyperbolic null structure will be present between the two positive sources, as before, in a plane perpendicular to the bifurcation axis.

In the case of negative total flux, since the negative source (1) is stronger than the sum of the two positive sources, for $s/s_1 \gg 1$, B_s is negative. B_s is also negative for $s < s_1$, since B_1 and B_{2+3} are both negative there. For $s > s_1$, B_1 and B_{2+3} oppose one another and so may cancel. $B_{2+3}(s)$ will again have the type of profile shown in Figure 6.8.

Can we obtain a second-order null on the bifurcation axis in this case? Consider Figure 6.9(a). From this graph we can see that it is indeed possible. Note that for the dashed and dot-dashed B_1 curves, when the curve for $-B_{2+3}$ moves down and touches the curve for B_1 , it climbs up above it again because B_1 dominates B_{2+3} at large distances. So, if the positive sources can be moved in such a way that at some point, or in some region, $|B_{2+3}| > |B_1|$ then a local bifurcation will occur. From Figure 6.9(a), we expect the second-order null to appear at some point $s' > s_1$. Note that, as in the case of three positive sources, the second-order null is created at the point where a separatrix line splits, or equivalently, where two separatrices initially become coincident (see Figure 6.2(c)). Note also from Figure 6.2 that the second-order null appears at $s' > s_1$, as predicted in the bifurcation axis analysis. Once again, the curves in Figure 6.9(a) can be considered as analogous to $\lambda < 0$, $\lambda = 0$ and $\lambda > 0$. In a general non-symmetric configuration (Section 6.4), the case of negative total flux corresponds to the enclosed and separate states, with the touching state being the bifurcated state (see Figure 6.2(a), (b) and (c)). In the non-generic symmetric configuration described above we have the separate and touching states, and a special form of the enclosed state, shown in Figures 12 and 13 in Priest et al. (1997).

6.3.3 Two positive sources and one negative - Positive total flux

In the case of positive total flux, B_s is positive for $s/s_1 \gg 1$, since the negative source is weaker than the sum of the two positive sources. For $s/s_1 \ll 1$, however, $B_s < 0$. So there must always be a first-order null on the bifurcation axis where B_s changes direction. For $s < s_1$, B_1 and B_{2+3} are both negative, so the null must be at some distance $s' > s_1$. In this case it is not possible to create a second-order null (a null on both sides of which the field is in the same direction) as shown in Figure 6.9(b). This is because B_1 decays more quickly than B_{2+3} at large distances so that, once $|B_1|$ drops to $|B_{2+3}|$ (with increasing s), it will fall further and further below it. This explains why there are no local bifurcations in the case of two positive sources and one negative source with positive total flux. This case corresponds to the topologies shown in Figure 6.2(d), (e) and (f), which show the intersecting, detached and nested states.

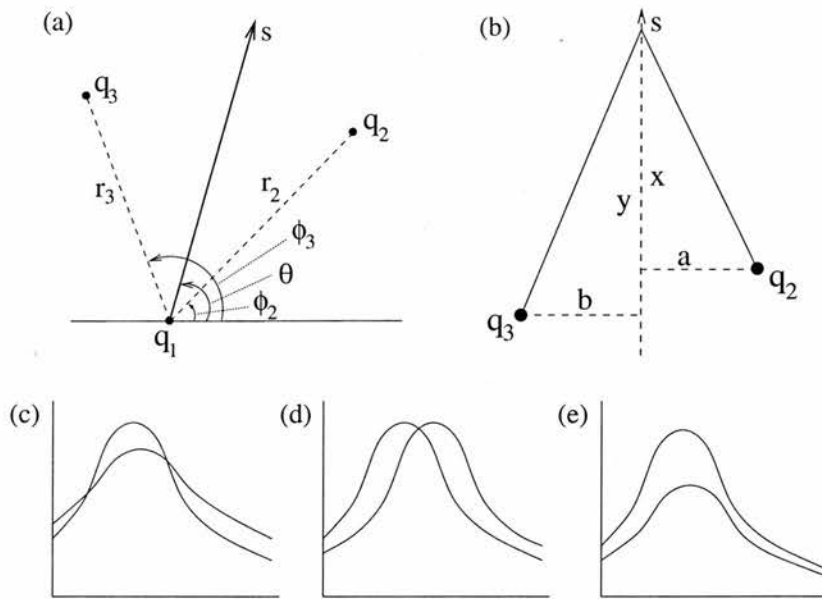


Figure 6.10: (a) The general parameterisation for a three-source non-symmetric state and (b) the parameterisation used to consider the field at large distances. (c), (d) and (e) show schematic field profiles for B_2 and $-B_3$ for the cases when B_\perp has (c) two zeros, (d) one zero and (e) no zeros.

6.4 Three-source non-symmetric states

We now extend the symmetric case described in the previous section to consider a general non-symmetric configuration, where source 1 does not lie on the perpendicular bisector of 2-3 and $q_2 \neq q_3$. We parametrise this non-symmetric problem as follows, by working in plane polar coordinates with respect to source 1 situated at the origin. Sources 2 and 3 are placed at (r_2, ϕ_2) and (r_3, ϕ_3) , respectively, and are taken to be of the same sign. Can we then reconstruct the bifurcation axis argument of the previous section along an s -axis which passes through the origin at an angle θ along which s increases linearly, with θ taking values between ϕ_2 and ϕ_3 (see Figure 6.10(a))? We search for points (s, θ) at which there is a second-order zero in the field parallel to the s -axis ($B_{||}$), coincident with a first-order zero in the perpendicular field (B_\perp). If we can find such a second-order null, then we can conclude that, for the right perturbation to the source configuration, a local separator bifurcation will indeed occur.

6.4.1 Zeros in the perpendicular field

The main complication that arises with non-symmetric source configurations is that, due to the loss of symmetry, we no longer simply have a straight line along which the perpendicular field is zero. Since we are again considering an s -axis which runs through source

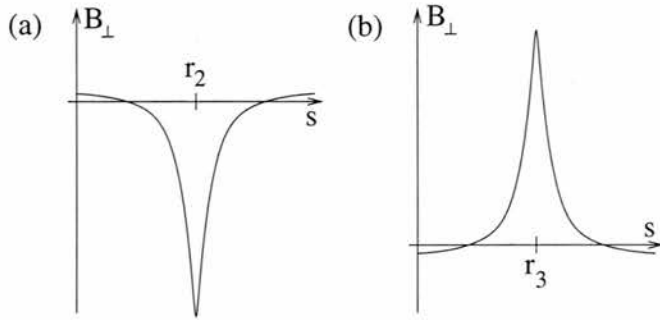


Figure 6.11: Schematic field profiles for B_\perp when (a) $\theta \gtrsim \phi_2$ and (b) $\theta \lesssim \phi_3$.

1, the perpendicular field (i.e., the field B_\perp perpendicular to the s -axis) depends only on sources 2 and 3. It is given by

$$B_\perp = \frac{q_3 A}{((s - G)^2 + A^2)^{3/2}} - \frac{q_2 B}{((s - H)^2 + B^2)^{3/2}} \quad (6.6)$$

where

$$\begin{aligned} A &= r_3 \sin(\phi_3 - \theta), & B &= r_2 \sin(\theta - \phi_2), \\ G &= r_3 \cos(\phi_3 - \theta), & H &= r_2 \cos(\theta - \phi_2), \end{aligned}$$

and the negative θ direction is taken as the positive B_\perp direction. Hence $B_\perp = 0$ is given by

$$(1 - D)s^2 - 2(H - DG)s + (r_2^2 - Dr_3^2) = 0, \quad (6.7)$$

where

$$D = \left(\frac{q_2 r_2 \sin(\theta - \phi_2)}{q_3 r_3 \sin(\phi_3 - \theta)} \right)^{2/3}.$$

This is a quadratic in s , and hence, for a given value of θ , we may have two zeros, one zero, or no zeros, in the region of interest, $s > 0$, as shown in Figures 6.10 (c), (d), and (e), respectively. The number of zeros present depends on the sign of the determinant of (6.7), which is given by

$$4 \left((H - DG)^2 - (1 - D)(r_2^2 - Dr_3^2) \right). \quad (6.8)$$

Consider now a fixed source configuration. What happens to the zeros in B_\perp as we vary θ from ϕ_2 to ϕ_3 (i.e., swing the bifurcation axis round from source 2 to source 3)?

If the bifurcation axis passes close to source 2, then B_2 must dominate B_\perp for $s \approx r_2$, and similarly for source 3. What about the perpendicular field at infinity? Consider the parametrisation in Figure 6.10(b). Then,

$$\begin{aligned} B_\perp &= \frac{q_3 b}{(y^2 + b^2)^{3/2}} - \frac{q_2 a}{(x^2 + a^2)^{3/2}} \\ &\approx \frac{q_3 b - q_2 a}{s^3} \quad \text{as } s \rightarrow \infty. \end{aligned}$$

So the sign of B_\perp at infinity is given by the sign of $(q_3 b - q_2 a)$. Hence, if the bifurcation axis passes close to source 2, a is very small and source 3 dominates. Similarly, source 2 dominates at infinity if $\theta \approx \phi_3$. So for $\theta \approx \phi_2$ or ϕ_3 we have two zeros in B_\perp , close to r_2 or r_3 , respectively, as shown in Figure 6.11. As θ is varied from ϕ_2 to ϕ_3 , the field evolves between these two shapes, and may have one or no zeros for different values of θ .

We know the behaviour of the zeros in B_\perp when $\theta \approx \phi_2$ or ϕ_3 , but what is the shape of the curve $B_\perp = 0$ in the whole s - θ plane? Some examples of the different possible topologies for this curve are shown in Figure 6.12.

Figure 6.12(a) shows the symmetric case from Section 3.2. Figure 6.12(b) is an example of the case where the determinant (6.8) is always positive, whereas in Figure 6.12(c) the determinant (6.8) is negative for intermediate values of θ , which implies there are no solutions to $B_\perp = 0$. The evolution between these topologies can be seen in Figure 6.13 where the single parameter q_3 is varied. The same effect can be achieved by varying the angle $(\phi_2 - \phi_3)$ or one of the lengths r_2 or r_3 .

6.4.2 Zeros in the parallel field

For a null point to be present in the magnetic field we require the zeros in the perpendicular field to coincide with zeros in the parallel field. We therefore now consider the field parallel to the bifurcation axis (B_{\parallel}), and try to apply the same argument as in the symmetric case.

The shape of the parallel field due to sources 2 and 3 ($B_{2+3\parallel}$) is observed to be the same as before (see Figure 6.14(a)). Hence, by the same argument as in the symmetric case, we can create a second-order zero in the parallel field by choosing q_1 so that the B_1 curve just touches the $-B_{2+3}$ curve. We find that the flux considerations are the same here as well; if source 1 is of opposite sign to sources 2 and 3 then we require $|q_1| > |q_2 + q_3|$

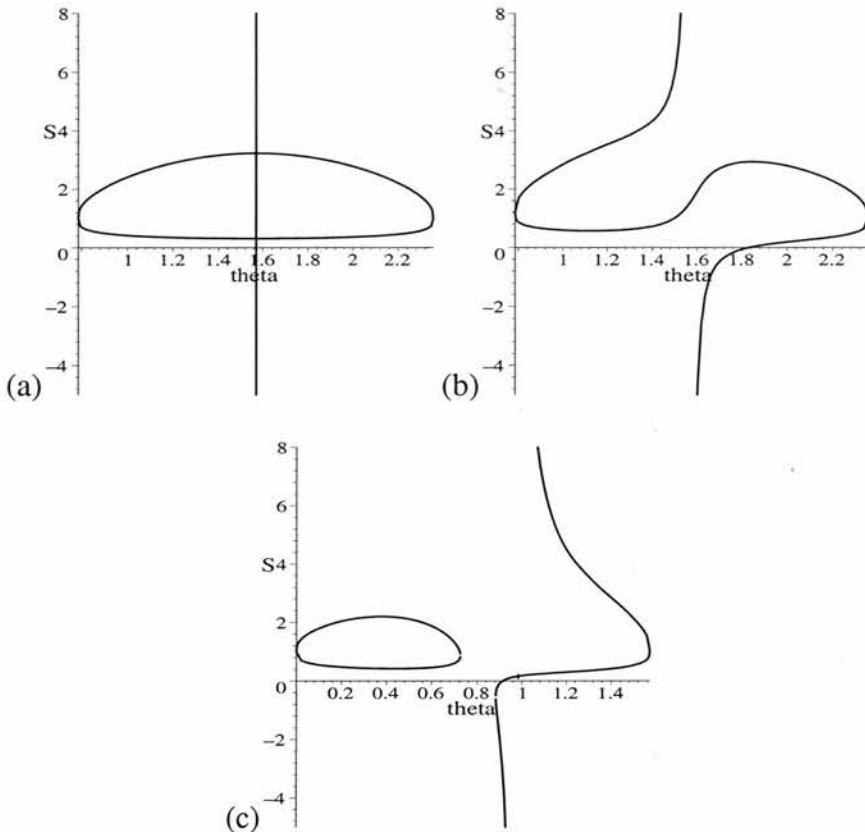


Figure 6.12: The curve $B_{\perp} = 0$ in the $s - \theta$ plane, for (a) the symmetric case; $r_2 = r_3 = 1$, $q_2 = q_3 = 1$, $\phi_2 = \pi/4$, $\phi_3 = 3\pi/4$, (b) $r_2 = 1.2$, $r_3 = 1$, $q_2 = 1$, $q_3 = 1.2$, $\phi_2 = \pi/4$, $\phi_3 = 3\pi/4$, and (c) $r_2 = 1.4$, $r_3 = 1$, $q_2 = 1$, $q_3 = 2$, $\phi_2 = \pi/4$, $\phi_3 = 3\pi/4$.

to obtain a second-order null. Figure 6.14(c) shows where $B_{\parallel} = 0$ in the $s - q_1$ plane, for a typical source configuration and typical value of θ . Note that when source 1 has opposite sign to sources 2 and 3 and $|q_1| < |q_2 + q_3|$, there is only one zero, and so there is a single first-order null in the parallel field.

We now want to plot the curve $B_{\parallel} = 0$ in the $s - \theta$ plane and look for its intersections with the $B_{\perp} = 0$ curve (Figure 6.12). Consider first extreme values of θ . For θ close to ϕ_2 , B_{\parallel} due to source 2 grows very large in magnitude as s approaches r_2 , at which point it drops to zero, and then becomes very large in the opposite direction when s is just greater than r_2 (see Figure 6.14(b)). We can see from Figure 6.14(b) that in this situation we have one zero of B_{\parallel} at $s \approx r_2$ and another at $s \ll r_2$. As θ increases, the $B_{2+3\parallel} = 0$ curve flattens out, and the zeros move closer together. The same argument can be followed for $\theta \approx \phi_3$. Depending on the source strengths, and of course positions, the $B_{\parallel} = 0$ curves in the $s - \theta$ plane should have one of the topologies shown schematically in Figure 6.15. Due to the shapes of these curves close to ϕ_2 and ϕ_3 , we can see that they must intersect the relevant $B_{\perp} = 0$ curve, to give the two standard first-order nulls we expect

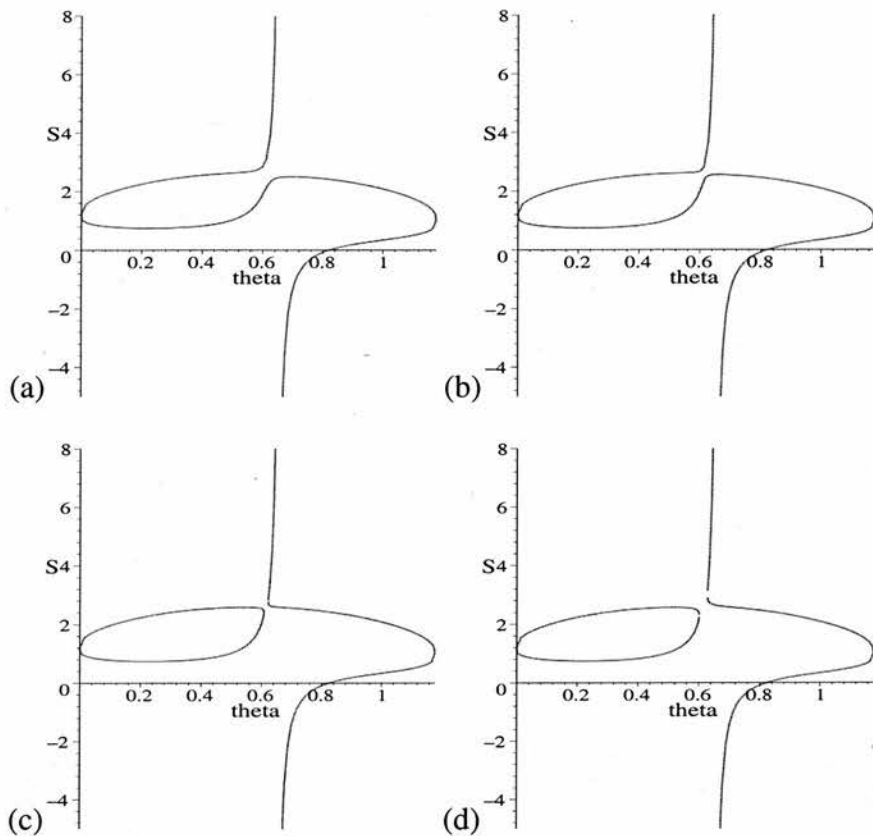


Figure 6.13: The curve $B_{\perp} = 0$ in the $s - \theta$ plane, for $r_2 = 1.2$, $r_3 = 1$, $q_2 = 1$, $\phi_2 = 0$, $\phi_3 = 3\pi/8$ and (a) $q_3 = 1.450$, (b) $q_3 = 1.460$, (c) $q_3 = 1.465$, and (d) $q_3 = 1.470$.

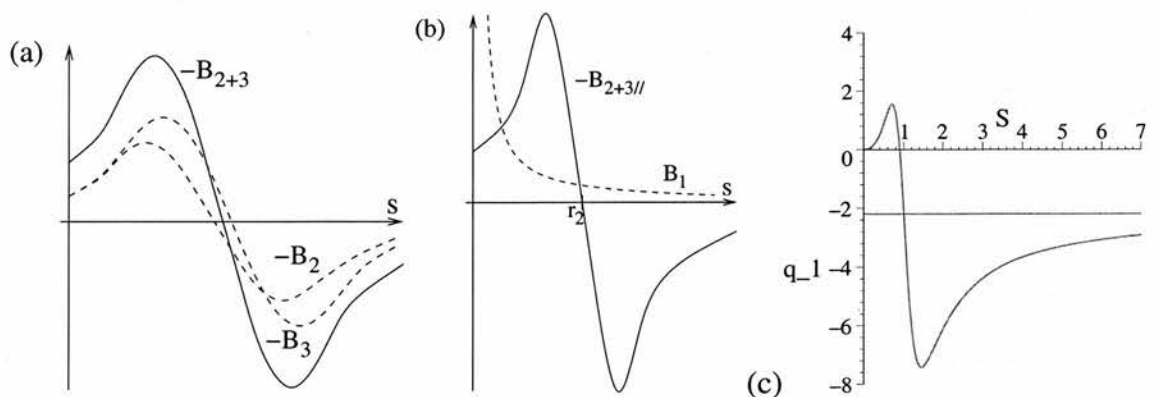


Figure 6.14: (a) Schematic diagram of $-B_{2+3||}$ for q_2 and q_3 positive. (b) The parallel field when $\theta \approx \phi_2$. The dashed curve indicates a typical B_1 field profile for $q_1 > 0$ (for $q_1, q_2, q_3 > 0$). (c) Position of zeros in $B_{||}$ along $\theta = \pi/2$ as a function of q_1 for $r_2 = 1.1$, $r_3 = 1$, $q_2 = 1.2$, $q_3 = 1$, $\phi_2 = \pi/3$ and $\phi_3 = 2\pi/3$. The horizontal line indicates the asymptotic value $-(q_2 + q_3)$.

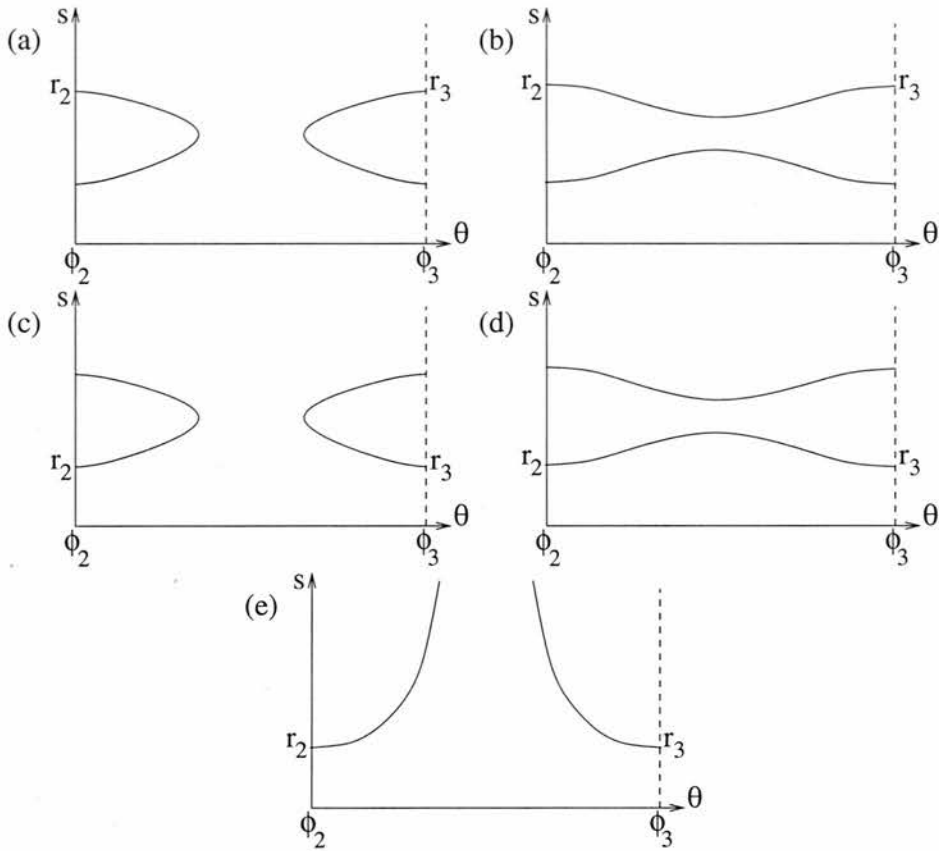


Figure 6.15: Schematic diagrams showing the curve $B_{\parallel} = 0$. When q_1 is the same sign as q_2 and q_3 , the curve may take shape (a) or (b). When q_1 is of opposite sign to q_2 and q_3 , it takes the shape (c), (d) or (e), where (c) and (d) correspond to $|q_1| > |q_2 + q_3|$ and (e) to $|q_1| < |q_2 + q_3|$.

in a three-source configuration. But can there ever be a second-order null, and hence a bifurcation?

6.4.3 Bifurcation to touching state

In the following two subsections we search for examples of bifurcations, guided by the parameter values in Brown and Priest (1999b) at which local separator bifurcations are observed to take place.

For bifurcation to the touching state we start in a separate or enclosed topological state with source 1 and sources 2 and 3 of opposite signs. Beginning with a source configuration which is close to symmetric gives one continuous curve for $B_{\perp} = 0$, as shown in Figure 6.12(b). We start with $q_1 = 1$, $q_2 = q_3 = -0.28$, $r_2 = 1$, $r_3 = 1.05$, $\phi_2 = 0$ and $\phi_3 = 0.45\pi$, and increase ϕ_3 . The resulting behaviour of the curves $B_{\perp} = 0$ and $B_{\parallel} = 0$ is shown in Figure 6.16(a), (b) and (c). Here it is the dashed section of the $B_{\perp} = 0$ curves

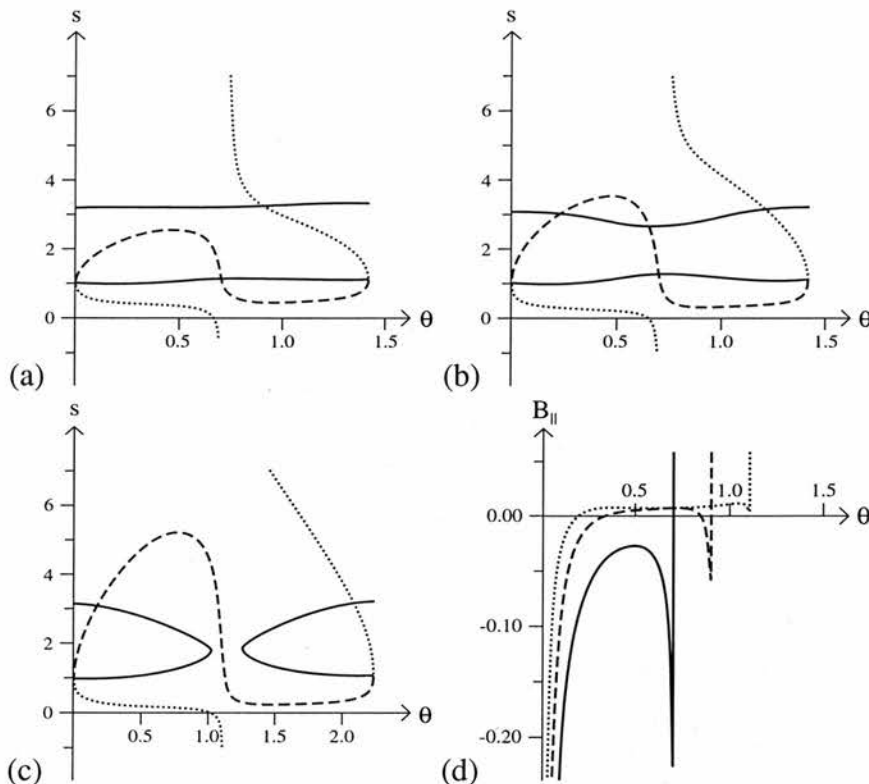


Figure 6.16: Zeros in the perpendicular and parallel fields for ϕ_3 = (a) 0.45π , (b) 0.58π , and (c) 0.71π . The dashed curve is the root of $B_{\perp} = 0$ reached by taking the '+' sign in the quadratic root formula (6.7). The negative root is dotted, and the curve $B_{\parallel} = 0$ is the solid line. (a) corresponds to the enclosed state, (b) to the touching state, and (c) to the separate state. Note that sources 2 and 3 are located where the solid line intersects the line $B_{\perp} = 0$ at the point where it changes from dotted to dashed. (d) B_{\parallel} plotted along the dashed part of $B_{\perp} = 0$ for $\phi_3 = 0.45\pi$ (solid line), 0.58π (dashed), and 0.71π (dotted).

which is cut two extra times by the curve $B_{\parallel} = 0$. Plotting the value of the parallel field along this dashed curve for the different values of ϕ_3 , yields the three graphs shown in Figure 6.16(d).

We see clearly that when $\phi_3 = 0.45\pi$ and $\phi_3 = 0.7\pi$ there is one first-order zero in $B_{\parallel} = 0$, whereas when $\phi_3 = 0.58\pi$ there are three. So when $\phi_3 = 0.58\pi$ we have a total of four nulls and we must be in the touching state.

We can also have a local separator bifurcation when the $B_{\perp} = 0$ curve has the broken topology as in Figure 6.12(c). Figure 6.17 shows the bifurcation occurring as before. This time, $q_1 = 1$, $q_2 = -0.28$, $q_3 = -0.33$, $r_2 = 1$, $r_3 = 1.05$, $\phi_2 = 0$ and again we vary ϕ_3 .

For highly non-symmetric source configurations, however, local separator bifurcations do not occur. For example, if we consider the same configuration as above, but this time with $q_3 = -0.75$, then, as ϕ_3 is varied from 0 to π , the shape of the B_{\parallel} curve along

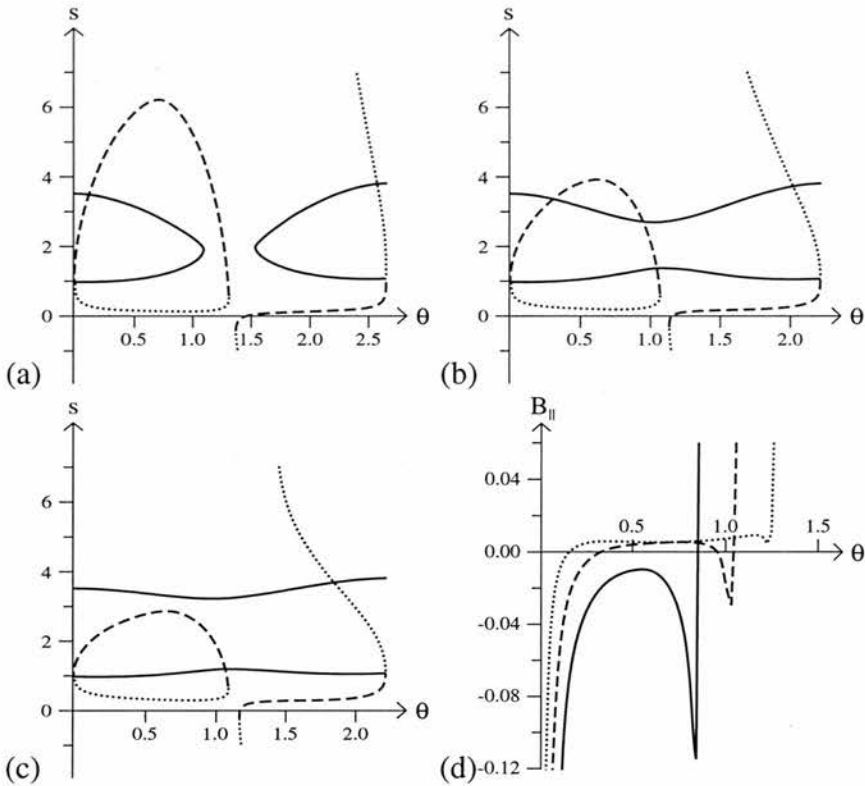


Figure 6.17: Zeros in B_{\perp} and B_{\parallel} for $\phi_3 =$ (a) 0.57π , (b) 0.7π , and (c) 0.84π . The dashed curve is the root of $B_{\perp} = 0$ reached by taking the '+' sign in the quadratic root formula (6.7). The negative root is dotted, and the curve $B_{\parallel} = 0$ is the solid line. (a), (b) and (c) correspond to the separate, touching and enclosed states respectively. (d) B_{\parallel} plotted along the dashed part of $B_{\perp} = 0$ for $\phi_3 = 0.57\pi$ (solid line), 0.7π (dashed), and 0.84π (dotted).

$B_{\perp} = 0$ is always similar to the solid curve shown in Figure 6.17(d).

6.4.4 Bifurcation to triangular state

For bifurcation to the triangular state we start with a divided state with all of the sources the same sign, say positive. This time we start with configuration parameters as follows: $q_1 = 1$, $q_2 = q_3 = 1.5$, $r_2 = 1$, $r_3 = 1.05$, $\phi_2 = 0$ and $\phi_3 = 3\pi/8$. q_2 and q_3 are then decreased, and we see extra nulls appear. The intersections of the curves $B_{\perp} = 0$ and $B_{\parallel} = 0$ are shown in Figure 6.18 (a), (b) and (c) and the shape of B_{\parallel} along the dashed portion of $B_{\perp} = 0$ is shown in Figure 6.18(d). Once again, this bifurcation can occur for more asymmetric cases than the ones described, though only up to a certain level of asymmetry.

In this section we have demonstrated that the results from Section 6.3, which discussed the symmetric case, are generic, and may be applied, with caution, to general

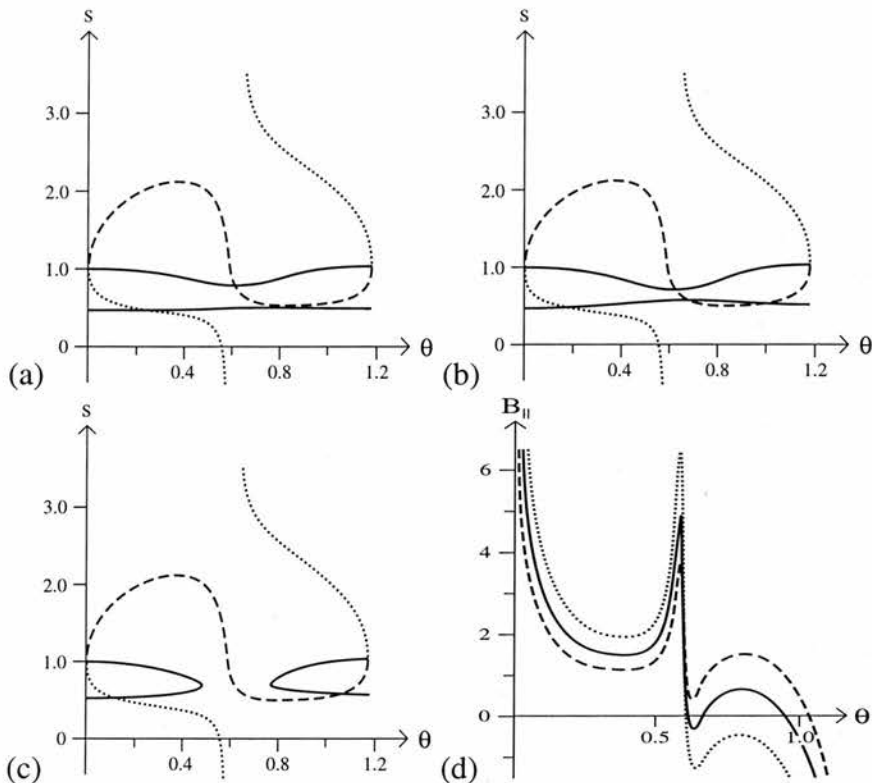


Figure 6.18: Zeros in B_{\perp} and B_{\parallel} for $q_2 = q_3 =$ (a) 1.5, (b) 1.1, and (c) 0.8. The dashed curve is the root of $B_{\perp} = 0$ reached by taking the '+' sign in the quadratic root formula (6.7), the negative root is dotted, and the curve $B_{\parallel} = 0$ is the solid line. (a) and (c) correspond to (globally) different divided states, and (b) to the triangular state. (d) B_{\parallel} plotted along the dashed part of $B_{\perp} = 0$ for $q_2 = q_3 = 1.5$ (dotted curve), 1.1 (solid), and 0.8 (dashed).

non-symmetric configurations.

6.5 More than three sources

Consider now the case of four photospheric sources. The topologies involved are more complicated and numerous than in the three-source case, the number of free parameters available in choosing the source configuration would make the task of fully documenting these topologies very time consuming. So, the question is, can we make any predictions about what the possible topologies might be from the simple analysis for the three source case? Which sets of sources might afford the possibility of a local separator bifurcation, and, for those which might, what configuration of sources would be required? (Local double separator bifurcations are also possible with four sources, but are beyond the scope of this analysis, for the moment).

The main issue here is the same as before; we want to look for sets of sources which might be able to produce a second-order null in the photosphere. We shall stick here to discussing the symmetric case, in the hope that once again the basic principles can be extended to ‘slightly’ non-symmetric cases.

As before, we require some kind of hyperbolic null structure local to our prospective second-order null point along one direction. So again we start with two same-sign sources, and consider the line which passes between them, across which their fields cancel. Further sources placed on this line will do nothing to destroy the hyperbolic null structure perpendicular to it, as their fields have no component in this direction. So by placing the two remaining sources on the bifurcation axis, we should be able to follow exactly the same arguments as before for the second-order null formation.

6.5.1 Same-sign sources on bifurcation axis

For four positive sources or two positive and two negative sources the situation seems fairly simple. Two same-sign sources placed on the bifurcation axis ‘close together’ should behave in basically the same way (for $s > 0$) as a single source of their combined strength placed somewhere between the two (see Figure 6.19(a)). The component of B_s (B_{1+4}) due to the sources on the bifurcation axis is still a monotonically decreasing function of s , though not exactly inverse-square. This should mean that, while flux and source-position considerations may be slightly different from the three source case, the same general arguments should apply. Suggestions for source configurations which could, for the right source positions and strengths, yield a second-order null are shown in Figures 6.19(b-d).

6.5.2 Opposite-sign sources on bifurcation axis

The situation is more complicated if we have two sources of different signs on the bifurcation axis. This happens when we have three positive sources and one negative, and we would expect different behaviour for positive and negative total flux. For opposite-sign sources, there is some point on the bifurcation axis where B_{1+4} is zero (see Figure 6.20).

One way of creating a second-order null point would be to again have dominance at infinity of the flux ($q_1 + q_4$) from sources on the bifurcation axis. So if we have a dominant source at $s=0$ and another smaller source at (say) $s = -1$ then $B_{1+4} \rightarrow B_1$ for $s > 0$ (see Figure 6.20(b)), and we have a situation very similar to the three-source case. As

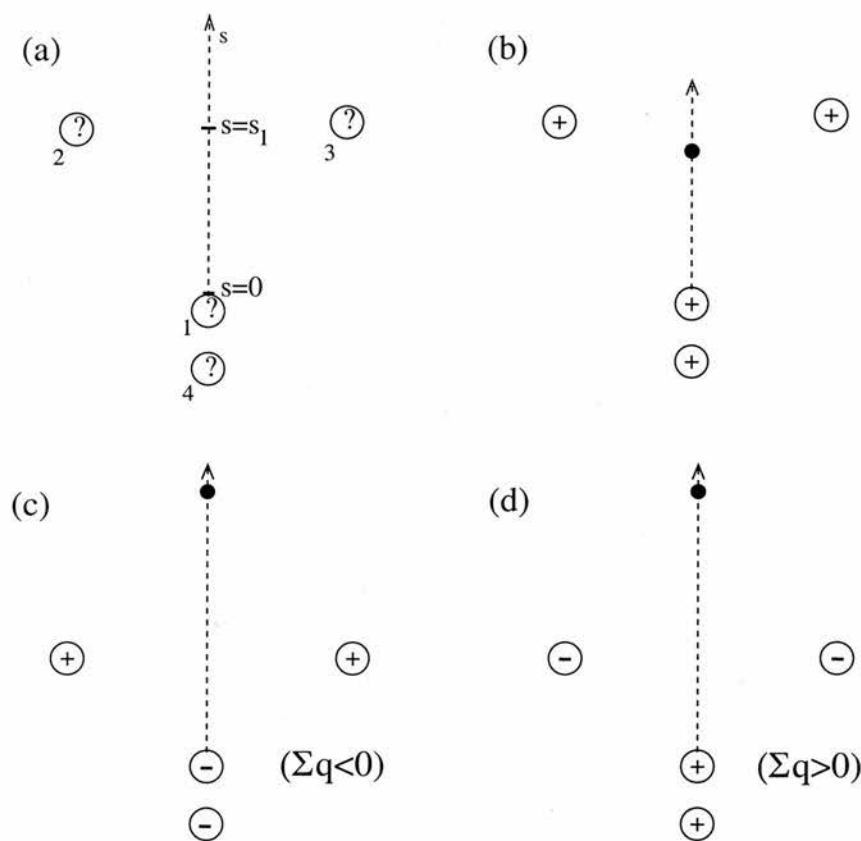


Figure 6.19: (a) The symmetric source configuration for four sources, where s is the distance along the bifurcation axis (dashed) from source 1. (b-d) Source configurations likely to yield second-order nulls on the bifurcation axis between two sources of the same sign. The large dots indicate qualitatively the localities where the second-order nulls are expected.

$|q_4/q_1| \rightarrow 1$, the field profile B_{1+4} drops very quickly to zero as s increases, so the decay is much more rapid than inverse-square (see Figure 6.20(c)). To have a second-order null for $|q_4/q_1| \approx 1$ would clearly require a very different configuration of sources 2 and 3, for example, s_1 much smaller or $q_2 = q_3$ small. One possible configuration which might give a second-order null is shown in Figure 6.21(a). For $|q_4/q_1| \gg 1$, B_{1+4} has a similar profile to B_1 for intermediate values of s , and so a second-order null may possibly be present, through similar considerations as before, though we would also have a first-order null on the bifurcation axis at $s > 0$ (see Figure 6.20(a)).

The final situation left to consider is three positive sources and one negative source with positive total flux. The usual setup with two positive sources opposing across the bifurcation axis and two sources close together on it cannot yield a second-order null if $q_1 + q_4 < 0$, because the total flux is positive and so we do not have flux dominance for these sources. However, if this is not the case, and $q_1 + q_4 > 0$, then a configuration which may yield a second-order null is shown in Figure 6.21(b). For $q_1 + q_4 < 0$, it seems less

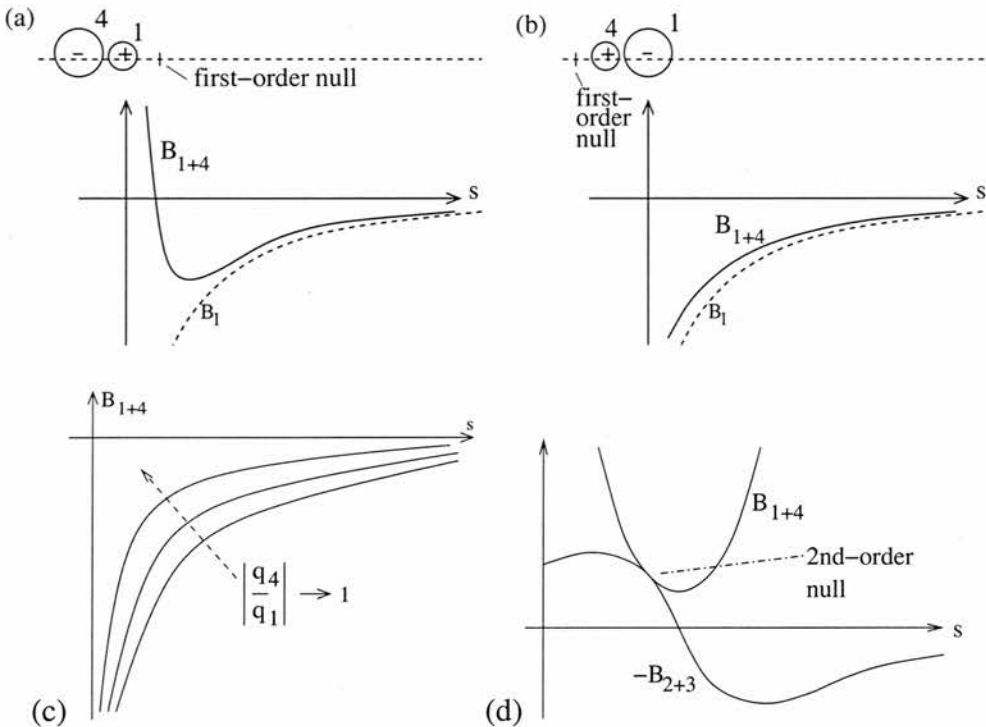


Figure 6.20: (a), (b) $B_{\parallel} = B_{1+4}$ along the bifurcation axis due to the sources shown, where the source sizes indicate their relative strengths. The dashed curve (marked B_1) indicates the field due to a single negative source of strength $q_1 + q_4$. (c) The variation as $|q_4/q_1| \rightarrow 1$ of the field B_{1+4} due to the two sources in (b). (d) The field profiles due to sources on and off the bifurcation axis for the configuration shown in Figure 6.21(c) which would give a second-order null point.

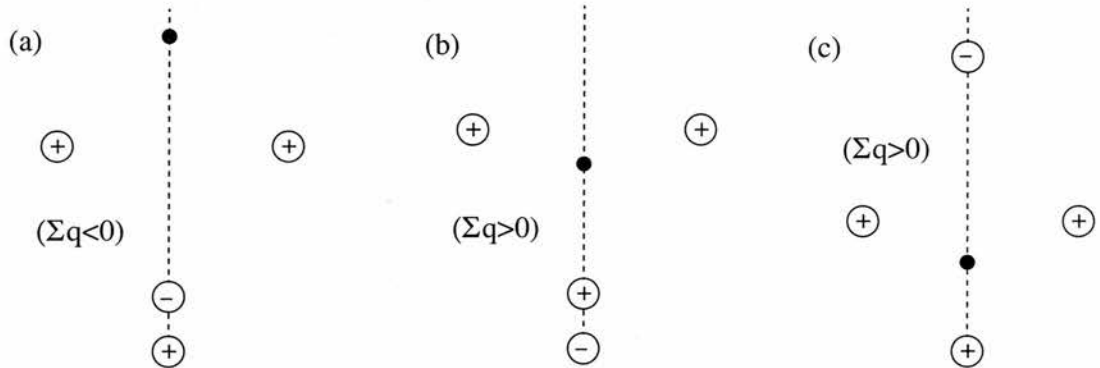


Figure 6.21: The source configurations which are likely to yield second-order nulls on the bifurcation axis, for opposite-sign sources on the bifurcation axis.

likely that we can use the same considerations as before and still come up with a second-order null. Consider, however, the source configuration in Figure 6.21(c). In the region of the positive sources this is ‘almost’ the three-positive-source case, and a possible field profile for B_s which would yield a second-order null is shown in Figure 6.20(d).

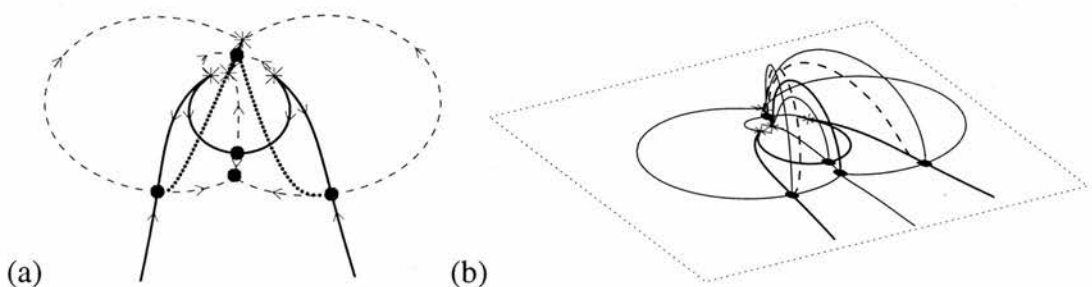


Figure 6.22: (a) Footprint in the $z = 0$ plane and (b) field line plot of a state created by a four-source local separator bifurcation (courtesy of Brown (1999)).

6.5.3 Observed four-source locally-bifurcating states

In fact, a number of local separator bifurcations have been found to occur with four sources, confirming some of the above predictions. Figure 6.22 shows an example (from Brown and Priest, 1999a), for two positive and two negative sources, of a state created by a local separator bifurcation (the *quintuple-separator state*). Although the configuration is not symmetric (the source strengths are 1, 0.5, -0.5, -1.2, where the left and right hand sources in Figure 6.22(a) are the negative ones), it does confirm that along a (close to straight) line which runs roughly through the negative sources and between the positive sources a second-order null appears. The total flux is negative, which gives dominance of flux from sources on the imaginary bifurcation axis, as expected. The source configuration is very similar to that pictured in Figure 6.19(c), and the bifurcation is marked as ‘l.s.b. (ii)’ in Figure 6.23.

A further example of a local bifurcation occurring when four sources are present is described in Brown (1999). The bifurcated state is the *triangular-intersecting state*, which has a source configuration similar to that shown in Figure 6.21(c). The bifurcation to this state is marked as ‘l.s.b. (i)’ in Figure 6.23.

6.5.4 More sources summary

A number of local bifurcations for given sets of sources have been predicted in this section, two of which have been previously found to occur. Figure 6.23 gives a summary of this and shows a full description of all of the different sets of four sources, and of how they can be built up from the three-source cases by bringing up small sources. The thick dashed lines indicate local separator bifurcations which should be able to occur according to the model. When four sources are present, a further local bifurcation known as a *local double-separator bifurcation* is also possible, which creates a null out of the $z = 0$ plane

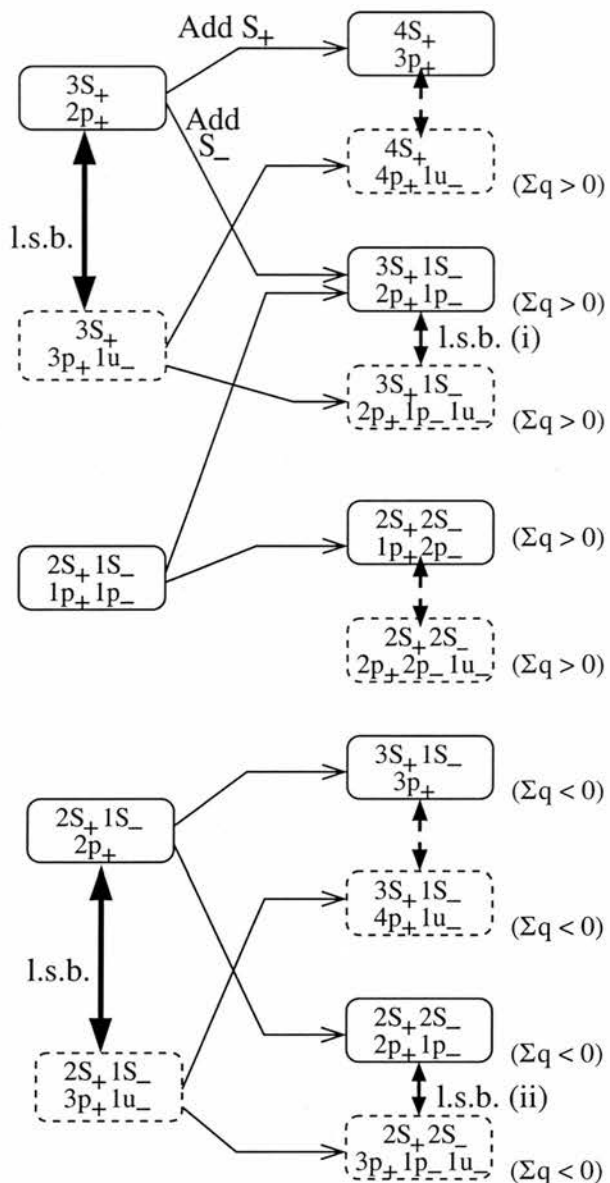


Figure 6.23: The different possible sets of four sources and the ways in which they can be attained from the three source states. The bold arrows indicate known local separator bifurcations, while the dashed bold lines indicate sets of sources between which they are predicted to take place in the analysis in this section. Solid-outlined states are basic states, while those with dashed outline contain ‘extra’ nulls, created by a local separator bifurcation.

(Brown and Priest, 2001).

One might continue to extend the analysis, as in this section, to include even more sources. For example, when five or more sources are present more than one pair of sources may ‘oppose’ across the bifurcation axis, with remaining sources lying on it. This may lead to ‘doubly-bifurcated’ states, i.e. states where more than one new pair of nulls has been added to the basic state.

6.6 Summary

In this chapter we have put forward (for three sources) an explanation of the local separator bifurcation, which produces an important change of magnetic field topology. The way in which the analysis may be extended when more sources are present has been sketched, with the hope that this extension may be continued for more complex fields due to higher numbers of sources, which commonly occur in the solar corona where the fields are often produced by an extremely complex network of flux fragments. This network evolves continually, and, as the topology of the resulting field changes, reconnective processes can trigger eruptive and heating events in the corona. However, the coronal field is thought to be largely made up of topological building blocks, resulting from small numbers of sources Brown and Priest (1999b). So if we can explain topology and topology changes in these building blocks, we hope to develop an understanding of the structures of magnetic field which lead to dynamic events.

We have developed here a method of searching for local separator bifurcations by looking for second-order null points, which are the crucial field structure involved. In the three-source symmetric case we find that a bifurcation can always occur when all three sources have the same sign, as the source on the bifurcation axis is brought up. When the source-signs are not the same, the source of different sign must have a flux of greater magnitude than the sum of the fluxes of the other two if we are to have a bifurcation. For non-symmetric source configurations the analysis is much more complicated and we cannot say too much in general about when bifurcations might occur, although for configurations ‘close’ to symmetric, we find the same as in the symmetric case.

In addition, when four or more sources are present, a *local double separator bifurcation* is also possible Brown and Priest (2001), which creates a new state with a null out of the photospheric plane in the corona. An additional method of predicting the birth of such coronal nulls would provide an invaluable tool for forecasting possible null reconnection sites in the corona.

Chapter 7

Summary and future work

“There is a theory which states that if anyone ever discovers exactly what the Universe is for and why it is here, it will instantly disappear and be replaced by something even more bizarre and inexplicable.

There is another theory which states that this has already happened.”

Douglas Adams, *The Restaurant at the End of the Universe*

7.1 Summary

Magnetic reconnection is a fundamental process in many areas of plasma physics. The theory in two dimensions is well developed, although little is known of the nature of reconnection in three dimensions. In most astrophysical plasmas, non-ideal effects are negligible, except in well-localised regions where length-scales collapse down to be very short. In this thesis, therefore, magnetic reconnection at an isolated non-ideal region was considered.

In Chapter 2, some of the key differences between two- and three-dimensional reconnection were described. This was done by first describing a two-dimensional kinematic solution to the MHD equations, and then the result of a naive 3D extension of this solution. Some new properties of 3D kinematic reconnection, consequences simply of Ohm’s law, were discussed. These properties have been previously described by Priest et al. (2003a), and demonstrated to be present in a 3D reconnection process in the absence of a magnetic null point by Hornig and Priest (2003). The new properties are, briefly;

1. The non-existence of a unique field line velocity.

2. Field lines continually change their connections throughout the non-ideal region.
3. In general, the mapping between field line footpoints is continuous.
4. On their continuation through and out of the other side of the non-ideal region, field lines do not move at the ideal plasma velocity.
5. There is no one-to-one reconnection of field lines, and as a result, for steady reconnection, no one-to-one reconnection of flux tubes either.

In Chapter 3, a model was presented which described steady kinematic reconnection at a magnetic null point with *spine*-aligned current. It was shown, in the elementary solution, that a rotational flow is present, with this flow being confined within the ‘envelope’ of magnetic flux which threads the diffusion region. It was demonstrated that this rotational flow is due simply to the structure of the magnetic field, and is independent of the profile chosen for the resistivity, η . As a result of this flow, the magnetic field lines continually change their connections, also in a rotational fashion. In the composite solution, an ideal stagnation-point flow was added to the elementary solution, and a number of different types of field line behaviour were discovered. In particular, it was found that in one region of the flow, the field line behaviour shares some of the characteristics of 2D reconnection. Properties (1)-(5) were demonstrated to be present for these solutions. The effect of adding a simple time-dependence was also considered, and it was shown that this results in the one-to-one reconnection of particular pairs of magnetic flux tubes.

In Chapter 4, the complementary model to that of Chapter 3 was presented, for steady kinematic reconnection at a 3D null point with *fan*-aligned current. In the first solution, with constant current, the plasma was shown to cross both the spine and the fan, resulting in field line behaviour reminiscent of the spine and fan reconnection of Priest and Titov (1996). The fan-crossing flow is an important one for topological considerations in global fields, and was again shown to be independent of the profile chosen for the resistivity, but due solely to the structure of the magnetic field. Two further solutions were described, in the first of which the current was zero in the fan resulting in a flow, and so a reconnection of field lines, only across the spine. In the final solution, the current was zero on the spine, and field lines were found to be advected only across the fan. Once again, each solution demonstrates the properties (1)-(5).

In Chapter 5, a numerical experiment was described which models 3D reconnection in the absence of a null point, in a so-called hyperbolic flux tube (Titov et al., 2003). In a number of runs of the experiment the full MHD equations were solved, and the aim was

to test the previously described results of the kinematic experiments. The presence of the properties (1)-(4) was indeed verified: most importantly, the non-existence of a unique field line velocity was demonstrated, as well as the resulting continual and continuous change of field line connections within the non-ideal region. The presence of background rotational flows was also shown, as well as the importance for the reconnection of a parallel electric field. Experiments with differently prescribed resistivities, and so different non-ideal regions, were found to show qualitatively the same characteristics.

Finally, in Chapter 6, a model was described for predicting the allowed topological states in the coronal magnetic field of the Sun. In particular, a model for the local separator bifurcation was proposed, and was shown to successfully predict the behaviour due to three magnetic sources. Predictions for more than three sources were also made.

7.2 Future work

The majority of the work in this thesis has been focussed on gaining an understanding of three-dimensional magnetic reconnection. This is an extremely complex topic, the study of which is only in its very early stages, and much more work is required before a full understanding may be reached.

In Chapters 2, 3 and 4, the steady kinematic MHD equations were solved in order to determine the nature of 3D reconnection at an isolated non-ideal region. In each case, only a resistive non-ideal term ($\eta \mathbf{j}$) was included in Ohm's law, and the result of other non-ideal effects, such as Hall currents and electron inertial effects, might also be considered (as in Craig and Watson (2002)). Furthermore, the resistive non-ideal term used in each model was always localised by imposing a localised resistivity, so that it was possible to have as simple a magnetic field as possible. A much more realistic way of localising the resistive term would be to have a localised region of current, and for the resistivity to be dependent on this current. In order to localise the current, more complex magnetic field structures would be required. In addition, at present, each of the models currently has a steady magnetic field, while having a magnetic field which varied in time (e.g. collapsing to form a localised current concentration) would again provide a more realistic model for non-steady reconnection.

The major way in which the kinematic solutions of Chapters 3 and 4 should be extended in the future is to include the full set of MHD equations, as in Chapter 5. In this way it will be possible to test the results of the kinematic solutions, in order to find out

whether the basic nature of the behaviour is the same in the dynamical regime.

In Chapter 5, a numerical experiment which models 3D reconnection in the absence of a magnetic null point was described. There are many more aspects of this experiment which might be studied, such as the energy conversion and helicity evolution during the process. It would also be interesting to investigate the effect of ‘turning off’ the driving velocity in the experiment (at some time after reconnection is initiated), to see to what extent the reconnection would continue without extra driving. The effect of having driving velocities or magnetic field profiles which are not symmetric between the two driven boundaries might also be investigated. Furthermore, the ‘efficiency’ of magnetic flux reconnection could also be considered, by calculating the total flux which would be reconnected if the field were to remain potential (and so reconnect unimpeded) and compare with the reconnected flux calculated in Section 5.4.3. In addition, it will in the future be important to test whether or not property (5) from the previous section still holds in this configuration. Preliminary indications are that indeed it does, although the nature of the mismatching of reconnected field lines and flux tubes has not been investigated in detail.

The reconnection process in the simulation described in Chapter 5 is ‘driven’, in the sense that it progresses because the boundary motions continually twist the magnetic flux in the domain and force it together. It would be very interesting to consider a scenario where the reconnection is not driven, but where for example an equilibrium magnetic field (of similar structure) is perturbed sufficiently for reconnection to occur, and then the reconnection allowed to proceed as the field relaxes. This may help to test the nature of the elementary or pure solutions more easily, without the strong stagnation flow of Chapter 5.

Of course the aim of each of the reconnection models described in this thesis is eventually to gain understanding of the physical processes in which the reconnection plays a role. The work done here might therefore be followed up by considering what effect the new behaviour of the magnetic flux has on such processes, where the ‘local’ reconnection regions considered here are embedded in a global configuration.

Lastly, in Chapter 6, a model for a topological bifurcation in the solar corona was described. In this chapter, the coronal magnetic field was modelled by a potential field, although clearly a more realistic model would use a field able to store energy, such as a force-free field (see, for example, Longcope (1996), Brown and Priest (2000) and Maclean et al. (2004), for preliminary studies on topology in force-free fields). An obvious extension to this chapter would be to make predictions for states which might undergo the local separator bifurcation with greater numbers of sources, and to go on to test the pre-

dictions for four and more sources. Finally, when four or more sources are present, a *local double separator bifurcation* is also possible (Brown and Priest, 2001), which creates a new state with a null in the corona. A method of predicting the birth of such coronal nulls, using a similar model to that described in Chapter 6, would provide an invaluable tool for forecasting possible null reconnection sites.

Appendix A: Flux and field line motion

The motion of magnetic flux and field lines in an ideal environment is relatively simple. The field is frozen to the plasma and so moves everywhere with it. In a non-ideal environment, however, the field lines are allowed to slip through the plasma, resulting in a number of different possible behaviours. There are three possibilities;

1. The field lines slip through the plasma, but flux and field line conservation still hold.
2. Field line conservation still holds, but flux conservation does not.
3. Neither flux conservation nor field line conservation hold.

Examples illustrating these three possible types of behaviour are described below. We concentrate here on two-dimensional solutions of Maxwell's equations and Ohm's law only, and in that sense these solutions are 2D kinematic ones (except the second example), intended simply to illustrate the concepts. In the first and third cases, the magnetic field and diffusivity are first imposed, and then the plasma and field line velocities calculated. In two dimensions, a field line velocity may be found, satisfying

$$\mathbf{E} + \mathbf{w} \times \mathbf{B} = 0 \quad (\text{A.1})$$

(which is unique up to a gradient term on the RHS, which we set to zero here). To calculate the field line velocity, take the vector product of this equation with \mathbf{B} to give

$$\mathbf{w} = \frac{\mathbf{E} \times \mathbf{B}}{B^2}, \quad (\text{A.2})$$

where the component of \mathbf{w} parallel to \mathbf{B} is assumed to be zero. Similarly, taking the vector product of Ohm's law with \mathbf{B} gives the plasma velocity perpendicular to \mathbf{B} ;

$$\mathbf{v}_\perp = \frac{(\mathbf{E} - \eta \mathbf{j}) \times \mathbf{B}}{B^2}, \quad (\text{A.3})$$

as before, where the non-ideal term is again assumed to be resistive.

A.1 Slippage with flux and field line conservation

Consider a region in which there exists a linearly increasing one-dimensional magnetic field, with uniform diffusion. Assume a steady state, so

$$\mathbf{E} = E \hat{\mathbf{z}}. \quad (\text{A.4})$$

Let

$$\mathbf{B} = B_0 x \hat{\mathbf{y}}, \quad (\text{A.5})$$

where B_0 is constant, so that $\mathbf{j} = B_0 \hat{\mathbf{z}}$, and let

$$\eta = \eta_0, \quad (\text{A.6})$$

constant. From Equations (A.2) and (A.3), the field line and plasma velocities can now be calculated;

$$\mathbf{w} = -\frac{E}{B_0 x} \hat{\mathbf{x}}, \quad (\text{A.7})$$

$$\mathbf{v} = -\frac{E - \eta_0 B_0}{B_0 x} \hat{\mathbf{x}}. \quad (\text{A.8})$$

Note that we must consider this as an approximate solution, in some region far from $x = 0$, to avoid singularities.

It is obvious from these two expressions that the field line velocity and plasma velocity are different, and so the field lines are slipping through the plasma. However, since the magnetic field and plasma flow are both one-dimensional, it is also obvious that all plasma elements connected by a field line at one time will remain connected by a field line for all time (see Figure A.1). To see that the flux is conserved, consider

$$\nabla \times \mathbf{R} = \nabla \times (\eta \mathbf{j}) = \nabla \times (\eta_0 B_0 \hat{\mathbf{z}}) = 0. \quad (\text{A.9})$$

Figures A.1(a) and (b) illustrate this example at two different times. In Figure A.1(a), red plasma elements lie on red field lines, and blue plasma elements on blue field lines, while three field lines, representing three units of flux, pass through the loop defined by the

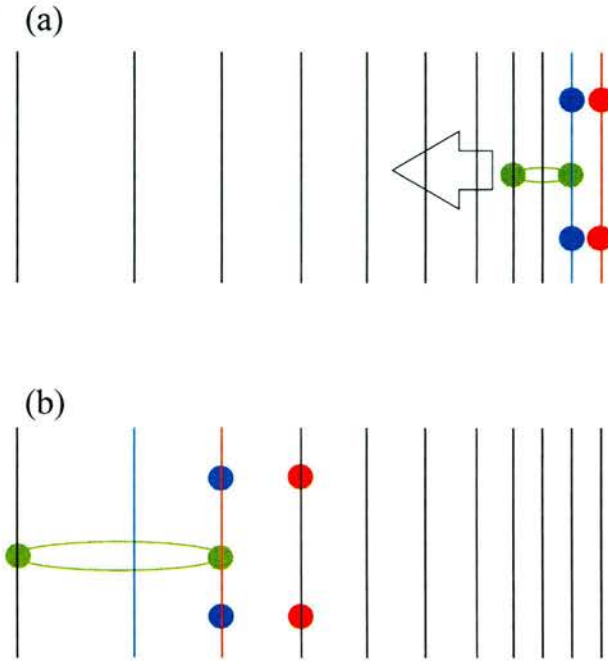


Figure A.1: Slippage of field lines maintaining field line and flux conservation. The circles are plasma elements, the straight lines magnetic field lines and the green loop is a loop of plasma elements.

green plasma elements. Figure A.1(b) shows the situation some time later. Although red and blue plasma elements no longer lie on red and blue field lines, respectively, each pair of plasma elements is still connected by a field line, and so field line conservation holds. Likewise, although the field lines have diffused through the plasma, three field lines, or three units of flux, still pass through the loop of plasma elements, showing that the flux is also conserved.

A.2 Field line conservation without flux conservation

To illustrate field line conservation without flux conservation, we consider the stagnation-point flow model of Sonnerup and Priest (1975). Here, the magnetic field is once again one-dimensional ($\mathbf{B} = B(x)\hat{\mathbf{y}}$), and the diffusivity is constant ($\eta' = \eta_0$) and a steady state is assumed, so $\mathbf{E} = E\hat{\mathbf{z}}$. This solution in fact also satisfies the steady state equation of motion (with $\nabla \cdot \mathbf{v} = 0$), and so is a solution of the full MHD equations. The plasma velocity is a stagnation flow of the form

$$\mathbf{v} = \left(-\frac{Ux}{a}, \frac{Uy}{a} \right), \quad (\text{A.10})$$

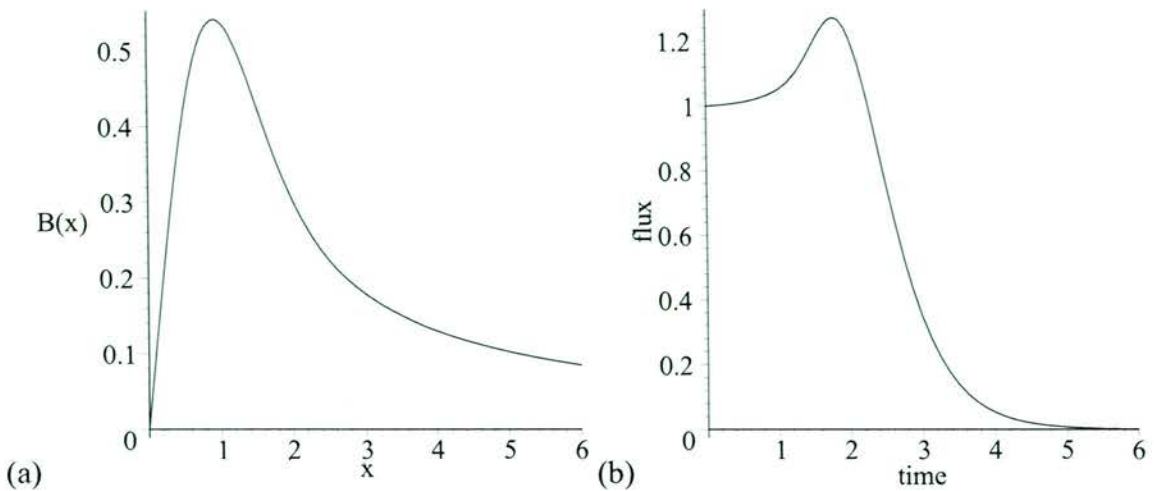


Figure A.2: (a) Profile of B_x , for parameters $E = a = U = l = 1$ and (b) the change of flux in time through a typical loop moving with the plasma, for the same choice of parameters.

where U and a are constants. The magnetic field can be found from Ohm's law, the z -component of which is

$$E - \frac{Ux}{a}B = \eta_0 \frac{dB}{dx}. \quad (\text{A.11})$$

The solution for the magnetic field is

$$B(x) = \frac{2Ea}{Ul} e^{-x^2/l^2} \int_0^x e^{X^2/l^2} dX, \quad (\text{A.12})$$

where $l = \sqrt{2\eta_0 a/U}$. The variation of B with x is shown in Figure A.2(a). A field line velocity can be calculated using Equation (A.2). Once again, since the field lines are lines of $y = \text{const}$, and v_x is independent of y , it is clear that field line conservation must hold. However, it can be shown that $\nabla \times (\eta \mathbf{j}) \neq 0$, so the flux is not conserved. Consider a loop moving with the plasma, lying on $y = 0$ (Figure A.3). Far from the y -axis, $\mathbf{j} \approx 0$, and so the flux is approximately conserved. However, close to the origin, the flow strength decreases with x , and so the loop gets smaller. In this region the magnetic field strength is also decreasing, and so it is clear that the flux through the loop must decrease (see Figure A.2(b)). This example is illustrated in Figure A.3, as well as in an animation on the accompanying CD. It can be seen that although plasma elements starting on the same field line (coloured blue) remained joined by a field line for all time (field line conservation), the flux through the loop moving with the plasma (red) decreases with time (flux non-conservation).

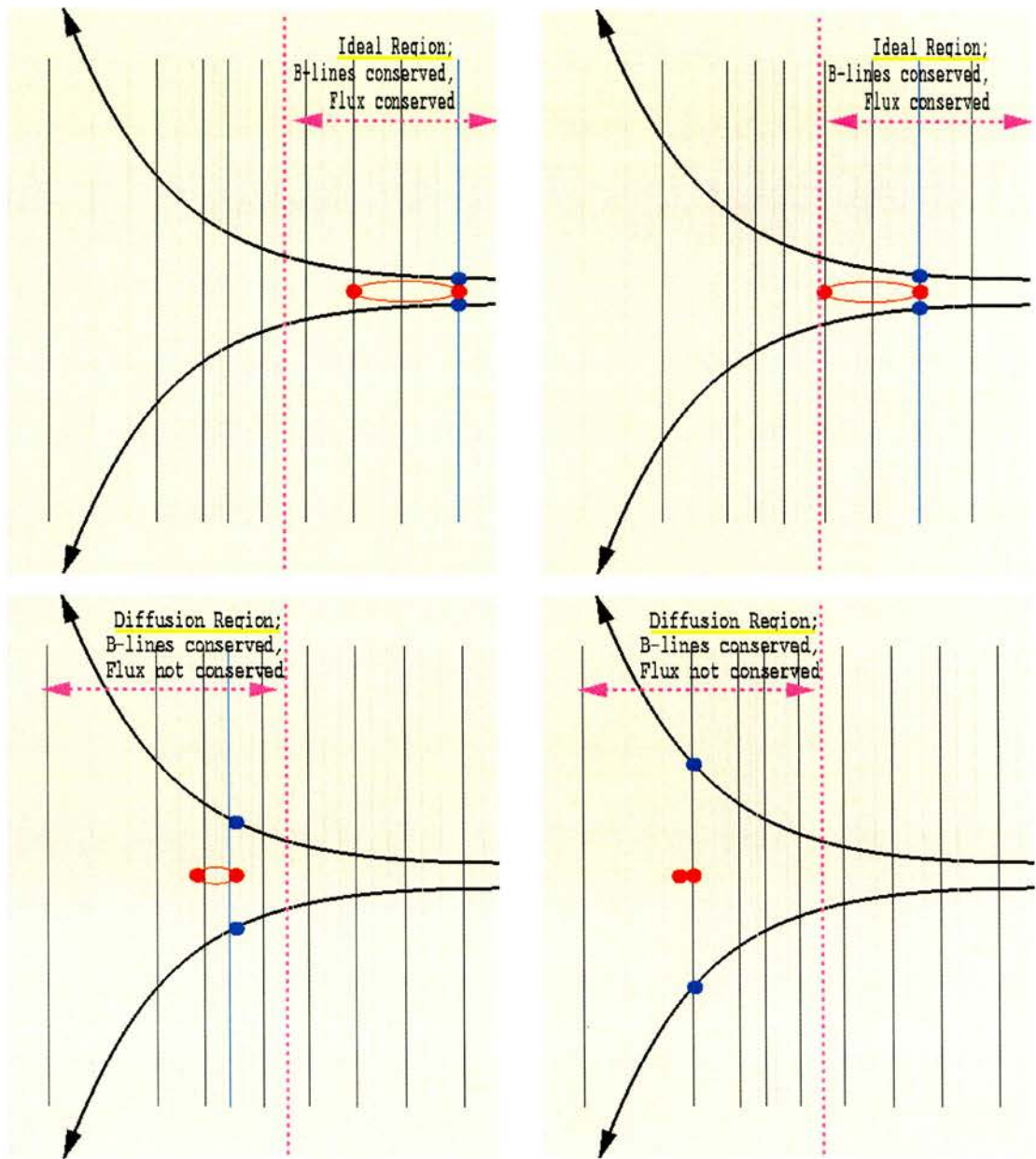


Figure A.3: Frames from the animation showing field line conservation without flux conservation. The thick lines are flow lines of \mathbf{v} , thin lines magnetic field lines, circles plasma elements. The red loop moves with the plasma.

A.3 Field line and flux non-conservation

Once again, consider for simplicity a uni-directional magnetic field $\mathbf{B} = B(x)\hat{\mathbf{y}}$. This time, let

$$\mathbf{B} = B_0/x \hat{\mathbf{y}}, \quad (\text{A.13})$$

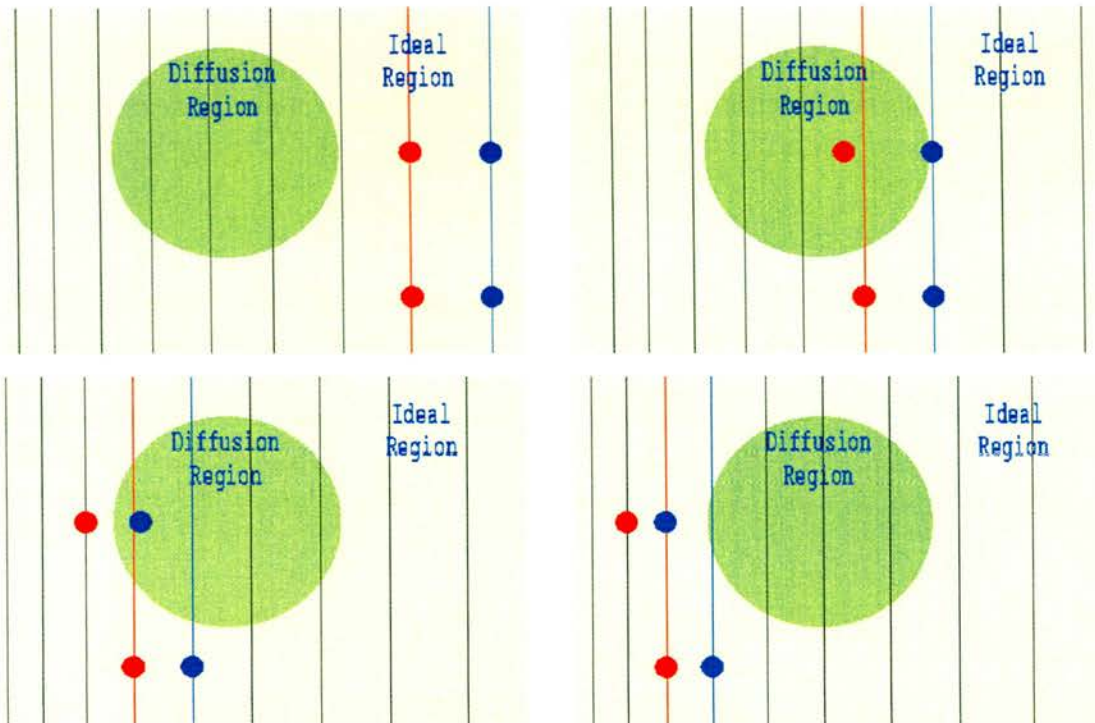


Figure A.4: Frames from the animation showing field line non-conservation. The thin lines are magnetic field lines, the circles plasma elements, and the green shading shows the non-ideal region.

where B_0 is a constant, and where once again it is assumed that the model represents the situation at some distance from $x = 0$. Again assume that the situation is in a steady state, so that

$$\mathbf{E} = E \hat{\mathbf{z}}. \quad (\text{A.14})$$

For a breakdown in field line conservation, it is necessary that, unlike in the previous two examples, the strength of diffusion is dependent on y . Let the diffusivity be concentrated in a circular region centred on $(a, 0)$, and be of the form

$$\eta(x, y) = \eta_0 \begin{cases} (1 - (x - a)^2 - y^2)^2 & (x - a)^2 - y^2 < 1 \\ 0 & \text{otherwise,} \end{cases} \quad (\text{A.15})$$

where η_0 and a are constant. Once again, \mathbf{w} and \mathbf{v} can be calculated to be

$$\mathbf{w} = \frac{Ex}{B_0} \hat{\mathbf{x}} \quad (\text{A.16})$$

and

$$\mathbf{v} = \left(E + \frac{B_0}{x^2} \eta(x, y) \right) \frac{x}{B_0} \hat{\mathbf{z}}. \quad (\text{A.17})$$

It can be shown that $\nabla \times (\eta \mathbf{j}) \neq \mathbf{0}$, and also $\mathbf{B} \times (\nabla \times (\eta \mathbf{j})) \neq \mathbf{0}$, so that neither field lines nor flux are conserved. This breaking of the field line conservation is illustrated in Figure A.4, which shows frames from the animation contained on the accompanying CD.

Appendix B: Diffusion of a toroidal flux tube

Here we investigate the behaviour of a magnetic field which is confined to a single toroidal tube, under the effects of a resistive dissipation. It is shown that the magnetic flux is not conserved, but rather decays to zero. This model also describes the behaviour of flux at an O-type null point of a magnetic field in 2D.

We consider the initial magnetic field

$$\mathbf{B}(t = 0) = B_0 \delta(r - R)\hat{\theta} \quad (\text{B.1})$$

in cylindrical polar coordinates, where B_0 is a constant and R is a constant greater than zero. This represents a toroidal magnetic flux tube centred on the z -axis localised at $r = R$, which is uniform in the z -direction. The behaviour of this ring of flux is investigated under simple diffusion, when the magnetic field evolves according to

$$\frac{\partial \mathbf{B}}{\partial t} = \eta' \nabla^2 \mathbf{B}. \quad (\text{B.2})$$

We assume that $\eta' = \eta_0$, constant. We have $\mathbf{B} = B(r)\hat{\theta}$, and in order to solve the above equation for the evolution of \mathbf{B} , we write \mathbf{B} in terms of a flux function A , defined by

$$\mathbf{B} = \nabla \times (A(r)\hat{\mathbf{z}}). \quad (\text{B.3})$$

It is now possible to obtain an equation for the evolution of A by substituting (B.3) into (B.2). In order to do this it is necessary to use the vector identities

$$\nabla^2 \mathbf{D} = \nabla(\nabla \cdot \mathbf{D}) - \nabla \times (\nabla \times \mathbf{D}) \quad (\text{B.4})$$

and

$$\nabla \cdot (\nabla \times \mathbf{D}) = 0. \quad (\text{B.5})$$

Now, substitution of (B.3) into (B.2) gives

$$\frac{\partial}{\partial t} (\nabla \times (A \hat{\mathbf{z}})) = \eta_0 \nabla^2 (\nabla \times (A \hat{\mathbf{z}})). \quad (\text{B.6})$$

The order of the space and time integration on the left-hand side (LHS) may be simply reversed, while the right-hand side (RHS) may be expanded using the identity (B.4), to give

$$\nabla \times \left(\frac{\partial A}{\partial t} \hat{\mathbf{z}} \right) = \eta_0 [\nabla (\nabla \cdot (\nabla \times (A \hat{\mathbf{z}}))) - \nabla \times (\nabla \times (\nabla \times (A \hat{\mathbf{z}})))].$$

The first term in the square bracket on the RHS vanishes, due to (B.5), and the second term may be expanded, by using a rearrangement of (B.4), so that

$$\nabla \times \left(\frac{\partial A}{\partial t} \hat{\mathbf{z}} \right) = -\eta_0 \nabla \times [\nabla \times (\nabla \cdot (A \hat{\mathbf{z}})) - \nabla^2 A \hat{\mathbf{z}}].$$

Once again the first term in the square bracket on the RHS vanishes, since $\nabla \cdot (A \hat{\mathbf{z}}) = \partial A / \partial z = 0$, and so

$$\nabla \times \left(\frac{\partial A}{\partial t} \hat{\mathbf{z}} \right) = \eta_0 \nabla \times (\nabla^2 A \hat{\mathbf{z}}). \quad (\text{B.7})$$

Since η_0 is constant, this equation may be integrated to give

$$\frac{\partial A}{\partial t} = \eta_0 \nabla^2 A, \quad (\text{B.8})$$

where in general any gradient function may be added to the RHS, although we set this here to zero without loss of generality, since this gradient function has no effect on the magnetic field.

To find the time evolution of A , and hence \mathbf{B} , this equation may now be solved, with the help of the relevant Green's function. We also require an initial condition for A , which

can be found from (B.1). Using the definition of A ,

$$\begin{aligned} A(r, 0) &= - \int_0^r B(r, 0) dr \\ &= -B_0 \int_0^r \delta(r - R) dr \\ &= \begin{cases} 0 & r < R \\ -B_0 & r > R. \end{cases} \end{aligned} \quad (\text{B.9})$$

Hence, the solution of (B.8) is given by

$$A(r, t) = \int_0^\infty G(r, s, t) A(s, 0) ds, \quad (\text{B.10})$$

where

$$G(r, s, t) = \frac{s}{2\eta_0 t} e^{-\left(\frac{r^2+s^2}{4\eta_0 t}\right)} I_0\left(\frac{rs}{2\eta_0 t}\right) \quad (\text{B.11})$$

and I_0 is the zero-order hyperbolic Bessel function (see Barton, 1989). A description of the properties of $I_0(x)$ is given in Spanier and Oldham (1987). Hence,

$$A(r, t) = -\frac{B_0}{2\eta_0 t} e^{-\left(\frac{r^2}{4\eta_0 t}\right)} \int_a^\infty s e^{-\left(\frac{s^2}{4\eta_0 t}\right)} I_0\left(\frac{rs}{2\eta_0 t}\right) ds, \quad (\text{B.12})$$

An expression for $B_\theta(r, t)$ may now be found by substitution into the definition (B.3). The way that the magnetic field evolves is shown in Figure B.1, from which it can be seen that the flux diffuses both inwards towards the z -axis and outwards.

To investigate whether or not the flux is conserved, we consider the total flux per unit length in the z -direction (F), given by

$$\begin{aligned} F &= \int_0^\infty B_\theta dr \\ &= - \int_0^\infty \frac{\partial A}{\partial r} dr \\ &= A(0, t) - A(\infty, t). \end{aligned} \quad (\text{B.13})$$

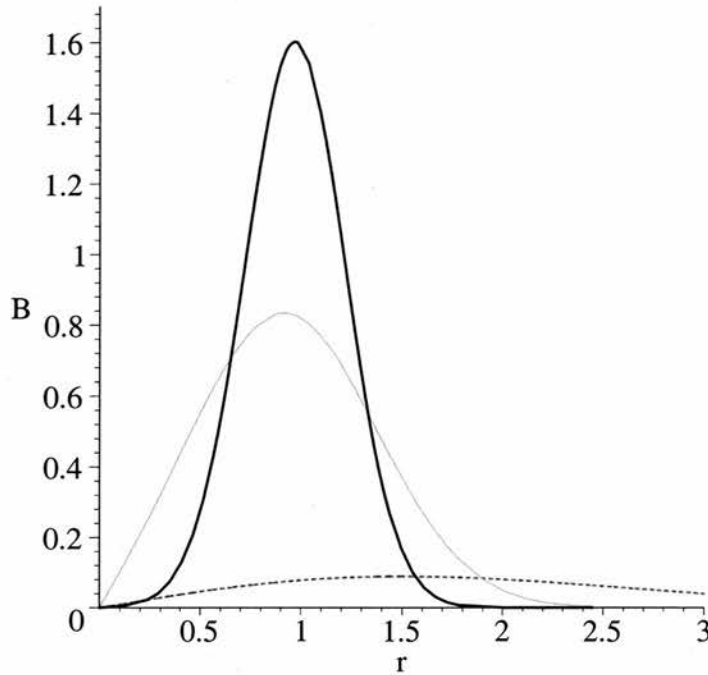


Figure B.1: B_θ plotted against radius for times $t = 0.03$ (black), $t = 0.1$ (grey) and $t = 1$ (dashed).

Now, the first term in (B.13) can be evaluated (using the property $I_0(0) = 1$) as

$$\begin{aligned}
 A(0, t) &= \frac{-B_0}{2\eta_0 t} \int_a^\infty s e^{-\frac{s^2}{4\eta_0 t}} ds \\
 &= \frac{-B_0}{2\eta_0 t} \left[-2\eta_0 t e^{-\frac{s^2}{4\eta_0 t}} \right]_a^\infty \\
 &= B_0 \left[0 - e^{-\frac{a^2}{4\eta_0 t}} \right] \\
 &= -B_0 e^{-\frac{a^2}{4\eta_0 t}}.
 \end{aligned} \tag{B.14}$$

Evaluating the second term in (B.13)

$$A(\infty, t) = \lim_{r \rightarrow \infty} \frac{-B_0}{2\eta_0 t} \int_a^\infty s e^{-\left(\frac{r^2+s^2}{4\eta_0 t}\right)} \sqrt{\frac{\eta_0 t}{\pi r s}} e^{\frac{rs}{2\eta_0 t}} ds,$$

using the property of the hyperbolic Bessel function that $I_0(x) \approx \frac{1}{\sqrt{2\pi x}} e^x$, $x \rightarrow \infty$. Simplifying, we obtain

$$A(\infty, t) = \lim_{r \rightarrow \infty} \frac{-B_0}{2\eta_0 t} \sqrt{\frac{\eta_0 t}{\pi r}} \int_a^\infty \sqrt{s} e^{-\frac{(s-r)^2}{4\eta_0 t}} ds.$$

Now, setting $S = s - r$ gives

$$A(\infty, t) = \lim_{r \rightarrow \infty} \frac{-B_0}{2\sqrt{\pi\eta_0 t}} \int_{a-r}^{\infty} \sqrt{\frac{r+S}{r}} e^{-\frac{S^2}{4\eta_0 t}} dS,$$

and since the term within the square root in the integrand approaches 1 as r approaches ∞ , this can be written as

$$A(\infty, t) = \frac{-B_0}{2\sqrt{\pi\eta_0 t}} \int_{-\infty}^{\infty} e^{-\frac{S^2}{4\eta_0 t}} dS.$$

Setting $u = S/\sqrt{4\eta_0 t}$ and simplifying gives

$$A(\infty, t) = \frac{-B_0}{\sqrt{\pi}} \int_{-\infty}^{\infty} e^{-u^2} du.$$

Now, we use the standard result $\int_{-\infty}^{\infty} e^{-U^2} dU = \sqrt{\pi}$ to finally obtain

$$A(\infty, t) = -B_0. \quad (\text{B.15})$$

Substituting (B.14) and (B.15) into (B.13), we find that the total magnetic flux behaves as

$$F = B_0 \left(1 - e^{\frac{a^2}{4\eta_0 t}} \right), \quad (\text{B.16})$$

and so as $t \rightarrow \infty$, $F \rightarrow 0$, and so the flux all decays away.

The result shows that in a configuration which is purely two-dimensional, magnetic flux can be ‘destroyed’ at an O-type null point of the magnetic field. The flux diffuses in towards the z -axis and eventually all annihilates there.

Appendix C: Non-existence of unique field line velocity in 3D

Theorem: For an isolated non-ideal region in a 3D MHD environment, a flux-conserving flow (\mathbf{w}) does not exist in general.

The term flux conserving flow is used to mean a flow which transports the magnetic flux, i.e. a flux or field line velocity. The proof is by contradiction.

Proof: Assume that a flux-conserving velocity (\mathbf{w}) does exist in the vicinity of an isolated non-ideal region (D), satisfying

$$\frac{\partial \mathbf{B}}{\partial t} = \nabla \times (\mathbf{w} \times \mathbf{B}). \quad (\text{C.1})$$

This equation may be integrated to give, in general,

$$\mathbf{E} + \mathbf{w} \times \mathbf{B} = \nabla \Phi, \quad (\text{C.2})$$

where Φ is a scalar potential. Outside D , in the ideal plasma, $\mathbf{w} = \mathbf{v}$ and $\nabla \Phi = 0$, i.e. Φ is a constant.

Taking the scalar product of (C.2) with \mathbf{B} gives

$$\mathbf{B} \cdot \mathbf{E} = \mathbf{B} \cdot \nabla \Phi, \quad (\text{C.3})$$

and so Φ can be calculated by evaluating

$$\Phi = \int E_{\parallel} ds, \quad (\text{C.4})$$

where E_{\parallel} is the component of \mathbf{E} parallel to \mathbf{B} , and the integration is performed along the magnetic field, so that s is a parameter along a magnetic field line.

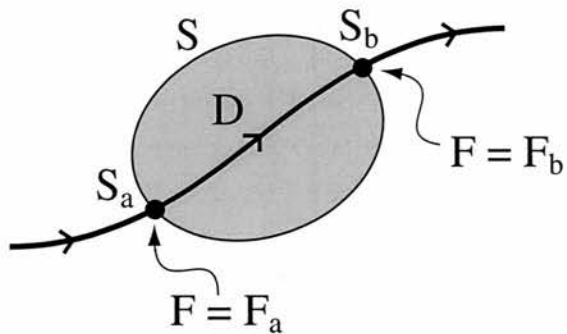


Figure C.1: A field line passing through the non-ideal region (D) enters D through the surface S_a , where the potential $\Phi = \Phi_a$, and leaves D through S_b , where $\Phi = \Phi_b$.

Now split the surface of the non-ideal region D into two parts, S_a and S_b , where S_a is defined as the part of the surface through which flux enters D , and so flux leaves D through S_b . Let Φ_a be the value of Φ on S_a , and $\Phi = \Phi_b$ on S_b (see Figure C.1). Assume that $\Phi_a = 0$. Since $\nabla\Phi = 0$ outside D , it follows that $\Phi_b = \Phi_a = 0$. However, since $\mathbf{E} \cdot \mathbf{B} \neq 0$ in general for reconnection in 3D, Equation (C.4) implies that in general $\Phi_b \neq 0$. This is a contradiction, thus invalidating the assumption that w exists. The proof demonstrates that there is no unique field line velocity which is consistent with the ideal surroundings.

Appendix D: CD information

Attached to this thesis is an accompanying CD, which contains additional material for many of the thesis chapters. To access this information, the file '*index.html*' should be opened in any web browser. This page gives a list of links to the files contained on the CD, together with descriptions of the parts of the thesis to which they are relevant.

The majority of the material on the CD is contained on HTML pages which can be accessed from this index page, and which should again be viewable in any standard web browser. Linked into these pages are a number of animations, which are of MPEG format, and so it may be necessary to download a relevant browser plug-in, for example RealPlayer, from the web browser homepage (for example, for Netscape browsers, see <http://wp.netscape.com/plugins/index.html>). Alternatively, the animations may be viewed in a suitable package directly from the files on the CD.

Finally, a number of extra calculations are provided for the models described in Chapters 3 and 4. These calculations have been carried out within the package 'Maple', and the worksheets provided were constructed in Maple version 8, although they should also compile in newer versions. These worksheets are contained within the folder '*maple_wksheets/*' on the CD. The output from each line in the Maple code on the worksheets has been suppressed for clarity. In order to view the output of a particular execution group, the colon at the end of the command should be replaced by a semi-colon. Information on Maple software may be found at <http://www.maplesoft.com>.

Appendix E: Maple commands

This appendix contains lists of the commands used in the symbolic computation package *Maple*, in order to do some of the calculations described in Chapters 3 and 4. The original Maple worksheets are contained on the CD which accompanies the thesis, and were constructed in Maple version 8.0. In addition to the commands themselves, in the following sections numbering (in parentheses) has been added in order to clearly distinguish each command from the next, and is not part of the worksheets themselves.

E.1 Input for maple worksheet *sp_rec_zsurf.mws*

The following gives the Maple commands used in the calculation described in Chapter 3.

```
> restart;with(plots):with(linalg):
> (1)

> B:=[B0*R, B0*j*R/2, B0*(-2)*z];
> (2)

> divB:=diverge(B, [R, theta, z], coords=cylindrical);
> (3)

> J:=curl(B, [R, theta, z], coords=cylindrical);
```

```
> (4)
> eta:=eta0*piecewise(R^2< a^2 and
> z^2< b^2, ((R/a)^6-1)^2*((z/b)^6-1)^2, 0);
> (5)
> eta_inner:=eta0*((R/a)^6
> -1/6)^2*((z/b)^6-1)^2;
> JdotB:=dotprod(J,B, orthogonal):
> (7)
> integrand:=simplify(subs(z=z0*exp(-2*B0*s),
> R=R0*exp(B0*s),JdotB*expand(eta_inner))): 
> (8)
> Phi:=simplify(int(intrand,
> s=ln((abs(z0/b))^(1/(2*B0)))..s1)):
> (9)
> Phimax:=simplify(subs(s1=ln((a/R0)^(1/B0)),Phi)):
> (10)
> Phi_R0z0:=piecewise(s1<ln((abs(z0/b))^(1/(2*B0)))
> ,0,s1<ln((a/R0)^(1/B0)) and R0^2*z0< a^2*b,Phi,
> s1>ln((abs(z0/b))^(1/(2*B0))) and
> R0^2*z0< a^2*b,Phimax,0):
> (11)
> Phi_Rz:=simplify(subs(R0=R*sqrt(z/z0),
> z0=z*exp(2*s1*B0),Phi_R0z0),assu
> me=positive):
```

```
> #Manual simplification necessary-
> (12)
> Phi_Rz_simp := 
> PIECEWISE([signum(z)*72/91*B0*j*eta0*b, b^2<z^2],
> [1/455*B0*j*eta0*(65*R
> ^12*z^13-910*R^12*z^7*b^6-91*R^12*b^12*z
> -91*R^6*z^13*a^6+455*R^6*z^7*a
> ^6*b^6+455*R^6*a^6*b^12*z+35*a^12*z^13
> -130*a^12*z^7*b^6+455*a^12*b^12*
> z+signum(z)*936*z^6*R^12*b^7
> -819*a^6*R^6*z^3*b^10)/a^12/b^12, R<a and
> R^4*z^2-a^4*b^2 < 0],
> [9/455*B0*j*eta0*(R^26*z^13-
> 65*R^14*z^7*b^6*a^12+91*a^24*R^2*z*b^12
> +signum(z)*104*R^12*z^6*b^7*a^14
> -91*a^20*R^6*z^3*b^10)/a^26/b^12,
> R^4*z^2-a^4*b^2 < 0],
> [signum(z)*72/91*B0*j*eta0*b, otherwise]): 
> (13)
> Phimax_simp := 
> PIECEWISE([9/455*B0*j*eta0*
> (R^26*z^13-65*R^14*z^7*b^6*a^12+91*a^24*R^2
> *z*b^12+signum(z)*104*R^12*z^6*b^7*a^14
> -91*a^20*R^6*z^3*b^10)/a^26/b^1
> 2, R^4*z^2-a^4*b^2 < 0],
> [signum(z)*72/91*B0*j*eta0*b, otherwise]): 
> (14)
> E:=grad(Phi_Rz_simp,
> [R, theta, z], coords=cylindrical):
```

```
> (15)
> v_perp:=simplify(crossprod(matadd(E,-eta*J),
> B/dotprod(B,B,orthogonal))):
> (16)
> v := simplify(matadd(v_perp, -v_perp[3]/B[3]*B)):
> (17)
> Bcart:=[B0*(x-j*y/2),
> B0*(y+j*x/2),B0*(-2*z)]:
> (18)
> v_perp_cart:=simplify(subs(R=sqrt(x^2+y^2),
> [v_perp[1]*x/(x^2+y^2)^(1/2) -
> v_perp[2]*y/(x^2+y^2)^(1/2) ,
> v_perp[1]*y/(x^2+y^2)^(1/2) +
> v_perp[2]*x/(x^2+y^2)^(1/2)])):
> #Now add an ideal flow-
> (19)
> phi_id :=
> phi0*(-cos(1/4*j*ln(z0/z))*x^2*sin(1/4*j*ln(z0/z))
> +2*cos(1/4*j*ln(z0/z
> ))^2*x*y-x*y+y^2*sin(1/4*j*ln(z0/z))*_
> cos(1/4*j*ln(z0/z)))/z0*z
> (20)
> E_id:=grad(phi_id, [x,y,z]):
> (21)
> v_id:=simplify(crossprod(E_id,Bcart/
> (dotprod(Bcart,Bcart,orthogonal)),
> orthogonal)):
> (22)
> phitot:=phi_id+subs(R=sqrt(x^2+y^2),Phi4):
```

```
> (23)
> phitot:=phi_id+subs(R=sqrt(x^2+y^2),Phi_Rz_simp):
> (24)
> vtot:=matadd(v_id,[v_perp_cart[1],
> v_perp_cart[2],subs(R=sqrt(x^2+y^2),
> v_perp[3])]):
> (25)
> vtot1 := simplify(matadd(vtot,
> -vtot[3]/Bcart[3]*Bcart)):
> (26)
> Phi_in:=phi_id:
> (27)
> Phi_out:=phi_id+subs(R=sqrt(x^2+y^2),Phimax_simp):
> (28)
> w_perp_in:=simplify(crossprod(grad(Phi_in,
> [x, y, z]),Bcart/dotprod(Bcart,Bcart,
> orthogonal))):
> (29)
> w_perp_out:=simplify(crossprod(grad(Phi_out,
> [x, y, z]),Bcart/dotprod(Bcart,Bcart,
> orthogonal))):
```

E.2 Input for maple worksheet *fan_rec_jconst.mws*

The following gives the Maple commands for the calculations carried out in Chapter 4, when solving to find the electric field and plasma velocity in the case where the current is constant.

```
> (1)
> restart:with(plots):with(linalg):
```

```
> (2)
> B:=[B0*x, B0*(y-j*z),B0*(-2*z)];
> (3)
> J:=curl(B,[x, y, z]);
> (4)
> JdotB:=dotprod(J,B,orthogonal);
> (5)
> Blines:=dsolve({diff(X(s),s)= B0*X(s),diff(Y(s),s)=
> B0*(Y(s)-j*Z(s)), diff(Z(s),s)=B0*(-2*Z(s))} ,
> {X(s),Y(s),Z(s)}):
> (6)
> eval(subs(Z(s)=z0,s=0,Blines[1])):
> eval(subs(s=0,X(s)=x0,Blines[2])):
> eval(subs(s=0,Y(s)=y0,Blines[3])):
> (7)
> Blin:=subs(_C3 = x0, _C2=z0,_C1=y0-j/3*z0,Blines);
> (8)
> Blineq:=simplify(solve(%,{x0,y0,z0})):
> (9)
> eta:=piecewise(R_1<a and
> z^2< b^2,eta0*((R_1/a)^2-1)^2*((z/b)^2-1)^2,0);
> (10)
> R0_1:=sqrt(x0^2+(y0-j*z0/3)^2);
> (11)
> R_1:=sqrt(x^2+(y-j*z/3)^2);
```

```
> (12)
> eta_inner:=
> eta0*((R_1/a)^2-1)^2*((z/b)^2-1)^2;
> (13)
> eta_in:=simplify(subs(z=z0*exp(-2*B0*s),
> x=x0*exp(B0*s), y=1/3*exp(-2*B0*s)*j*z0
> +exp(B0*s)*(y0-1/3*j*z0),eta_inner));
> (14)
> JdotB:=dotprod(J,B,orthogonal);
> (15)
> integrand:=eta_in*subs(x=x0*exp(B0*s),JdotB);
> (16)
> assume(R>0);assume(R0>0);assume(b>0);
> (17)
> Phi_0:=q*j*B0*x0;
> (18)
> Phi:=Phi_0+simplify(int(intrand,s=0..s1));
> (19)
> Phimax:=simplify(subs(s1=1/B0*ln(a/R0_1),Phi));
> (20)
> Phi_X0:=subs(piecewise(z^2>b^2,
> Phi_0,R_1<a and z<a^2*b/R_1^2
> ,Phi,R_1>a and z<a^2*b/R_1^2,Phimax,Phi_0));
> (21)
> Phi_final:=simplify(subs(x0 =
> x*exp(-B0*s1),y0=-1/3*(-3*y*exp(-2*B0*s1)-
> j*z*exp(-2*B0*s1)-exp(B0*s1)
> *j*z)*exp(B0*s1),
> s1=1/2/B0*ln(z0/z),z0=b, Phi_X0));
```

```
> (22)
> qstar:=32/21*eta0;
> (23)
> phi_neg:=subs(y=-y,z=-z,Phi_final):
> (24)
> Phi_final_tot:=piecewise(z>=0,Phi_final,
> z<0,phi_neg):
> (25)
> E:=grad(Phi_final_tot,[x,y,z]):
> (26)
> v_perp:=simplify(crossprod(matadd(E,-eta*J),
> B/dotprod(B,B,orthogonal))):
```

```
> (27)
> Phi_max:=piecewise(z<a^2*b/R_1^2,Phimax,Phi_0):
> (28)
> Phi_in:=simplify(subs(x0=x*exp(-B0*s1),
> s1=1/2/B0*ln(z0/z),z0=b,Phi_0)):
> (29)
> Phi_out:=simplify(subs(x0=x*exp(-B0*s1),
> y0=-1/3*(-3*y*exp(-2*B0*s1)+j*z*exp(-2*B0*s1)-
> exp(B0*s1)*j*z)*exp(B0*s1),
> s1=1/2/B0*ln(z0/z),z0=b, Phi_max)):
> (30)
> phi_in_neg:=subs(y=-y,z=-z,Phi_in):
> (31)
> phi_out_neg:=subs(y=-y,z=-z,Phi_out):
> (32)
> Phi_final_in:=piecewise(z>=0,Phi_in,
> z<0,phi_in_neg):
> (33)
> Phi_final_out:=piecewise(z>=0,Phi_out,
> z<0,phi_out_neg):
> (34)
> w_out:=simplify(crossprod(
> grad(Phi_final_out,[x,y,z]),
> B/dotprod(B,B,orthogonal))):
> (35)
> w_in:=simplify(crossprod(
> grad(Phi_final_in,[x,y,z]),
> B/dotprod(B,B,orthogonal))):
```

E.3 Input for maple worksheet *fan_rec_spcross.mws*

The following gives the Maple commands for the calculations carried out in Chapter 4, when solving to find the electric field and plasma velocity in the case where the current is zero in the fan plane.

```

> (1)

> restart:with(plots):with(linalg):
> (2)

> B:=[B0*x, B0*(y-j*z^3),B0*(-2*z)];

> (3)

> J:=curl(B,[x, y, z]);
> (4)

> Blines:=dsolve({diff(X(s),s)= B0*X(s),diff(Y(s),s)=
> B0*(Y(s)-j*(Z(s))^3),
> diff(Z(s),s)=B0*(-2*Z(s))},{X(s),Y(s),Z(s)}):
> (5)

> subs(_C2=z0,Blines[2]): 

> subs(% ,Blines[3]): 
> (6)

> simplify(diff(exp(s)*(y0 + j*z0^2/5*(exp(-5*s)-1)),s)):
> (7)

> Blines:={X(s)=x0*exp(B0*s),
> Y(s)=exp(B0*s)*(y0+j*z0^3/7*(exp(-7*B0*s)-1)),
> Z(s)=z0*exp(-2*B0*s)};
> (8)

> Blineq:=simplify(solve(%,{x0,y0,z0})); 

> (9)

> R_1:=sqrt((y-j*z^3/7)^2+x^2);
> (10)

> eta:=piecewise(R_1<a and
> z^2< b^2,eta0*((R_1/a)^2-1)^2*((z/b)^2-1)^2,0);

```

```
> (11)
> eta_in:=simplify(subs(z=z0*exp(-2*B0*s),
> x=x0*exp(B0*s),
> y=exp(B0*s)*(y0+1/7*j*z0^3*(exp(-7*B0*s)-1))
> ,eta0*((R_1/a)^2-1)^2*((z/b)^2-1)^2));
> (12)
> JdotB:=dotprod(J,B,orthogonal):
> (13)
> integrand:=eta_in*subs(z=z0*exp(-2*B0*s),
> x=x0*exp(B0*s),JdotB):
> (14)
> x_env:=sqrt(a^2*b/z-(y-j*z^3/7)^2);
> (15)
> Phi_0:=q*x0*z0^2;
> (16)
> Phi:=Phi_0+simplify(int(integrand,s=0..s1)):
> (17)
> Phimax:=simplify(subs
> (s1=ln((a/((y0-j*z0^2/5)^2+x0^2))^(1/2/B0)),Phi)):
> (18)
> Phi1:=subs(piecewise(z^2>=b^2,Phi_0,R_1<a and
> x^2<x_env^2,Phi,R_1>a
> and x^2<x_env^2,Phimax,Phi_0));
> (19)
> Phi2:=simplify(subs
> (y0=1/5*(5*y*exp(-4*B0*s1)-exp(-4*B0*s1)*j*z^2+
> exp(B0*s1)*j*z^2)*exp(3*B0*s1), x0=x*exp(-B0*s1),
> s1=1/2/B0*ln(z0/z), Phi1));
> (20)
> qstar:=-384160*eta0*B0*j*b^6*a^4/(924385*b^6*a^4);
```

```

> (21)
> phi_pos:=subs(z0=b,Phi2):
> (22)
> phi_neg:=subs(z0=b,y=-y,z=-z,Phi2):
> (23)
> Phitot:=piecewise(z>=0,phi_pos,z<0,phi_neg):
> (24)
> E:=simplify(grad(Phitot,[x,y,z])):
> (25)
> v_perp:=simplify(crossprod(matadd(E,-eta*J),
> B/dotprod(B,B,orthogonal)
> )):
```

E.4 Input for maple worksheet *fan_rec_fancross.mws*

The following gives the Maple commands for the calculations carried out in Chapter 4, when solving to find the electric field and plasma velocity in the case where the current is zero on the spine.

```

> (1)
> restart:with(plots):with(linalg):
> (2)
> B:=[B0*x, B0*y,B0*(-2*z+j*y^3/3)];
> (3)
> J:=curl(B,[x, y, z]);
> (4)
> Blines:=dsolve({diff(X(s),s)=
> B0*X(s),diff(Y(s),s)=B0*Y(s),
> diff(Z(s),s)=B0*(-2*Z(s)+j*(Y(s))^3/3)},
> {X(s),Y(s),Z(s)}):
> (5)
> subs(_C2=y0,Blines[2]): simplify(subs(% ,Blines[3])):
```

```
> (6)
> zz:=simplify(subs(_C1=z0-j*y0^3/15,
> 1/3*(B0*j*y0^3*int(exp(5*B0*s),s) +
> 3*_C1)*exp(-2*B0*s)) :
> (7)
> Blines:=(X(s)=x0*exp(B0*s), Y(s)=y0*exp(B0*s),
> Z(s) = 1/15*(j*y0^3*exp(5*B0*s)+15*z0-j*y0^3)*
> exp(-2*B0*s));
> (8)
> Blineq:=simplify(solve(%,{x0,y0,z0})); 
> (9)
> R=R0*exp(B0*s);
> (10)
> Z_1=Z_1_0*exp(-2*B0*s);
> (11)
> eta:=piecewise(R<a and z_1^2<b^2,
> eta0*((R/a)^2-1)^2*((z_1/b)^2-1)^2,0);
> (12)
> eta_in:=simplify(subs(R=R0*exp(B0*s),
> z_1=z_1_0*exp(-2*B0*s)
> ,eta0*((R/a)^2-1)^2*((z_1/b)^2-1)^2)):
> (13)
> JdotB:=simplify(dotprod(J,B,orthogonal)):
> (14)
> integrand:=subs(R0=sqrt(x0^2+y0^2),eta_in)*
> subs(x=x0*exp(B0*s),y=y0*exp(B0*s),JdotB);
```

```
> (15)
> assume(b>0);
> (16)
> Phi:=simplify(int(integrand,s=0..s1)):
> (17)
> Phimax:=simplify(subs(
> s1=ln((a/(sqrt(y0^2+x0^2)))^(1/B0)),Phi)):
> (18)
> Phi1:=subs(piecewise(
> z_1^2>=b^2,0,R<a and z_1<(a^2*b)/R^2 ,Phi,R>a and
> z_1<(a^2*b)/R^2 ,Phimax,0)):
> (19)
> Phi_pos:=simplify(subs(
> x0=x*exp(-B0*s1), y0=y*exp(-B0*s1),
> z_1_0=z_1*exp(2*B0*s1),
> s1=1/2/B0*ln(z_1_0/z_1), z_1_0=b, Phi1)):
> (20)
> Phi_neg=subs(z_1=-z_1,Phi_pos):
> (21)
> b:='b';
```

```
> #Manual simplification necessary-
> (22)
> Phi_pos2:=PIECEWISE([0, b^2 <= z_1^2],
> [-1/105*eta0*B0*y^2*x*
> (448*y^2*z_1^(5/2)*b^(3/2)*a^2-
> 420*x^2*b^2*a^2*z_1^2+42*y^2*b^4*a^2-
> 70*y^2*a^2*z_1^4+448*x^2*z_1^(5/2)*b^(3/2)*a^2-
> 70*x^2*a^2*z_1^4-35*a^4*b^4+105*x^4*z_1^4+
> 210*x^2*y^2*z_1^4+70*y^4*b^2*z_1^2+
> 224*b^(5/2)*z_1^(3/2)*a^4-210*a^4*b^2*z_1^2-
> 420*y^2*b^2*a^2*z_1^2+21*a^4*z_1^4-
> 30*x^2*b^4*y^2-160*b^(1/2)*z_1^(7/2)*x^4-
> 160*b^(1/2)*z_1^(7/2)*y^4+105*y^4*z_1^4-
> 15*y^4*b^4-15*x^4*b^4+70*x^4*b^2*z_1^2-
> 320*b^(1/2)*z_1^(7/2)*x^2*y^2+42*x^2*b^4*a^2+
> 140*x^2*b^2*y^2*z_1^2)/a^4/b^4,
> (x^2+y^2)^(1/2)-a < 0 and
> (z_1*(x^2+y^2)-a^2*b)/(x^2+y^2) < 0]
> ,
```

```

> [-1/105*eta0*B0*y^2*x*
> (-320*x^2*z_1^(7/2)*y^2+448*x^2*z_1^(5/2)*b*a^2-
> 420*b^(3/2)*a^3/((x^2+y^2))^(1/2)*y^2*z_1^2-
> 160*x^4*z_1^(7/2)-160*y^4*z_1^(7/2)+
> 21/b^(1/2)/a*(z_1*(x^2+y^2))^(5/2)*z_1^(3/2)+
> 140*b^(3/2)*a^3/((x^2+y^2))^(3/2)*x^2*z_1^2*y^2-
> 70/b^(1/2)/a*(z_1*(x^2+y^2))^(3/2)*x^2*z_1^(5/2)+
> 70*b^(3/2)*a^3/(x^2+y^2)^(3/2)*y^4*z_1^2-
> 420*b^(3/2)*a^3/(x^2+y^2)^(1/2)*x^2*z_1^2+
> 210/b^(1/2)/a*(z_1*(x^2+y^2))^(1/2)*x^2*z_1^(7/2)*y^2+
> 42*x^2*b^(7/2)*a^7/((x^2+y^2))^(5/2)-
> 30*b^(7/2)*a^7/((x^2+y^2))^(7/2)*x^2*y^2+
> 224*a^4*b^2*z_1^(3/2)+448*y^2*z_1^(5/2)*b*a^2-
> 15*b^(7/2)*a^7/((x^2+y^2))^(7/2)*y^4-
> 15*b^(7/2)*a^7/((x^2+y^2))^(7/2)*x^4+
> 105/b^(1/2)/a*(z_1*(x^2+y^2))^(1/2)*y^4*z_1^(7/2)+
> 42*y^2*b^(7/2)*a^7/((x^2+y^2))^(5/2)+
> 105/b^(1/2)/a*(z_1*(x^2+y^2))^(1/2)*x^4*z_1^(7/2)-
> 70/b^(1/2)/a*(z_1^2*(x^2+y^2))^(3/2)*y^2*z_1-
> 210*b^(3/2)*a^3*((x^2+y^2))^(1/2)*z_1^2-
> 35*b^(7/2)*a^7/((x^2+y^2))^(3/2)+
> 70*b^(3/2)*a^3/((x^2+y^2))^(3/2)*x^4*z_1^2)/b^(7/2)/a^4,
> -(x^2+y^2)^(1/2)+a < 0 and
> (z_1*(x^2+y^2)-a^2*b)/(x^2+y^2) < 0],
> [0, otherwise]):
```

(23)

```

> Phi_neg2:=subs(z_1=-z_1,Phi_pos2):
> (24)
> Phitot:=piecewise(z_1>0, Phi_pos2, Phi_neg2):
```

```
> (25)
> E:=simplify(grad(subs
> (R=sqrt(x^2+y^2),z_1=z-j*y^3/15,Phitot),
> [x,y,z])):
> (26)
> v_perp:=simplify(crossprod(matadd
> (E,-subs(R=sqrt(x^2+y^2),z_1=z-j*y^3/15,eta)*J),
> B/dotprod(B,B,orthogonal))):
```

Bibliography

- Alfvén, H. (1950). *Cosmical electrodynamics*. Oxford University Press.
- Antiochos, S. K., Karpen, J. T., and DeVore, C. R. (2002). Coronal magnetic field relaxation by null-point reconnection. *Astrophys. J.*, 575:578–584.
- Aubrey, M. P., Russell, C. T., and Kivelson, M. G. (1970). Inwards motions of the magnetopause before a substorm. *J. Geophys. Res.*, 75:7018–7031.
- Baker, D. A. (1984). *Magnetic reconnection in space and laboratory plasmas*, pages 332–340. Amer. Geophys. Union, Washington DC.
- Barton, G. (1989). *Elements of Green's functions and propagation*. Oxford Science Publications.
- Berger, M. A. (1984). Rigorous new limits on magnetic helicity dissipation in the solar corona. *Geophys. Astrophys. Fluid Dynamics*, 30:79–104.
- Berger, M. A. (1986). Topological invariants of field lines rooted to planes. *Geophys. Astrophys. Fluid Dynamics*, 34:265–281.
- Berger, M. A. (1999). Introduction to magnetic helicity. *Plasma Phys. Control. Fusion*, 41:B167–B175.
- Biskamp, D. (2000). *Magnetic reconnection in plasmas*. Cambridge University Press, Cambridge.
- Boyd, T. J. M. and Sanderson, J. J. (2003). *The physics of plasmas*. Cambridge University Press, Cambridge.
- Brown, D. S. (1999). *Three-dimensional topology of solar coronal magnetic fields*. PhD thesis, University of St Andrews.
- Brown, D. S. and Priest, E. R. (1999a). The topological behaviour of stable magnetic separators. *Solar Phys.*, 190:25–33.
- Brown, D. S. and Priest, E. R. (1999b). Topological bifurcations in three-dimensional magnetic fields. *Proc. R. Soc. Lond. A*, 455:3931–3951.
- Brown, D. S. and Priest, E. R. (2000). Topological differences and similarities between force-free and potential models of coronal magnetic fields. *Solar Phys.*, 194:197–204.

- Brown, D. S. and Priest, E. R. (2001). The topological behaviour of 3D null points in the Sun's corona. *Astron. Astrophys.*, 367:339–346.
- Bulanov, S. V. and Olshanetsky, M. A. (1984). Magnetic collapse near zero points of the magnetic field. *Phys. Lett.*, 100:35–38.
- Bulanov, S. V. and Sakai, J. (1997). Magnetic collapse in incompressible plasma flows. *J. Phys. Soc. Jpn.*, 66(11):3477–3483.
- Coroniti, F. V. (1981). On the magnetic viscosity in Keplerian accretion disks. *Astrophys. J.*, 244:587–599.
- Cowley, S. W. H. (1973). A qualitative study of the reconnection between the Earth's magnetic field and an interplanetary field of arbitrary orientation. *Radio Sci.*, 8:903–913.
- Craig, I. J. D. and Fabling, R. B. (1996). Exact solutions for steady-state, spine, and fan magnetic reconnection. *Astrophys. J.*, 462:969–976.
- Craig, I. J. D. and Watson, P. G. (2002). Magnetic reconnection solutions based on a generalised Ohm's law. *Solar Phys.*, 214:131–150.
- Crooker, N. U. (1979). Dayside merging and cusp geometry. *J. Geophys. Res.*, 84:951–959.
- Dahlburg, R. B., Antiochos, S. K., and Norton, D. (1997). Magnetic flux tube tunneling. *Phys. Rev. E*, 56:2094–2103.
- Dubrovin, B. A., Fomenko, A. T., and Novikov, S. P. (1990). *Modern geometry - Methods and applications. Part II. The geometry and topology of manifolds*. Springer-Verlag, New York.
- Finn, J. M. and Guzdar, P. N. (1991). Formation of a flux-core spheromak. *Phys. Fluids B*, 3:1041–1051.
- Fletcher, L., Metcalf, T. R., Alexander, D., Brown, D. S., and Ryder, L. A. (2001). Evidence for the flare trigger site and three-dimensional reconnection in multiwavelength observations of a solar flare. *Astrophys. J.*, 554:451–463.
- Forbes, T. G. (1988). Magnetic reconnection models of flares. In *Activity in cool star envelopes*, pages 115–124. Kluwer Academic Publishers, Dordrecht.
- Forbes, T. G. and Priest, E. R. (1984). Numerical simulation of reconnection in an emerging magnetic flux region. *Solar Phys.*, 94:315–340.
- Galsgaard, K. (2000). Dynamical investigation of three-dimensional reconnection in quasi-separatrix layers in a boundary-driven magnetic field. *J. Geophys. Res.*, 105:5119–5134.
- Galsgaard, K. and Nordlund, A. (1996). Heating and activity of the solar corona: 1.

- Boundary shearing of an initially homogeneous magnetic field. *J. Geophys. Res.*, 101:13445–13460.
- Galsgaard, K. and Nordlund, A. (1997). Heating and activity of the solar corona: 3. Dynamics of a low beta plasma with 3D null points. *J. Geophys. Res.*, 102:231–248.
- Galsgaard, K., Priest, E. R., and Nordlund, A. (2000). Three-dimensional separator reconnection- How does it occur? *Solar Phys.*, 193:1–16.
- Galsgaard, K., Reddy, R. V., and Rickard, G. J. (1997). Energy release sites in magnetic fields containing single or multiple nulls. *Solar Phys.*, 176:299–325.
- Galsgaard, K., Titov, V. S., and Neukirch, T. (2003). Magnetic pinching of hyperbolic flux tubes. II. Dynamic numerical model. *Astrophys. J.*, 595:506–516.
- Golub, L. and Pasachoff, J. M. (2001). *Nearest Star: The surprising science of our sun*. Harvard University Press.
- Gorbachev, V. S. (1988). *The field topology and frozen-in magnetohydrodynamic flows of plasma in the strong field approximation*. PhD thesis, Moscow Institute of Physics and Engineering.
- Greene, J. M. (1988). Geometrical properties of three-dimensional reconnecting magnetic fields with nulls. *J. Geophys. Res.*, 93:8583–8590.
- Heyvaerts, J., Priest, E. R., and Rust, D. M. (1977). An emerging flux model of the solar flare phenomenon. *Astrophys. J.*, 216:123–137.
- Hones, E. W., J. (1973). Plasma flow in the plasma sheet and its relation to substorms. *Radio Sci.*, 8:979–990.
- Hornig, G. (2001). *An introduction to the geometry and topology of fluid flows*, pages 295–313. Kluwer, Dordrecht.
- Hornig, G. and Priest, E. R. (2003). Evolution of magnetic flux in an isolated reconnection process. *Phys. Plasmas*, 10(7):2712–1721.
- Hornig, G. and Schindler, K. (1996). Magnetic topology and the problem of its invariant definition. *Phys. Plasmas*, 3:781–791.
- Hyman, J. M. (1979). A method of lines approach to the numerical solution of conservation laws. In *Advances in computer methods for partial differential equations III*, pages 313–343. IMACS.
- Imshennik, V. S. and Syrovatsky, S. I. (1967). Two-dimensional flow of an ideally conducting gas in the vicinity of the zero line of a magnetic field. *Sov. Phys. JETP*, 25:656–664.
- Innes, D. E., Inhester, B., Axford, W. I., and Wilhelm, K. (1997). Bi-directional plasma jets produced by magnetic reconnection on the Sun. *Nature*, 386:811–813.

- Inverarity, G. W. and Priest, E. R. (1999). Magnetic null points due to multiple sources of solar photospheric flux. *Solar Phys.*, 186:99–121.
- Inverarity, G. W. and Titov, V. S. (1997). Formation of current layers in three-dimensional inhomogeneous coronal magnetic fields by photospheric motions. *J. Geophys. Res.*, 102:22285–22293.
- Klapper, I. (1998). Constraints on finite-time current sheet formation at null points in two-dimensional ideal incompressible MHD. *Phys. Plasmas*, 5:910–914.
- Klapper, I., Rado, A., and Tabor, M. (1996). A Lagrangian study of dynamics and singularity formation at magnetic null points in ideal three-dimensional magnetohydrodynamics. *Phys. Plasmas*, 3(11):4281–4283.
- Kliem, B. and Schumacher, J. (2001). Dynamic three-dimensional spontaneous reconnection in a sheared current sheet. In *Space plasma simulation*, pages 264–267. Katlenburg-Lindau: Copernicus Gesellschaft.
- Lau, Y. T. and Finn, J. M. (1990). Three dimensional kinematic reconnection in the presence of field nulls and closed field lines. *Astrophys. J.*, 350:672–691.
- Lau, Y. T. and Finn, J. M. (1996). Magnetic reconnection and the topology of interacting twisted flux tubes. *Phys. Plasmas*, 3:3983–3997.
- Linton, M. and Antiochos, S. K. (2002). Theoretical energy analysis of reconnecting twisted magnetic flux tubes. *Astrophys. J.*, 581:703–717.
- Linton, M., Dahlburg, R. B., and Antiochos, S. K. (2001). Reconnection of twisted flux tubes as a function of contact angle. *Astrophys. J.*, 553:905–921.
- Linton, M. and Priest, E. R. (2003). Three-dimensional reconnection of untwisted flux tubes. *Astrophys. J.*, 595:1259–1276.
- Longcope, D. W. (1996). Topology and current ribbons: A model for current, reconnection and flaring in a complex, evolving corona. *Solar Phys.*, 169:91–121.
- Longcope, D. W., Brown, D. S., and Priest, E. R. (2003). On the distribution of magnetic null points above the solar photosphere. *Phys. Plasmas*, 10:3321–3334.
- Lothian, R. M. and Browning, P. K. (1995). Coronal magnetic field equilibrium with discrete flux sources. *Solar Phys.*, 161:289–316.
- Maclean, R. C., Beveridge, C., Longcope, D. W., Brown, D. S., and Priest, E. R. (2004). A topological analysis of the magnetic breakout model for an eruptive solar flare. Submitted to *Proc. R. Soc. Lond.*
- Mellor, C., Gerrard, C., Galsgaard, K., Hood, A. W., and Priest, E. R. (2004). Numerical simulations of the flux tube tectonics model for coronal heating. Submitted.
- Mellor, C., Titov, V. S., and Priest, E. R. (2002). Linear collapse of spatially linear 2D

- null points. *J. Plasma Phys.*, 68:221–235.
- Mellor, C., Titov, V. S., and Priest, E. R. (2003). Linear collapse of spatially linear 3D potential null points. *Geophys. Astrophys. Fluid Dynamics*, 97(6):489–505.
- Mestel, L. (1999). *Stellar magnetism*. Oxford University Press, Oxford.
- Mestel, L. and Strittmatter, P. A. (1967). The magnetic field of a contracting gas cloud. II. Finite diffusion effects - an illustrative example. *Mon. Not. Roy. Astron. Soc.*, 137:95–105.
- Milano, L. J., Dmitruk, P., Mandrini, C. H., Gómez, D. O., and Démoulin, P. (1999). Quasi-separatrix layers in a reduced magnetohydrodynamic model of a coronal loop. *Astrophys. J.*, 521:889–897.
- Milroy, R. D. (1984). *Magnetic reconnection in space and laboratory plasmas*, pages 305–312. Amer. Geophys. Union, Washington DC.
- Moffatt, H. K. (1978). *Magnetic field generation in electrically conducting fluids*. Cambridge University Press, Cambridge.
- Mullan, D. (1986). *The M-type stars*, pages 455–479. NASA SP-492, Washington DC.
- Neukirch, T., Titov, V. S., and Galsgaard, K. (2004). Magnetic pinching of hyperbolic flux tubes. III. Quasi-static force-free evolution. In preparation.
- Newcomb, W. A. (1958). Motion of magnetic lines of force. *Ann. Phys.*, 3:347–385.
- Nordlund, A. and Galsgaard, K. (1997). A 3D MHD code for parallel computers. Technical report, Astronomical Observatory, Copenhagen University.
- Parker, E. N. (1979). *Cosmical magnetic fields*. Clarendon Press, Oxford.
- Parnell, C. E. and Galsgaard, K. (2004). Elementary heating events - Magnetic interactions between two flux sources. II Flux connectivity. *Astron. Astrophys.*, in press.
- Parnell, C. E., Neukirch, T., Smith, J. M., and Priest, E. R. (1997). Structure and collapse of three-dimensional magnetic neutral points. *Geophys. Astrophys. Fluid Dynamics*, 84:245–271.
- Parnell, C. E., Priest, E. R., and Golub, L. (1994). The three-dimensional structures of X-ray bright points. *Solar Phys.*, 151:57–74.
- Parnell, C. E., Smith, J. M., Neukirch, T., and Priest, E. R. (1996). The structure of three-dimensional magnetic neutral points. *Phys. plasmas*, 3(3):759–770.
- Petschek, H. E. (1964). *Magnetic field annihilation*, pages 425–439. NASA SP-50, Washington, D.C.
- Pontin, D. I., Hornig, G., and Priest, E. R. (2004a). Kinematic reconnection at a magnetic null point: Fan-aligned current. submitted.
- Pontin, D. I., Hornig, G., and Priest, E. R. (2004b). Kinematic reconnection at a magnetic

- null point: Spine-aligned current. *Geophys. Astrophys. Fluid Dynamics*, 98:407–428.
- Pontin, D. I., Priest, E. R., and Longcope, D. (2003). A framework for understanding the topology of complex coronal structures. *Solar Phys.*, 212:319–342.
- Priest, E. R. (1982). *Solar magnetohydrodynamics*. Kluwer Academic Publishers.
- Priest, E. R., Bungey, T. N., and Titov, V. S. (1997). The 3D topology and interaction of complex magnetic flux systems. *Geophys. Astrophys. Fluid Dynamics*, 84:127–163.
- Priest, E. R. and Démoulin, P. (1995). Three-dimensional magnetic reconnection without null points. 1. Basic theory of magnetic flipping. *J. Geophys. Res.*, 100:23443–23463.
- Priest, E. R. and Forbes, T. G. (1986). New models for fast steady-state magnetic reconnection. *J. Geophys. Res.*, 91:5579–5588.
- Priest, E. R. and Forbes, T. G. (2000). *Magnetic reconnection: MHD theory and applications*. Cambridge University Press, Cambridge.
- Priest, E. R., Heyvaerts, J. F., and Title, A. M. (2002). A Flux-tube tectonics model for solar coronal heating driven by the magnetic carpet. *Astrophys. J.*, 576:533–551.
- Priest, E. R., Hornig, G., and Pontin, D. I. (2003a). On the nature of three-dimensional magnetic reconnection. *J. Geophys. Res.*, 108(A7):SSH6–1.
- Priest, E. R. and Lee, L. C. (1990). Nonlinear magnetic reconnection models with separatrix jets. *J. Plasma Phys.*, 44:337–360.
- Priest, E. R., Longcope, D. W., and Titov, V. S. (2003b). Binary reconnection and the heating of the solar corona. *Astrophys. J.*, 598:667–677.
- Priest, E. R. and Titov, V. S. (1996). Magnetic reconnection at three-dimensional null points. *Phil. Trans. R. Soc. Lond. A*, 354:2951–2992.
- Proctor, M. R. E., Matthews, P. C., and Rucklidge, A. M. (1993). *Solar and planetary dynamos*. Cambridge University Press, Cambridge.
- Romanova, M. M. and Lovelace, R. V. E. (1992). Magnetic field reconnection and particle acceleration in extragalactic jets. *Astron. Astrophys.*, 262:26–36.
- Russell, C. T. and Elphic, R. C. (1978). Initial ISEE magnetometer results: magnetopause observations. *Space Sci. Rev.*, 22:681–715.
- Schindler, K., Hesse, M., and Birn, J. (1988). General magnetic reconnection, parallel electric fields, and helicity. *J. Geophys. Res.*, 93(A6):5547–5557.
- Schrijver, C. J. and Title, A. M. (2002). The topology of a mixed-polarity potential field, and inferences for the heating of the quiet solar corona. *Solar Phys.*, 207:223–240.
- Schrijver, C. J. and Zwaan, C. (2000). *Solar and stellar magnetic activity*. Cambridge University Press, Cambridge.
- Seehafer, N. (1986). On the magnetic field line topology in solar active regions. *Solar*

- Phys.*, 105:223–235.
- Sonnerup, B. U. Ö., Paschmann, G., Papamastorakis, I., Sckopke, N., Haerendel, G., Bame, S. J., Asbridge, J. R., Gosling, J. T., and Russell, C. T. (1981). Evidence for magnetic field reconnection at the Earth’s magnetopause. *J. Geophys. Res.*, 86:10049–10067.
- Sonnerup, B. U. Ö. and Priest, E. R. (1975). Resistive MHD stagnation-point flows at a current sheet. *J. Plasma Phys.*, 14:283–294.
- Spanier, J. and Oldham, K. B. (1987). *An atlas of functions*. Hemisphere Publishing, New York.
- Sweet, P. A. (1958). The neutral point theory of solar flares. In *Electromagnetic phenomena in cosmical plasmas*, pages 123–134. Cambridge University Press, Cambridge.
- Title, A. M. (2000). Magnetic fields below, on and above the solar surface. *Phil. Trans. R. Soc. Lond.*, A358:657.
- Titov, V. S., Démoulin, P., and Hornig, G. (1999). Quasi-separatrix layers: Refined theory and its application to solar flares. In *Magnetic fields and solar processes*, pages 715–722. Eur. Space Agency Spec. Publ., Noordwijk.
- Titov, V. S., Galsgaard, K., and Neukirch, T. (2003). Magnetic pinching of hyperbolic flux tubes. I. Basic estimations. *Astrophys. J.*, 582:1172–1189.
- Titov, V. S., Hornig, G., and Démoulin, P. (2002). The theory of magnetic connectivity in the corona. *J. Geophys. Res.*, 107:SSH 3–1.
- Tout, C. and Pringle, J. E. (1992). Accretion disk viscosity - A simple model for a magnetic dynamo. *Mon. Not. Roy. Astron. Soc.*, 259:604–612.
- Verbunt, F. (1982). Accretion disks in stellar X-ray sources. *Space Sci. Rev.*, 32:379–404.
- Wesson, J. A. (1997). *Tokamaks*. Clarendon Press, Oxford.
- Yamada, M., Ono, Y., Hayakawa, A., and Katsurai, M. (1990). Magnetic reconnection of plasma toroids with cohelicity and counterhelicity. *Phys. Rev. Lett.*, 65:721–724.